Measurement of CP-Violating Asymmetries in the Flavor-Changing Neutral Current Decays of the B Meson

Yu Nakahama
Department of Physics, The University of Tokyo

February 2009

Abstract

B meson decays proceeding via flavor-changing neutral current $b \to s\overline{q}q$ or $b \to d\overline{q}q$ transitions, where q is a quark, are suppressed in the Standard Model $\mathcal{O}(10^{-5\sim-7})$ and may be sensitive to New Physics contributions affecting the internal quark loop of second order decay diagrams. Such New Physics contributions can add new weak phases and subsequently cause deviations from the Standard Model expectation for CP asymmetries. Due to the differences in weak phases and decay amplitudes in $b \to s$ and $b \to d$ transitions within the Standard Model, independent searches for new weak phases are possible.

The $B^0 \to \phi K^0_S$ decay, dominated by $b \to s\overline{s}s$ transitions, is considered to be the golden mode of $b \to s$ transitions due to its small theoretical uncertainty, while the $B^0 \to K^0_S K^0_S$ decay, dominated by $b \to d\overline{s}s$ transitions, is the analogous mode of $b \to d$ transitions.

We present measurements of CP asymmetries in the B^0 decays with $K^0_S K^+ K^-$ final state including $B^0 \to \phi K^0_S$, non-resonant $B^0 \to K^0_S K^+ K^-$ and $B^0 \to f_0 K^0_S$, as well as in the $B^0 \to K^0_S K^0_S$ decay. These results are obtained from a data sample containing 657×10^6 $B\overline{B}$ pairs collected on the $\Upsilon(4S)$ resonance with the Belle detector at the KEKB asymmetric-energy e^+e^- collider.

Using the traditional quasi-two-body time-dependent CP analysis, we have achieved the world's most precise measurement of CP asymmetry in the $B^0 \to K^0_S K^0_S$ decay, which is the only mode whose CP asymmetry is measured in $b \to d\overline{q}q$ transitions due to their extremely small branching fractions. We find no significant CP asymmetry in this decay and the result is consistent with the Standard Model expectation within the current statistics.

By newly employing the time-dependent Dalitz plot analysis to the B^0 decays with $K^0_S K^+ K^-$ final state, we directly measure the CP-violating phases in each significant decay channel, considering the interferences between them and potentially resolving two-fold ambiguity in the weak phases that arises in quasi-two-body time-dependent CP analyses. Evidence for CP violation at a significance of $3.9\,\sigma$ is found in the $B^0 \to \phi K^0_S$ decay and the result is consistent with the Standard Model expectation.

Acknowledgments

First, I would like to express my warm appreciation to my supervisor, Prof. H. Aihara, for giving me the opportunity to work on this research and his great supervision.

I appreciate Prof. M. Iwasaki for her helpful advice. I am also thankful to Dr. H. Kakuno for his powerful support and advice throughout my studies.

I am grateful to the members, students and alumni of our group at the University of Tokyo: Dr. T. Abe, Dr. N. Hastings, Dr. T. Uchida and Ms. K. Kono; Mr. H. Nakayama, Mr. H. Miyatake, Mr. H. Fujimori, Mr. S. Mineo, and Mr. C. Ng; Dr. A. Kusaka, Mr. K. Tanabe, Mr. R. Ishida, Mr. K. Ito and Mr. K. Yamada.

I would like to express my gratitude to all the members of the CP-fit, $b \to s$ and SVD groups in Belle, especially the members who were deeply involved in these analyses with me, Prof. Y. Sakai, Prof. H. Ishino, Dr. J. Dalseno, Dr. A. Garmash and Dr. P. Krokovny for fruitful discussions and suggestions. I especially wish to thank Dr. K. Sumisawa for his appropriate support and encouragement during this research for two years; and to the members who kindly taught me many essential analysis techniques and attitudes during my training days for CP analyses, Dr. T. Higuchi, Dr. K. Hara, and Dr. O. Tajima.

I also wish to express my thanks my friends in the Tsukuba Hall at KEK: Dr. J. Dalseno and Ms. M. Fujikawa for their encouragement and making my life pleasant there with them.

Finally, I am deeply indebted to my family; they always cheered me up whenever needed.

Contents

List of Figures

List of Tables

Chapter 1

Introduction

CP violation in the B-meson system was established by the observation of large mixing-induced CP asymmetry in $b \to c\bar{c}s$ tree transition decays [1, 2] measured by the two B factory experiments: Belle [3] at KEK and BaBar [4] at SLAC in 2001. CP violation can be explained by an irreducible phase in the quark mixing matrix [5] in the Standard Model of Particle Physics. Currently, experimental procedures to measure mixing-induced CP asymmetries [6] are firmly in place and contribute to the success of the Standard Model.

However, the field of Particle Physics still holds many exciting prospects where the effects of New Physics beyond the Standard Model can be explored. There are two possible approaches for this; the one is a direct search covered by the Large Hadron Collider [7], and the other is an indirect search through an interference between a New Physics process and the Standard Model process covered by the B factories mainly using B meson decays. In this thesis, we focus on the latter.

1.1 Research Motivations

The B meson decays mediated by flavor-changing neutral currents, such as $b \to sg$ and $b \to dg$ quark transitions, where g is a gluon, could be unique and good probes for New Physics beyond the Standard Model such as Supersymmetry by the following reasons: (1) Since first-order tree transitions are forbidden in the Standard Model in the flavor-changing neutral current B decays, leading order diagrams are box or loop diagrams such as $b \to sg$ and $b \to dg$ transitions, which are suppressed in the Standard Model $\mathcal{O}(10^{-5\sim-7})$. (2) Very massive particles from New Physics can exist in the $b \to sg$ and $b \to dg$ loop transitions due to the Uncertainty Principal. A probe of some New Physics contributions requires loop or box diagram: for example, contribution of Supersymmetric particles requires to be as a pair due to the conservation of R-parity. The $b \to sg$ and $b \to dg$ loop transitions can be sensitive to such processes. (3) Since generic B meson decays that proceed via $b \to c$ transitions are suppressed by the square of an quark mixing matrix elements, $|V_{cb}|^2 \sim 10^{-3}$,

rare B meson decay processes that are sensitive to contributions of New Physics are not too rare experimentally. We can somehow access these B decays by B factories using $\mathcal{O}(10^8)$ $B\overline{B}$ pairs. (4) Clear evidence of New Physics may be enhanced by the measurements of CP asymmetries in the $b \to sg$ and $b \to dg$ decays. Possible weak phase differences with and without the massive particles could induce deviations from the expectation of CP asymmetry from the Standard Model. The latter is well understood from quark mixing and free from the uncertainties from QCD hadronization. Possible weak phase differences in between the Standard model processes and New Physics processes can induce deviation from the expected CP asymmetry in the Standard Model. The CP asymmetry is not affected by any non-perturbative QCD effect and is well expected from quark mixing in the Standard Model if the specified $b \to sg$ and $b \to dg$ decay processes could be dominated by a single decay diagram.

To search for new weak phases in the flavor-changing neutral current B decays, CP asymmetries in $b \to sg$ transitions have actively been measured using several $b \to s$ decays. Figure 1.1 shows CP asymmetry measurements in selected $b \to s$ decays at the B factories.

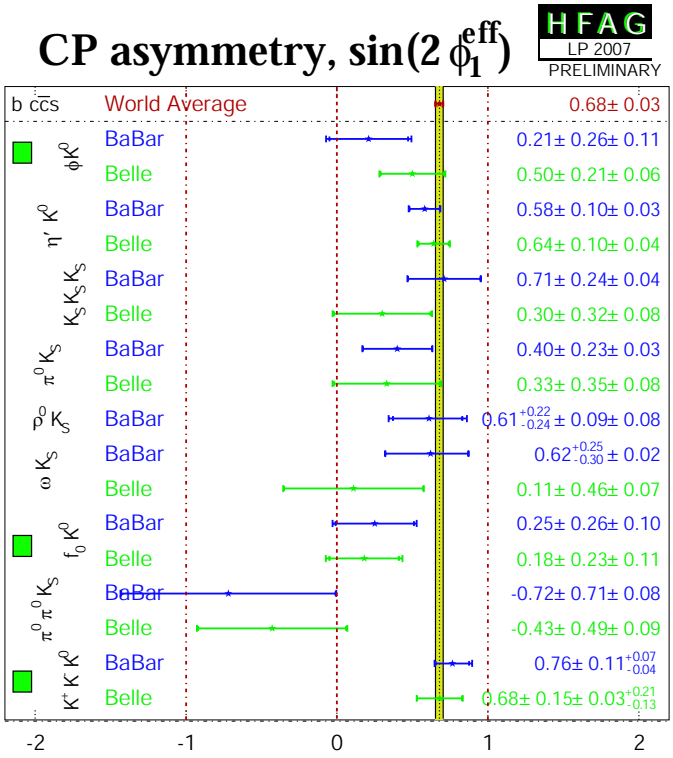

Figure 1.1: CP asymmetry measurements in selected $b \to s$ decays at the B factories. The $B^0 \to \phi K^0_S$, $B^0 \to f_0 K^0_S$ and non-resonant $B^0 \to K^0_S K^+ K^-$ decays, marked with the green boxes, are covered by this thesis. The leading-order expectation of CP asymmetry in $b \to s$ decays is CP asymmetry in $b \to c\overline{c}s$ tree decays, such as $B^0 \to J/\psi K^0_S$. The world average of the measurements in $b \to c\overline{c}s$ tree decays is shown in red.

Among the $b \to s$ decays listed above, the $B^0 \to \phi K^0_S$ decay via pure $b \to sg \to s\overline{s}s$ transition, with the branching fraction of $(4.3 \pm 0.6) \times 10^{-6}$, is the golden mode for New Physics searches. The reasons are that the CP asymmetry expected in the Standard Model has the smallest uncertainty, the decay is experimentally the cleanest due to the negligible contribution from tree transitions and clear understanding of QCD hadronization of the resonance ϕ with narrow decay width [8], and that we can reconstruct the decay with the signal yield of $\mathcal{O}(10^2)$ and experimentally accessible with the current statistics. However, the $B^0 \to \phi K^0_S$ decay still has interfering contaminations from the B^0 decays with the same final state, for example, $f_0 K^0_S$ and a non-resonant $K^0_S K^+ K^-$ component [9], which will give the largest uncertainty when the statistics increases. Due to the smaller data sample [1], a series of the previous analyses did not treat these contaminations properly, which caused ambiguities on the CP asymmetry measurements.

To solve these ambiguities, we have employed a more precise method with the first "time-dependent Dalitz plot analysis" on the B^0 decays with $K^0_S K^+ K^-$ final state with larger data sample of 657 $\times 10^6$ $B\overline{B}$ pairs at Belle. By including additional kinematic variables in the time evolution information of the neutral B meson decays, the interferences between the dominant decay channels with the same final state can be simultaneously modeled and, in addition, the two-fold ambiguity in the weak phases, which arises in previous quasi-two-body time-dependent CP analyses, could potentially be resolved. In this analysis, we cover CP asymmetry measurements in the $B^0 \to \phi K^0_S$, non-resonant $B^0 \to K^0_S K^+ K^-$ and $B^0 \to f_0 K^0_S$ decays, marked with the green boxes in Fig. 1.1.

On the other hand, the B^0 meson decays mediated by the $b \to dg$ transitions are even more sensitive to New Physics than $b \to sg$ because this process is highly suppressed in the Standard Model due to the smaller amplitude of the quark mixing matrix element $\boldsymbol{V}_{td}$ than $\boldsymbol{V}_{ts}$ [10]. They had been inaccessible at Belle until now due to their extremely small branching fractions.

We have opened the research field of search for New Physics using CP asymmetry measurements in $b \to d$ decays at Belle by focusing on the $B \to K^0_S K^0_S$ decay via pure $b \to dg \to d\overline{s}s$ transition, which is experimentally the cleanest among the $b \to dg$ decays. The $B^0 \to K^0_S K^0_S$ decay had been observed with the signal yield of 23 ± 6 using 449×10^6 $B\overline{B}$ pairs and the branching fraction is measured to be $(4.8 \pm 1.0) \times 10^{-7}$. We improve the reconstruction efficiency by $\sim$40% and measure time-dependent CP asymmetry in the $B^0 \to K^0_S K^0_S$ decay with 657×10^6 $B\overline{B}$ pairs.

Since $b \to s$ and $b \to d$ transitions have the different weak phases and the different sizes of the decay amplitudes within the Standard Model, independent searches for new weak phases are possible. Since new weak phase that may arise from New Physics is totally unknown, these independent searches are important to give possible constraints to New Physics. In addition, even after the direct discovery of New Physics by the LHC, search for new weak phases through the multiple quark transition processes such as $b \to s$ and $b \to d$ transitions will still be important in terms of the understanding of the flavor structure of New Physics.

[1] The most recent previous analysis used the data sample of 535 $\times 10^6$ $B\overline{B}$ pairs.

In this thesis, we present measurements of CP asymmetries in the B^0 decays with $K^0_S K^+ K^-$ final state including $B^0 \to \phi K^0_S$, non-resonant $B^0 \to K^0_S K^+ K^-$ and $B^0 \to f_0 K^0_S$, as well as in the $B^0 \to K^0_S K^0_S$ decay. These results are obtained from a data sample containing 657×10^6 $B\overline{B}$ pairs collected on the $\Upsilon(4S)$ resonance with the Belle detector at the KEKB asymmetric-energy e^+e^- collider.

1.2 Outline of Analysis Procedure

We utilize the decay chain $\Upsilon(4S) \to B^0\overline{B^0} \to f_{CP} f_{\rm tag}$, where one of the neutral B mesons decays at time t_{CP} to a CP eigenstate (f_{CP}), $B^0 \to K^0_S K^0_S$ and $B^0 \to K^0_S K^+ K^-$ in this thesis, and the other decays at time $t_{\rm tag}$ to a flavor specific state ($f_{\rm tag}$) that distinguishes between B^0 and $\overline{B^0}$. The event topology of the decay chain is shown in Fig. 1.2. CP asymmetry is present when B^0 and $\overline{B^0}$ decay to the common CP eigenstate and is realized as the time-dependent decay rate asymmetry in B^0 and $\overline{B^0}$, which is a function of the proper-time difference (Δt) between the two neutral B mesons and the b flavor of $f_{\rm tag}$ [6].

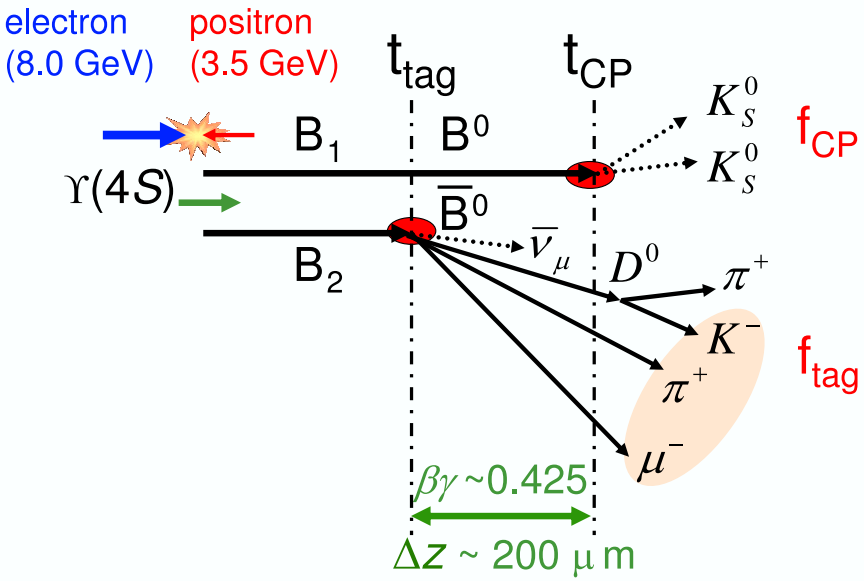

Figure 1.2: Event topology of the decay chain $\Upsilon(4S) \to B^0\overline{B^0} \to f_{CP} f_{\rm tag}$ at the KEKB. In this figure, $B^0 \to K^0_S K^0_S$ and $\overline{B^0} \to D^{*+}\mu^-\nu_\mu$ are selected as the final states of CP eigenstate and flavor-specific state, respectively.

First, we reconstruct the signal decay candidate events from $B\overline{B}$ pairs and extract the signal yield to be utilized to calculate an event-by-event signal fraction. Then, we measure Δt and identify the b flavor of $f_{\rm tag}$ by its decay products. At the KEKB, the $\Upsilon(4S)$ resonance is produced with a Lorentz boost of $\beta\gamma = 0.425$ nearly along the z axis, which is defined as the direction anti-parallel to the e^+ beamline. Since the B^0 and $\overline{B^0}$ mesons are approximately at rest in the $\Upsilon(4S)$ center-of-mass system, Δt can be determined from the displacement in z between f_{CP} and $f_{\rm tag}$ decay vertices: $\Delta t \equiv t_{CP} - t_{\rm tag} \sim \Delta z/(\beta\gamma c)$. The average B decay length becomes $\sim 200\mu$m, which can be determined by the vertex detector with precisely enough resolution. Since a $B\overline{B}$ pair is produced with a single coherent quantum state, the neutral $B\overline{B}$ pair becomes only $B^0\overline{B^0}$ at the same time as a consequence of Bose statistics. We can know whether f_{CP} is B^0 or $\overline{B^0}$ at time t_{CP} by the b flavor of $f_{\rm tag}$. Finally, we determine CP asymmetry from the difference between the Δt distributions for $f_{\rm tag} = B^0$ and $f_{\rm tag} = \overline{B^0}$ using an unbinned maximum likelihood fit.

In this analysis, the statistical uncertainty dominates the total uncertainty. As a basis, we perform *blind analysis* to avoid any event selections that is based on statistically biased data samples. Otherwise, such biased event selection will pick up some specific events artificially and will result in the possible biases in the CP asymmetry measurements and other measured quantities. First, the analysis requirements in reconstructing the signal decays are determined by the distributions of GEANT-based signal Monte-Carlo (MC) [11] and experimental background data. The MC samples are confirmed or calibrated by experimental data of control sample decays beforehand. Then, validity checks of the analysis procedures are performed by the MC samples or high statistics control sample data. After confirming the validity, we measure the central values and the statistical uncertainties. Systematic uncertainties include (1) the possible differences between data and MC whose contributions are not calibrated (2) the possible biases found in the validity checks and (3) using data after box open.

This thesis is organized as follows: in Chapter 2, we describe the phenomenology of CP asymmetry in flavor-changing neutral current B decays; in Chapter 3, we explain the experimental apparatus used to collect $B\overline{B}$ pairs; in Chapter 4, we give detailed description on "time-dependent Dalitz plot analysis," which is newly performed on the B^0 decays with $K^0_S K^+ K^-$ final state at Belle; in Chapters 5 and 6, we describe the analysis procedure and the results of the CP asymmetry measurements in the $B^0 \to K^0_S K^0_S$ and $B^0 \to K^0_S K^+ K^-$ decays, in parallel; for the $B^0 \to K^0_S K^0_S$ decay, we follow the traditional quasi-two-body time-dependent CP analysis, and for the $B^0 \to K^0_S K^+ K^-$ decay, we focus on the additional points; in Chapter 7, we interpret the results of the CP asymmetry measurements and demonstrate search for new weak phases beyond the Standard Model using our results; we also discuss the differences in the fitted results between the "time-dependent Dalitz plot CP analysis" and previously-employed "quasi-two-body time-dependent CP analysis"; chapter 8 concludes this thesis.

Chapter 2

Phenomenology of CP Asymmetries in B-Meson Decays

In this chapter, we first describe CP-violating phases in B meson system originated from the quark mixing, then, construct the formalism and the phenomenology of CP asymmetries in B-meson decays. Finally, we derive the theoretical prediction of the CP asymmetries in $b \to c\bar{c}s$ tree transitions and flavor-changing neutral current B decays from the quark mixing.

2.1 CP-Violating Phases in Quark Mixing in the Standard Model

The charged-current weak interaction mediated by the $W^{\pm}$ boson is described [5] by the non-leptonic charged current interaction Lagrangian $\mathcal{L}_{\rm int}^{\rm CC}$ as

$$\mathcal{L}_{\rm int}^{\rm CC} = -\frac{g}{\sqrt{2}}(\overline{u}_L, \overline{c}_L, \overline{t}_L)\gamma^{\mu}\boldsymbol{V}_{CKM}\begin{pmatrix} d_L \\ s_L \\ b_L \end{pmatrix} W_{\mu}^{+} + h.c, \tag{2.1}$$

where W_{μ}^{+} denotes the W^{+} boson, g is the gauge coupling corresponding to the gauge group $SU(2)_L$, and $\boldsymbol{V}_{CKM}$ is the Cabibbo-Kobayashi-Maskawa (CKM) matrix [5], which connects the electroweak eigenstates of the down, strange and bottom quarks with their mass eigenstates. Due to misalignment between the up-type and down-type quark fields, the charged current induces quark transitions among different generations.

The CKM matrix $\boldsymbol{V}_{CKM}$ is written as

$$\boldsymbol{V}_{CKM} = \begin{pmatrix} \boldsymbol{V}_{ud} & \boldsymbol{V}_{us} & \boldsymbol{V}_{ub} \\ \boldsymbol{V}_{cd} & \boldsymbol{V}_{cs} & \boldsymbol{V}_{cb} \\ \boldsymbol{V}_{td} & \boldsymbol{V}_{ts} & \boldsymbol{V}_{tb} \end{pmatrix}. \tag{2.2}$$

An approximate parameterization, the so-called Wolenstein parameterization [12], is often used, in which one expands the CKM matrix in terms of $\lambda \equiv \sin\theta_C = |\boldsymbol{V}_{us}| \sim 0.22$, where θ_C is the Cabibbo angle [13],

$$\boldsymbol{V}_{CKM} = \begin{pmatrix} 1-\frac{1}{2}\lambda^2 & \lambda & A\lambda^3(\rho-i\eta) \\ -\lambda & 1-\frac{1}{2}\lambda^2 & A\lambda^2 \\ A\lambda^3(1-\rho-i\eta) & -A\lambda^2 & 1 \end{pmatrix} + \mathcal{O}(\lambda^4), \tag{2.3}$$

where A, ρ and η are real parameters of order unity. A complex phase that induces CP violation is conventionally put to most of off-diagonal elements. From unitarity of the CKM matrix, $\boldsymbol{V}_{CKM}\boldsymbol{V}^{\dagger}_{CKM} = \boldsymbol{I}$, the following six conditions, $\sum_{q=(u,c,t)} \boldsymbol{V}_{qq'}\boldsymbol{V}^*_{qq''} = 0$, where $(q',q'')=(d,s)$, (s,b), (d,b) and $\sum_{q=(d,s,b)} \boldsymbol{V}_{qq'}\boldsymbol{V}^*_{qq''}$, where $(q',q'')=(u,c)$, (t,c), (t,u), are obtained. These relations can be schematically written as triangles. Among these, the triangle with the following relation is related to B decays,

$$\underbrace{V_{ud}V^*_{ub}}_{\mathcal{O}(\lambda^3)} + \underbrace{V_{cd}V^*_{cb}}_{\mathcal{O}(\lambda^3)} + \underbrace{V_{td}V^*_{tb}}_{\mathcal{O}(\lambda^3)} = 0, \tag{2.4}$$

and is interesting because all the sides are of the same order in λ. This indicates large internal angles and therefore, large CP-violating effects may be observed in B decays.

It is convenient to normalize Eq. 2.4, so that one side becomes aligned to the real axis with a magnitude of unity. The rescaled CKM unitary triangle is shown in Fig. 2.1 where

$$\phi_1 \equiv \pi - \arg\left(\frac{-V_{td}V^*_{tb}}{-V_{cd}V^*_{cb}}\right),\ \phi_2 \equiv \arg\left(\frac{V_{td}V^*_{tb}}{-V_{ud}V^*_{ub}}\right),\ \phi_3 \equiv \arg\left(\frac{V_{ud}V^*_{ub}}{-V_{cd}V^*_{cb}}\right) \text{ and, } \tag{2.5}$$

$$\overline{\rho} \equiv (1-\frac{\lambda^2}{2})\rho,\ \overline{\eta} \equiv (1-\frac{\lambda^2}{2})\eta. \tag{2.6}$$

These three phases, ϕ_1, ϕ_2, and ϕ_3, represent CP-violating phases in B-meson system originated from the quark mixing.

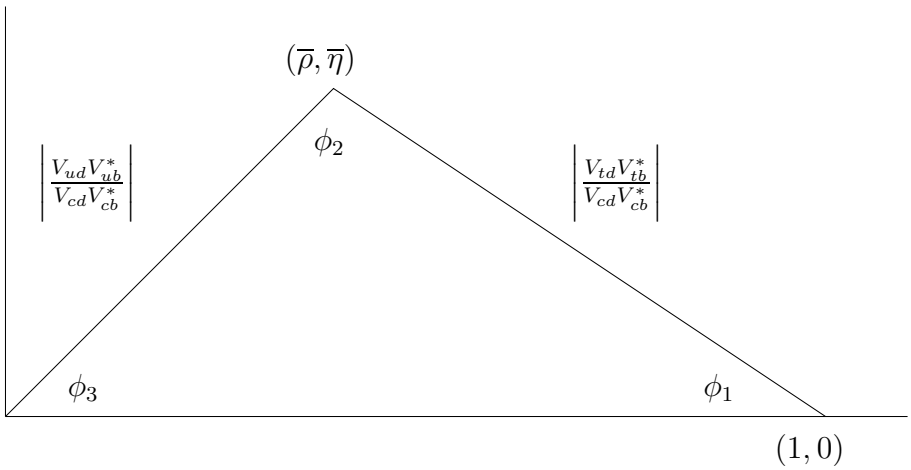

Figure 2.1: Rescaled CKM Unitary triangle

2.2 Formalism of CP Asymmetries in the B-Meson System

After explaining the time evolution in a neutral pseudo-scaler meson system, we describe the time evolution and introduce the formalism of CP asymmetries in the B-meson system by using its special properties.

The decay amplitudes A of a pseudo-scaler neutral meson M and its CP conjugate $\overline{M}$ are given by

$$A_f = \langle f|H|M\rangle,\ \overline{A}_f = \langle f|H|\overline{M}\rangle,\ A_{\overline{f}} = \langle \overline{f}|H|M\rangle,\ \text{and}\ \overline{A}_{\overline{f}} = \langle \overline{f}|H|\overline{M}\rangle, \tag{2.7}$$

where f and $\overline{f}$ are a final state and its CP conjugate state, and H is the Hamiltonian that represents weak interactions. If f is a CP eigenstate, the state $|f\rangle$ will be equal to $|\overline{f}\rangle$. By applying the CP transformation, one can find that A_f and $\overline{A}_{\overline{f}}$ have the same amplitude.

Assume that the initial state is a linear combination of M and $\overline{M}$ alone as follows,

$$|\Psi(0)\rangle = a(0)|M\rangle + \overline{a}(0)|\overline{M}\rangle. \tag{2.8}$$

The Schrödinger equation for the state $|\Psi\rangle$ is written as

$$i\hbar\frac{\partial}{\partial t}\Psi(t) = H\Psi(t) \tag{2.9}$$

$$\Psi(t) = \begin{pmatrix} a(t) \\ \overline{a}(t) \end{pmatrix}, \tag{2.10}$$

where H is an effective Hamiltonian that describes the time evolution in a simplified formalism. The matrix H is given by

$$H = M - \frac{i}{2}\Gamma, \tag{2.11}$$

where M and Γ are 2×2 Hamiltonian matrices and are related to the transitions between M and M ($\overline{M}$) states. The diagonal elements of H govern the transitions of $M \to M$ and $\overline{M} \to \overline{M}$, and the off-diagonal elements are related to $M \to \overline{M}$ and $\overline{M} \to M$ transitions. With CPT invariance, the diagonal elements of M and Γ have the following relations,

$$M_{11} = M_{22},\ \Gamma_{11} = \Gamma_{22}. \tag{2.12}$$

In the following, CPT invariance is assumed.

The mass eigenstates of H are given by

$$|M_L\rangle = p|M\rangle + q|\overline{M}\rangle,\ |M_H\rangle = p|M\rangle - q|\overline{M}\rangle, \tag{2.13}$$

where p and q are complex parameters and the states $|M_L\rangle$ and $|M_H\rangle$ are the lighter and heavier mass eigenstates. The eigenvalues of H are written using the parameters (m_L, m_H, Γ_L and Γ_H) as

$$M_L = m_L - i\Gamma_L,\ M_H = m_H - i\Gamma_H. \tag{2.14}$$

Their real and imaginary parts are related to their masses and decay widths,

$$\Delta m \equiv m_H - m_L,\ \Delta\Gamma \equiv \Gamma_H - \Gamma_L. \tag{2.15}$$

By solving the eigenvalue problem for H, the ratio between q and p is given by

$$\frac{q}{p} = +\sqrt{\frac{M_{12}^* - \frac{i}{2}\Gamma_{12}^*}{M_{12} - \frac{i}{2}\Gamma_{12}}}, \tag{2.16}$$

where the sign of the right-hand side of Eq. 2.16 is selected as a convention [1]. The CP violating observables are generally expressed by the amplitudes A_f, $\overline{A}_f$, $A_{\overline{f}}$, $\overline{A}_{\overline{f}}$ and the ratio, q/p.

Consider the expression including the oscillations between M and $\overline{M}$. With an initial pure $|M\rangle$ or $|\overline{M}\rangle$ state, the states $|M(t)\rangle$ and $|\overline{M}(t)\rangle$ at proper time t are given by

$$|M(t)\rangle = g_+(t)|M\rangle - \frac{q}{p}g_-(t)|\overline{M}\rangle,\ |\overline{M}(t)\rangle = g_+(t)|\overline{M}\rangle - \frac{p}{q}g_-(t)|M\rangle, \tag{2.17}$$

where $g_\pm(t) = \frac{1}{2}(e^{-im_H t - \frac{1}{2}\Gamma_H t} \pm e^{-im_L t - \frac{1}{2}\Gamma_L t})$. The time-dependent decay rates are

$$\begin{aligned}
\frac{d\Gamma[M(t)\to f]}{dt} = \ & e^{-\Gamma t}\ [(|A_f|^2 + |\frac{q}{p}\overline{A}_f|^2)\cosh(\frac{1}{2}\Delta\Gamma t) \\
& +\ (|A_f|^2 - |\frac{q}{p}\overline{A}_f|^2)\cos(\Delta m_d t) \\
& +\ 2\mathrm{Re}(\frac{q}{p}A_f^*\overline{A}_f)\sinh(\frac{1}{2}\Delta\Gamma t) - 2\mathrm{Im}(\frac{q}{p}A_f^*\overline{A}_f\sin(\Delta m_d t))],
\end{aligned} \tag{2.18}$$

$$\begin{aligned}
\frac{d\Gamma[\overline{M}(t)\to f]}{dt} = \ & e^{-\Gamma t}\ [(|\frac{p}{q}A_f|^2 + |\overline{A}_f|^2)\cosh(\frac{1}{2}\Delta\Gamma t) \\
& +\ (|\frac{p}{q}A_f|^2 - |\overline{A}_f|^2)\cos(\Delta m_d t) \\
& +\ 2\mathrm{Re}(\frac{p}{q}A_f\overline{A}_f^*)\sinh(\frac{1}{2}\Delta\Gamma t) - 2\mathrm{Im}(\frac{p}{q}A_f\overline{A}_f^*\sin(\Delta m_d t))].
\end{aligned} \tag{2.19}$$

The decay rates of $M(t)\to\overline{f}$ and $\overline{M}(t)\to\overline{f}$ can be obtained by replacing f with $\overline{f}$ from the equation above. The $M\overline{M}$ oscillation are related to the terms with $|\frac{q}{p}\overline{A}|^2$ or $|\frac{p}{q}A|^2$, and are not associated with the other terms that are proportional to $|A_f|^2$ or $|\overline{A}_f|^2$. The interference terms are associated with $\sinh(\Delta\Gamma t/2)$ and $\sin(\Delta m_d t)$.

For the $B^0\overline{B^0}$ system, the lighter and heavier B meson mass eigenstates are given by

$$|B_L\rangle = p|B^0\rangle + q|\overline{B^0}\rangle,\ |B_H\rangle = p|B^0\rangle - q|\overline{B^0}\rangle. \tag{2.20}$$

In the B_d^0 meson system, $\Delta\Gamma$ is much smaller than Γ, where

$$\Gamma \equiv \frac{1}{2}(\Gamma_L + \Gamma_H), \tag{2.21}$$

[1] This sign comes from the definition of $\Delta m_d \equiv m_H - m_L$ and all the CP analyses follow this convention.

and, thus, the B_d lifetime, τ_{B^0}, can be obtained assuming there is no decay width difference and defined as

$$\tau_{B^0} \equiv \frac{1}{\Gamma}. \tag{2.22}$$

If we define the average mass, M, and the mass difference, Δm_d, as

$$M \equiv \frac{1}{2}(M_H + M_L) \text{ and } \Delta m_d \equiv M_H - M_L, \tag{2.23}$$

the time evolution of $|B^0\rangle$ or $|\overline{B^0}\rangle$ state can be rewritten as

$$|B^0(t)\rangle = g_+(t)|B^0\rangle - \frac{q}{p}g_-(t)|\overline{B^0}\rangle,\ |\overline{B^0}(t)\rangle = g_+(t)|\overline{B^0}\rangle - \frac{p}{q}g_-(t)|B^0\rangle, \tag{2.24}$$

where q/p is given by Eq. 2.16 with a normalization of $\sqrt{|p|^2 + |q|^2} = 1$. Here, $g_\pm(t)$ is rewritten as follows,

$$g_+(t) = e^{-iMt}e^{-\Gamma t/2}\cos(\Delta m_d t/2),\ g_-(t) = e^{-iMt}e^{-\Gamma t/2} i \sin(\Delta m_d t/2). \tag{2.25}$$

Mixing of $B^0\overline{B^0}$ mesons proceeds through the second order box diagram shown in Fig. 2.2. The b and d quarks couple to W bosons and u, c, t quarks.

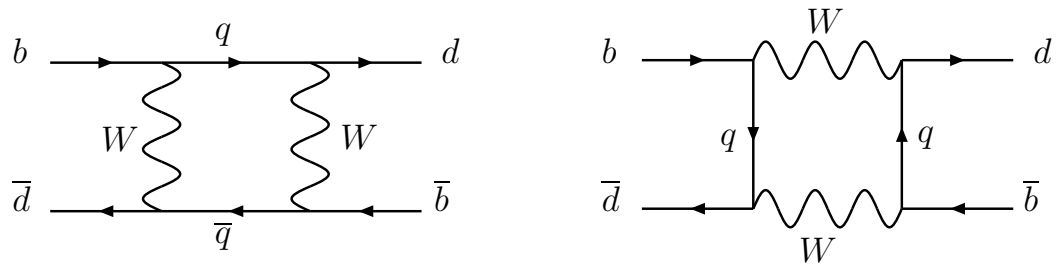

Figure 2.2: Feynman diagram for $B^0\overline{B^0}$ mixing.

However, the intermediate mixing state may be dominated by the virtual t quark because of $V_{tb} \gg V_{cb} \gg V_{ub}$ and $m_t \gg m_c \gg m_u$ using GIM cancellations. Theory [14, 15, 16, 17] indicates that

$$M_{12} \propto (V_{tb}V_{td}^*)^2 m_t^2 \text{ and } \Gamma_{12} \propto (V_{tb}V_{td}^*)^2 m_b^2. \tag{2.26}$$

If we expand Eq. 2.16,

$$\begin{aligned} \frac{q}{p} &\simeq \sqrt{\frac{M_{12}^*}{M_{12}}} + \mathcal{O}\left(\frac{\Gamma_{12}}{M_{12}}\right) \\ \Rightarrow \left|\frac{q}{p}\right| &= \left|\frac{V_{td}V_{tb}^*}{V_{td}^*V_{tb}}\right| + \mathcal{O}\left(\frac{m_b^2}{m_t^2}\right) \quad \text{but } m_b^2/m_t^2 \sim \mathcal{O}(10^{-3}) \\ \Rightarrow \left|\frac{q}{p}\right| &\simeq 1 \end{aligned} \tag{2.27}$$

Detailed explanations can be found elsewhere in [18].

Considering a final state f_{CP} that is common to B^0 and $\overline{B^0}$ and using the approximation of $\Delta\Gamma \to 0$, the time-dependent decay rate in Eq. 2.20 can be rewritten for B^0 and $\overline{B^0}$ as

$$\begin{aligned}\frac{d\Gamma[B^0(t) \to f_{CP}]}{dt} &\propto e^{-\Gamma_B t}|A_{f_{CP}}|^2 \\ &\quad [(1+|\lambda_{f_{CP}}|^2) + (1-|\lambda_{f_{CP}}|^2)\cos(\Delta m_d t) - 2\mathrm{Im}(\lambda_{f_{CP}})\sin(\Delta m_d t)] \end{aligned} \tag{2.28}$$

$$\begin{aligned}\frac{d\Gamma[\overline{B^0}(t) \to f_{CP}]}{dt} &\propto e^{-\Gamma_B t}|\overline{A}_{f_{CP}}|^2 \\ &\quad [(1+|\lambda_{f_{CP}}|^{-2}) + (1-|\lambda_{f_{CP}}|^{-2})\cos(\Delta m_d t) - 2\mathrm{Im}(\lambda_{f_{CP}}^{-1})\sin(\Delta m_d t)], \end{aligned} \tag{2.29}$$

where $\lambda_{f_{CP}}$ is given by

$$\lambda_{f_{CP}} = \frac{q}{p}\frac{A[\overline{B^0}(t) \to f_{CP}]}{A[B^0(t) \to f_{CP}]} = \frac{q}{p}\frac{\overline{A}_{f_{CP}}}{A_{f_{CP}}}. \tag{2.30}$$

Therefore, the time-dependent CP asymmetry in the B-meson system as a function of t is given by

$$\begin{aligned} A_{CP}(t) = \frac{\frac{d\Gamma[\overline{B^0}(t)\to f_{CP}]}{dt} - \frac{d\Gamma[B^0(t)\to f_{CP}]}{dt}}{\frac{d\Gamma[\overline{B^0}(t)\to f_{CP}]}{dt} + \frac{d\Gamma[B^0(t)\to f_{CP}]}{dt}} &= \frac{|\lambda_{f_{CP}}|^2 - 1}{|\lambda_{f_{CP}}|^2 + 1}\cos(\Delta m_d t) + \frac{2\mathrm{Im}(\lambda_{f_{CP}})}{|\lambda_{f_{CP}}|^2 + 1}\sin(\Delta m_d t) \\ &\equiv \mathcal{A}_{CP}\cos(\Delta m_d t) + \mathcal{S}_{CP}\sin(\Delta m_d t), \end{aligned} \tag{2.31}$$

where $\mathcal{A}_{CP}$ and $\mathcal{S}_{CP}$ denote the parameters for direct and mixing-induced CP violation. An alternative notation is used by BaBar, which is the other B factory experiment at SLAC; $\mathcal{C}_{CP}$=-$\mathcal{A}_{CP}$. Here, the CP-violating parameters are defined as

$$\mathcal{A}_{CP} \equiv \frac{|\lambda_{f_{CP}}|^2 - 1}{|\lambda_{f_{CP}}|^2 + 1}, \quad \mathcal{S}_{CP} \equiv \frac{2\mathrm{Im}(\lambda_{f_{CP}})}{|\lambda_{f_{CP}}|^2 + 1} \tag{2.32}$$

and the interpretation of $\mathcal{A}_{CP}$ and $\mathcal{S}_{CP}$ is as follows.

Recall the definition of $\lambda_{f_{CP}}$ in Eq. 2.30 contains 2 distinct parts. The q/p part describes mixing while $\overline{A}_{CP}/A_{CP}$ describes the decay amplitudes. This implies that $\lambda_{f_{CP}}$ can be written as,

$$\lambda_{f_{CP}} \sim e^{-i\phi_{\mathrm{Mixing}}}\frac{|\overline{A}_{CP}|}{|A_{CP}|}e^{-i\phi_{\mathrm{Decay}}} = \frac{|\overline{A}_{CP}|}{|A_{CP}|}e^{-i(\phi_{\mathrm{Mixing}}+\phi_{\mathrm{Decay}})} \tag{2.33}$$

where ϕ_{Mixing} represent a weak phase difference in $B^0\overline{B^0}$ mixing and ϕ_{Decay} represents a weak phase difference in the decay amplitudes.

Consider the case where there is a difference in the decay rates, that is, $\Gamma(B^0 \to f) \neq \Gamma(\overline{B^0} \to f)$. Then, $|\overline{A}_{CP}|^2/|A_{CP}|^2 \neq 1 \Rightarrow \mathcal{A}_{CP} \neq 0$. This is called direct CP violation. Now

consider the case where there is interference between the mixing and decay phase differences, $\phi_{\text{Mixing}} + \phi_{\text{Decay}} \neq 0$. Thus, $\text{Im}(\lambda_{f_{CP}}) \neq 0 \Rightarrow \mathcal{S}_{CP} \neq 0$. This is called mixing-induced CP violation.

Notice how the right hand of Eq. 2.31 looks like the equation for a circle while the asymmetry of left hand side may only take on values between -1 and $+1$ by definition. So, $(\mathcal{A}_{CP}, \mathcal{S}_{CP})$ is physically restricted to lie within the unit circle in CP-violating space.

In summary, the effects of CP violation can be divided into three categories by their sources as demonstrated in Fig. 2.3.

- Category (1)
  CP violation arises from the differences between the amplitudes of a final state and its CP conjugate state:
  $$|\overline{A}_{\overline{f}}/A_f| \neq 1. \tag{2.34}$$
  CP asymmetry is given by
  $$A_{CP} = \frac{\Gamma(\overline{M} \to \overline{f}) - \Gamma(M \to f)}{\Gamma(\overline{M} \to \overline{f}) + \Gamma(M \to f)}. \tag{2.35}$$
  This asymmetry is called *direct* CP asymmetry, which is the only possible source of CP asymmetry in charged B decays.

- Category (2)
  CP violation appears in $B^0\overline{B^0}$ mixing and requires the condition:
  $$|q/p| \neq 1, \tag{2.36}$$
  which occurs in the semi-leptonic B^0 decays, such as $B^0 \to \ell^- \nu_\ell D^{(*)+}$ decays. CP asymmetry is given by
  $$A_{CP} = \frac{\Gamma(\overline{M} \to \ell^+ X) - \Gamma(M \to \ell^- X)}{\Gamma(\overline{M} \to \ell^+ X) + \Gamma(M \to \ell^- X)}. \tag{2.37}$$

- Category (3)
  CP violation arises from the interferences between a decay $M \to f$ and the other decay $M \to \overline{M} \to f$. The final state should be a CP eigenstate, which is common to M and $\overline{M}$. CP violation requires the condition:
  $$\text{Im}(\lambda_{f_{CP}}) \neq 0. \tag{2.38}$$
  The resulting CP asymmetry is time-dependent and is given by
  $$A_{CP}(t) = \frac{\Gamma(\overline{M}(t) \to f_{CP}) - \Gamma(M(t) \to f_{CP})}{\Gamma(\overline{M}(t) \to f_{CP}) + \Gamma(M(t) \to f_{CP})}. \tag{2.39}$$

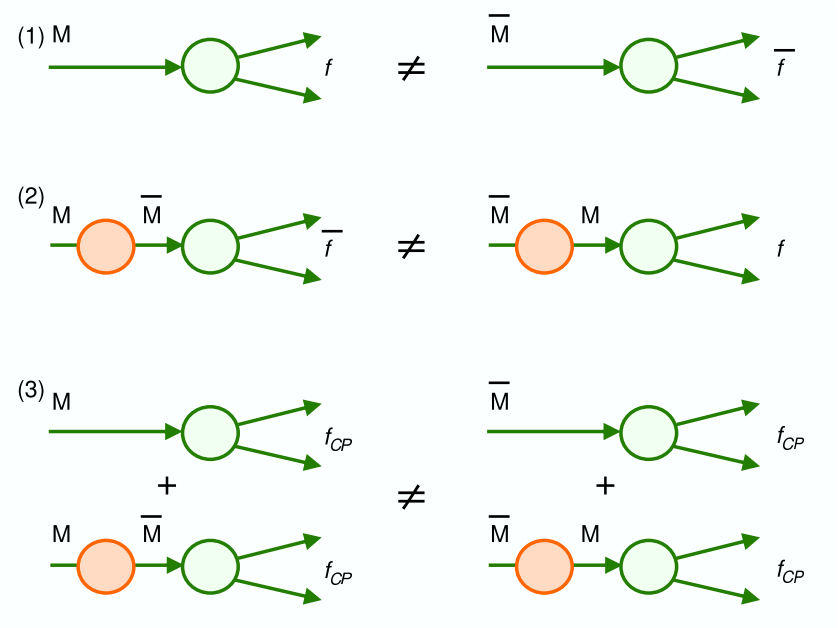

Figure 2.3: Three categories of CP violation. In category (1), without $B^0\overline{B^0}$ mixing, CP violation may arise from the difference in the amplitudes between $M \to f$ and $\overline{M} \to \overline{f}$. In category (2), CP violation may arise from $|q/p| \neq 1$ with $B^0\overline{B^0}$ mixing. In category (3), if the final state is a CP eigenstate (f_{CP}), CP violation occurs in the interferences between the amplitude of $M \to f$ and the amplitude with mixing $M \to \overline{M} \to f$.

2.3 Phenomenology of CP Asymmetries at a B Factory

So far, the time-dependent decay rate asymmetry in Eq. 2.31 requires the flavor of the B meson to be known at the time of production. For a CP eigenstate where both B^0 and $\overline{B^0}$ decay to the same final state, and in addition, may also have mixed in the decay time, t, after production, one can not distinguish whether an event follows Eq. 2.28 or Eq. 2.29 from experimental information of a CP eigenstate. flavor identification is not experimentally possible.

However, B mesons produced in the $\Upsilon(4S) \to B^0\overline{B^0}$ decay inherit the quantum numbers, $J^{CP} = 1^{--}$, because they are conserved in the strong interaction. Since B^0 is a pseudo-scalar particle, the $B^0\overline{B^0}$ system should have an orbital angular momentum of $L = 1$. Therefore, by Bose-Einstein statistics, the states $B^0 - B^0$ or $\overline{B^0} - \overline{B^0}$ are forbidden and thus the $B^0\overline{B^0}$ pair must oscillate coherently as follows,

$$|B_1(t_1), B_2(t_2)\rangle = \frac{1}{\sqrt{2}}\Big(|B_1^0(t_1)\rangle|\overline{B^0}_2(t_2)\rangle - |\overline{B^0}_1(t_1)\rangle|B_2^0(t_2)\rangle\Big). \tag{2.40}$$

By plugging in Eq. 2.24, the time evolution of the $B^0\overline{B^0}$ system becomes,

$$|B_1(t_1), B_2(t_2)\rangle = \frac{1}{\sqrt{2}}e^{-\Gamma(t_1+t_2)/2}\left[\cos\frac{\Delta m_d \Delta t}{2}\Big(|B_1^0\rangle|\overline{B^0}_2\rangle - |\overline{B^0}_1\rangle|B_2^0\rangle\Big) + i\sin\frac{\Delta m_d \Delta t}{2}\Big(\frac{q}{p}|B_1^0\rangle|\overline{B^0}_2\rangle - \frac{p}{q}|\overline{B^0}_1\rangle|B_2^0\rangle\Big)\right], \tag{2.41}$$

where $\Delta t = t_2 - t_1$ and here, t_i is the decay time of each B meson.

Take again the specific case where one B decays to a CP eigenstate, f_{CP}, and the other B meson decays to a flavor-specific state, $f_{\rm tag}$, from which the flavor can be determined. A schematic of this case is shown in Fig. 2.4.

In this case, the time-dependent decay rate in terms of t_1 and t_2 is

$$\begin{aligned} d\Gamma/dt_1dt_2 &\propto |A(t_1,t_2)|^2 \\ &= \begin{cases} e^{-\Gamma(t_1+t_2)}|A_{f_+}|^2\Big[|A_{f_1}|^2 + |\overline{A}_{f_1}|^2 \\ \quad -(|A_{f_1}|^2 - |\overline{A}_{f_1}|^2)\cos(\Delta m_d\Delta t) + 2{\rm Im}\left(\frac{q}{p}\overline{A}_{f_1}A^*_{f_1}\right)\sin(\Delta m_d\Delta t)\Big] & (f_{\rm tag} = f_+) \\ e^{-\Gamma(t_1+t_2)}|\overline{A}_{f_-}|^2\Big[|A_{f_1}|^2 + |\overline{A}_{f_1}|^2 \\ \quad +(|A_{f_1}|^2 - |\overline{A}_{f_1}|^2)\cos(\Delta m_d\Delta t) - 2{\rm Im}\left(\frac{q}{p}\overline{A}_{f_1}A^*_{f_1}\right)\sin(\Delta m_d\Delta t)\Big] & (f_{\rm tag} = f_-), \end{cases} \end{aligned} \tag{2.42}$$

where f_+ is a final state to which only B^0 can decay, f_- is its CP conjugate, i.e. $f_- = \overline{f}_+$, and we assume $|q/p| = 1$. Since no direct CP violation in $B^0 \to f_+$ decays is expected [2], the

[2]There is a possible CP violation effect in tag-side and is called tag-side interference, whose effect is considered in the systematic errors.

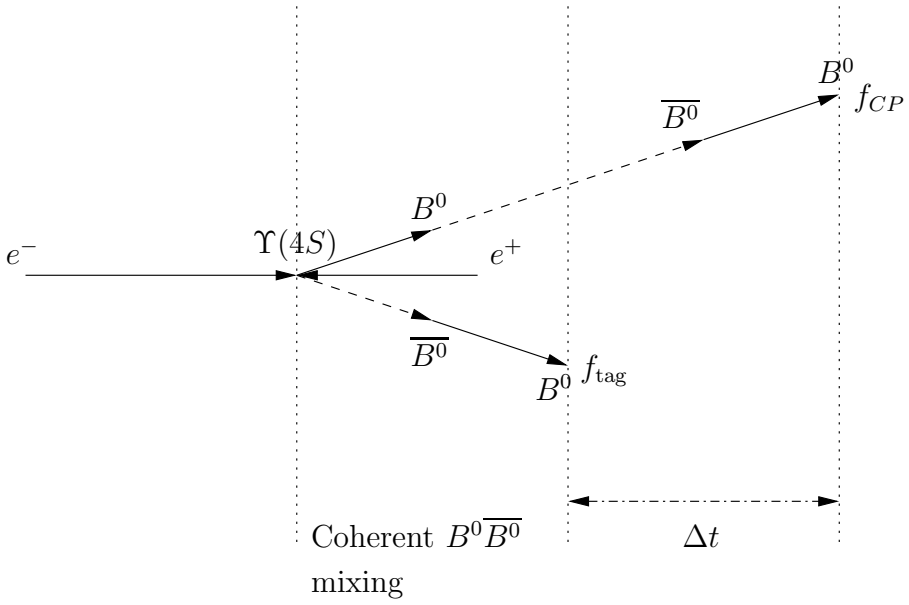

Figure 2.4: The illustration of the decay chain, $e^+e^- \to \Upsilon(4S) \to B^0\overline{B^0} \to f_{CP}f_{\rm tag}$, used to measure CP asymmetries in the B factories. Case in which two neutral B mesons, B^0 and $\overline{B^0}$, are produced in a coherent state from the $\Upsilon(4S)$ decay. After $B^0\overline{B^0}$ mixing, one B meson decays to a CP eigenstate, f_{CP}, while the other B meson decays a flavor-specific state, $f_{\rm tag}$, with the proper time difference, Δt.

following relation is assumed,

$$|A_{f_+}| = |\overline{A}_{f_-}|. \tag{2.43}$$

Thus, we can simplify Eq. 2.42 as

$$\begin{aligned} d\Gamma/dt_1dt_2 \propto & e^{-\Gamma(t_1+t_2)}\Big[|A_{f_1}|^2 + |\overline{A}_{f_1}|^2 \\ & - q_{\rm tag}\cdot(|A_{f_1}|^2 - |\overline{A}_{f_1}|^2)\cos(\Delta m_d\Delta t) + q_{\rm tag}\cdot 2{\rm Im}\left(\frac{q}{p}\overline{A}_{f_1}A^*_{f_1}\right)\sin(\Delta m_d\Delta t)\Big], \end{aligned} \tag{2.44}$$

where $q_{\rm tag}$ denotes the flavor of $f_{\rm tag}$. $q_{\rm tag}$ is an experimental observable and $q_{\rm tag} = +1(-1)$ for $f_{\rm tag} = f_{+(-)}$.

At B-factories, we can only measure Δt and cannot measure $t_1 + t_2$. By integrating Eq. 2.44 over the unmeasurable $t_1 + t_2$, we obtain

$$\begin{aligned} d\Gamma/d\Delta t \equiv & \int_{|\Delta t|}^{+\infty} d(t_1+t_2)\frac{d\Gamma}{dt_1dt_2} \\ \propto & \; e^{-\Gamma|\Delta t|}\Big[|A_{f_1}|^2 + |\overline{A}_{f_1}|^2 \\ & - q_{\rm tag}\cdot(|A_{f_1}|^2 - |\overline{A}_{f_1}|^2)\cos(\Delta m_d\Delta t) + q_{\rm tag}\cdot 2{\rm Im}\left(\frac{q}{p}\overline{A}_{f_1}A^*_{f_1}\right)\sin(\Delta m_d\Delta t)\Big]. \end{aligned} \tag{2.45}$$

For CP eigenstates, this can be written in terms of $A_{f_{CP}}$ and $\overline{A}_{\overline{f}_{CP}}$ as

$$\begin{aligned} d\Gamma/d\Delta t \propto e^{-\Gamma|\Delta t|}\Big[&|A_{f_{CP}}|^2 + |\overline{A}_{\overline{f}_{CP}}|^2 \\ &- q_{\rm tag}\cdot(|A_{f_{CP}}|^2 - |\overline{A}_{\overline{f}_{CP}}|^2)\cos(\Delta m_d\Delta t) \\ &+ q_{\rm tag}\cdot\eta_{f_{CP}}2{\rm Im}\left(\frac{q}{p}\overline{A}_{\overline{f}_{CP}}A^*_{f_{CP}}\right)\sin(\Delta m_d\Delta t)\Big]. \end{aligned} \tag{2.46}$$

Note that the additional factor $\eta_{f_{CP}}$ is introduced when we transform $\overline{A}_{f_{CP}}$ into $\overline{A}_{\overline{f}_{CP}}$.

To connect with CP-violating parameters, we take $|A_{f_{CP}}|^2 + |\overline{A}_{\overline{f}_{CP}}|^2$ as an overall normalization and rewrite the time-dependent decay rate in terms of Δt as

$$d\Gamma/d\Delta t \propto e^{-\Gamma|\Delta t|}\Big[1 + q_{\rm tag}\cdot\mathcal{A}_{f_{CP}}\cos(\Delta m_d\Delta t) + q_{\rm tag}\cdot\mathcal{S}_{f_{CP}}\sin(\Delta m_d\Delta t)\Big], \tag{2.47}$$

with

$$\mathcal{A}_{f_{CP}} \equiv \frac{|\overline{A}_{\overline{f}_{CP}}|^2 - |A_{f_{CP}}|^2}{|\overline{A}_{\overline{f}_{CP}}|^2 + |A_{f_{CP}}|^2} = \frac{|\lambda_{f_{CP}}|^2 - 1}{|\lambda_{f_{CP}}|^2 + 1}\,, \tag{2.48}$$

$$\mathcal{S}_{f_{CP}} \equiv \eta_{f_{CP}}\frac{2\,{\rm Im}\left(\frac{q}{p}\overline{A}_{\overline{f}_{CP}}A^*_{f_{CP}}\right)}{|\overline{A}_{\overline{f}_{CP}}|^2 + |A_{f_{CP}}|^2} = \eta_{f_{CP}}\frac{2{\rm Im}\lambda_{f_{CP}}}{|\lambda_{f_{CP}}|^2 + 1}. \tag{2.49}$$

and

$$\lambda_{f_{CP}} \equiv \frac{q}{p}\frac{\overline{A}_{\overline{f}_{CP}}}{A_{f_{CP}}}. \tag{2.50}$$

Then, the resulting time-dependent CP asymmetry as a function of Δt becomes

$$\begin{aligned} A_{CP}(\Delta t) &\equiv \frac{\frac{d\Gamma[\overline{B^0}\to f_{CP}]}{d\Delta t} - \frac{d\Gamma[B^0\to f_{CP}]}{d\Delta t}}{\frac{d\Gamma[\overline{B^0}\to f_{CP}]}{d\Delta t} - \frac{d\Gamma[B^0\to f_{CP}]}{d\Delta t}} \\ &= \mathcal{A}_{CP}\cos\Delta m_d\Delta t + \mathcal{S}_{CP}\sin\Delta m_d\Delta t, \end{aligned} \tag{2.51}$$

where $\frac{d\Gamma[\overline{B^0}(B^0)\to f_{CP}]}{d\Delta t}$ is obtained from Eq. 2.47 at $q_{\rm tag} = +1(-1)$. Equation 2.51 has the same form in Δt as Eq. 2.31 which means that CP violation in the B meson decays can be measured experimentally.

2.4 CP Asymmetries from Quark Mixing

In this section, we derive prediction of CP asymmetries for the decays mediated by the $b\to c\bar{c}s$ tree transitions and by the flavor-changing neutral current of $b\to s$ and $b\to d$ transitions based on the formalism in § 2.4.2. In this thesis, we focus on the latter decays.

2.4.1 CP Asymmetries in $b \to c\bar{c}s$ Tree Transitions

The decay mediated by the $b \to c\bar{c}s$ tree (first order) transitions, such as $B^0 \to J/\psi K^0_S$, has a very small theoretical uncertainty in prediction of CP violation. Especially, the $B^0 \to J/\psi K^0_S$ decay is the "golden mode" to measure the angle ϕ_1 because this mode can be reconstructed with high purity (∼97%) due to a relatively large branching fraction and a small amount of background. The direct CP asymmetry is expected to be very small in the Standard Model.

The $B^0 \to J/\psi K^0_S$ decay is described by Feynman diagrams shown in Fig. 2.5 including the tree and penguin contributions.

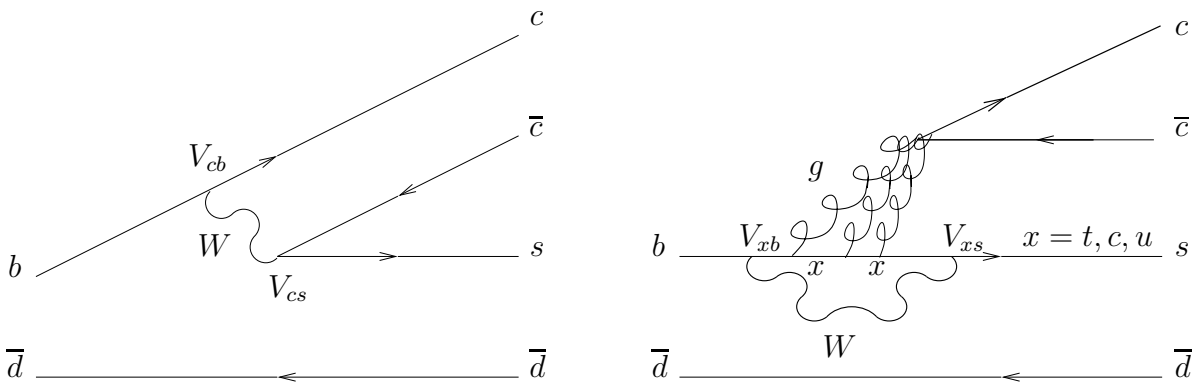

Figure 2.5: Feynman diagram for tree (left) and penguin (right) amplitudes in the $B^0 \to J/\psi K^0_S$ decay. The penguin contribution is expected to be negligible ($\mathcal{O}(10^{-3})$) for $\sin 2\phi_1$ measurement in the Standard Model [19]. In the case of electroweak penguin, the gluons are replaced by a Z boson or a γ.

The amplitude of $B^0 \to J/\psi K^0$ is given by

$$A_{J/\psi K} = (V^*_{cb}V_{cs})T_{J/\psi K} + \sum_{q=u,c,t}(V^*_{qb}V_{qs})P^q_{J/\psi K}, \tag{2.52}$$

where $T_{J/\psi K}$ and $P^q_{J/\psi K}$ are the amplitudes exclusive of the CKM matrix elements. By introducing the unitarity constraint,

$$\sum_{q=u,c,t}(V^*_{qb}V_{qs}) = 0, \tag{2.53}$$

the amplitude can be rewritten as

$$\begin{aligned} A_{J/\psi K} &= (V^*_{cb}V_{cs})(T_{J/\psi K} + P^c_{J/\psi K}) + (V^*_{ub}V_{us})P^u_{J/\psi K} + (V^*_{tb}V_{ts})P^t_{J/\psi K} \\ &= (V^*_{cb}V_{cs})(T_{J/\psi K} + P^c_{J/\psi K} - P^t_{J/\psi K}) + (V^*_{ub}V_{us})(P^u_{J/\psi K} - P^t_{J/\psi K}). \end{aligned} \tag{2.54}$$

As the ratio $(V^*_{ub}V_{us})/(V^*_{cb}V_{cs})$ is of order $\mathcal{O}(\lambda^2)$, the amplitude is

$$A_{J/\psi K} \sim (V^*_{cb}V_{cs})T_{J/\psi K} + (V^*_{cb}V_{cs})(P^c_{J/\psi K} - P^t_{J/\psi K}). \tag{2.55}$$

Thus, the ratio of amplitudes for the $B^0 \to J/\psi K^0_S$ decay is given by

$$\frac{\overline{A}_{J/\psi K}}{A_{J/\psi K}} = \frac{V_{cb}V^*_{cs}}{V^*_{cb}V_{cs}}. \tag{2.56}$$

Since the final state includes a K^0_S, an extra factor for $K^0\overline{K^0}$ mixing should be considered. The state K^0_S is a mixture of K^0 and $\overline{K^0}$ as follows,

$$|K^0_S\rangle = p_K|K^0\rangle + q_K|\overline{K^0}\rangle. \tag{2.57}$$

Thus, the amplitude becomes

$$A_{J/\psi K^0_S} = \langle J/\psi K^0_S|B^0\rangle = \langle K^0_S|K^0\rangle\langle J/\psi K^0|B^0\rangle = p^*_K A_{J/\psi K}, \tag{2.58}$$

$$\overline{A}_{J/\psi K^0_S} = \langle J/\psi K^0_S|\overline{B^0}\rangle = q^*_K A_{J/\psi K}, \tag{2.59}$$

where the extra factor is calculated in a way similar to $B^0\overline{B^0}$ mixing,

$$\frac{V_{cs}V^*_{cd}}{V^*_{cs}V_{cd}}. \tag{2.60}$$

The parameter $\lambda_{J/\psi K^0_S}$ is obtained to be

$$\lambda_{J/\psi K^0_S} = \frac{q}{p}\frac{\overline{A}_{J/\psi K^0_S}}{A_{J/\psi K^0_S}} = \frac{q}{p}\frac{q^*_K}{p^*_K}\frac{\overline{A}_{J/\psi K}}{A_{J/\psi K}} \tag{2.61}$$

$$\sim \frac{V^*_{tb}V_{td}}{V_{tb}V^*_{td}} \cdot \frac{V_{cs}V^*_{cd}}{V^*_{cs}V_{cd}} \cdot \frac{V_{cb}V^*_{cs}}{V^*_{cb}V_{cs}} = -\exp(-2i\phi_1), \tag{2.62}$$

where the minus sign represents the CP-odd state of the $J/\psi K^0_S$ and from Eq. 2.49. By substituting $\lambda_{J/\psi K^0_S}$ in Eq. 2.48 and 2.49, CP-violating parameters in the $B \to J/\psi K^0_S$ decay are expected from the quark mixing to be

$$\mathcal{A}_{J/\psi K^0_S} = 0 \text{ and } \mathcal{S}_{J/\psi K^0_S} = \sin 2\phi_1. \tag{2.63}$$

Therefore, by substituting Eq. 2.63 for Eq. 2.51, the time-dependent CP asymmetry in is expected to be

$$A_{CP}(t) = \sin 2\phi_1 \sin(\Delta m_d \Delta t). \tag{2.64}$$

On the other hand, $\mathcal{A}_{CP}$ and $\sin 2\phi_1$ are measured [20] to be

$$\mathcal{A}_{CP}(B^0 \to J/\psi K^0) = +0.002 \pm 0.020 \text{ and} \tag{2.65}$$

$$\sin 2\phi_1(B^0 \to J/\psi K^0) = +0.657 \pm 0.025, \tag{2.66}$$

where large mixing-induced CP violation has been confirmed and direct CP is consistent with zero. This measurement gives the tightest experimental constraint to the CKM unitary triangle as shown in Fig. 2.6. In addition, the measurements of CP asymmetries in the $b \to c\overline{c}s$ transition decays will be assumed as the Standard Model expectation when we search for new weak phases in $b \to s$ decays in § 7.4.1.

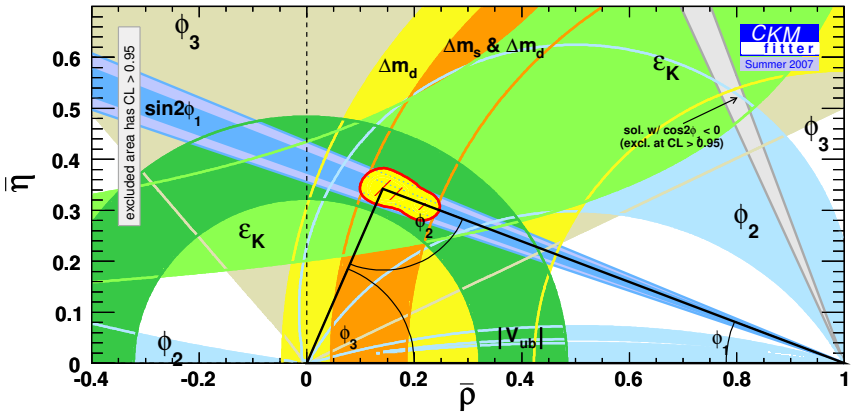

Figure 2.6: Current experimental constraints to the CKM unitary triangle [21]. Previously unmentioned parameters in this figure include the CP violating parameters in the neutral kaon system, ϵ_K, and the mass difference between the B_s mass eigenstates, Δm_s.

2.4.2 CP Asymmetries in Flavor-Changing Neutral Current B^0 Decays

In contrast to $b \to c$ transitions that are induced by the charged current, the neutral current is flavor-conserving, which is ensured by the unitarity of the CKM matrix. Thus, Flavor Changing Neutral Currents (FCNC), such as in $b \to s$ and $b \to d$ transitions, proceed via second order decay processes that can be represented by a one loop or a box diagram.

CP Asymmetries in $b \to s$ Transitions

The $B^0 \to \phi K^0_S$ decays via almost pure $b \to\to sgs\overline{s}s$ transition, dominated by a loop diagram called penguin diagram, as shown in Fig. 2.7 and is considered to be the "golden mode" of $b \to s$ transitions due to its small theoretical uncertainty [8].

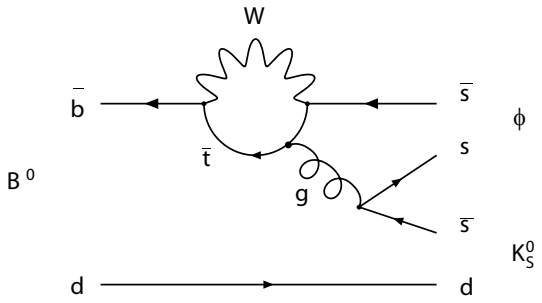

Figure 2.7: Feynman diagram in the $B^0 \to \phi K^0_S$ decay. If only Standard Model particles appear in this diagram, the CP-violating phase in the mixing and this decay is ϕ_1.

The amplitude of $B^0 \to \phi K^0_S$ is

$$A_{\phi K} = \sum_{q=u,c,t} (V^*_{qb} V_{qx}) P^q_{\phi K}, \tag{2.67}$$

where $P^q_{\phi K}$ are the penguin amplitudes for the $B^0 \to \phi K^0_S$ decay. Using a unitary constraint, $\sum_{q=u,c,t}(V^*_{qb}V_{qs}) = 0$,

$$A_{\phi K} = (V^*_{cb}V_{cs})(P^c_{\phi K} - P^t_{\phi K}) + (V^*_{ub}V_{us})(P^u_{\phi K} - P^t_{\phi K}). \tag{2.68}$$

Since $V^*_{ub}V_{us} \ll V^*_{cb}V_{cs}$, the ratio of amplitudes for the $B^0 \to \phi K^0_S$ decay is given by

$$\frac{\overline{A}_{\phi K}}{A_{\phi K}} \sim \frac{V_{cb}V^*_{cs}}{V^*_{cb}V_{cs}}, \tag{2.69}$$

which is the same as that of the $B^0 \to J/\psi K^0_S$ decay. The parameter $\lambda_{\phi K^0_S}$ is obtained to be

$$\lambda_{\phi K^0_S} = \frac{q}{p}\frac{\overline{A}_{\phi K^0_S}}{A_{\phi K^0_S}} = \frac{q}{p}\frac{q^*_K}{p^*_K}\frac{\overline{A}_{\phi K}}{A_{\phi K}} \tag{2.70}$$

$$\sim -\exp(-2i\phi_1), \tag{2.71}$$

where the minus sign represents the CP-odd state of the ϕK^0_S. From Eq. 2.48 and Eq. 2.49, CP asymmetry in the $B^0 \to \phi K^0_S$ decay is expected from the quark mixing to be

$$\mathcal{A}_{CP} = 0 \text{ and } \mathcal{S}_{CP} = \sin 2\phi_1. \tag{2.72}$$

Therefore, the time-dependent CP asymmetry is expected to be

$$A_{CP}(t) = \sin 2\phi_1 \sin(\Delta m_d \Delta t). \tag{2.73}$$

Within the loop diagram, a heavy particle unknown in the Standard Model may appear due to the Uncertainty Principle. This amplitude may interfere with that in the Standard Model if its magnitude is sizable. If the CP-violating new weak phase is different from that in the Standard Model, the measured CP asymmetry may contain a sizable contribution from the new weak phase. In some models, the value of $\mathcal{S}_{CP}$ may differ from $\sin 2\phi_1$ by more than a few percent and thus, $b \to s$ modes are an excellent probe for New Physics. Taking into account New Physics effects, the CP-violating phase (ϕ_1) and mixing-induced CP-violating parameter ($\mathcal{S}_{CP}$) are sometimes written as $\phi_1^{\rm eff}$ and $\mathcal{S}^{\rm eff}_{CP}$, respectively.

Other $b \to s$ decay channels, such as $B^0 \to \eta' K^0_S$, non-resonant $B^0 \to K^0_S K^+ K^-$ and $B^0 \to f_0 K^0_S$, have similar properties and can be used to search for new weak phases through CP asymmetry measurements. The prediction described in this section are originated from the first order approximation in the Quark Mixing, ignoring smaller effects such as QCD factorization. The theoretical uncertainties within the Standard Model will be mentioned in § 7.4.1.

CP Asymmetries in $b \to d$ Transitions

The $b \to d$ transitions are also induced by FCNC, but they have much smaller branching fractions than $b \to s$ transitions in the Standard Model because $|V_{td}|^2/|V_{ts}|^2 \sim 1/25$. Due to their smaller decay amplitudes, they may be even more sensitive to New Physics effects than $b \to s$ decays. In addition, since the weak phase in $b \to d$ transitions differs from that in $b \to s$ transitions, CP asymmetry measurements in $b \to d$ transitions could be used as a probe for possible new weak phases independently of those in $b \to s$ transitions.

The $B^0 \to K^0_S K^0_S$ decay via a pure $b \to dg \to d\bar{s}s$ transition as shown in Fig. 2.8 and is considered to be the "golden mode" of $b \to d$ transitions due to its small theoretical uncertainty [10].

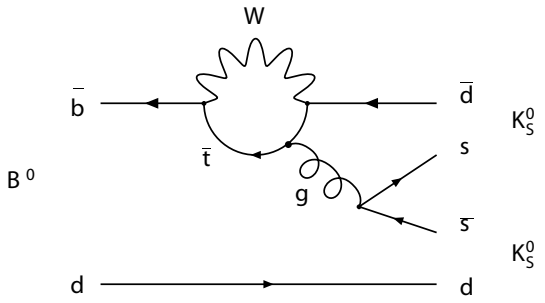

Figure 2.8: Feynman diagram in the $B^0 \to K^0_S K^0_S$ decay. If only Standard Model particles appear in this diagram, no CP violation is expected.

The amplitude is written as

$$A_{B^0 \to K^0_S K^0_S} = V^*_{tb} V_{td} P_t, \tag{2.74}$$

where P_t is the penguin amplitude. Thus, one gets

$$\lambda_{K^0_S K^0_S} = \frac{V^*_{tb} V_{td}}{V_{tb} V^*_{td}} \cdot \frac{V_{tb} V^*_{td}}{V^*_{tb} V_{td}} = 1. \tag{2.75}$$

Note that the CP-violating phase in the decay amplitude (ϕ_1) cancels that in the $B^0\overline{B^0}$ mixing. From Eq. 2.48 and Eq. 2.49, CP asymmetry in the $B^0 \to K^0_S K^0_S$ decay is expected from the quark mixing to be

$$\mathcal{A}_{K^0_S K^0_S} = 0 \text{ and } \mathcal{S}_{K^0_S K^0_S} = 0. \tag{2.76}$$

Non-zero contributions from loops with intermediate up and charm quarks can result in both types of effects (as usual, a strong phase difference is required for direct CP violation to occur). The theoretical uncertainties from light-quark effects as well as possible deviation sources within the Standard Model will be mentioned in § 7.4.1.

Chapter 3

Experimental Apparatus

The Belle experiment is designed to resolve the nature of CP violation, which holds one of the key to the origin of the universe. The experiment is located at the High Energy Accelerator Research Organization (KEK) in Japan, and utilizes the Belle detector and the KEKB factory. The KEKB accelerator, which is the world-highest luminosity collider, produces huge number of $B\overline{B}$ pairs and the Belle detector measure their decays.

In this chapter, we explain the experimental apparatus utilized to collect $B\overline{B}$ data sample.

3.1 The KEKB Accelerator

The KEKB accelerator [22] is a high luminosity energy-asymmetric e^+e^- collider that is designed to produce $B\overline{B}$ meson pairs in a clean environment. The configuration of the KEKB accelerator is shown in Fig. 3.1. The KEKB accelerator has two rings with a diameter of 1 km: a low-energy ring (LER) for positrons and a high-energy ring (HER) for electrons. The beam energies are 3.5 GeV for e^+ and 8.0 GeV for e^- and the center-of-mass energy is 10.580 GeV which coincides with the $\Upsilon(4S)$ resonance just above the $B\overline{B}$ production threshold. In this analysis, we assume equal production of pairs of charged and neutral B mesons in the $\Upsilon(4S)$ decay. The $\Upsilon(4S) \to B\overline{B}$ process has a cross section of 1.05 nb [1], while the $e^+e^- \to q\overline{q}$ ($q = u$, d, s, or c) continuum process has a cross section of 3.7 nb.

The typical flight length of a B-meson in the $\Upsilon(4S)$ center-of-mass frame is only 2 μm which is not sufficient to measure Δt for a time-dependent CP analysis. However, using the asymmetric energy, B meson pairs are generated with a Lorenz boost factor ($\beta\gamma$) of ~ 0.425. Then, the average distance in the laboratory frame between decay vertices of the two B mesons in the z direction is about 200 μm, where the z axis is defined as the direction opposite to the e^+ beam.

[1] 1 $b = 10^{-24}$ cm^2.

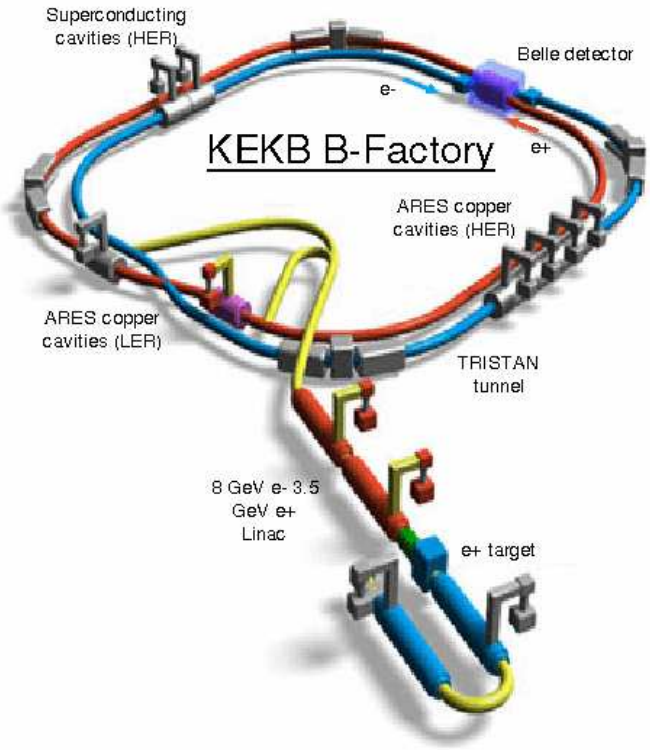

Figure 3.1: The configuration of the KEKB accelerator. The KEKB accelerator has two rings with a diameter of 1 km with 22 mrad crossing angle, LER for positrons and HER for electrons.

Table 3.1: Machine parameters of the KEKB as of Nov. 2006, when the KEKB achieved the highest peak luminosity.

Ring	LER	HER	Unit
Beam current I	1.65	1.33	A
# of bunches per ring	1389		
Bunch current	1.19	0.96	mA
# of particles per bunch	7.9×10^{10} e^+	5.6×10^{10} e^-	
Bunch spacing	1.8-2.4		m
Emittance ϵ_x	18	24	nm
Horizontal beta function at IP β_x^*	59	56	cm
Vertical beta function at IP β_y^*	0.65	0.59	cm
Horizontal beam size at IP σ_x	103	116	μm
Vertical beam size at IP σ_y	1.9	1.9	μm
Beam-beam tune shift ξ_x	0.115	0.075	
Beam-beam tune shift ξ_y	0.101	0.056	
Bunch length	7	6	mm
Luminosity $\mathcal{L}$	1.712		10^{34} cm$^{-2}s^{-1}$

Luminosity represents the parameter on beam intensity defined as $\mathcal{L} = R\sigma$, where R and σ are the cross section and the event rate, respectively. The branching fraction of B decays used for CP asymmetry measurements are order of $10^{-4} \sim 10^{-7}$. The KEKB is designed to achieve high luminosity of $\sim 10^{34}$ cm$^{-2}s^{-1}$, which corresponds to $\sim 10^8 B\overline{B}$ pairs a year. The luminosity $\mathcal{L}$ can be expressed as

$$\mathcal{L} = 2.2 \times 10^{34} \xi_{\pm y} (1 + \frac{\sigma_y^*}{\sigma_x^*}) (\frac{E \cdot I}{\beta_y^*})_{\pm}, \tag{3.1}$$

where $\xi_y, \frac{\sigma_y^*}{\sigma_x^*}, E, I, \beta_y^*$ represent the beam-beam tune shift parameter in the vertical direction, the ratio of the beam sizes in the horizontal and vertical directions, the beam energy (GeV), the beam current (A) and the beta function (cm) at Interaction Point (IP,) respectively, and the sign of + and - corresponds to the case of LER and HER, respectively. Each ring stores a few thousand bunches, which are clusters of several hundred billion electrons or positrons. The luminosity highly depends on three kinds of parameters, the beam current I, beam-beam parameter ξ and vertical beta function β_y^* at IP. The machine parameters of the KEKB are summarized in Table 3.1.

In order to reduce parasitic collisions near the interaction region, the KEKB has a unique design setting a 22 mrad crossing angle of the e^+e^- beams instead of using bending magnets, which delivers higher peak luminosities with less beam-induced background to the Belle detector.

The commissioning of the KEKB accelerator started in 1998 and was designed to operate with a peak luminosity of 10^{34} cm$^{-2}s^{-1}$. Now the accelerator operates routinely with a peak luminosity of $\sim 1.712 \times 10^{34}$ cm$^{-2}s^{-1}$, which well exceeds the designed goal. In early 2004,

a new operation method called "continuous injection" was successfully introduced, which removes the dead time of the ordinary injection method. Without continuous injection, one had to stop data taking and had to lower the detector HVs to protect readout electronics from beam injection that is performed every one hour [2]. Now the KEKB factory can produce 1 fb^{-1} per day. In early 2007, new cavities, called "crab cavities" were installed in both rings. They tilt the bunches by a half of the beam crossing angle just before collision so that they can collide head-on.

3.2 The Belle Detector

The Belle detector [23] is a large-solid-angle magnetic spectrometer for the study of CP violation in the B meson system. A schematic of the Belle detector is shown in Fig. 3.2. B meson decay vertices are reconstructed precisely by the silicon vertex detector (SVD) surrounding the beam pipe close to the IP. Charged particles are tracked and reconstructed by a central drift chamber (CDC). Charged kaons and pions are identified by the combined information from dE/dx measured by CDC, the array of aerogel threshold Cerenkov counters (ACC) and the time-of-flight scintillation counters (TOF). The electrons and photons are identified with an electromagnetic calorimeter (ECL), which are located inside a superconducting solenoid coil that provides a 1.5 T magnetic field. To detect K_L^0 mesons and to identify muons, the iron flux return (KLM) is instrumented outside of the coil. Two inner detector configurations were used. A 2.0 cm-radius beam pipe and a 3-layer SVD (SVD1) was used for the first data sample of 152×10^6 $B\overline{B}$ pairs, while a 1.5 cm-radius beam pipe, a 4-layer SVD (SVD2) [24], and a small-cell inner drift chamber were used to record the remaining 505×10^6 $B\overline{B}$ pairs. Performance parameters of the Belle detector are summarized in Table 3.2. and further details can be found in Ref. [23].

Beam Pipe

The beam pipe for SVD1 has an inner radius of 2.0 cm and an outer outer radius of 2.3 cm, respectively. The central part (-4.6 cm $< z <$ 10.1 cm) of the beam pipe consists of double beryllium cylinders each with 0.5 mm thickness. The gap between these two beryllium walls provides a channel for helium gas, which is used as a coolant. The maximum temperature increase for the inner beryllium is estimated to be 25 degrees assuming a uniformly distributed 100 W heat load on the inner wall and a 2 g/s He flow. The beryllium central section is brazed to aluminium pipes that allows the synchrotron x-rays generated in the innermost bending magnets to pass through without hitting the inner beryllium wall. A mask made of gold is used to absorb the back-scattered photons with a critical energy of less than 2 keV. Particle backgrounds are severe at KEKB. The rate of particles from both beams hitting the beam pipe is calculated to be around 130 kHz in a 10^{-9} Torr vacuum. Movable masks are

[2] Especially in the proposed upgraded KEKB experiment (Super-KEKB), lifetime of beam can be order of ten minutes and the dead time during such frequent beam injection would have a serious problem.

Table 3.2: Performance parameters for the Belle detector. Two configurations of inner detectors, SVD1 and SVD2, are used to collect two data sets.

Sub detector	Type	Configuration	Readout	Performance
Beam pipe for SVD1	Beryllium double wall	Cylindrical, $r = 20$ mm 0.5/2.5/0.5 (mm)= Be/He/Be with He gas cooled		
Beam pipe for SVD2	Beryllium double wall	Cylindrical, $r = 15$ mm 0.5/2.5/0.5 (mm) = Be/PF200/Be		
SVD1	Double-sided Si strip	3-layers: 8/10/14 ladders Strip pitch: 25(p)/50(n) μm	ϕ : 40.96k z : 40.96k	$\sigma(z_{CP})$ ~ 78.0 μm for $B \to \phi K^0_S$
SVD2	Double-sided Si strip	4-layers: 6/12/18/18 ladders Strip pitch: 75(p)/50(n) μm (layer1-3) 73(p)/65(n) μm (layer4)	ϕ: 55.296k z: 55.296k	$\sigma(z_{CP})$ ~ 78.9 μm for $B \to \phi K^0_S$
CDC	Small cell drift chamber	Anode : 50 layers $r = 8.3 - 86.3$ cm -77 cm$\leq z \leq$160 cm	Anode : 8.4k $\sigma_{p_t}/p_t =$ 0.3% $\sqrt{p_t^2 + 1}$ $\sigma_{dE/dx} = 0.6$ %	$\sigma_{r\phi} = 130$ μm $\sigma_z =$ 200$\sim$1400 μm
ACC	Silica aerogel	960 barrel/228 end-cap FM-PMT readout		$N_{p.e.} \geq 6$ K/π separation: $1.2 < p < 3.5$ GeV/c
TOF/TSC	Scintillator	128/64 ϕ segmentation $r = 120$ cm, 3-cm long	128×2 / 64 64	$\sigma_t = 100$ ps K/π separation: up to 1.2 GeV/c
ECL	CsI (Towered-structure)	Barrel : $r =$ 125-162 cm End-cap : $z =$ -102 cm and +196 cm	6624 1152(F) 960(B)	$\sigma_E/E =$ 1.3 %/$\sqrt{E}$ $\sigma_{\rm pos} = 0.5$ cm/$\sqrt{E}$ (E in GeV)
KLM	Resistive plate counters	14 layers (5 cm Fe + 4 cm gap) 2 RPCs in each gap	θ : 16k ϕ : 16k	$\Delta\phi$=$\Delta\theta = 30$ mrad for K^0_L ~ 1 % hadron fake
EFC	BGO	Photodiode readout Segmentation : 32 in ϕ, 5 in θ	160×2	Energy resolution: (RMS) 7.3% at 8.0 GeV 5.8% at 2.5 GeV
Magnet	Super-conducting	Inner radius = 170 cm		$B = 1.5$ T

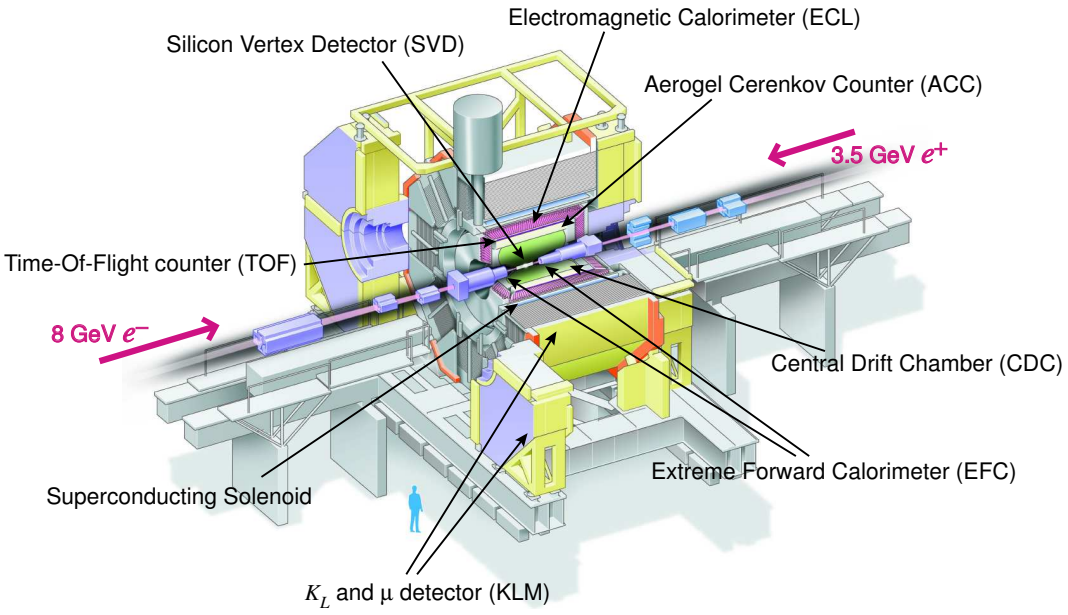

Figure 3.2: Schematic of the Belle Detector.

installed to reduce the radiation levels at injection.

The beam pipe for SVD2 is redesigned, placing it closer to the IP, to have an inner radius of 1.5 cm, so that the silicon vertex detector can be placed closer to the IP.

Silicon Vertex Detector (SVD)

Figure 3.3 shows the configuration from of the first version of SVD (SVD1). SVD1 was a three layers Double-sided Silicon Detector (DSSD) in a barrel-only design, comprising of 8, 10, and 14 ladders in the inner, middle, and outer layers, respectively. Each ladder is constructed from two joined half-ladders. SVD1 covers $23\ ^\circ < \theta < 139\ ^\circ$, corresponding to 86 % coverage of the solid angle. The radii of these layers are 30.0 mm, 45.5 mm, and 60.5 mm. The DSSDs were originally developed for the DELPHI micro-vertex detector and produced by Hamamatsu Photonics (HPK). Each DSSD has 1280 striped sensors and 640 readout pads on opposite sides. The z-strip ($r\phi$-strip) pitch is 42 (25) μm, and readout z-strip ($r\phi$-strip) pitch is 84 (50) μm, respectively. The size of the active region in DSSD is 53.5×32.0 mm^2 on the z-side and 54.5×32.0 mm^2 on the $r\phi$-side.

SVD2, which was installed in summer 2003, has four detector layers, consisting of 6, 12, 18, and 18 ladders from the innermost layer, respectively. The side-view of SVD2 system is illustrated in Fig. 3.3. Detector acceptance is also improved by a larger coverage, $17\ ^\circ < \theta < 150\ ^\circ$, which is the same as the CDC. The first layer is even closer to the interaction region than SVD1. The beam pipe is also replaced by a smaller (1.5 cm in radius) one. Two kinds of DSSDs are installed: 34.9×76.4 mm^2 DSSDs are used for the fourth layer,

and 28.4×79.6 mm^2 DSSDs are used for the other three layers. For the inner three layers, the z-strip pitch is 75 μm and the $r\phi$-strip pitch is 50 μm. For the fourth layer, the z-strip ($r\phi$-strip) pitch is 73 (65) μm.

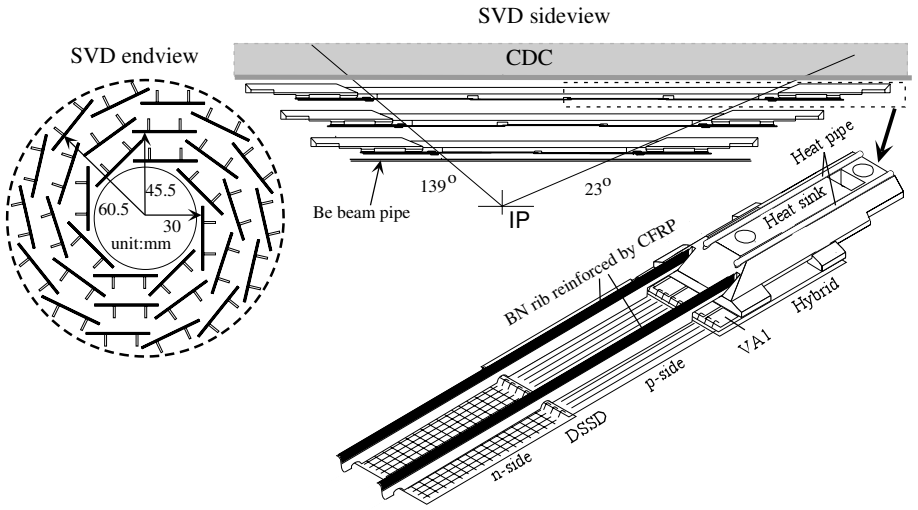

Figure 3.3: The configuration of SVD1.

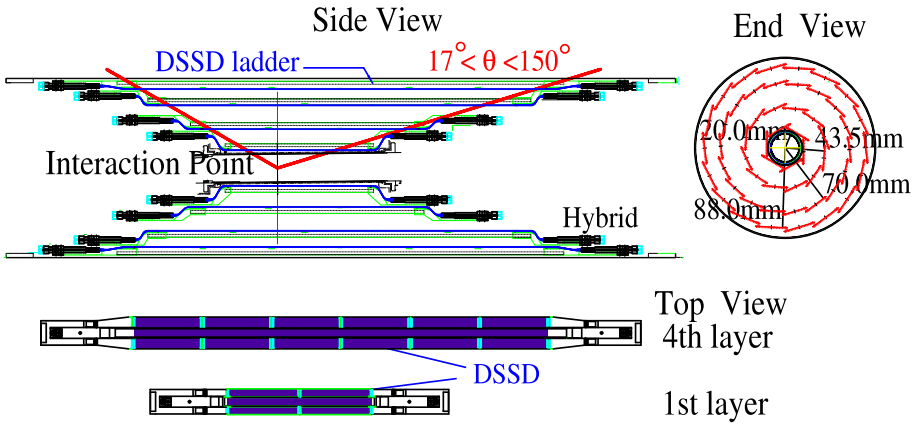

Figure 3.4: An illustration of SVD2.

The SVD readout employs "Track and Hold" system. Signals from each side of the DSSDs are read out by the 128 ch readout chip, called VA1TA, with a peaking time of 800 ns. [3] When the pre-hold trigger arrives, the shaper output is held by the capacitors. When the readout trigger arrives (Level-1), the output voltage is read out sequentially, then multiplexed onto a single output and finally sampled by the Flash Analogue to Digital Converter (FADC) at 5 MHz.

[3]The pre-hold trigger (the so-called Level-0 trigger), which is made from the TOF and CDC signal, comes after 800 ns from the collision. The average Level-0 trigger rate is around 2 kHz and the hold efficiency is $\sim$ 95 %.

The SVD DAQ control system consists of a data manager, a run manager, and an interlock. The data from the FADC output is transferred to an event builder by the data manager, while the DAQ hardware is controlled by the run manager. The running conditions are monitored by the interlock system,

SVD-matched tracks are defined as the interpolated tracks from CDC that have associated SVD hits. At least two layers of z information and one $r\phi$ layer hit is required. The SVD matching efficiency is defined as the ratio between numbers of SVD matched tracks and all CDC tracks. The average SVD matching efficiency is estimated to be greater than 98.7 %.

Using cosmic-ray data, the impact parameter resolution at the IP is measured. As shown in Fig. 3.5, the impact parameter resolution at the IP for SVD2 is better than that for SVD1 because the first layer is closer to the IP: $\sigma_{r\phi} = 19.2 \oplus 54.0/\tilde{p}$ μm, $\sigma_z = 42.2 \oplus 44.3/\tilde{p}$ μm, for SVD1, and $\sigma_{r\phi} = 21.9 \oplus 35.5/\tilde{p}$ μm, $\sigma_z = 27.8 \oplus 31.9/\tilde{p}$ μm, for SVD2, where $\tilde{p}$ is the pseudo-momentum defined as $p\beta \sin^{3/2}\theta (p\beta \sin^{5/2}\theta)$ for $r-\phi(z)$ side, p is the track momentum and θ is the polar angle.

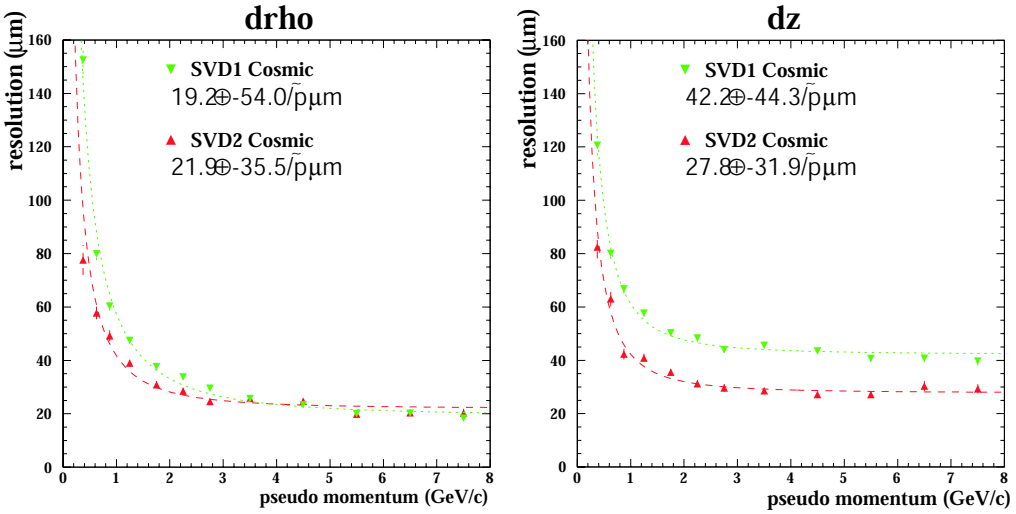

Figure 3.5: The impact parameter resolution at the IP for SVD1 and SVD2 using cosmic ray data.

Central Drift Chamber (CDC)

The central drift chamber (CDC) [25] is used to detect charged tracks and measure dE/dx. The signal is made by the charged particles ionizing the gas contained in the CDC. Since most of the daughter particles from B decays have momenta lower than 1 GeV/c, a low-Z gas: a 50 % helium and 50 % ethane mixture, is selected to minimize multiple scattering and thus provide good momentum resolution. The CDC consists of 50 cylindrical layers and 8400 drift cells and its structure is shown in Fig. 3.6. The CDC has 32 axial anode wire layers for x-y measurement and 18 small-angle stereo wire layers for z measurement. At the inner

layers of the CDC, three cathode-strip layers are made for higher precision z measurement where the particles enter the CDC. The CDC covers the polar angle between $17° < \theta < 150°$, corresponding to a 92 % coverage of the solid angle.

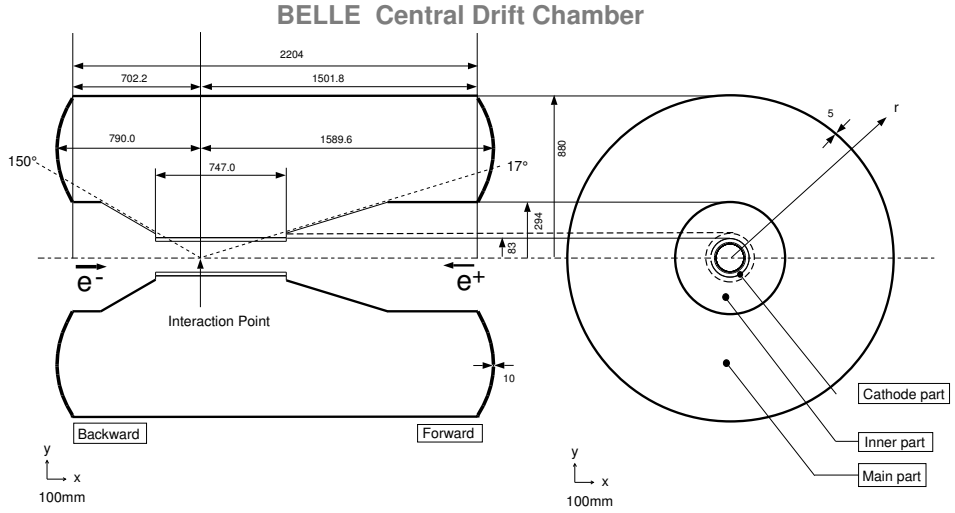

Figure 3.6: Overview of the CDC structure. The directions of e^+e^- beams and position of the interaction point are also marked. The units are in mm.

The typical position resolution is measured to be ~ 120 μm, but it has small variations by $\sim$ 20 μm depending on the incident angles and layers. The transverse momentum, p_t, resolution is measured using cosmic ray data as shown in Fig. 3.7: $\sigma_{p_t}/p_t = \sqrt{(0.28p_t)^2 + (0.35/\beta)^2}$ with only CDC information, while $\sigma_{p_t}/p_t = \sqrt{(0.19p_t)^2 + (0.30/\beta)^2}$ with both CDC and SVD information. Using dE/dx information with a given momentum, the populations of π, K, p and e are clearly separated. Figure 3.8 shows the measured dE/dx as a function of momentum, together with the expected mean energy loss for different particle species. The dE/dx resolution for minimum ionized pions from $K^0_S \to \pi^+\pi^-$ decays is measured to be $\sigma_{dE/dx}/ < dE/dx >= 7.8$ % with their momtmum between 0.4 and 0.6 GeV/c.

Aerogel Čerenkov Counter (ACC)

The aerogel Čerenkov counter (ACC) [26] is designed to discriminate between charged kaons and pions with momenta between 1.5 GeV and 3.5 GeV. The ACC is essential to select charged kaons against pions in $B \to K^0_S K^+ K^-$ analysis.

The ACC consists of blocks of silica aerogel. The silica aerogel is a transparent solid material with a colloidal form of glass that can provide a Čerenkov light threshold to suitably separate kaons and pions with the momentum of $\mathcal{O}(1)$ GeV. A typical ACC module consists of five aerogel tiles in a thin aluminium box with the size of $12\times12\times12$ cm^3. The Čerenkov light is detected using fine-mesh photo-multipliers (FM-PMT), which can operate even in a 1.5 T magnetic field. There are 960 ACC modules in the barrel region and 228 in the endcap

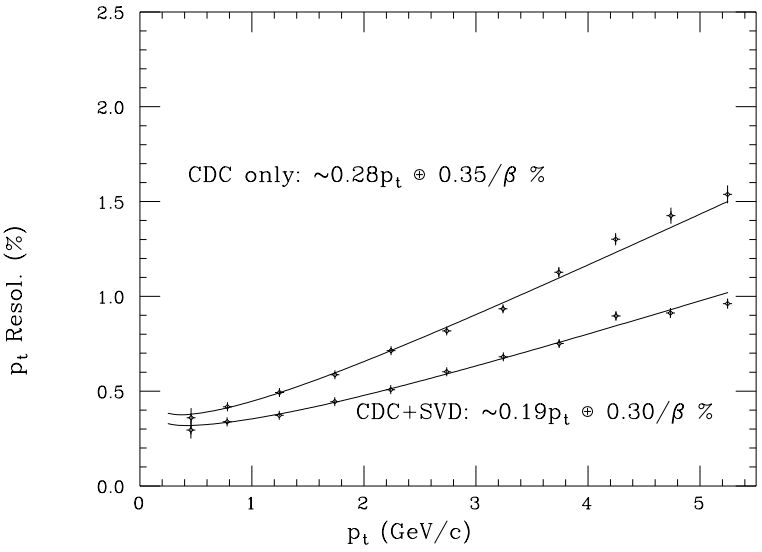

Figure 3.7: The transverse momentum resolution using cosmic ray data.

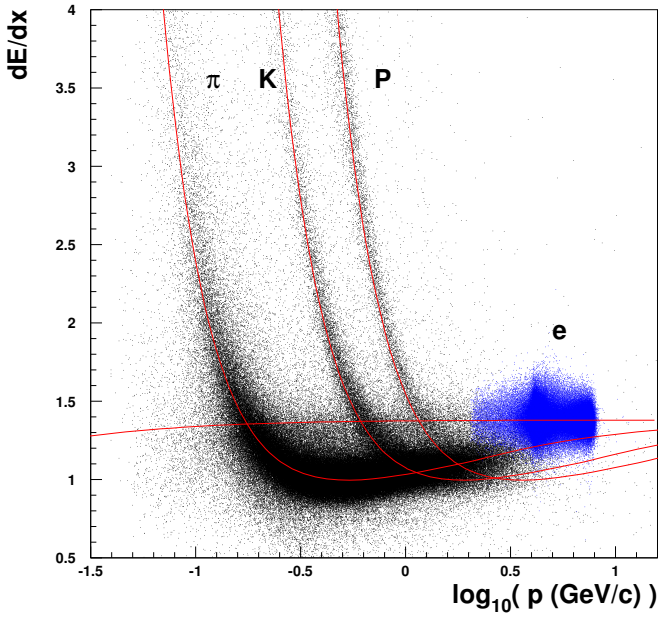

Figure 3.8: Measured dE/dx as a function of the charged track momentum using collision data.

region. The configuration of the ACC system from the side-view is shown in Fig. 3.9. The index of refraction, n, in the barrel region varies with the polar angle regions and is optimized to correspond to the high momentum range of the daughter particles in B-meson two-body decays. The refractive index in the endcap region is chosen for the middle momentum range of charged kaons in cascade B decays. These kaons are utilized in b-flavor tagging.

The ACC is an on-off device. The number of photo-electrons measured by the FM-PMT depends on the particle species and momentum. Figure 3.10 shows the distribution of the number of photo-electrons, N_{pe}, for charged pions and kaons tagged by $D^{*\pm}$ decays. Clear separation between kaons and pions can be seen. For kaons, there is a sharp peak at $N_{pe} = 0$, while pions form a broad distribution.

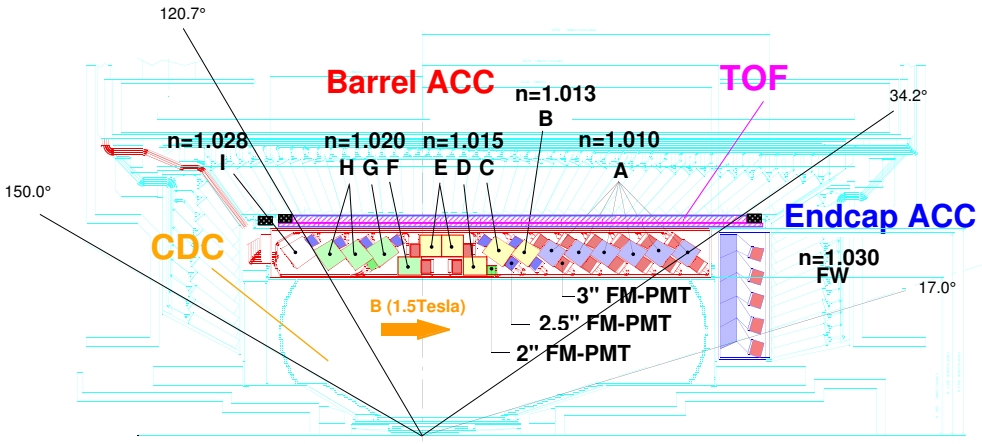

Figure 3.9: Side view of the ACC system together with other nearby detectors. The refractive index, n, is also given for each ACC module.

Time Of Flight Counter (TOF)

The time of flight (TOF) system [27] is important to identify charged particles with low momentum: below 1.2 GeV/c, which covers 90 % of the particles produced in B meson decays. This momentum region is not covered by the CDC or ACC. Thin trigger scintillation counters (TSC) are additionally introduced to provide the fast timing signal for the Belle trigger system. The configuration of a TOF/TSC module is illustrated in Fig. 3.11.

The TOF system consists of 128 TOF plastic scintillation counters combined with 64 TSC modules with 2 cm gaps. The TOF and TSC modules are located at a radius of 1.2 m from the interaction point, and cover a polar angle from 34 ° to 120 °. The TOF measures the difference between the collision time at the IP and the time when the particles pass through the TOF module, yielding the velocity of the particle. Together with the momentum from the CDC, the mass of the particles is calculated.

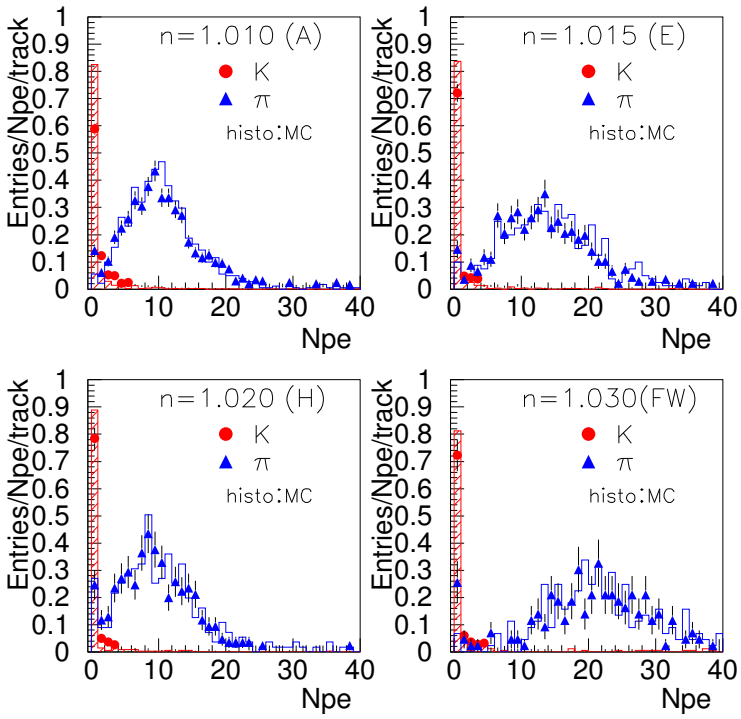

Figure 3.10: The distribution of the number of photo electrons measured by the ACC using $\pi^{\pm}$ and $K^{\pm}$ in $D^{*\pm}$ decays. Each figure corresponds to the different modules as labelled in Fig. 3.9. The expectation using MC simulation is also shown as histograms.

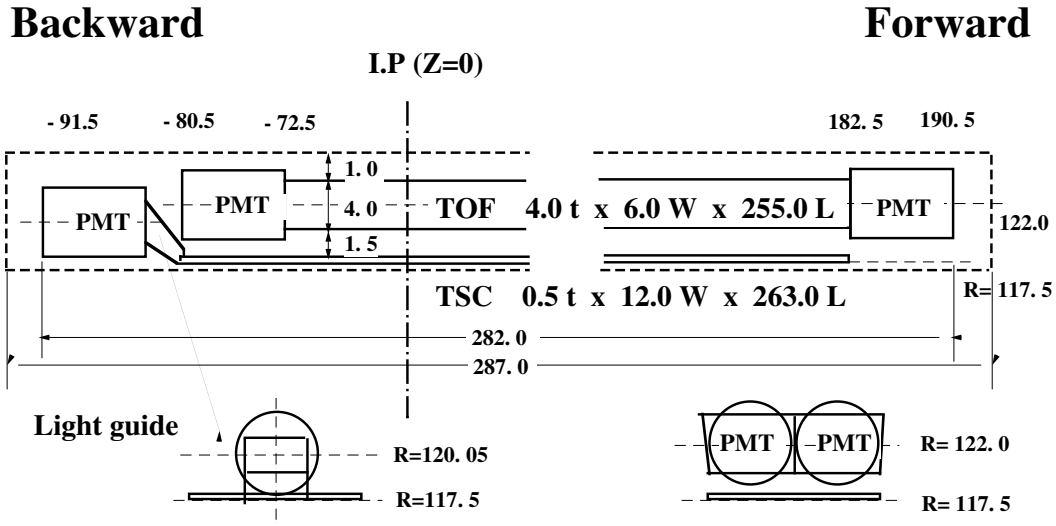

Figure 3.11: An illustration of a TOF/TSC module. The units are in mm.

Fine-mesh phototubes (FM-PMTs) are also used in the TOF readout. Each PMT signal is split into two. One is sent to a Q-to-T converter and a multi-hit TDC for charge measurement, while the other signal generates two different threshold levels: a high level (HL) and a low level (LL), where LL is used for TOF timing signals and HL provides a trigger signal.

Figure 3.12 shows the timing resolution as a function of the z position using $e^+e^- \to \mu^+\mu^-$ decays. Using the weighted average of the TOF measurements from both ends of each counter, the timing resolution is measured to be $\sigma_t = 100$ ps at the center, which meets the requirements for K/π separation with 3 σ for the momentum range up to 1.2 GeV/c.

Using the collision data, a clear separation among $K^\pm$, $\pi^\pm$ and $p^\pm$ with momentum below 1.25 GeV/c can be seen in Fig. 3.13.

Electromagnetic Calorimeter (ECL)

The electromagnetic calorimeter (ECL) [28] is used to detect photons from B decays with good energy and position resolution. Most of the photons are products of cascade decays, thus, good performance with photons below 500 MeV is necessary. Besides these cascade photons, direct production from two-body B decays such as $B \to K^\star\gamma$ requires a good energy resolution up to 4 GeV. The ECL is also used for electron identification by the Bremsstrahlung and pair-production mechanisms. To separate two nearby photons for high momentum π^0 detection, the ECL is finely segmented.

The ECL system consists of a highly segmented array of CsI(Tl) crystals with readout photodiodes. The overall configuration is shown in Fig. 3.14. ECL consists of a barrel section of 3.0 m in length with an inner radius of 1.25 m and endcap sections at $z = +2.0$ m

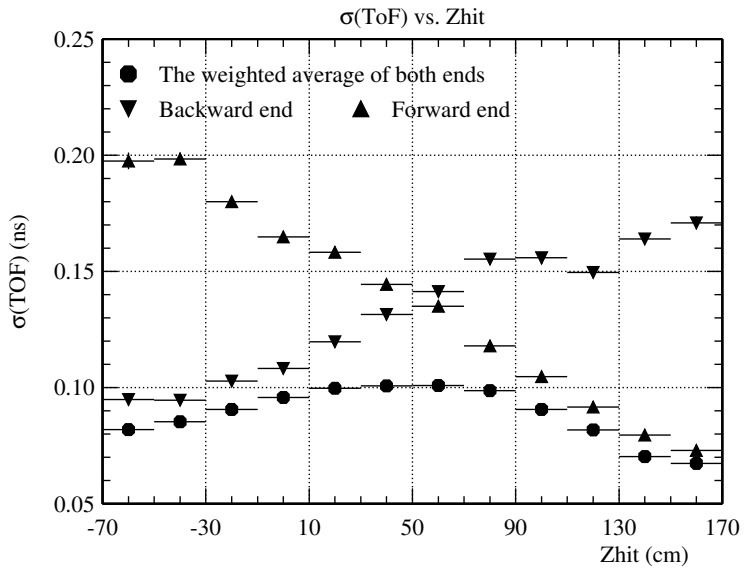

Figure 3.12: TOF timing resolution as a function of z position using $e^+e^- \to \mu^+\mu^-$ decays.

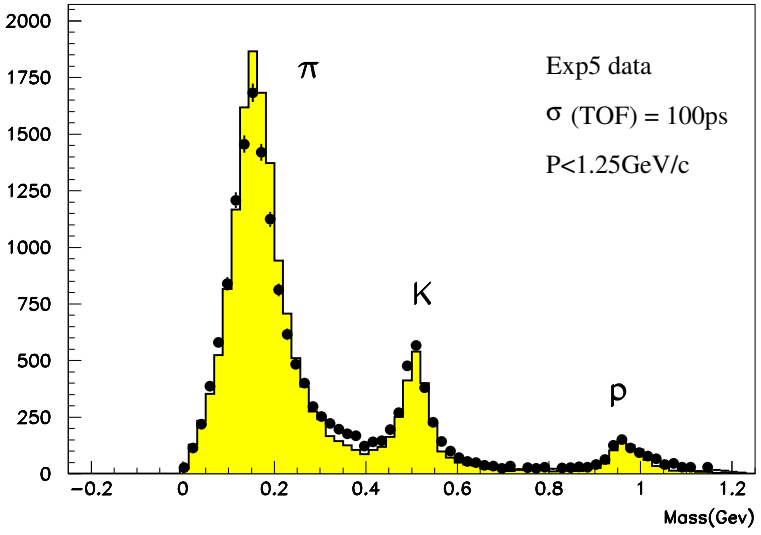

Figure 3.13: Mass distribution calculated from the measured time-of-flight and momentum for charged particles with momentum below 1.25 GeV/c using data.

and z = -1.0 m from the IP. Each CsI crystal is 30 cm long, which corresponds to 16.1 radiation lengths. The crystals are assembled in a tower shape with a tilt angle that is arranged to point towards the IP. The ECL covers the polar angle region of 17.0 ° $< \theta <$ 150 °, corresponding to a 91 % coverage of the solid angle. There are 6624, 1216, and 1040 crystals in the barrel, forward endcap, and backward endcap sections, respectively.

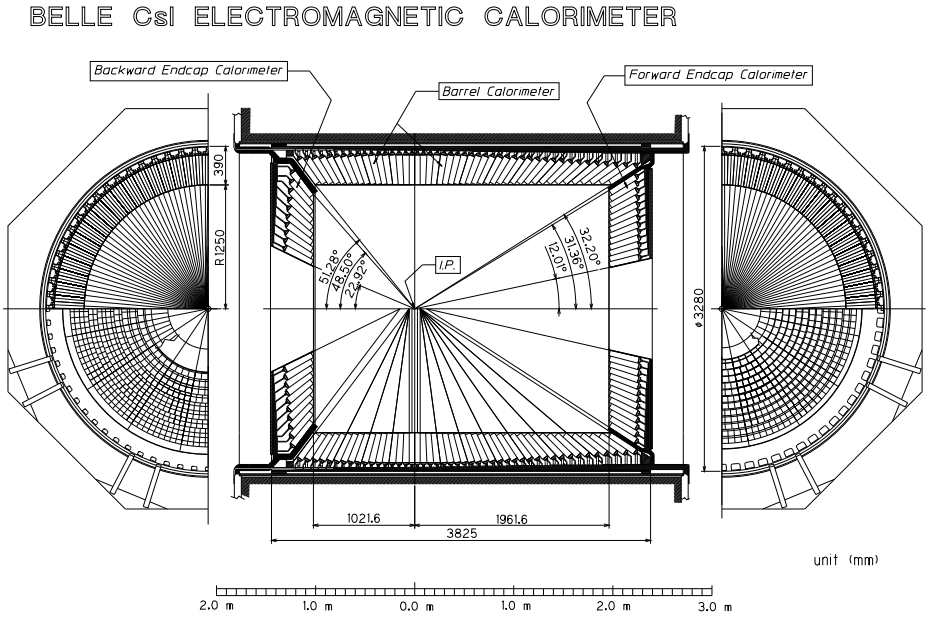

Figure 3.14: The overall configuration of the ECL.

From beam tests before installation, the energy resolution is measured to be σ_E/E (%) = $0.066/E \oplus 0.81/E^{1/4} \oplus 1.34$ and the position resolution is measured to be $\sigma_{\rm pos}$ (mm)=0.27 + $3.4/\sqrt{E} + 1.8/\sqrt[4]{E}$, where the unit of E is GeV. After the absolute energy is calibrated using Bhabha $e^+e^- \to e^+e^-$ data, the energy resolution is 1.5 %, 1.9 % and 2.5 % for the barrel, forward endcap and backward endcap regions, respectively.

Solenoid Magnet

The super-conducting solenoid magnet provides a magnetic field of 1.5 T parallel to the beam pipe over the tracking volume to measure the momentum of charge particles by their curved trajectories. The super-conducting coil consists of a single layer of niobium-titanium copper alloy embedded in a high purity aluminium stabilizer. It is wound around the inner surface of an aluminium support cylinder with a diameter between 3.4 m and 4.4 m. Indirect cooling is provided by liquid helium circulating through a tube on the inner surface of the cylinder.

K_L^0 and Muon Detector (KLM)

The KLM [29] is used to detect neutral kaons, K_L^0, and muons with momenta above 600 MeV/c. The KLM consists of an alternating sandwich of 4.7 cm thick iron plates and glass resistive plate counters (RPCs) located outside the superconducting magnet. The KLM covers the polar angle, 45 °$< \theta <$ 125 ° in the barrel section and 20 ° $< \theta <$ 155 ° in the endcaps. There are 15 detector layers and 14 iron layers in the barrel section, and 14 detector layers are placed in the endcap sections.

The iron plates have 3.9 times the interaction length of the material. Through the K_L^0 interaction with the iron plates, a shower of ionizing particles is generated widely and the location of the shower provides the direction of the K_L^0. Extrapolated charged tracks that have associated KLM hits are identified as muons.

RPC modules consist of two parallel plates with a gas-filled gap, which provides a high resistivity, as shown in Fig. 3.15. The modules are operated with a voltage of 8 kV during data taking. An ionized particle passing through the gap induces a streamer in the gas, and results in a local discharge of the plates. The discharge generates a signal, and the location and time are recorded.

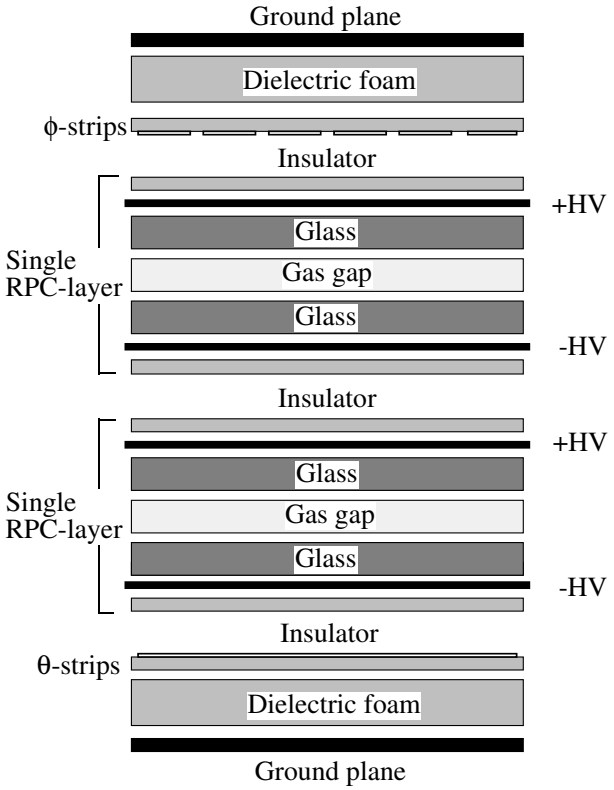

Figure 3.15: Cross section of an RPC.

Extreme Forward Calorimeter (EFC)

The EFC is mainly used as supplementary luminosity monitor for Belle and is also to tag the two photon $e^+e^- \to \gamma\gamma$ decays. The EFC extends the polar angle covered by the ECL to $6.4\ ^\circ < \theta < 11.5\ ^\circ$ in the forward direction and $163.3\ ^\circ < \theta < 171.2\ ^\circ$ in the backward direction. The EFC is also required to function as a beam mask to reduce background to the CDC. Since the EFC is placed in the very high radiation level area around the beam pipe near the IP, a radiation-hard BGO (Bismuth Germanate, $Bi_4Ge_3O_{12}$) crystal is used. The EFC consists of 32 (5) segmented-crystals in ϕ (θ) for both the forward and backward directions, respectively. The radiation lengths of crystals in the forward and backward direction are 12 and 11, respectively.

Trigger (TRG)

The Belle trigger system primarily consists of the Level-1 hardware trigger. The Level-1 trigger consists of 6 sub detector trigger systems and central trigger system called the Global Decision Logic (GDL) as shown in Fig. 3.16. The trigger system provides the trigger signal in 2.2 μs after the e^+e^- collision. The trigger efficiency for the hadronic events is more than 99 %. The event rates for physics processes and backgounds are 100 Hz and ∼300 Hz, respectively, at a luminosity of 10^{34} cm^{-2}s^{-1}. The total rate is well under the present data acquisition limit.

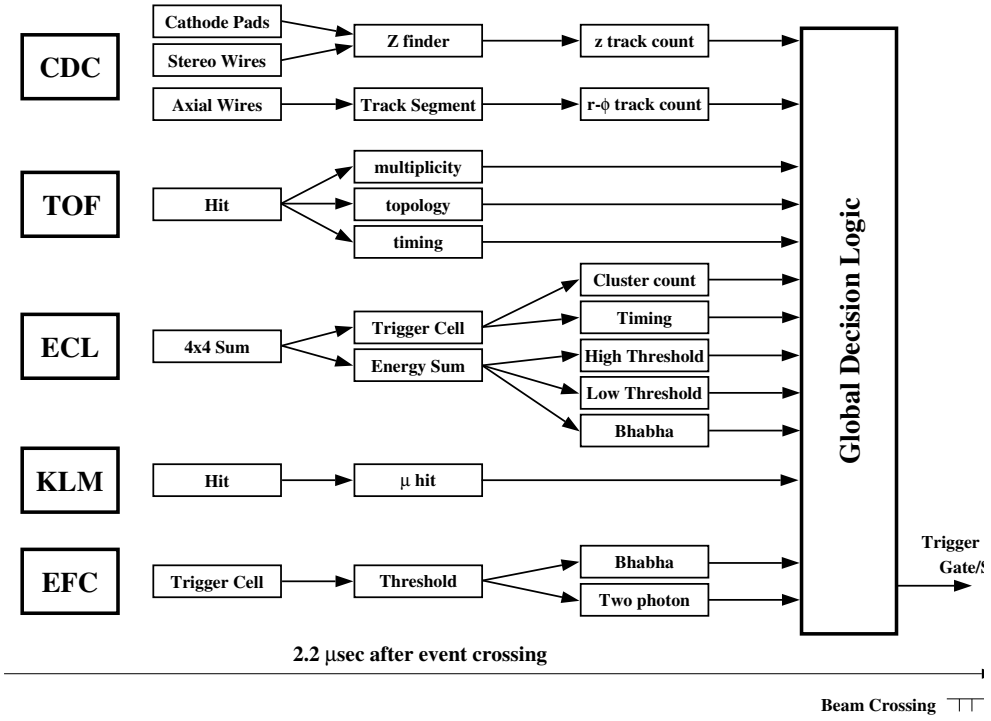

Figure 3.16: Logic diagram of the Level-1 trigger system.

Data Acquisition System (DAQ)

The Belle Data Acquisition (DAQ) system deals with the data flow from the analog signals acquired by the individual sub-detectors to their digitized form which is saved in mass storage for offline data processing as shown in Fig. 3.17. The Belle DAQ system consists of three parts: a front-end readout part, an event building part and a mass storage part. For the front-end readout part, each sub detector uses the commonly developed FASTBUS TDC system or Common Pipelined Platform for Electronic Readout (COPPER) TDC, except for SVD. The data from SVD is digitized by FADC and processed by a PC-based readout system and is sent to the event building farm directly via the network. Since the current readout system is not fully pipelined, the DAQ dead time is $\sim$5 % at a luminosity of 10^{34} cm^{-2}s^{-1}. For the event building part, data flow is divided into two parallel streams in order to prevent saturation by the network limit. After partial event building, the event is sent to storage for offline data processing.

In offline data processing, events must have at least one track originating from the IP, $dr < 1.0$ cm and $|dz| < 4.0$ cm, with $p_t > 300$ MeV/c. Events passing this requirement undergo full event reconstruction. Tracks are reconstructed with hits in the CDC, then these tracks are extrapolated towards the IP to search for associated SVD hits. They are also extrapolated outwards to search for hits in the outer detectors. Thus, 4-vectors and particle identification likelihoods can be assigned. Clusters are also reconstructed to form photons. This information along with many other calculated variables are stored in a format available to collaborators for analysis.

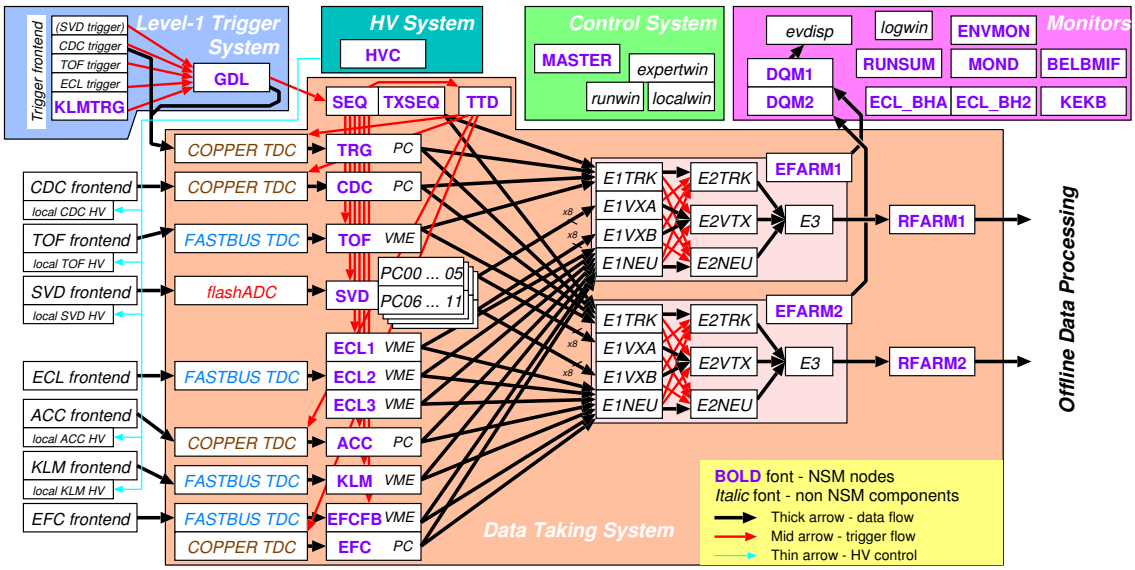

Figure 3.17: Global design of the DAQ.

Chapter 4

Time-Dependent Dalitz Plot Analysis

The previous quasi-two-body CP asymmetry measurement in the $B^0 \to \phi K^0_S$ decay suffered from an uncertainty originating from the interference from the $B^0 \to f_0 K^0_S$ decay that has the same $B^0 \to K^0_S K^+ K^-$ final state but opposite CP eigenvalue. In addition, the non-resonant $B^0 \to K^0_S K^+ K^-$ three-body decay is a mixture of CP-even and CP-odd state. The fraction of CP-even state ($f_{\rm even}$) is determined by an external information and the resulting dilution is included in the systematic error in the previous CP asymmetry measurement. Furthermore, due to the quasi-two-body analysis used in these measurements, a two-fold ambiguity in $\phi_1^{\rm eff}$ remains.

To treat the interference effects correctly, to extract the CP-even and CP-odd components by the amplitude analysis, and to potentially resolve the two-fold ambiguity, we employ a "Time-Dependent Dalitz Plot Analysis" to the B^0 decays with a $B^0 \to K^0_S K^+ K^-$ final state.

In this chapter, we first describe the motivations for the time-dependent Dalitz plot analysis by focusing on the ambiguities of the previous analyses, and then, we give a detailed description of the time-dependent Dalitz plot technique. Finally, we introduce a Dalitz parameter transformation that enlarges $B^0 \to K^0_S K^+ K^-$ regions of interest in the Dalitz plane.

4.1 Motivation for a Time-Dependent Dalitz Plot Analysis

4.1.1 Evaluation of the Contamination from $f_0 K^0_S$ with the Opposite CP Eigenstate to the $B^0 \to \phi K^0_S$ Decay

A quasi-two-body time-dependent analysis has been performed on the $B^0 \to \phi K^0_S$ decay at Belle in 2006 [9], and the result is

$$\mathcal{A}_{CP}(B^0 \to \phi K^0) = +0.07 \pm 0.15\ (\text{stat}) \pm 0.05\ (\text{syst}),\ \text{and} \quad (4.1)$$
$$\sin 2\phi_1^{\text{eff}}(B^0 \to \phi K^0) = +0.50 \pm 0.21\ (\text{stat}) \pm 0.06\ (\text{syst}). \quad (4.2)$$

However, a two-body approach to these modes is not ideal due to interference from other resonances as well as the non-resonant decay into the same final state.

It is interesting to note that the largest contribution to the systematic uncertainty of this measurement comes from the contribution from the $B^0 \to f_0 K^0_S$ decay, 0.01 for $\mathcal{A}_{CP}$ and 0.02 for $\sin 2\phi_1^{\text{eff}}$, due to their opposite CP eigenvalue. This contribution estimation considered only the dilution from the CP-violating phase in the $B^0 \to f_0 K^0_S$ decay and ignore the dilution from the interferences originating from the decay phase difference between the $B^0 \to \phi K^0_S$ and $B^0 \to f_0 K^0_S$ decays. These effects cannot be reduced with increased statistics but can be taken into account with a time-dependent Dalitz plot fit. For example, in the $B^0 \to K^0_S K^+ K^-$ system, the contribution of the non-resonant component is about 50%, which may induce large interferences with resonances that have wide decay widths.

4.1.2 Solution for CP Mixture Property of the Non-resonant $B^0 \to K^0_S K^+ K^-$ Three-Body Decay

Since the non-resonant $B^0 \to K^0_S K^+ K^-$ decay has the second largest statistics in $b \to s$ decays [1], it is experimentally one of the best decay modes in $b \to s$ decays. Unlike the two-body $B^0 \to \phi K^0_S$ decay with the fixed CP eigenstate, the three-body $B^0 \to K^0_S K^+ K^-$ decay is in general a mixture of CP-even and CP-odd component.

In the previous CP asymmetry measurement, the fraction of CP-even state is determined using measured branching fraction of $B^0 \to K^0 K^+ K^-$ and $B^+ \to K^0 \overline{K^0} K^+$ with assuming the following isospin relation:

$$B.F.(B^0 \to K^0 K^+ K^-) = B.F.(B^+ \to K^0 \overline{K}^0 K^+)\ \frac{\tau_{B^0}}{\tau_{B^+}}. \quad (4.3)$$

[1] The $B^0 \to \eta' K^0_S$ decay has the largest statistics in $b \to s$ decays and CP violation of this decay is measured at Belle to be $\sin 2\phi_1^{\text{eff}}(B^0 \to \eta' K^0_S) = 0.674^{+0.102}_{-0.105}$ (stat) with the signal yield of 1421^{+46}_{-44} (stat) using 535 $\times 10^6$ $B\overline{B}$ pairs in 2006 [9], in which we have achieved the first observation of CP violation in $b \to s$ decays.

From Bose statistics, $K^0\overline{K^0}$ system with even orbital momenta, which is CP even state, can only decay to $K^0_S K^0_S$ or $K^0_L K^0_L$. Thus, the fraction of the CP even state in the three-body kaon decay $f_{\rm even}$ can be determined as

$$\begin{aligned} f_{\rm even} &= 2\,\frac{B.F.(B^+ \to K^+ K^0_S K^0_S)}{B.F.(B^+ \to K^+ K^0 \overline{K}^0)} \qquad (4.4) \\ &= \frac{B.F.(B^+ \to K^+ K^0_S K^0_S)}{B.F.(B^0 \to K^+ K^- K^0_S)}\,\frac{\tau_{B^0}}{\tau_{B^+}} \\ &= 0.93 \pm 0.09\ (\text{stat})\ \pm 0.05\ (\text{syst}) \qquad (4.5) \end{aligned}$$

using 338 $\times 10^6$ $B\overline{B}$ pairs [30] and the effective CP eigenvalue η_{CP} is given as

$$\eta_{CP} = f_{\rm even} - (1 - f_{\rm even}) = 0.86 \pm 0.18\ (\text{stat})\ \pm 0.09\ (\text{syst}). \qquad (4.6)$$

This isospin method can be well introduced even in a smaller data sample. However, non unity η_{CP} dilute the CP asymmetry and thus affect the statistical error, and also the uncertainty of η_{CP} affect the systematic error. Previous result, which has the signal yield of 840.3 ± 34.3 using 535 $\times 10^6$ $B\overline{B}$ pairs [31] at Belle in 2006, is obtained as,

$$\begin{aligned} \mathcal{A}_{CP}(B^0 \to K^0_S K^+ K^-) &= -0.09 \pm 0.10\ (\text{stat}) \pm 0.05\ (\text{syst}),\ \text{and} \qquad (4.7) \\ \sin 2\phi_1^{\rm eff}(B^0 \to K^0_S K^+ K^-) &= +0.68 \pm 0.15\ (\text{stat}) \pm 0.03\ (\text{syst})^{+0.21}_{-0.13}\ (CP\ \text{mixture}) \qquad (4.8) \end{aligned}$$

As can be seen in this result, the measured $\sin 2\phi_1^{\rm eff}$ is significantly diluted. It is also found that the uncertainty from CP mixture property is the largest.

The CP eigenvalues of the three-body $K^0_S K^+ K^-$ state are determined by $(-1)^l$, where l is the orbital angular momentum of the K^+K^- pair relative to the remaining K^0_S. Since the total angular momentum of this three-body system should be zero, l is equal to the relative orbital momentum of the two charged kaons. Thus, the fractions of the CP-even and CP-odd components can be treated directly by the amplitude of the $B^0 \to K^0_S K^+ K^-$ Dalitz plot. In practice, we can directly measure $\phi_1^{\rm eff}$, but not $\mathcal{S}_{CP}^{\rm eff}(= -\eta_{CP} \sin 2\phi_1^{\rm eff})$.

4.1.3 Disentanglement of Two-Fold Ambiguity in $\phi_1^{\rm eff}$

The interference terms depend on the cosine of the difference of the effective weak phase in $B^0\overline{B^0}$ mixing, $\phi_1^{\rm eff}$. By including the interference terms to the probability density function (PDF), we can potentially resolve the two-fold ambiguity in $\phi_1^{\rm eff}$ present in the previous quasi-two-body analyses, which determines $\sin 2\phi_1^{\rm eff}$. Current direct measurements of $\cos 2\phi_1$ from $b \to c\bar{c}s$ transitions prefer the solution of $\phi_1 = 21.5^\circ$ over $\phi_1 = 68.5^\circ$ [32]. It is important to resolve this quadratic ambiguity in $b \to q\bar{q}s$ transitions as well.

4.2 Formalism of the Time-Dependent Dalitz Plot

4.2.1 Dalitz Model of B^0 Decays to $K^0_S K^+ K^-$ Final State

The two independent variables of the Dalitz plot are the invariant squared masses,

$$s_\pm \equiv (p_\pm + p_0)^2, \tag{4.9}$$

where p_+, p_- and p_0 are four-momentum of K^+, K^- and K^0_S, respectively. The third variable $s_0 \equiv (p_+ + p_-)^2$ can be obtained from 4-vector conservation,

$$s_0 = m^2_{B^0} + 2m^2_{K^+} + m^2_{K^0_S} - s_+ - s_-. \tag{4.10}$$

The differential B^0 decay width with respect to the Dalitz plot is

$$d\Gamma(K^0_S K^+ K^-) = \frac{1}{(2\pi)^3}\frac{|A|^2}{32m^3_{B^0}} ds_+ ds_-, \tag{4.11}$$

where A is the Lorentz-invariant amplitude of the decay. In the isobar approximation [33], the total amplitude of $B^0(\overline{B^0}) \to K^0_S K^+ K^-$ is written as the sum of decay channels with that final state,

$$A(s_+, s_-) = \sum_i a'_i F_i(s_+, s_-), \quad \bar{A}(s_-, s_+) = \sum_i \bar{a}'_i \bar{F}_i(s_-, s_+), \tag{4.12}$$

where $a'_i \equiv a_i e^{ib_i}$ are complex coefficients describing the relative magnitudes and phases between the decay channels and carry the weak phase dependence. The Dalitz-dependent amplitudes, $F_i(s_+, s_-)$ contain only strong dynamics and thus, $F_i(s_+, s_-) = \bar{F}_i(s_-, s_+)$ [2]. They can be expanded in terms of invariant mass and angular distribution probabilities,

$$F^L_i(s_+, s_-) \equiv X^L_i(\vec{p}^*) \times X^L_i(\vec{q}) \times Z^L_i(\vec{p}, \vec{q}) \times R_i(s_+, s_-), \tag{4.13}$$

where $\vec{p}^*$ is the momentum of the bachelor particle in the B^0 rest frame, $\vec{p}$ and $\vec{q}$ are the momenta of the bachelor particle and one of the resonance daughters in the resonance frame, respectively, L is the orbital angular momentum between the resonance and the bachelor while X^L_i are the Blatt-Weisskopf barrier factors [34].

The angular distribution, $Z^L_i(\vec{p}, \vec{q})$ depends on L,

$$\begin{aligned} Z^0_i(\vec{p}, \vec{q}) &= 1, \\ Z^1_i(\vec{p}, \vec{q}) &= -4\vec{p} \cdot \vec{q}. \end{aligned} \tag{4.14}$$

The mass shapes are denoted as $R_i(s_+, s_-)$ which differ depending on the decay channel. We use the Relativistic Breit-Wigner (RBW) [35] and Flatté [36] line shapes. These lineshapes

[2] Since the distance ranges that the weak interaction inside the Feynman diagram and the strong interaction in the hadronizations outside the Feynman diagram affect are completely different, we can factorize the amplitude, $A(s_+, s_-)$, into those related to the weak and strong interactions.

Table 4.1: Summary of the resonances considered in the $B^0 \to K^0_S K^+ K^-$ signal model.

Resonances	Fixed parameters (GeV)	Form Factor, $R_i(s_+,s_-)$	L
f_0	$M = 0.965 \pm 0.010$ [39]	Flatté	0
	$g_\pi = 0.165 \pm 0.018$		
	$g_K = (4.21 \pm 0.09) g_\pi$		
ϕ	$M = 1.019455 \pm 0.020$ [35]	RBW	1
	$\Gamma = 0.00426 \pm 0.00004$		
$f_{\rm X}$	$M = 1.524 \pm 0.014$ [37]	RBW	0
	$\Gamma = 0.136 \pm 0.023$		
χ_{c0}	$M = 3.41475 \pm 0.00035$ [35]	RBW	0
	$\Gamma = 0.0104 \pm 0.0007$		
$(K^+K^-)_{\rm NR}$		$e^{-\alpha s^0}$	
$(K^0_S K^+)_{\rm NR}$		$e^{-\alpha s^+}$	
$(K^0_S K^-)_{\rm NR}$		$e^{-\alpha s^-}$	

are described in Appendix C. The non-resonant component is empirically modelled by the sum of three exponential functions as described in the previous time-integrated Dalitz plot analysis of the $B^+ \to K^+K^+K^-$ decay from Belle [37].

Table 4.1 summarises the resonances considered in the $B^0 \to K^0_S K^+ K^-$ signal model, which was motivated by the time-integrated Dalitz plot analysis of the $B^+ \to K^+K^+K^-$ decay [37]. The $f_{\rm X}$ resonance with unknown spin that appears in the table was first introduced in Ref. [37] and also considered in the analyses from BaBar [38] in order to account for an enhancement of signal events observed at $M(K^+K^-) \sim 1.5{\rm GeV}/c^2$ with the wide K^+K^- mass range. Since it is best described as a scaler [3], we assume the spin of $f_{\rm X}$ to be 0. Figure 4.1 show the magnitude distributions of the Dalitz-dependent amplitudes ($F_i(s_+, s_-)$) of each resonance (i). Note that most of the decay channels, such as $f_0 K^0_S$, ϕK^0_S, $f_0 K^0_S$ and $K^0_S(K^+K^-)_{\rm NR}$, populate the kinematic boundary with low s_0 (the diagonal region across the Dalitz plane of s_- and s_+.)

4.2.2 Time-Dependence in the Dalitz Model

The decay of the $\Upsilon(4S)$ produces a $B\overline{B}$ pair of which one (f_{CP}) may be reconstructed as $K^0_S K^+ K^-$ while the other ($f_{\rm tag}$) may reveal its flavor. Since the CP eigenstate of K^0_S is

[3] $f_{\rm X}(1500)$ is often referred as $f_0(1500)$. Further details can be found in the mini-reviews titled "NOTE ON SCALER MESONS" in Ref. [35].

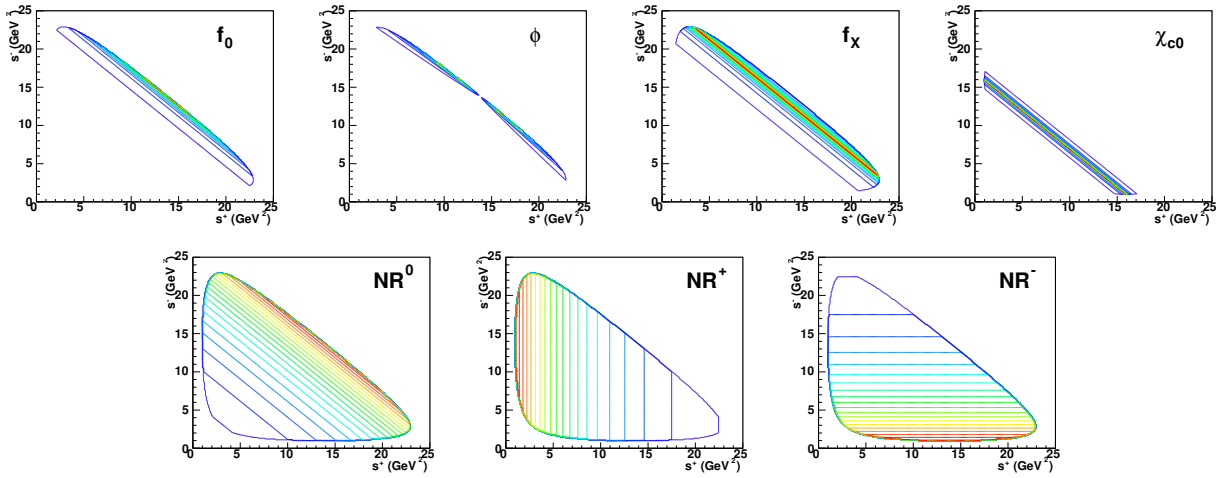

Figure 4.1: The $|F_i(s_+, s_-)|$ distribution of each resonance (i) included in our $B^0 \to K^0_S K^+ K^-$ signal model.

$\eta_{CP} = +1$, the time-dependent decay rate in Eq. 2.46 becomes

$$|A(\Delta t, q_{\rm tag})|^2 = \frac{e^{-|\Delta t|/\tau_{B^0}}}{4\tau_{B^0}}\Big[(|A|^2 + |\bar{A}|^2) - q_{\rm tag}(|A|^2 - |\bar{A}|^2)\cos\Delta m_d \Delta t \tag{4.15}$$

$$+2q_{\rm tag}{\rm Im}(\bar{A}A^*)\sin\Delta m_d\Delta t\Big], \tag{4.16}$$

where no CP violation in mixing, $|q/p| = 1$, is assumed.

The Dalitz-dependent amplitudes, A, were previously defined in Eq. 4.12 and we choose a convention where the $B^0\overline{B^0}$ phase of q/p is absorbed into the $\overline{B^0}$ decay amplitude, $\bar{a}'_i$. These complex coefficients can be redefined in a way that depends on the decay amplitude,

$$a'_i \equiv a_i(1 + c_i)e^{i(b_i+d_i)} \tag{4.17}$$

for A and,

$$\bar{a}'_i \equiv a_i(1 - c_i)e^{i(b_i-d_i)} \tag{4.18}$$

for $\bar{A}$ and thus a resonance, i, has a direct CP violation asymmetry given by

$$\mathcal{A}_{CP}(i) \equiv \frac{|\bar{a}'_i|^2 - |a'_i|^2}{|\bar{a}'_i|^2 + |a'_i|^2} = \frac{-2c_i}{1 + c_i^2}, \tag{4.19}$$

where c_i are restricted by its definition to lie between -1 and 1.

For a CP eigenstate, the CKM angle, $\phi_1(i)$, is reduced to a fitted parameter,

$$\phi_1(i) \equiv \frac{\arg(a'_i\bar{a}'^*_i)}{2} = d_i, \tag{4.20}$$

and its effective mixing-induced CP violation asymmetry is calculated as

$$-\eta_i \mathcal{S}_{CP}(i) \equiv \frac{-2\mathrm{Im}(\bar{a}'_i a'^*_i)}{|a'_i|^2 + |\bar{a}'_i|^2} = \frac{1-c_i^2}{1+c_i^2}\sin 2\phi_1(i), \tag{4.21}$$

where η_i is the CP eigenvalue of the final state. Note that $\mathcal{A}_{CP}(i)$ and $\mathcal{S}_{CP}(i)$ are restricted by these definitions to lie in the physical region.

4.3 Dalitz Plot Transformation (Square Dalitz Plot)

In this section, we explain a Dalitz parameter transformation that enlarges interesting regions of phase space in our $B^0 \to K^0_S K^+ K^-$ signal model.

If we create the Dalitz plot from the parameters (s_+, s_-) in Eq. 4.9, signal and continuum events populate its kinematic boundaries with low s_0, which correspond to the ϕ and f_0 resonances. Large variations in a small area of the Dalitz plane are difficult to describe if non-parametric shapes such as histograms are used to describe the background. Therefore, we apply the transformation,

$$ds_+ ds_- \to |\mathrm{det}J|\mathrm{d}m'\mathrm{d}\theta', \tag{4.22}$$

which defines the "Square Dalitz Plot". The square Dalitz plot was first introduced officially at BaBar in the time-integrated Dalitz plot analysis in $B^\pm \to \pi^\pm\pi^\pm\pi^\pm$ [40].

The parameters m' and θ' are given by

$$m' \equiv \frac{1}{\pi}\arccos(2\frac{m_0 - m_0^{\mathrm{min}}}{m_0^{\mathrm{max}} - m_0^{\mathrm{min}}} - 1), \text{ and} \tag{4.23}$$

$$\theta' \equiv \frac{1}{\pi}\theta_0, \tag{4.24}$$

where m_0 is K^+K^- invariant mass, m_0^{max} and m_0^{min} are kinematic limits of m_0, θ_0 is the helicity angle, defined as the angle between the K^- and the K^0_S in the K^+K^- rest frame, and J is the Jacobian of the transformation. The determinant of the Jacobian is given by

$$|\mathrm{det}J| = 4|\mathbf{p}^*_+||\mathbf{p}^*_0|m_0 \cdot \frac{\partial m_0}{\partial m'} \cdot \frac{\partial \cos\theta_0}{\partial \theta'}\ , \tag{4.25}$$

where $|\mathbf{p}^*_+| = \sqrt{E^{*2}_+ - m^2_{K^+}}$ and $|\mathbf{p}^*_0| = \sqrt{E^{*2}_0 - m^2_{K^0_S}}$, are the K^+ and K^0_S momenta defined in the K^+K^- rest frame. Figure 4.2 show the $F_i(s_+, s_-)$ distributions with the Square Dalitz parametrization, m' and θ', which correspond to Fig. 4.1 with the usual Dalitz parametrization, s_+ and s_-. Figure 4.3 show the Dalitz distributions based on our signal model with the usual Dalitz parametrization, s_+ and s_-, and the Square Dalitz parametrization, m' and θ', respectively. As can be seen, the highlighted region where most of the signal and background events are populated, is magnified in the Square Dalitz parametrization.

In the Dalitz fit the Jacobian is a constant because it is the function of m' and θ' and does not depend on the fitted parameters. In the maximum likelihood fit, the likelihoods, $\mathcal{L}_{\rm Square}$ and $\mathcal{L}_{\rm Normal}$, calculated in the Square and Normal Dalitz parameterizations, have the following relation, $\log \mathcal{L}_{\rm Square} = \log \mathcal{L}_{\rm Normal} + (\text{constant})$. Thus, if parametric shapes are used, the fitted results obtained with the normal Dalitz parametrization and Square Dalitz parametrization should be equivalent.

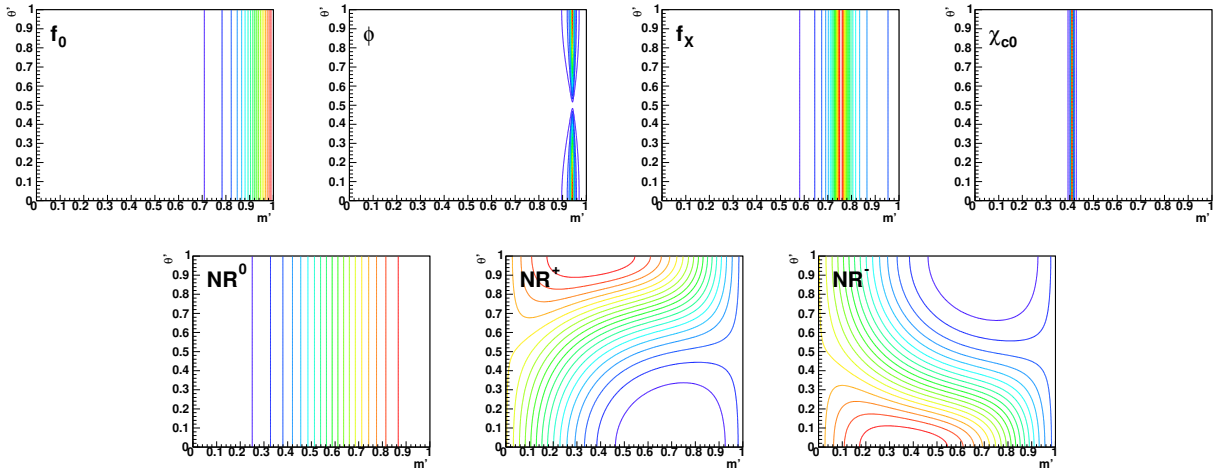

Figure 4.2: The $|F_i(s_+, s_-)|$ distribution of each resonance (i) with the Square Dalitz parametrization, m' and θ'.

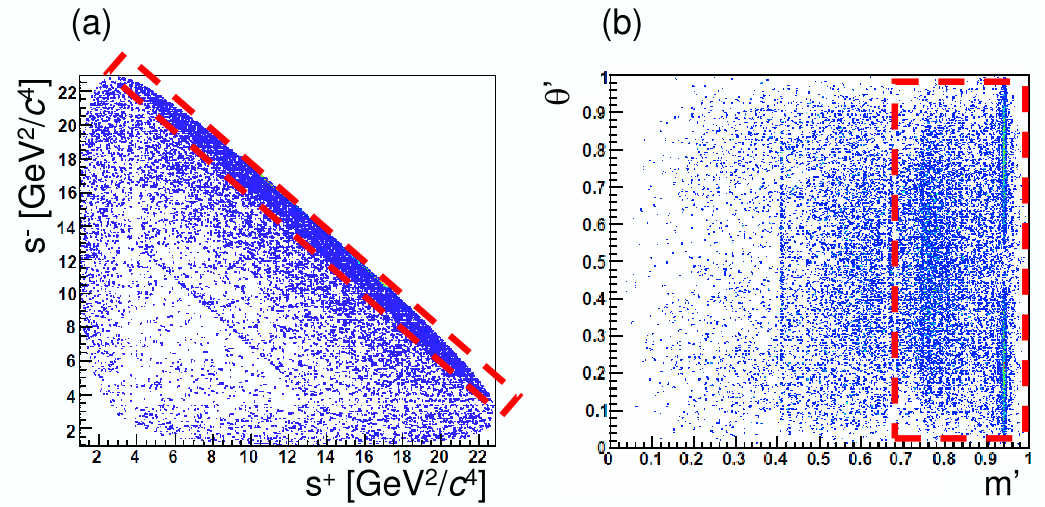

Figure 4.3: The Dalitz distribution based on our $B^0 \to K^0_S K^+ K^-$ signal model of GEANT-based signal MC (a) with the normal Dalitz parametrization, s_+ and s_-, and (b) with the Square Dalitz parametrization, m' and θ'. The dotted-line red boxes indicate the regions indicate the region where most of the signal components and the background are populated.

Chapter 5

Event Reconstruction and Signal Extraction

In this chapter, we describe the procedure for the reconstruction of signal B decay candidates and the signal yield extraction. We use the results of the signal extraction fits to calculate an event-by-event signal fraction, which is an input value for the CP asymmetry determinations described in § 6. The following decays are considered for CP asymmetry measurements in $b \to d$ and $b \to s$ transitions: $B^0 \to K^0_S K^0_S$ and $B^0 \to K^0_S K^+ K^-$, respectively.

First, B mesons are reconstructed from their daughter particles. The selection criteria for each decay are introduced. The selection requirements for the reduction of $e^+e^- \to q\overline{q}$ continuum background events are discussed. For $B^0 \to K^0_S K^+ K^-$ decays, the additional requirements on the invariant mass of the two kaons are imposed to suppress $B\overline{B}$ background decays originating from charmed B decays with the same final state. For the selected B candidates, B decay vertices in both the CP side and the tag side are reconstructed and the b flavor is also determined, which is essential for CP asymmetry measurement and is also utilized for the event selection. Finally, the signal yield is extracted using an extended unbinned maximum likelihood fit to a set of kinematic variables for selected B candidates.

5.1 Reconstruction of Signal Candidates

5.1.1 Data Set

These analyses are performed with a data sample of 605 fb^{-1} recorded by the Belle detector from January 2000 to December 2006. This integrated luminosity corresponds to a sample of 657×10^6 $B\overline{B}$ pairs.

5.1.2 $B\overline{B}$ Event Selection

The following selection criteria are used to suppress non-hadronic non-$B\overline{B}$ events and select $B\overline{B}$ events [41].

At least three "good" charged tracks must exist, where a "good" charged track is defined as having $p_{\rm track} > 0.1$ GeV/c, $dr < 2.0$ cm and $|dz| < 4.0$ cm, where $p_{\rm track}$ is the transverse momentum and dr and $|dz|$ are impact parameters which describe the distance of the closest approach to the IP. The primary event vertex calculated from the "good" charged tracks must satisfy $dr < 1.5$cm and $|dz| < 3.5$ cm.

At least two "good" neutral clusters must be observed in the barrel region of the ECL where a "good" neutral cluster has $E_{\rm cluster} > 0.1$ GeV and $-0.7 < \cos\theta < 0.9$, where $E_{\rm cluster}$ is the energy deposit and θ is the polar angle from the beam axis.

The sum of momentum magnitudes in the z-direction calculated in the $\Upsilon(4S)$ rest frame, $|p_z^{\rm CMS}|$, must be less than half the total available energy, $\sqrt{s}$, $\sum |p_z^{\rm CMS}| \leq 0.5\ \sqrt{s}$, which enables to suppress the background from two-photon process and the beam-induced background.

Assuming the pion mass for "good" charged tracks, the total visible energy in the $\Upsilon(4S)$ rest frame, $E_{\rm vis}^{\rm CMS}$, should be $E_{\rm vis}^{\rm CMS} > 0.18\ \sqrt{s}$, which enables to suppress the background from two-photon process efficiently.

The total energy of "good" neutral clusters in the $\Upsilon(4S)$ rest frame, $E_{\rm cluster}^{\rm CMS}$, has to be inside $0.1\ \sqrt{s} < \sum E_{\rm cluster}^{\rm CMS} < 0.8\ \sqrt{s}$, which enables to suppress the background from Bhabha scattering process with huge cross section.

The invariant mass of particles in each hemisphere defined as perpendicular to the boost, $M_{\rm jet}$, must satisfy, $M_{\rm jet} > 1.8$ GeV/c^2, which enables to suppress the background from continuum process efficiently.

These selection criteria retain more than 99 % of $B\overline{B}$ events [1] while reducing the contamination from non-hadronic processes to less than 5 %.

5.1.3 Reconstruction of $B^0 \to K_S^0 K_S^0$

K_S^0 Reconstruction

A K_S^0 from a $B^0 \to K_S^0 K_S^0$ decay tends to have high momentum, $p > 2$ GeV/c, because of two-body decay kinematics. The K_S^0 selection criteria is optimized by using signal MC and continuum data of $B^0 \to K_S^0 K_S^0$ decays and $B\overline{B}$ background MC, which enables an increase

[1] Due to the requirements of at least three "good" and primary charged tracks, the efficiency of $B^0 \to K_S^0 K_S^0$ process in $B\overline{B}$ event selection is ~ 95 %.

in reconstruction efficiency of 13 % compared to the standard K^0_S selection criteria used in most of Belle analyses.

A $K^0_S \to \pi^+\pi^-$ candidate is reconstructed from a pair of oppositely charged tracks having $\Delta M_{K^0_S} < 15$ MeV/c^2 corresponding to ~ 3 standard deviations (σ), where $\Delta M_{K^0_S}$ is the difference between their invariant mass and the nominal K^0_S mass and σ is the estimated resolution of $\pi^+\pi^-$ invariant mass. The K^0_S vertex is determined from a kinematic fit using its daughter charged pion pair. Due to the K^0_S finite lifetime, $c\tau \sim 2.68$ cm, this decay vertex has a relatively large displacement from its production vertex. Figure 5.1 (a) shows the smaller impact parameter, dr, among the two charged tracks. We calculate the Figure of Merit according to the requirements to dr as shown in Fig. 5.1 (b) and impose the requirement of $dr > 100$ μm to maximize the Figure of Merit.

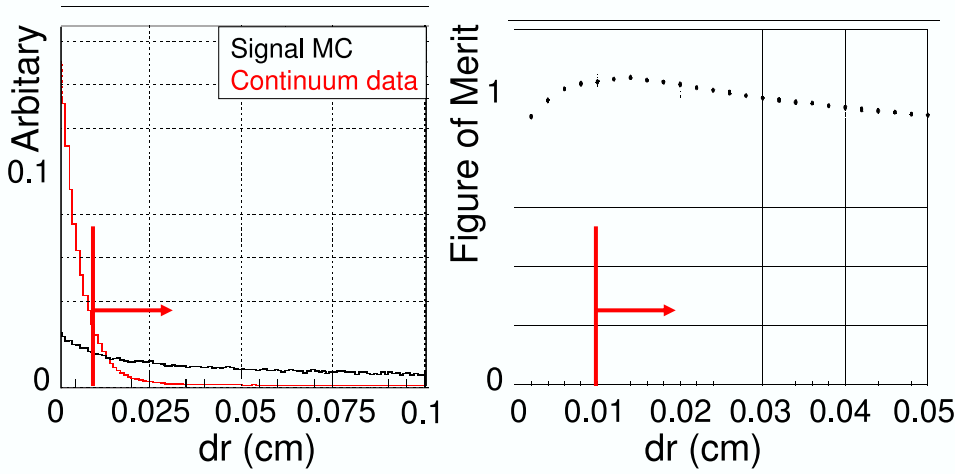

Figure 5.1: (a) The distributions of the impact parameter dr of $B^0 \to K^0_S K^0_S$ signal MC (red) and continuum data (black) for $B^0 \to K^0_S K^0_S$ candidates, respectively. (b) The Figure of Merit distribution as a function of dr requirement for $B^0 \to K^0_S K^0_S$ from signal MC and continuum data. The requirement $dr > 0.01$ cm is also shown as the region defined by the red arrows.

The angle in the transverse plane between the K^0_S momentum vector and the direction defined by the K^0_S vertex and the IP should be less than 50 mrad. In order to suppress incorrect combinations of the two charged tracks, the mismatch in the z direction at the K^0_S vertex point for the two charged tracks is required to be less than 15 cm.

Figure 5.2 shows the $\pi^+\pi^-$ invariant distribution of $B^0 \to K^0_S K^0_S$ data after applying all

the K_S^0 requirements above. We assume the correctly reconstructed K_S^0 as a sum of two Gaussians and the fake K_S^0 coming from the wrong accidental combination of tracks as flat. The purity is estimated to be ~ 83 %.

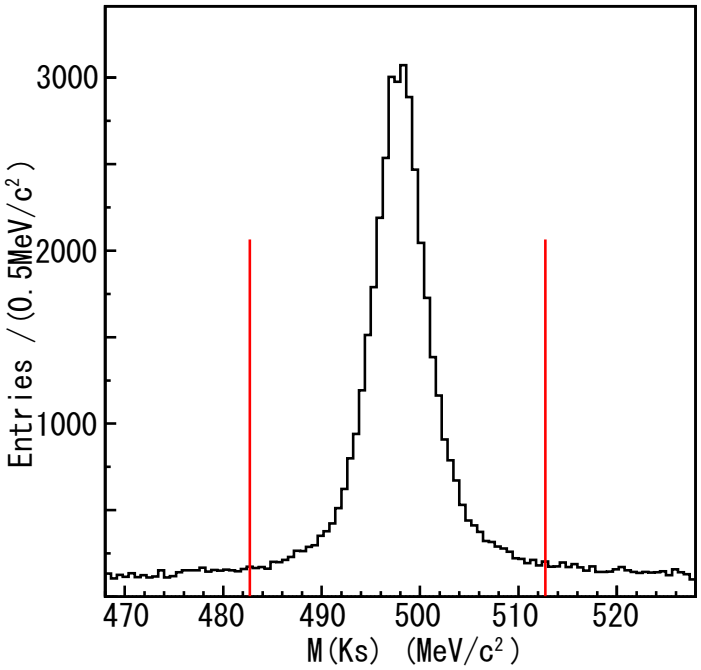

Figure 5.2: $\pi^+\pi^-$ invariant mass distribution of $B^0 \to K_S^0 K_S^0$ data after applying the K_S^0 requirements.

$B^0 \to K_S^0 K_S^0$ Reconstruction

A candidate of $B^0 \to K_S^0 K_S^0$ decay is reconstructed by combining two K_S^0 candidates. To identify B decay candidates, we use two kinematic variables:

$$\text{the energy difference, } \Delta E \equiv E_B^{\rm CMS} - E_{\rm beam}^{\rm CMS}, \text{ and} \tag{5.1}$$

$$\text{the beam} - \text{energy constrained mass, } M_{\rm bc} \equiv \sqrt{(E_{\rm beam}^{\rm CMS})^2 - (p_B^{\rm CMS})^2}, \tag{5.2}$$

where $E_{\rm beam}^{\rm CMS}$ is the beam energy in the center-of-mass (CMS), and $E_B^{\rm CMS}$ and $p_B^{\rm CMS}$ are the CMS energy and momentum of the reconstructed B candidate, respectively. Figures 5.3 show the distributions of ΔE and $M_{\rm bc}$ for $B^0 \to K_S^0 K_S^0$ signal MC.

If there are only charged particles in the final state, the ΔE width is dominated by the track momentum resolution, ~ 15 MeV, and the contribution to the total ΔE width from the beam energy spread, ~ 2.6 MeV, becomes negligible. In general, since a B meson is produced almost at rest in the CMS and the B meson momentum, $p_B^{\rm CMS}$ in the CMS is much smaller than its total energy, the uncertainty in the measured $p_B^{\rm CMS}$ gives a small contribution

to the $M_{\rm bc}$ width. Thus, the $M_{\rm bc}$ width is dominated by the beam energy spread and in general does not depend on the final state, unless photons are present in the reconstructed final states. We take these contributions into account in practice as follows, we model the ΔE and $M_{\rm bc}$ shapes as a sum of two Gaussians [2] and a single Gaussian using signal MC of the decays but calibrate the mean and width of the shapes by applying the correction factors between data and signal MC determined from the higher statistics control sample.

We select $B^0 \to K^0_S K^0_S$ candidates that satisfy the following ΔE and $M_{\rm bc}$ region,

$$-0.2 \text{ GeV} < \Delta E < 0.2 \text{ GeV and } 5.2 \text{ GeV}/c^2 < M_{\rm bc} < 5.3 \text{ GeV}/c^2. \tag{5.3}$$

We find 1307 (4648) candidates in SVD1 (SVD2) data sample. For the CP asymmetry measurement described in § 6.1, we use candidates in a signal region defined as,

$$-0.1 \text{ GeV} < \Delta E < 0.1 \text{ GeV and } 5.27 \text{ GeV}/c^2 < M_{\rm bc} < 5.30 \text{ GeV}/c^2. \tag{5.4}$$

For the continuum background study, we use a data sample in the sideband region defined as -0.1 GeV $< \Delta E < 0.2$ GeV and 5.20 GeV/c^2 $< M_{\rm bc} <$ 5.26 GeV/c^2, where the signal and $B\overline{B}$ components are absent. Figure 5.4 shows the definitions of the regions together with the $M_{\rm bc}$-ΔE distribution of $B^0 \to K^0_S K^0_S$ signal MC decays.

We find that ~ 0.2 % of the selected events have multiple candidates. In those events, we choose only one $B^0 \to K^0_S K^0_S$ candidate having the smallest $\sum(\Delta M_{K^0_S})^2$.

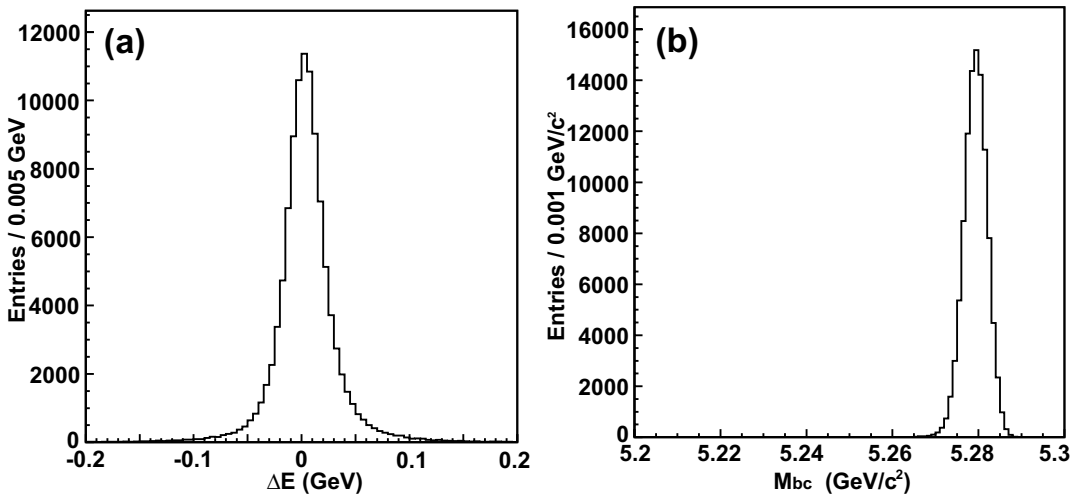

Figure 5.3: The distribution of (a) ΔE and (b) $M_{\rm bc}$ for $B^0 \to K^0_S K^0_S$ signal MC.

[2]The effect of the drift time in the CDC to the tracking is taken into account as an additional single Gaussian with wide width.

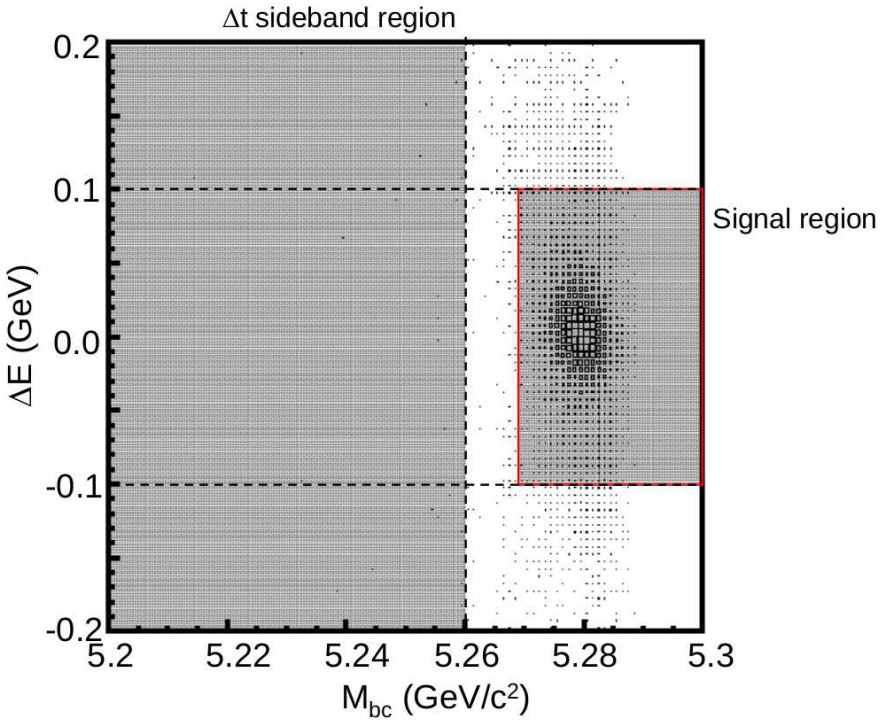

Figure 5.4: Definition of the signal region, -0.1 GeV $< \Delta E < 0.1$ GeV and 5.27 GeV/c^2 $< M_{\rm bc} <$ 5.30 GeV/c^2 and sideband region for Δt study (called as Δt sideband region) , -0.1 GeV $< \Delta E < 0.2$ GeV and 5.20 GeV/c^2 $< M_{\rm bc} <$ 5.26 GeV/c^2, in the $M_{\rm bc}$-ΔE plane, together the distribution of reconstructed $B^0 \to K^0_S K^0_S$ signal MC events.

5.1.4 Reconstruction of $B^0 \to K^0_S K^+ K^-$

$K^\pm$ Selection

A charged kaon candidate is selected with a set of track quality requirements based on the number of CDC hits and on the distance of closest approach to the IP: at least 7 axial and 3 stereo CDC hits, $dr < 0.5$ cm and $dz < 2.5$ cm. The total track momenta, p_{tot}, and transverse track momenta, p_t, are required to be $p_{tot} > 0.1$ GeV/c and $p_t > 0.05$ GeV/c, respectively, in order to reduce the low momentum combinatorial background. Charged tracks that are positively identified as pions, protons or electrons are excluded using the particle identification (PID) likelihood ratios, $\mathcal{R}_{K/\pi} > 0.6$, $\mathcal{R}_{p/K} < 0.95$ and $\mathcal{R}_{e/\mathrm{non}-e} < 0.95$. The details on PID can be found in Appendix B.

K^0_S Reconstruction

A K^0_S from $B^0 \to K^0_S K^+ K^-$ decays can have a wide momentum range between ~ 0.5 GeV/c and ~ 4.0 GeV/c because of three-body decay kinematics. The K^0_S selection criteria is optimized to be momentum independent so as not to complicate the Dalitz analysis.

A $K^0_S \to \pi^+\pi^-$ candidate is reconstructed from a pair of oppositely charged tracks having $\Delta M_{K^0_S} < 12$ MeV/c^2 corresponding to 3 σ. The K^0_S vertex reconstruction quality, reduced χ^2, is required to be less than 400 and the mismatch in the z direction at the K^0_S vertex point for the two charged tracks should be less than 1.5 cm. The angle in the x-y plane between the K^0_S momentum vector and the direction defined by the K^0_S vertex and the IP is required to be less than 0.32 rad. The transverse distance between the $\pi^+\pi^-$ vertex and IP in the x-y plane is required to be between 0.1 cm and 30.0 cm.

Reconstruction of $B^0 \to K^0_S K^+ K^-$ Candidate Events

A candidate of $B^0 \to K^0_S K^+ K^-$ decay is reconstructed by combining oppositely charged kaon tracks and a K^0_S candidate. We select candidates that satisfy the following ΔE and M_{bc} region,

$$-0.30 \text{ GeV} < \Delta E < 0.50 \text{ GeV and } 5.20\text{GeV}/c^2 < M_{\mathrm{bc}} < 5.30 \text{ GeV}/c^2. \quad (5.5)$$

We find 21541 (77625) candidates in SVD1 (SVD2) data sample. For the CP asymmetry measurement described in § 6.2, we use candidates in a signal region defined as an ellipse around the M_{bc} and ΔE mean values,

$$\frac{(M_{\mathrm{bc}} - M_{B^0})^2}{(8 \text{ MeV}/c^2)^2} + \frac{(\Delta E)^2}{(45 \text{ MeV})^2} < 1. \quad (5.6)$$

The sideband regions used for the continuum background study in Δt and the Dalitz distri-

butions are defined as follows,

$$5.2\ \mathrm{GeV}/c^2 < M_{\mathrm{bc}} < 5.26\ \mathrm{GeV}/c^2 \text{ and } -0.1\ \mathrm{GeV} < \Delta\mathrm{E} < 0.5\ \mathrm{GeV} \quad (5.7)$$
for the Δt distribution,

$$5.24\ \mathrm{GeV}/c^2 < M_{\mathrm{bc}} < 5.3\ \mathrm{GeV}/c^2 \text{ and } -0.1\ \mathrm{GeV} < \Delta E < 0.1\ \mathrm{GeV} \quad (5.8)$$
excluding the rectangular region of
$5.268\ \mathrm{GeV}/c^2 < M_{\mathrm{bc}} < 5.3\ \mathrm{GeV}/c^2$ and $-0.05\ \mathrm{GeV} < \Delta E < 0.05\ \mathrm{GeV}$
for the Dalitz distribution.

These regions are shown in Fig. 5.5.

Note that the sideband region for the Dalitz distribution is more restricted than that for the Δt distribution because the amount of phase space, $s_0 + s_+ + s_-$, depends on the invariant masses of the $K^0_S K^+ K^-$ system. If we use the wide sideband region, we can not correctly estimate s_0, s_+ and s_- for the background component, especially around the boundary of the phase space with low s_0 where the events including ϕ are populated. As we apply a B^0 mass-constrained fit [3] to extract the Dalitz variables s_+ and s_-, this tight sideband definition ensures that the structures in the $M(K^+K^-)(=\sqrt{s_0})$ distribution for the sideband region are not distorted compared to that for the signal region when rescaling the amount of phase space in the sideband region back to the signal region. MC studies show that these sideband definitions do not significantly affect structure positions in the sideband.

We find that 1.5 % of the selected events have multiple $B^0 \to K^0_S K^+ K^-$ candidates. In those events, we choose only one $B^0 \to K^0_S K^+ K^-$ candidate by requireing the highest kaon ID likelihood ratio ($\mathcal{R}_{K/\pi}$) and the smallest $\Sigma(\Delta M_{K^0_S})^2$ value.

5.2 Background Suppression

In this section, we describe the different methods of background suppression. In rare B decays such as $b \to s$ and $b \to d$, one of the dominant background comes from continuum events, $e^+e^- \to q\overline{q}$ where q=u, d, s and c, which have a cross-section about three times larger than that of $e^+e^- \to \Upsilon(4S) \to B\overline{B}$. These background can be reduced by using the difference in the event shapes. $B\overline{B}$ events including signal have a spherical topology while continuum events tend to be jet-like, as illustrated in Fig. 5.6.

For $B^0 \to K^0_S K^0_S$, which has an extremely small branching ratio ($\sim 10^{-6}$), the contribution from continuum is relatively high. Therefore, the further reduction of continuum background is necessary. For $B^0 \to K^0_S K^+ K^-$, which has a relatively higher branching ratio, different method is used because a tight continuum suppression is not needed.

Finally, we study the $B\overline{B}$ background contributions. The effects of the mis-reconstructed events are also mentioned.

[3] As shown in Eq. 4.10, the B^0 mass-constrained that B^0 is composed of a K^0_S, a K^+ and a K^- is given as $s_0 + s_+ + s_- = m^2_{B^0} + m^2_{K^+} + m^2_{K^-} + m^2_{K^0_S}$.

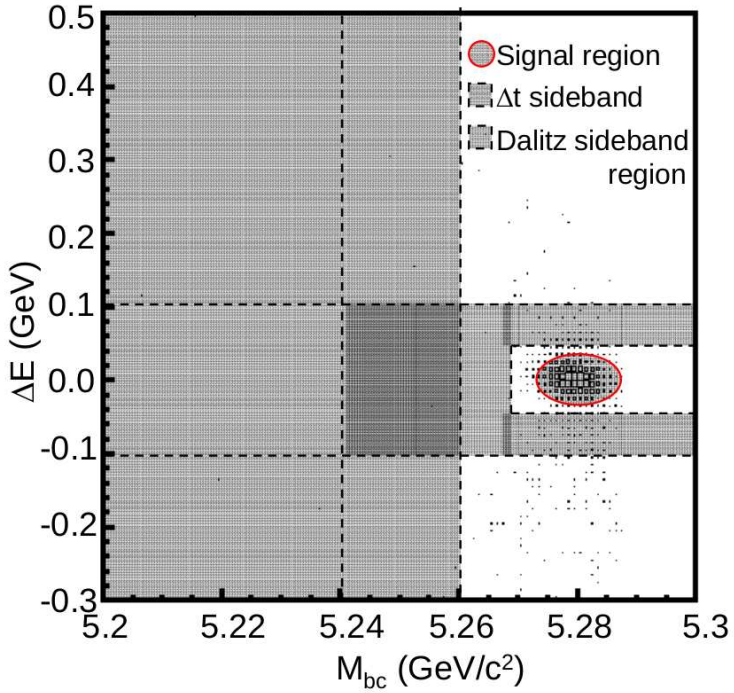

Figure 5.5: Definition of the signal region, $\frac{(M_{\rm bc}-M_{B^0})^2}{(8\ {\rm MeV}/c^2)^2}+\frac{(\Delta E)^2}{(45\ {\rm MeV})^2}<1$, and the sideband regions for Δt, 5.20 GeV/c^2 $< M_{\rm bc} <$ 5.26 GeV/c^2 and -0.1 GeV $< \Delta E <$ 0.5 GeV, and the Dalitz plot, 5.24 GeV/c^2 $< M_{\rm bc} <$ 5.30 GeV/c^2 and -0.1 GeV $< \Delta E <$ 0.1 GeV excluding the rectangular region of 5.268 GeV/c^2 $< M_{\rm bc} <$ 5.300 GeV/c^2 and -0.05 GeV $< \Delta E <$ 0.05 GeV in the $M_{\rm bc}$-ΔE plane, together with the reconstructed $M_{\rm bc}$-ΔE distribution of $B^0 \to K^0_S K^+ K^-$ signal MC.

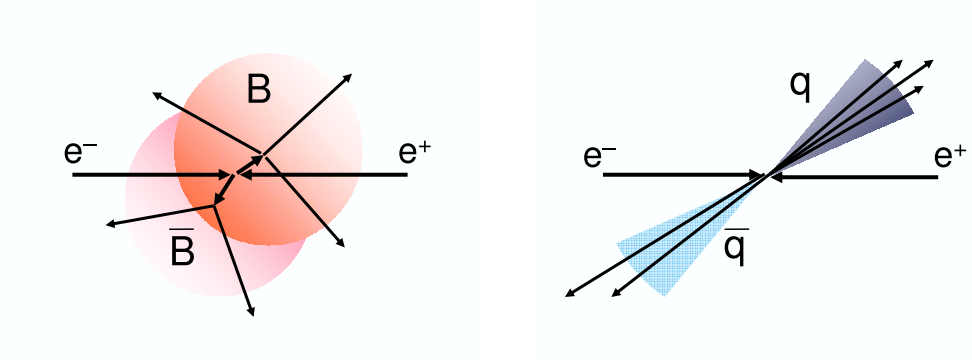

Figure 5.6: Illustration of the event topologies of $e^+e^- \to B\overline{B}$ (left) and $e^+e^- \to q\overline{q}$ (right) events, respectively.

5.2.1 Continuum Background

For $B^0 \to K^0_S K^0_S$ decays, we characterize the event topologies of the $B\overline{B}$ and $q\overline{q}$ events using the KSFW algorithm that Fisher discriminant based on modified Super Fox-Wolfram (SFW) moments, which is developed at Belle [42].

SFW combines six modified Fox-Wolfram moments as a linear combination so that it maximizes the separation between signal and continuum background (Fisher discriminant). Among the six modified Fox-Wolfram moments, the most powerful separation is provided by one of the second moment that is calculated using combinations of a K^0_S in the $B^0 \to K^0_S K^0_S$ candidate (i) and a rest of reconstructed particles in the events (j) as

$$R_2(so) \equiv \frac{\sum_i \sum_j |p_i||p_j| P_2(\cos\theta_{ij})}{\sum_i \sum_j |p_i||p_j| P_0(\cos\theta_{ij})}, \tag{5.9}$$

where $P_l(\cos\theta_{ij})$ is the l'th Legendre polynomial. $R_2(so)$ tend to be around zero (unity) if the K^0_S's in the signal candidate are uncorrelated (correlated) to the rest of the particles and event shape looks spherical (jet-like).

In KSFW, quality of a event is also taken into account: if there are large number of missing particles, separation is bad and if mostly all particles are reconstructed, separation is good. We subdivide events into seven categories according to their values of the missing mass. The missing mass becomes zero if more than one particles are not reconstructed. Since continuum background is jet-like, there are less number of the missing particles as shown in Fig. 5.7 (a). Then we calculate the coefficients of SFW moment separately for each interval region using $B^0 \to K^0_S K^0_S$ signal MC and data in the sideband region that is defined in Fig. 5.3. Figures 5.7 (b-h) show the distributions of SFW for respective interval regions. We use two-dimensional PDFs according to the binned PDF on the interval regions and the parameterized PDFs for the SFW distributions.

We also use the cosine of the B^0 flight direction in the CMS with respect to the z axis. Since $\Upsilon(4S)$ has the total angular momentum J of 1, $B^0\overline{B^0}$ pair has the orbit angular moment ℓ_z of 1. Thus, the $B\overline{B}$ events have an angular distribution of 1- $\cos\theta_B$. Due to the accidental combination of the particles from q and $\overline{q}$, the continuum events have a uniform angular distribution. Figure 5.8 shows the distribution of $\cos\theta_B$ for $B^0 \to K^0_S K^0_S$ signal MC and continuum events.

We form a likelihood $\mathcal{L}_{\rm sig}$ ($\mathcal{L}_{\rm q\overline{q}}$) for signal (continuum) events by combining the likelihood distributions of KSFW and $\cos\theta_B$. The likelihood ratio is defined as,

$$\mathcal{R} = \mathcal{L}_{\rm sig}/(\mathcal{L}_{\rm sig} + \mathcal{L}_{\rm q\overline{q}}) \tag{5.10}$$

and its distribution is shown in Fig. 5.9. To increase the statistics, we impose a loose requirement, $\mathcal{R} > 0.25$, which retains 89 % of the signal events and rejects 71 % of the continuum events. The event-by-event likelihood ratio value, $\mathcal{R}$, is included in the signal yield extraction to improve the precision. We succeed in increasing the reconstruction efficiency by ~ 40 % over the previous attempt [43].

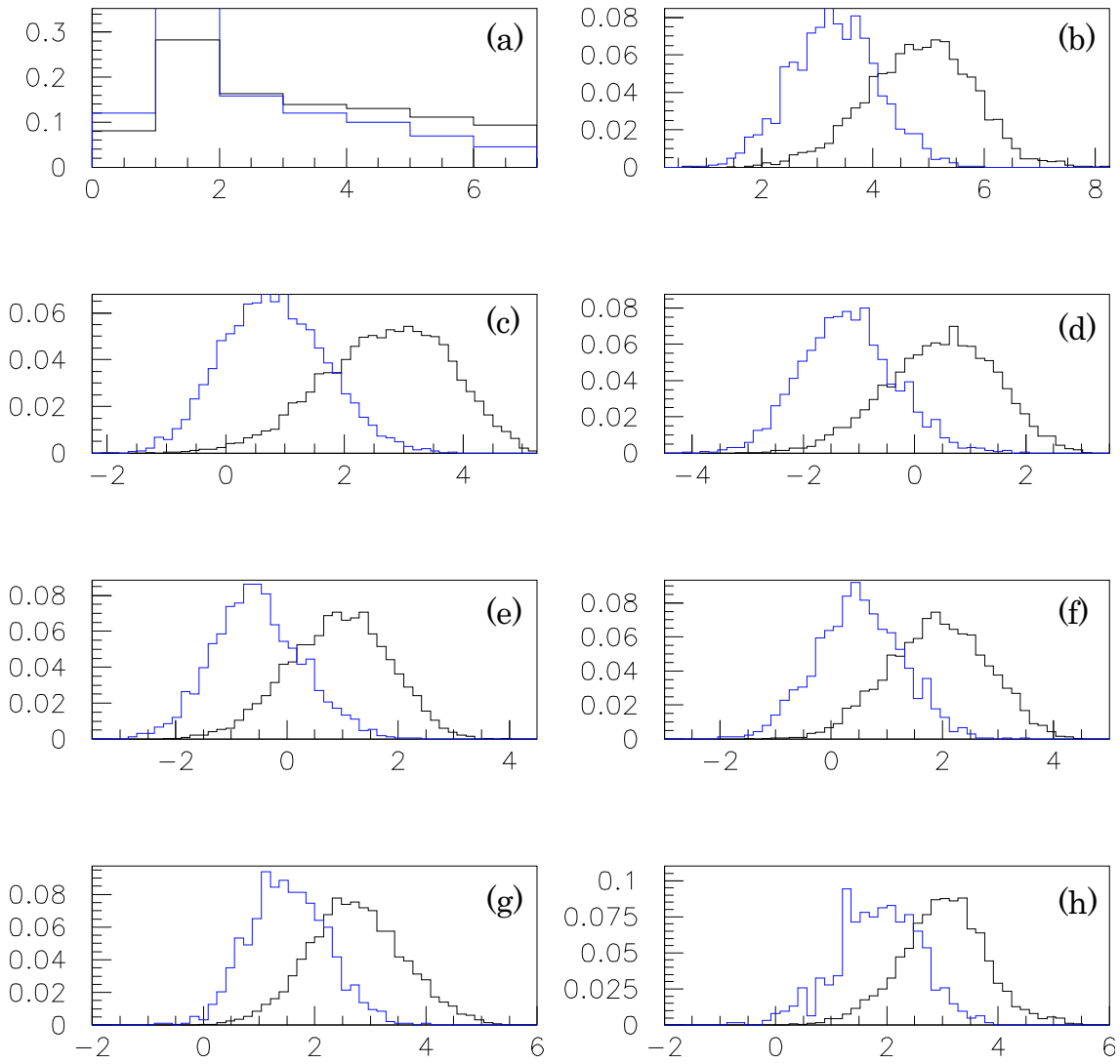

Figure 5.7: The distribution of (a) the interval regions according to the values of the missing mass and of (b-h) SFW from the KSFW algorithm for signal (black) and continuum (blue) events. (b-h) correspond to each interval region from that with larger missing mass to that with smaller missing mass. From (b-h), separations become worse.

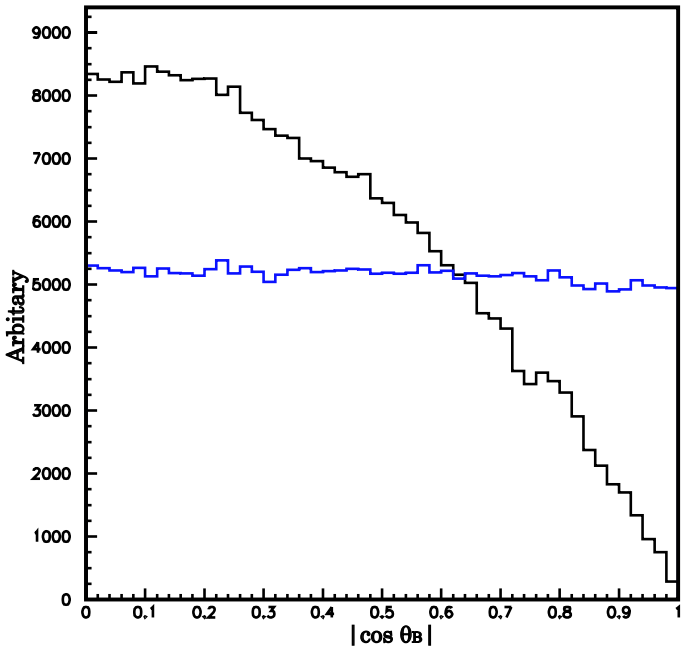

Figure 5.8: The distribution of $\cos\theta_B$ for $B^0 \to K^0_S K^0_S$ signal MC (black) and continuum (blue) events, respectively.

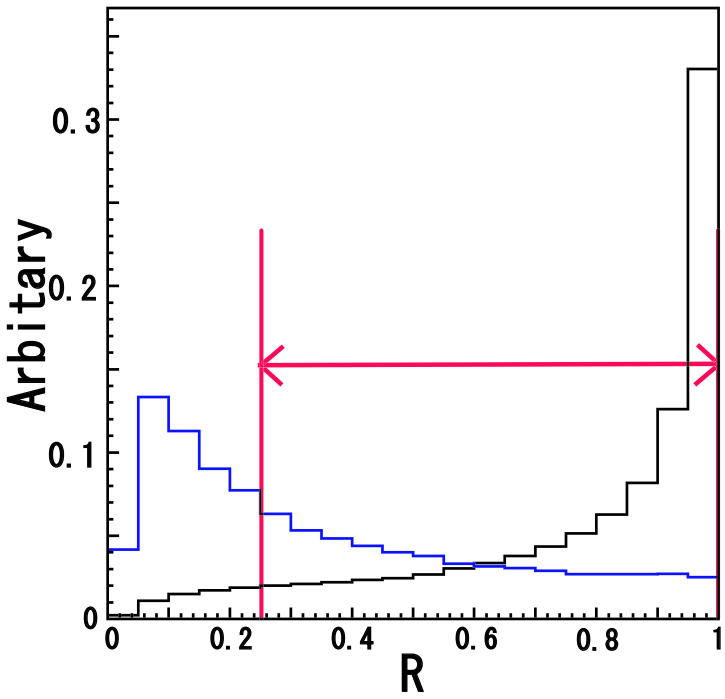

Figure 5.9: The distribution of $\mathcal{R}$ for $B^0 \to K^0_S K^0_S$ signal MC (black) and continuum (blue) events, respectively. The requirement $\mathcal{R} > 0.25$ is also shown as the region defined by the red arrows.

For $B^0 \to K^0_S K^+ K^-$ decays, we use the variable, $\cos\theta_{\rm thrust}$, which is defined as the cosine of the angle between the thrust axis of the $B^0 \to K^0_S K^+ K^-$ decay candidate and that of the remaining particles. As can be seen in Fig. 5.10, the distribution of $\cos\theta_{\rm thrust}$ is strongly peaked near $\cos\theta_{\rm thrust} = \pm 1.0$ for jet-like continuum events, while being nearly flat for $B^0 \to K^0_S K^+ K^-$ events because decay products of two pseudo-scaler B mesons have no angular correlations. The requirement $|\cos\theta_{\rm thrust}| < 0.8$ is imposed, which retains 83 % of the signal events and rejects 79 % of the continuum events.

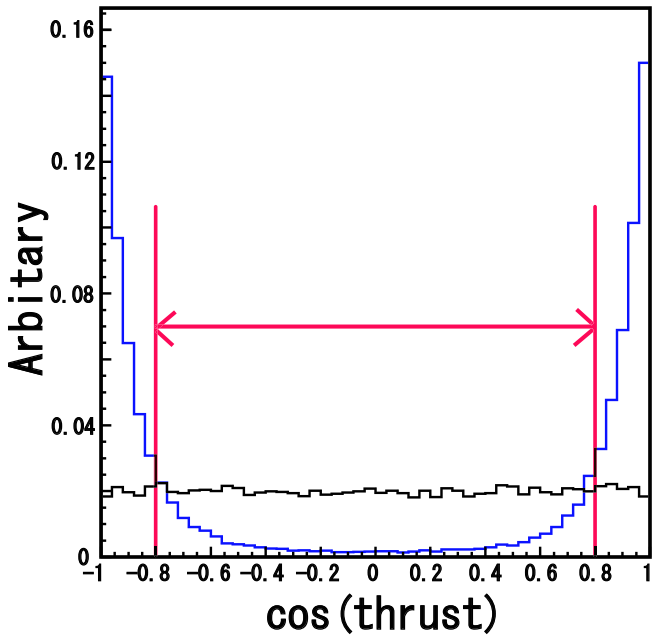

Figure 5.10: The distribution of $\cos\theta_{\rm thrust}$ for $B^0 \to K^0_S K^+ K^-$ signal MC (black) and data sample in the sideband region (blue), respectively. The requirement $|\cos\theta_{\rm thrust}| < 0.8$ is also shown as the region defined by the red arrows.

5.2.2 $B\overline{B}$ Background Originating From Other B Decays

The contribution of the background originating from other B decays, defined as $B\overline{B}$ background, is studied using a large sample of GEANT-based MC simulated events.

For $B^0 \to K^0_S K^0_S$ decays, although they proceed through the quark transition from the third generation, b, to the first one, d, they are expected to be free from $B\overline{B}$ background via $b \to s$ transitions with similar final states [4]. The total number of the $B\overline{B}$ background events in the real data is expected to be 0.6 ± 0.1, which corresponds to ~ 0.1 % of the number of

[4]The other decays in $b \to d$ transitions usually suffer from huge background decays in $b \to s$ transitions due to imperfect kaon ID with a probability of $\sim 10\%$, and give almost same $M_{\rm bc}$ but lower ΔE by ~ 40 MeV than the original ones; for example, $B^+ \to K^0_S K^+$ against $B^+ \to K^0_S \pi^+$ and $B^0 \to \rho^0\gamma$ against $B^0 \to K^{*0}\gamma$. These dilution is usually estimated by adding a PDF for it although separation is not good.

candidate events in the signal region and is negligibly small. We take into account only signal and continuum events in the nominal fit. The uncertainty due to a possible contribution from $B\overline{B}$ background is included in the systematic errors in the CP asymmetry measurement.

For $B^0 \to K^0_S K^+ K^-$ decays, the dominant $B\overline{B}$ background is found to originate from charm decays of the B meson and peaks in the signal region with the yield of ~ 60: $B^0 \to D^-[K^0_S K^-]K^+$ [5] and $B^0 \to J/\psi K^0_S$ decays. There are also potential backgrounds from $B^0 \to D^-_S[K^0_S K^-]K^+$ and $B^0 \to \overline{D^0}[K^+K^-]K^0_S$. Backgrounds due to $K-\pi$ mis-identification with the probability of $\sim 10\%$ are also found. All these peaking background decays are rejected by applying $\sim 2.5\sigma$ vetoes on the invariant masses as summarized in Table 5.1. For the backgrounds that arise from mis-identified particles, the invariant masses are re-calculated by assuming an alternate mass hypothesis for the charged kaon. The remaining contribution is included in the nominal fit as the $B\overline{B}$ background component.

Table 5.1: Summary of charm vetoes for $B^0 \to K^0_S K^+ K^-$ decays. The subscript in the region vetoed indicates that an alternate mass hypothesis has been applied to the kaon candidates used to calculate the invariant mass term.

Vetoed region	Vetoed mode
$\lvert M(K^0_S K^-) - M_{D^-}\rvert < 15$ MeV/c^2	$B^0 \to D^-[K^0_S K^-]K^+$
$\lvert M(K^+K^-) - M_{J/\psi}\rvert < 15$ MeV/c^2	$B^0 \to J/\psi[K^+K^-]K^0_S$
$\lvert M(K^0_S K^-) - M_{D^-_S}\rvert < 15$ MeV/c^2	$B^0 \to D^-_S[K^0_S K^-]K^+$
$\lvert M(K^+K^-) - M_{\overline{D^0}}\rvert < 15$ MeV/c^2	$B^0 \to \overline{D^0}[K^+K^-]K^0_S$
$\lvert M(K^0_S K^-)_\pi - M_{D^-}\rvert < 15$ MeV/c^2	$B^0 \to D^-[K^0_S \pi^-]K^+$
$\lvert M(K^+K^-)_\pi - M_{\overline{D^0}}\rvert < 15$ MeV/c^2	$B^0 \to \overline{D^0}[K^+\pi^-]K^0_S$

Mis-Reconstructed Events (Self Cross Feed)

Although either of B^0 and $\overline{B^0}$ originates from a signal decay, the event is sometimes reconstructed wrongly using some of the particles in the tag-side B decay, and is assumed as a signal decay. We define such events as mis-reconstructed events, so-called Self Cross Feed. Using a large sample of signal MC, the mis-reconstructed signal events are estimated.

For $B^0 \to K^0_S K^0_S$ decays, the contribution is estimated to be 0.69 ± 0.02 % of the signal yield, so its effect in both the signal yield extraction and CP measurement can be ignored.

For $B^0 \to K^0_S K^+ K^-$ decays, the contribution is estimated to be 0.38 ± 0.02 % of the total signal yield in the Dalitz plane and often occurs when one particle has low momentum, which may distort the signal distribution on the Dalitz plane. In the nominal CP asymmetry fit, we ignore its effect and include the difference in the fit to a large sample of only correctly reconstructed signal MC and the fit to the same sample that also includes mis-reconstructed signal MC as a systematic error.

[5] Throughout this thesis, the inclusion of the charge-conjugate decay mode is implied unless otherwise stated.

5.3 Reconstruction of the Proper Time Difference, Δt

The proper time difference, Δt, is defined as

$$\Delta t \equiv t_{CP} - t_{\rm tag} \simeq \frac{z_{CP} - z_{\rm tag}}{\beta\gamma c}, \tag{5.11}$$

where z_{CP} and $z_{\rm tag}$ are the decay vertex positions in the z direction of f_{CP} and $f_{\rm tag}$, respectively. We apply the B decay vertex reconstruction algorithm developed at Belle [44]. The methods of reconstructing the B decay vertices and calibrating Δt are described in the following.

5.3.1 Reconstruction of a B Decay Vertex on the CP Side

Reconstruction of a B Decay Vertex in a $B^0 \to K^0_S K^+ K^-$ Decay

The vertex position for a $B^0 \to K^0_S K^+ K^-$ candidate is reconstructed using the charged tracks and a constraint on the transverse components of the IP; The charged tracks are required to have a sufficient number of hits in the SVD: at least one layer with hits on both the z and r-ϕ sides and at least one additional layer with a hit on the z side for SVD1, and at least two layers with hits on both sides for SVD2. If there are no associated tracks with the required SVD hits in a candidate B meson, the event is excluded from the CP analysis. The typical vertex reconstruction efficiency is $\sim$95 % and the vertex position resolution with SVD1 (SVD2) is 78.0 μm (78.9 μm). These resolutions are calibrated using data and signal MC of high-statistics control samples as will be described in § 5.3.3.

The shape of the IP profiles is represented by a three-dimensional Gaussian distribution. Since the actual IP center position and its spread vary both with accelerator conditions and during the data taking in a single run, the standard deviation of each Gaussian is determined using pre-scaled hadronic events run by run, while the mean is evaluated per 10,000 events. The typical size is 100μm in x, 5μm in y, and 3mm in z. Since the size in the y direction is too small to be measured from the vertex distribution, it is taken from special measurements by the KEKB accelerator group. The IP profile is smeared by the finite B^0 flight length in the plane perpendicular to the z axis. Its smearing effect is represented by a single Gaussian with $\sigma = 21$ μm. Smallness of the IP profile in the y direction provides powerful constraint on B decay vertex position reconstruction. Because of this IP constraint, B decay vertex reconstruction using only a single track or K^0_S can be realized.

Reconstruction of a B Decay Vertex in a $B^0 \to K^0_S K^0_S$ Decay

Due to the finite lifetime of a K^0_S, $c\tau \sim 2.68$ cm, the B decay position is reconstructed using the $K^0_S \to \pi^+\pi^-$ pseudo-track and an IP constraint in the $x - y$ plane perpendicular to the z axis. Figure 5.11 shows the schematic on the reconstruction of B decay vertex in a

$B^0 \to K^0_S K^0_S$ Decay. This challenging technique was first introduced at BaBar [45], and also modified and applied at Belle [46]. Both charged pions from at least one K^0_S are required to have a sufficient number of hits in the SVD in the same way as the charged tracks in $B^0 \to K^0_S K^+ K^-$ decays.

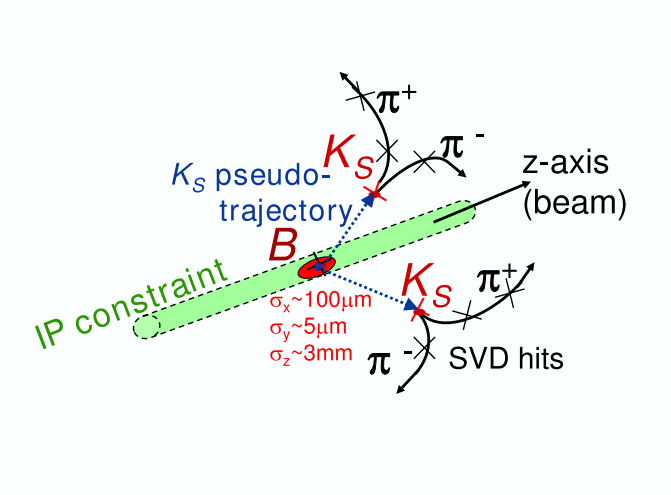

Figure 5.11: Schematic on the reconstruction of B decay vertex in a $B^0 \to K^0_S K^0_S$ decay.

From signal MC, the typical reconstruction efficiency of the B decay vertex with SVD2 (61 %) is found to be much higher than that with SVD1 (44 %) because SVD2 has the additional outer layer. If we save more events with SVD2 by the third layer and the fourth layer, in this case the position resolution becomes worse because we do not have more precise hit information from the inner layers. Since total position resolution of the B decay vertex depends on the ratio of "which layer the hits in the SVD start from", that with SVD2 becomes worse as follows: the position resolution of the B decay vertex in the z direction with SVD1 (SVD2) is 73 μm (105 μm) for the case where both K^0_S particles are used for the vertex reconstruction, and 141 μm (172 μm) for the case where a single K^0_S is used.

5.3.2 Reconstruction of a B Decay Vertex on the Tag Side

All the charged tracks is used except for the ones used to reconstruct the B decay in CP side. We select charged tracks that have the required SVD hits in the same way as the CP side. We also reject poorly-reconstructed tracks without enough SVD hits, with an estimated longitudinal position error larger than 500 μm, or with the impact parameters larger than 500 μm. The B decay vertex in the tag side is determined by repetitive fitting using the remaining charged tracks and the IP profile. If the reduced χ^2 per degrees of freedom is smaller than 20, we accept the vertex. If not, we exclude the charged track that gives the largest contribution to the vertex χ^2 and repeat the fit. However, we always keep high momentum leptons, $p^{\rm CMS}_\ell > 1.1$ GeV/c, as they are likely to originate from semi-leptonic $b \to c\ell\nu$ decays.

In the B vertex reconstruction of the tag side, we usually encounter non-primary charged daughter tracks from secondary D decays. Due to the finite D lifetime, the reconstructed B decay vertex point is shifted and the vertex resolution becomes deteriorated. The typical shift and resolution of B meson in the z direction on the tag side are estimated to be $\sim$ 20 μm and $\sim$ 140 μm in rms, respectively, estimated using a signal MC. The typical vertex reconstruction efficiency for $f_{\rm tag}$ decays is determined to be 93 %.

5.3.3 Calibration of the Δt Distribution

The resolution function ($\equiv R_{\rm sig}(\Delta t)$) for Δt is necessary for measurements of time-dependent CP asymmetries. Three independent sources are considered: the detector resolution, the effect on the B vertex reconstruction in the tag side from non-primary tracks and the kinematic approximation [6] as illustrated in Fig. 5.12. Further details can be found in Ref. [44].

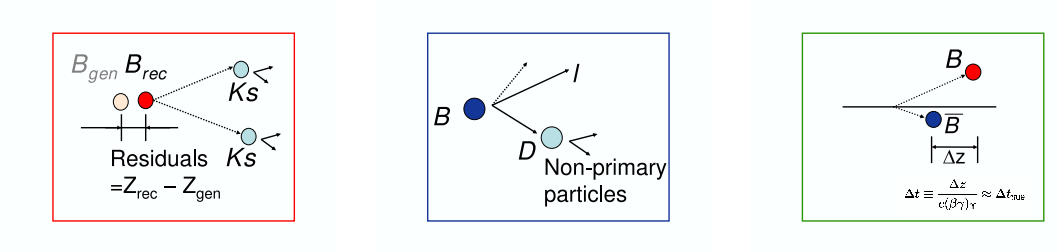

Figure 5.12: Illustration on the calibration of the Δt distribution. Left, middle and right figures show the effect of detector resolution, non-primary tracks in the tag side and the kinematic approximation, respectively.

Since the B^0 lifetime is $\sim$ 1.5 ps, the produced B mesons run with the distance of $\sim$ 200 μm before decaying, which is comparable to the Δz detector resolution of $\sim$ 200 μm by the SVD. Thus, the understanding of the systematic errors of Δt is essential.

We model the smearing effect due to the detector resolution by introducing the resolution function that will be convolved with the physics Δt distribution. The resolution function depends on event-by-event vertex qualities, σ_z and ξ, which is the vertex fit χ^2 along the z direction only. We model the function using MC as an event-by-event double Gaussian whose width is similar to σ_z but scaled according to ξ.

Using the data sample of 535×10^6 $B\overline{B}$ pairs, we update the parameters of this model to represent data well for the coming larger statistics. We simultaneously determine all the parameters of this model, the B lifetime and Δm_d in the maximum likelihood fit to

[6] The uncertainty from the kinematic approximation of ignoring the x and y directions of the B vertices can be analytically parametrized using the flight direction of the reconstructed B meson. Due to the extremely flat shape of the IP, this effect is not so large.

$\sim$ 700 thousand events of data in the control sample decays of B^0 and B^+ [7] and the fitted result to the Δt distribution of the neutral B control sample data is shown in Fig. 5.13 : $B^0 \to D^{(*)-}\ell^+\nu$, $B^0 \to D^{(*)-}\pi^+$, $B^0 \to D^{*-}\rho^+$, $B^+ \to \overline{D^0}\pi^+$, and $B^+ \to J/\psi K^+$. Since the obtained B^0 lifetime of 1.538 ± 0.008 ps (1.528 ± 0.005 ps) for SVD1 (SVD2) and Δm_d of 0.505 ± 0.005 ps^{-1} (0.506 ± 0.003 ps^{-1}) for SVD1 (SVD2) in the control data sample are consistent with PDG values [35] and our previous measurements, we confirm the validity of this resolution function. We treat the events with bad vertex resolutions that are categorized by neither signal nor background. We call this the outlier component. When we model the PDF of Δt, the contribution are taken into account as the outlier component as a single Gaussian with wide width of $\mathcal{O}(10)$ ps.

For the B decay vertices reconstructed using K^0_S only, the default Δt resolution function is modified and the vertex error is scaled depending on the K^0_S flight length and the number of K^0_S particles used for the vertex reconstruction. This dependence in the Δt resolution function is calibrated using a sample of 1939 $B^0 \to J/\psi K^0_S$ decays, where the vertex reconstruction occurred using only the K^0_S and IP profile. We measure the B^0 lifetime and CP asymmetry in this $B^0 \to J/\psi K^0_S$ data control sample, $\tau_{B^0} = 1.503 \pm 0.036$ ps(stat) and $\sin 2\phi_1 = 0.68 \pm 0.06$ (stat), which are in agreement with the world averages of τ_{B^0} and sin $2\phi_1$, respectively. We conclude that the vertex resolution where only K^0_S has been used for vertex reconstruction is also well understood.

To discard poorly measured B decay vertices, we impose requirements on the vertex quality, $\xi < 250$, for both sides, as well as on the proper time difference, $|\Delta t| < 70$ ps ($\sim 45\ \tau_{B^0}$). We lose ~ 2.5 % of the total events by the former requirement and ~ 0.2 % by the latter requirement. For $B^0 \to K^0_S K^+ K^-$ decays, we do not use events that have no vertex information while for $B^0 \to K^0_S K^0_S$ these events are still used to measure direct CP violation.

5.4 Flavor Tagging

The b flavor, whether B is B^0 or $\overline{B^0}$, is determined by the charge and the kinds of the charged particles among the decay products of $f_{\rm tag}$ as shown in Fig 5.14. Charged tracks that are not used to reconstruct $B^0 \to K^0_S K^+ K^-$ or $B^0 \to K^0_S K^0_S$ decays are used for flavor-tagging. We apply the flavor tag algorithm developed at Belle [47].

5.4.1 Flavor Tagging Algorithm

The flavor tagging algorithm looks for the following properties on the tag side to identify its flavor:

High momentum leptons from $B \to X\ell^\pm\nu$ decays,

[7] The parameters of Δt resolution function ($R_{B^+B^-}(\Delta t)$) for B^+B^- decays are determined using charged control sample decays.

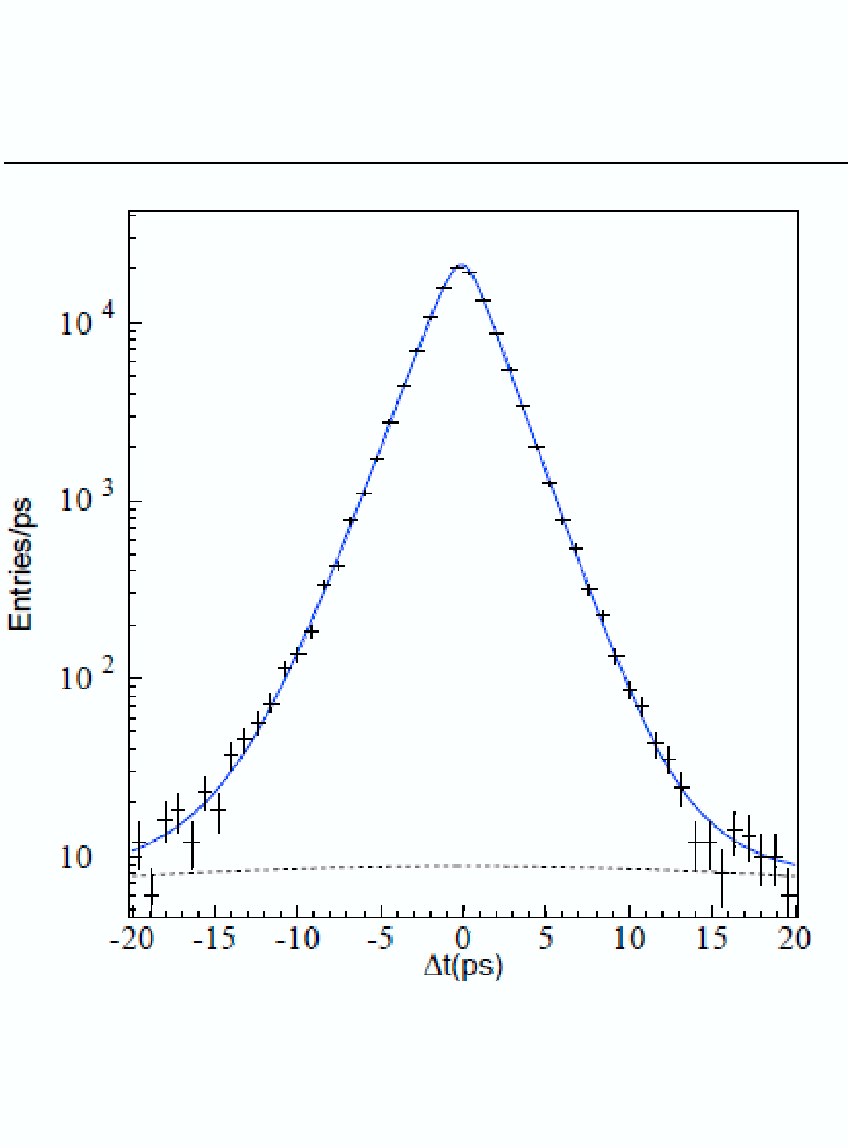

Figure 5.13: The Δt distribution of the neutral B control sample data. The solid line represents the result of the unbinned maximum likelihood fit. The dashed line corresponds to the outlier component.

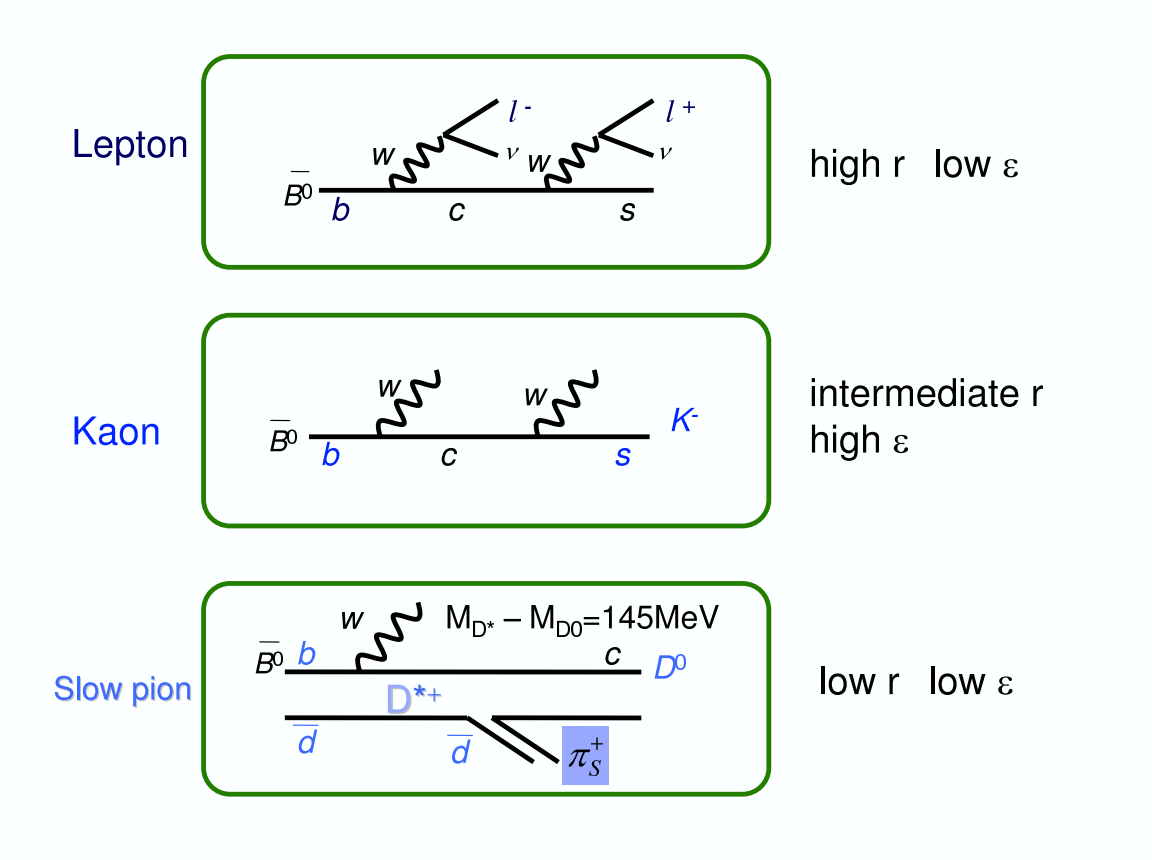

Figure 5.14: Concept of the b flavor tagging algorithm from the charged tracks such as lepton, kaon and slow pions. r and ϵ correspond to the quality and efficiency, respectively.

Kaons from $b \to c \to s$ cascade decays, $B \to D[K^{\pm}Y]X$,

Slow pions from $B \to D^{*\pm}[D\pi^{\pm}]X$,

Intermediate momentum leptons from $B \to D[K\ell^{\pm}\nu]X$ decays,

High momentum pions from $B \to D^{(*)}\pi^{\pm}$, and

Lambda from $b \to c \to s$ cascade decays.

Two parameters, $q_{\rm tag}$ and r, are used to represent the flavor tagging output. The parameter $q_{\rm tag}$ is defined as the flavor of $f_{\rm tag}$. When $f_{\rm tag}$ is $B^0(\overline{B^0})$, $q_{\rm tag}$ is +1(-1). The parameter r is an expected flavor dilution factor that ranges from zero for no flavor information and one for unambiguous flavor assignment.

Multiple discriminants such as charge, particle identification and momentum of charged tracks are used to estimate the best dilution factor, r. Using a multi-dimensional look-up table binned by the values of the discriminants, the signed probability, $q_{\rm tag} \cdot r$, is given by

$$q_{\rm tag} \cdot r = \frac{N(B^0) - N(\overline{B^0})}{N(B^0) + N(\overline{B^0})}, \tag{5.12}$$

where $N(B^0)$ and $N(\overline{B^0})$ are the numbers of B^0 and $\overline{B^0}$ in each bin of the table prepared from a large statistics MC event sample.

Figure 5.15 shows a diagram of the flavor tagging method. Flavor tagging proceeds in two stages, track-level and event-level. In track-level flavor tagging, each charged track is assigned to one of the four categories with associated flavor-tagging look-up tables: slow pion, lambda, kaon and leptons. The b-flavor and the dilution factor of each charged track in the four categories is estimated using discriminants such as track momentum, angle and particle identification. In event-level flavor tagging, the results from the track-level are combined to obtain the event-level $q_{\rm tag} \cdot r$ value.

Track-Level Flavor-Tagging

We describe how each category is assigned to the charged tracks.

Slow Pion Category
A charged track with a momentum smaller than 0.25 GeV/c in the CMS is assigned to this category. The flavor information from the charge of the slow pion track is used to identify the b-flavor of the tag side. Several variables are included in the table: the charge of the track, the momentum in the laboratory frame, the polar angle in the laboratory frame, the angle between the slow pion and the thrust axis of rest of the tag side particles in the CMS, $\theta_{\rm thr}$, and a pion/electron identification likelihood ratio, $R_{\pi/e}$. The angle, $\theta_{\rm thr}$, is used to suppress the background from non-D decays. The ratio $R_{\pi/e}$

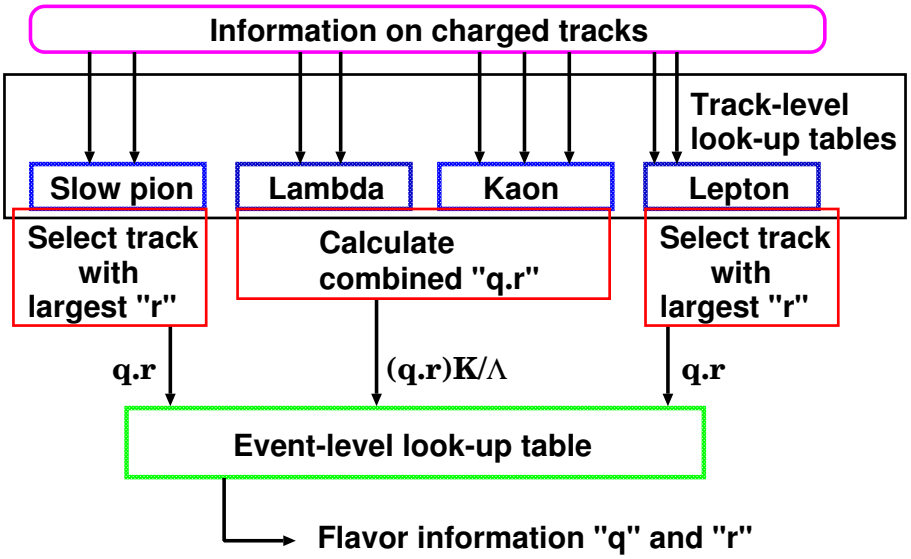

Figure 5.15: Flavor tagging method using charged tracks in two stages, track-level and event-level.

is used to remove background electrons from photon conversion. This category has a low tagging efficiency and poor tagging quality.

Lambda Category
A charged track that forms a Λ candidate with another charged track with the opposite charge is assigned to this category. The flavor information from Λ, Λ or $\bar{\Lambda}$, is used to identify the b-flavor of the tag side. One of the tracks should be identified as a proton. The Λ candidate is required to have an invariant mass, $M_{p\pi}$, between 1.1108 GeV/c^2 and 1.1208 GeV/c^2. The angle between the momentum vector of the Λ candidate and the vector formed by the IP and the vertex of the Λ candidate, $\theta_{\rm defl}$, should be less than 30 °. The minimum distance between the tracks in z axis, Δz, should be less than 4 cm, and the flight length of the Λ in the $x-y$ plane should be longer than 0.5 cm. The flavor of Λ, $M_{p\pi}$, $\theta_{\rm defl}$ and the presence of K^0_S candidates are included in the look-up table.

Kaon Category
A charged track that is not positively identified as a lepton or proton is assigned to this category. The flavor information of the kaon in $b \to c \to s$ decays is mainly used to identify the b-flavor of the tag side. Fast pions from $B \to D^{(*)}\pi^{\pm}$ are also included. The charge of the track, the presence of K^0_S candidates, the track momentum in the CMS, the polar angle of the track in the laboratory frame and the K/π ID likelihood ratio are included in the look-up table. This category has a high tagging efficiency but poor tagging quality.

Lepton Category
A charged track with a momentum larger than 0.4 GeV/c and an electron likelihood

larger than 0.8 is included as an electron candidate, while a charged track with a momentum larger than 0.8 GeV/c and a muon likelihood larger than 0.95 is included as a muon candidate. The flavor information from high momentum leptons in $B \to X\ell^{\pm}\nu$ decays and intermediate momentum leptons in $B \to D \to K\ell^{\pm}\nu$ decays are used to identify the b-flavor of the tag side. Several variables are included in the look-up table: the lepton momentum in the CMS, $p_{\ell}^{\rm cms}$, the polar angle of the track in the laboratory frame, $\theta_{\rm lab}$, the recoil mass, $M_{\rm recoil}$, and the missing momentum in the CMS, $p_{\rm miss}^{\rm cms}$. The former two variables are the most powerful since these can distinguish leptons from pions. The variables $p_{\ell}^{\rm cms}$, $M_{\rm recoil}$ and $p_{\rm miss}^{\rm cms}$ discriminate the primary lepton from $B \to X\ell^{\pm}\nu$ decays and the secondary lepton from $B \to D \to K\ell^{\pm}\nu$ decays. Since the charges of primary and secondary leptons are opposite, this discriminant is very useful. The variable, $M_{\rm recoil}$, indicates the presence of a D meson and the variable, $p_{\rm miss}^{\rm cms}$, indicates the existence of neutrinos. This category has a low tagging efficiency but high tagging quality.

With the exception of charged tracks assigned to the Λ and kaon categories, these tracks are required to originate from the IP: within 2 cm in the $x-y$ plane and 10 cm in the z direction.

Event-Level Flavor-Tagging

The event-level flavor tagging combines the results, $(q_{\rm tag} \cdot r)_x$ where x is the tagging category, for each track to determine a single $q_{\rm tag}$ and r output for each event. For the lepton and slow pion categories, the track with the highest r in each category is chosen as an input. For the kaon and Λ categories, the flavor and dilution factors of each track are combined by calculating the product of the flavor dilution factors in order to account for possible cases where there are multiple s quarks in the final state. By using a three-dimensional look-up table, the correlations between the flavor information for the four categories in track-level are correctly taken into account.

Figure 5.16 shows the $q_{\rm tag} \cdot r$ distributions from $\overline{B^0}(B^0) \to \phi K_S^0$ signal MC. The $q_{\rm tag} \cdot r$ distribution peaks at $q_{\rm tag} = +1$(-1) when $f_{\rm tag}$ is $B^0(\overline{B^0})$. The poorly tagged events populate the $q_{\rm tag} \cdot r \sim 0$ region while the events with nearly perfect tagging are located around $q_{\rm tag} \cdot r \sim 1$.

5.4.2 Calibration for Flavor Tagging

The performance of flavor tagging in data is characterized by the two parameters: ϵ and w_{tag}. The parameter ϵ is the raw tagging efficiency and the wrong tag fraction, w_{tag}, is the probability that the flavor tagging is wrong in data.

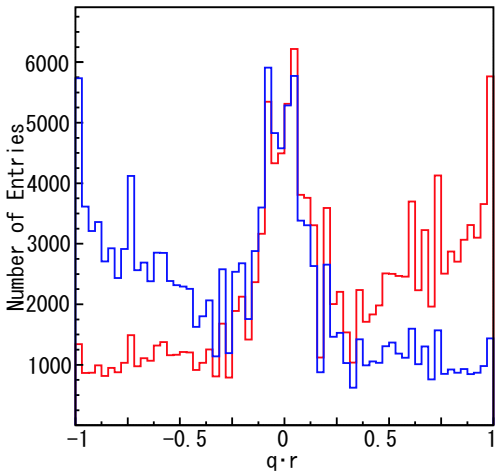

Figure 5.16: The $q_{\rm tag}\cdot r$ distribution for $B^0 \to K^0_S K^+ K^-$ signal MC. The red (blue) histogram indicates $\overline{B^0} \to K^0_S K^+ K^-$ ($B^0 \to K^0_S K^+ K^-$) signal MC when $f_{\rm tag}$ is $B^0(\overline{B^0})$.

In practice, the observed time-dependence becomes

$$\mathcal{P}^{\rm obs}_{\rm sig}(\Delta t, q_{\rm tag}, w_{tag}) = \epsilon \cdot [(1-w_{tag})\mathcal{P}^{\rm obs}_{\rm sig}(\Delta t, q_{\rm tag}) + w_{tag}(\mathcal{P}^{\rm obs}_{\rm sig}(\Delta t, -q_{\rm tag}))], \tag{5.13}$$

and the observed CP asymmetry is rewritten as

$$\mathcal{A}^{\rm obs}_{CP} = \frac{\mathcal{P}^{\rm obs}_{\rm sig}(\Delta t, q_{\rm tag}, w_{tag}) - \mathcal{P}^{\rm obs}_{\rm sig}(\Delta t, -q_{\rm tag}, w_{tag})}{\mathcal{P}^{\rm obs}_{\rm sig}(\Delta t, q_{\rm tag}, w_{tag}) + \mathcal{P}^{\rm obs}_{\rm sig}(\Delta t, -q_{\rm tag}, w_{tag})} = (1-2w_{tag})\mathcal{A}_{\rm CP}. \tag{5.14}$$

The observed CP asymmetry is diluted by $1-2w_{tag}$, which is called a dilution factor.

Since the statistical significance of the measured asymmetries is proportional to $(1-2w_{tag})\sqrt{\epsilon}$, the effective number of events is proportional to the factor $\epsilon(1-2w_{tag})^2$. Thus, an effective efficiency, $\epsilon_{eff} = \epsilon(1-2w_{tag})^2$, is introduced.

Note that r is determined from only MC-based information and the MC information represents data perfectly, $r = 1 - 2w_{\rm tag}$. To maximize the effective tagging efficiency while using $w_{\rm tag}$ values that are measured by data, events are subdivided based on their r values, each $w_{\rm tag}$ value that is measured in each r region is used for the analyses.

For this purpose, seven r-interval regions is introduced: $0 < r \leq 0.1$, $0.1 < r \leq 0.25$, $0.25 < r \leq 0.5$, $0.5 < r \leq 0.625$, $0.625 < r \leq 0.75$, $0.75 < r \leq 0.875$ and $0.875 < r \leq 1$. Note that we label each r-interval region as ℓ from 0 to 6 in this thesis.

The wrong tag fractions ($\equiv w_\ell$) and the differences in B^0 and $\overline{B^0}$ ($\equiv \Delta w_\ell$) in each r-interval region, ℓ, are obtained by fitting the time-dependent $B^0\overline{B^0}$ mixing oscillation of $B^0 \to D^{*-}\ell^+\nu$, $D^{(*)-}\pi^+$ and $D^{*-}\rho^+$ self-tagged events as shown in Fig. 5.17 [8]. The time

[8] The discrepancies around $\Delta t > 10$ ps are due to the outlier component.

Table 5.2: Wrong tag fractions, w_ℓ, and wrong tag fraction differences, Δw_ℓ, for each r-interval region, ℓ.

SVD1 r-interval region, ℓ	r-interval	w_ℓ	Δw_ℓ
0	0.000-0.100	0.5	0.0
1	0.100-0.250	0.423±0.007	0.06±0.01
2	0.250-0.500	0.337±0.008	0.01±0.01
3	0.500-0.625	0.235±0.010	-0.01±0.01
4	0.625-0.750	0.166±0.008	-0.01±0.01
5	0.750-0.875	0.105±0.008	0.008±0.009
6	0.875-1.000	0.026±0.006	0.003±0.006
SVD2 r-interval region, ℓ	r-interval	w_ℓ	Δw_ℓ
0	0.000-0.100	0.5	0.0
1	0.100-0.250	0.429±0.005	-0.039±0.007
2	0.250-0.500	0.327±0.006	-0.036±0.006
3	0.500-0.625	0.223±0.010	0.018 ±0.007
4	0.625-0.750	0.161±0.010	0.002±0.006
5	0.750-0.875	0.105±0.008	-0.027±0.006
6	0.875-1.000	0.019±0.005	-0.001±0.004

evolution of $B^0\overline{B^0}$ pairs with opposite flavor (OF) and same flavor (SF) is given by

$$\mathcal{P}_{\rm SF}^{\rm OF} = \frac{e^{-|\Delta t|/\tau_{B^0}}}{4\tau_{B^0}}[1 \mp q_{\rm tag}\Delta w_\ell \pm (1-2w_\ell)\cos(\Delta m_d \Delta t)], \tag{5.15}$$

and the OF-SF asymmetry is given by

$$\mathcal{A}_{\rm mix} = \frac{\mathcal{P}_{\rm OF} - \mathcal{P}_{\rm SF}}{\mathcal{P}_{\rm OF} + \mathcal{P}_{\rm SF}} = -q_{\rm tag}\Delta w_\ell + (1-2w_\ell)\cos(\Delta m_d \Delta t). \tag{5.16}$$

The obtained w_ℓ and Δw_ℓ are summarized in Table 5.2 for SVD1 and SVD2 data samples. The total effective tagging efficiency for data of control sample, defined as $\sum_\ell \epsilon_\ell \cdot (1-2w_\ell)^2$, is 29.20 ± 1.37 %.

For $B^0 \to K^0_S K^0_S$ decays, candidate events are selected to have the flavor tagging quality $r > 0.1$ because events with $r \leq 0.1$ are mostly continuum and a correlation between r and ΔE is found in the data sample in the sideband region. For $B^0 \to K^0_S K^+ K^-$ decays, the events with $r = 0$ are not used in the analysis due to the absence of flavor information.

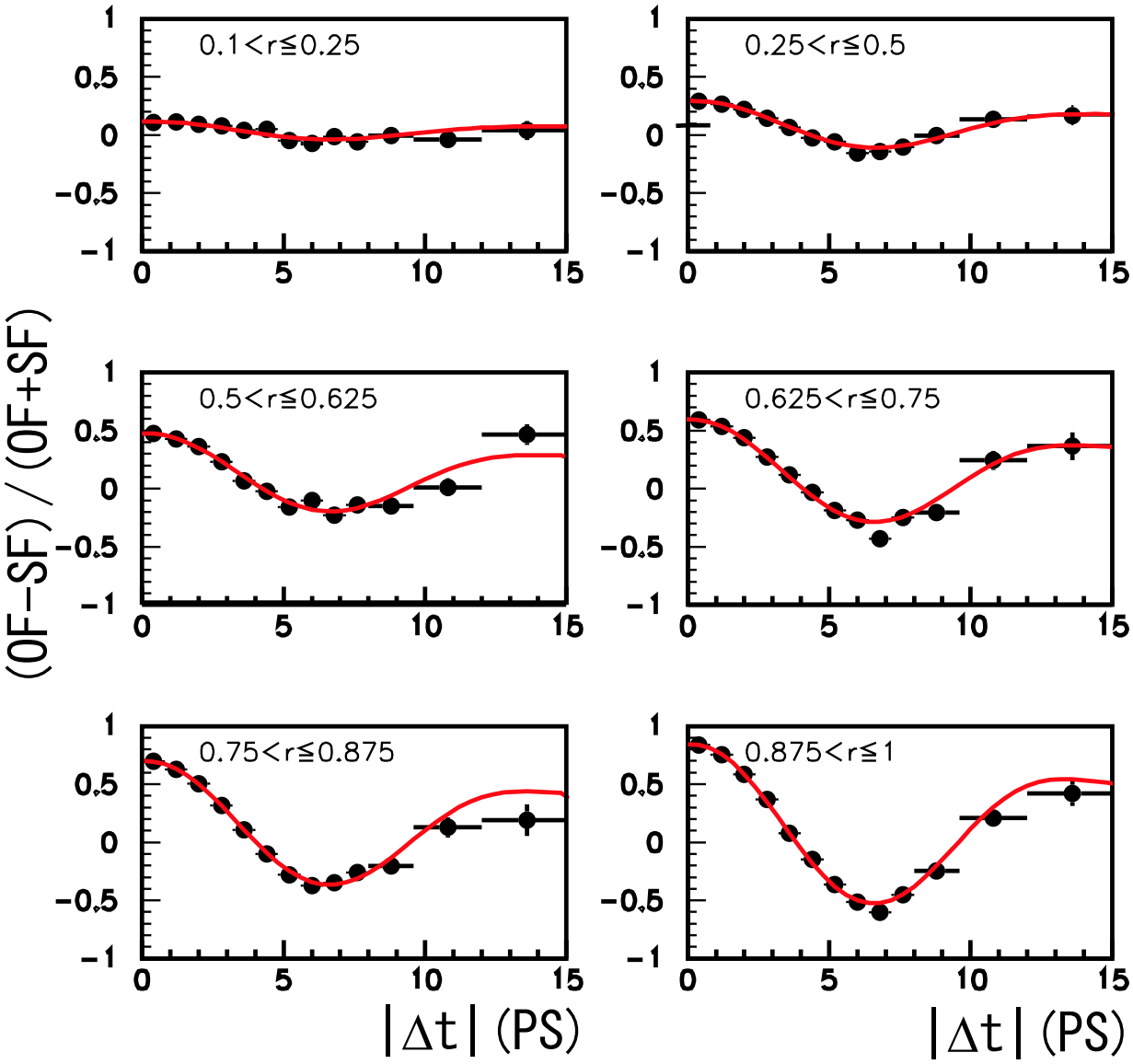

Figure 5.17: Time-dependent $B^0\overline{B^0}$ mixing oscillation fitted result to the control data sample of $B^0 \to D^{*-}\ell^+\nu$, $D^{(*)-}\pi^+$ and $D^{*-}\rho^+$ self-tagged decays. Each plot from the top-left, to the bottom-right corresponds to the subsample in each r-interval region (ℓ) from 1 to 6. The amplitudes in the oscillation become larger due to less dilution from wrong tagging.

5.5 Signal Extraction from Reconstructed Candidates

Signal yield is extracted by the unbinned extended maximum likelihood fits in the following distributions to the selected events: for $B^0 \to K^0_S K^0_S$ events selected in § 5.1.3, we use ΔE, $M_{\rm bc}$ and the likelihood ratio ($\mathcal{R}$ defined in § 5.2.1) distributions. For $B^0 \to K^0_S K^+ K^-$ events selected in § 5.1.4, we use the distributions of ΔE, $M_{\rm bc}$ and the flavor-tag quality (r) interval region (ℓ defined in Table 5.2). Details on the maximum likelihood method can be found in Appendix A. The signal fraction and PDFs obtained with this fit are used in the unbinned maximum likelihood fit in CP measurements described in § 6.1 and § 6.2.

Based on the background study in § 5.2, we include signal and continuum background components in the likelihood for $B^0 \to K^0_S K^0_S$ decays. We additionally introduce $B\overline{B}$ background component into the likelihood for $B^0 \to K^0_S K^+ K^-$ decays.

Thus, the combined likelihood for the fit to $B^0 \to K^0_S K^0_S$ candidates is written as the product over i candidates,

$$\mathcal{L}(N_{\rm tot}, N_{\rm sig}) = \frac{e^{-N_{\rm tot}}}{N!} \prod_i [N_{\rm sig} \cdot \mathcal{P}_{{\rm sig},i}(\Delta E, M_{\rm bc}, \mathcal{R}) + (N_{\rm tot} - N_{\rm sig}) \cdot \mathcal{P}_{q\overline{q},i}(\Delta E, M_{\rm bc}, \mathcal{R})], \quad (5.17)$$

where $N_{\rm tot}$ and $N_{\rm sig}$ are the numbers of total and signal events and N is the number of candidates, while $\mathcal{P}_{{\rm sig},i}$ and $\mathcal{P}_{q\overline{q},i}$ are the PDFs for the i-th event for each component, respectively.

The combined likelihood for the fit to $B^0 \to K^0_S K^+ K^-$ candidates is written as

$$\mathcal{L}(N_{\rm sig}, N_{q\overline{q}}, N_{B\overline{B}}) = \frac{e^{-(N_{\rm sig}+N_{q\overline{q}}+N_{B\overline{B}})}}{N!} \prod_i [N_{\rm sig} \cdot \mathcal{P}_{{\rm sig},i}(\Delta E, M_{\rm bc}, \ell) + N_{q\overline{q}} \cdot \mathcal{P}_{q\overline{q},i}(\Delta E, M_{\rm bc}, \ell) + N_{B\overline{B}} \cdot \mathcal{P}_{B\overline{B},i}(\Delta E, M_{\rm bc}, \ell)], \quad (5.18)$$

where $N_{q\overline{q}}$ and $N_{B\overline{B}}$ are the numbers of continuum and $B\overline{B}$ background events and $\mathcal{P}_{B\overline{B},i}$ is the PDF for i-th event for each component.

After describing the PDFs of the signal and background components, the signal extractions are shown.

5.5.1 $B^0 \to K^0_S K^0_S$ Extraction

PDF Description

For the signal and continuum components (j), PDF is defined as the product of those for ΔE, $M_{\rm bc}$ and $\mathcal{R}$ as follows,

$$\mathcal{P}_j(\Delta E, M_{\rm bc}, \mathcal{R}) = P_j(\Delta E) \cdot P_j(M_{\rm bc}) \cdot P_j(\mathcal{R}), \quad (5.19)$$

where P denotes the factorized PDF.

For the signal component, ΔE ($M_{\rm bc}$) shape is modeled using a sum of two Gaussians (a single Gaussian) as described in § 5.1.3 and shown in Fig. 5.3. The signal ΔE and $M_{\rm bc}$ PDFs are defined as

$$P_{\rm sig}(\Delta E) = (1-f_{\rm tail})G(\Delta E;\mu,\sigma_{\rm main}) + f_{\rm tail}G(\Delta E;\mu,\sigma_{\rm tail}) \quad (5.20)$$
$$P_{\rm sig}(M_{\rm bc}) = G(M_{\rm bc};\mu,\sigma), \quad (5.21)$$

where $G(x;\mu,\sigma) \equiv 1/(\sqrt{2\pi}\sigma)e^{-(x-\mu)^2/2\sigma^2}$ is a single Gaussian function.

A binned histogram is employed for the $\mathcal{R}$ distribution. The Gaussian parameters and the $\mathcal{R}$ distribution is obtained using signal MC. The mean and the widths of the Gaussian PDFs are corrected using a $B^0 \to K^0_S\pi^+$ control sample to take into account the possible differences between data and MC as listed in Table 5.3. The corrected μ and σ values for the signal ΔE and $M_{\rm bc}$ PDFs are summarized in Table 5.4. The $\mathcal{R}$ shape is obtained from signal MC as shown in Fig. 5.18 (a).

Table 5.3: The correction factors between data and MC obtained using a $B^0 \to K^0_S\pi^+$ control sample. The widths for ΔE are combined from the main and tail widths.

	ΔE		$M_{\rm bc}$	
	$\mu(K^0_S\pi^+)_{\rm Data} - \mu(K^0_S\pi^+)_{\rm MC}$	$\frac{\sigma(K^0_S\pi+)_{\rm Data}}{\sigma(K^0_S\pi^+)_{\rm MC}}$	$\mu(K^0_S\pi^+)_{\rm Data} - \mu(K^0_S\pi^+)_{\rm MC}$	$\frac{\sigma(K^0_S\pi^+)_{\rm Data}}{\sigma(K^0_S\pi^+)_{\rm MC}}$
SVD1	-1.1 ± 1.5 MeV	1.17 ± 0.09	-0.03 ± 0.18 MeV	0.96 ± 0.07
SVD2	-1.4 ± 0.8 MeV	1.25 ± 0.05	0.41 ± 0.10 MeV	1.00 ± 0.03

Table 5.4: The corrected μ and σ values for the signal ΔE and $M_{\rm bc}$ PDFs.

ΔE	μ	$\sigma_{\rm main}$	$\sigma_{\rm tail}$	$f_{\rm tail}$
SVD1	0.0022 ± 0.0015	0.0175 ± 0.0013	0.0460 ± 0.0034	0.6947 ± 0.0065
SVD2	0.0020 ± 0.0008	0.0176 ± 0.0007	0.0460 ± 0.0020	0.7025 ± 0.0041
$M_{\rm bc}$	μ	σ		
SVD1	5.27928 ± 0.00018	0.00255 ± 0.00017		
SVD2	5.27975 ± 0.00010	0.00267 ± 0.00008		

For the continuum background component, the ΔE ($M_{\rm bc}$) shape is modeled as a first-order polynomial (an ARGUS [48] function [9]). The continuum ΔE and $M_{\rm bc}$ PDFs are defined as

$$P_{q\overline{q}}(\Delta E) = a \cdot (1 + c\Delta E) \quad (5.22)$$
$$P_{q\overline{q}}(M_{\rm bc}) = b \cdot M_{\rm bc}\sqrt{1-\left(\frac{M_{\rm bc}}{E_{\rm beam}}\right)^2}\exp\left\{\alpha\left[1-\left(\frac{M_{\rm bc}}{E_{\rm beam}}\right)^2\right]\right\}, \quad (5.23)$$

[9] Since $B^0 \to K^0_S K^0_S$ candidates are reconstructed accidentally from the continuum background, the PDFs for the continuum background component represent the distributions of the phase space.

where a and b are the normalization factors that can be calculated analytically. The ΔE slope, c, and ARGUS slope parameter, α, are free in the fit. The $\mathcal{R}$ background shape is obtained from a data sample in the sideband region, $M_{\rm bc} < 5.26$ GeV/c^2, as shown in Fig. 5.18 (b). The statistical uncertainty in each bin is included in the systematic errors.

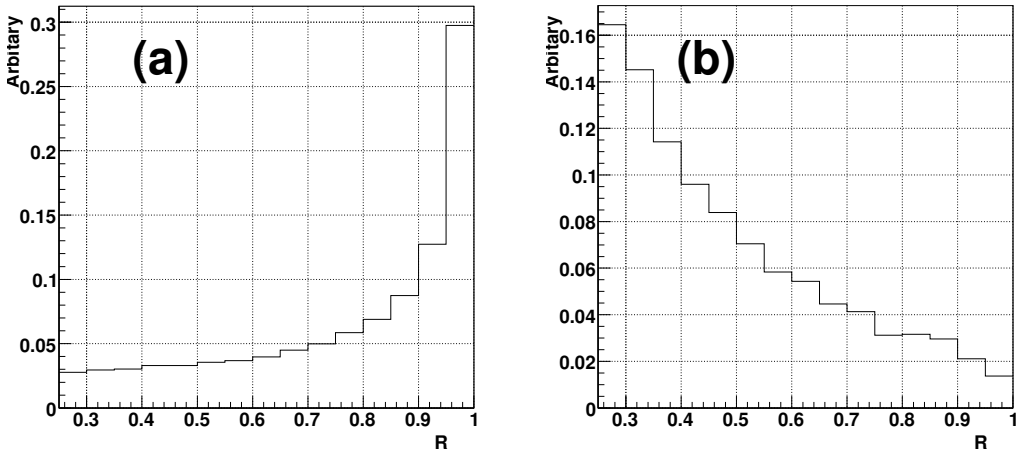

Figure 5.18: The binned histogram PDFs of the likelihood ratio $\mathcal{R}$, which is defined in § 5.2.1, for (a) signal events and (b) continuum events.

Possible correlations among ΔE, $M_{\rm bc}$ and $\mathcal{R}$ are found to be negligible for signal events from MC, and very small for continuum events from the data sideband. The effect of these extremely small correlations in the latter is taken into account in the systematic errors.

Fitted Result

The three-dimensional ΔE-$M_{\rm bc}$-$\mathcal{R}$ fit is performed to the 1307 (4648) candidates in SVD1 (2) separately, regardless of vertex information. In the fit, the signal and total yields and the parameters of the continuum ΔE-$M_{\rm bc}$ PDFs, c and α, are free. The fit yields 58 ± 11 signal events among 476 $B^0 \to K^0_S K^0_S$ candidate events in the signal region, where the error is statistical only. The fitted results of the parameters are summarised in Table 5.5. The projections of the ΔE, $M_{\rm bc}$ and $\mathcal{R}$ distributions for the candidate events are shown in Fig. 5.19. Small discrepancy in $\Delta E \sim -0.15$ GeV is seen due to the contribution from the $B\overline{B}$ background. We estimate this contribution as in 5.2.2 and take into account as a systematic error in CP asymmetry measurement.

Again, the event-by-event signal probability as a function of ΔE, $M_{\rm bc}$ and $\mathcal{R}$ obtained with this fit are used to in the unbinned maximum likelihood fit in CP measurements described in § 6.1.

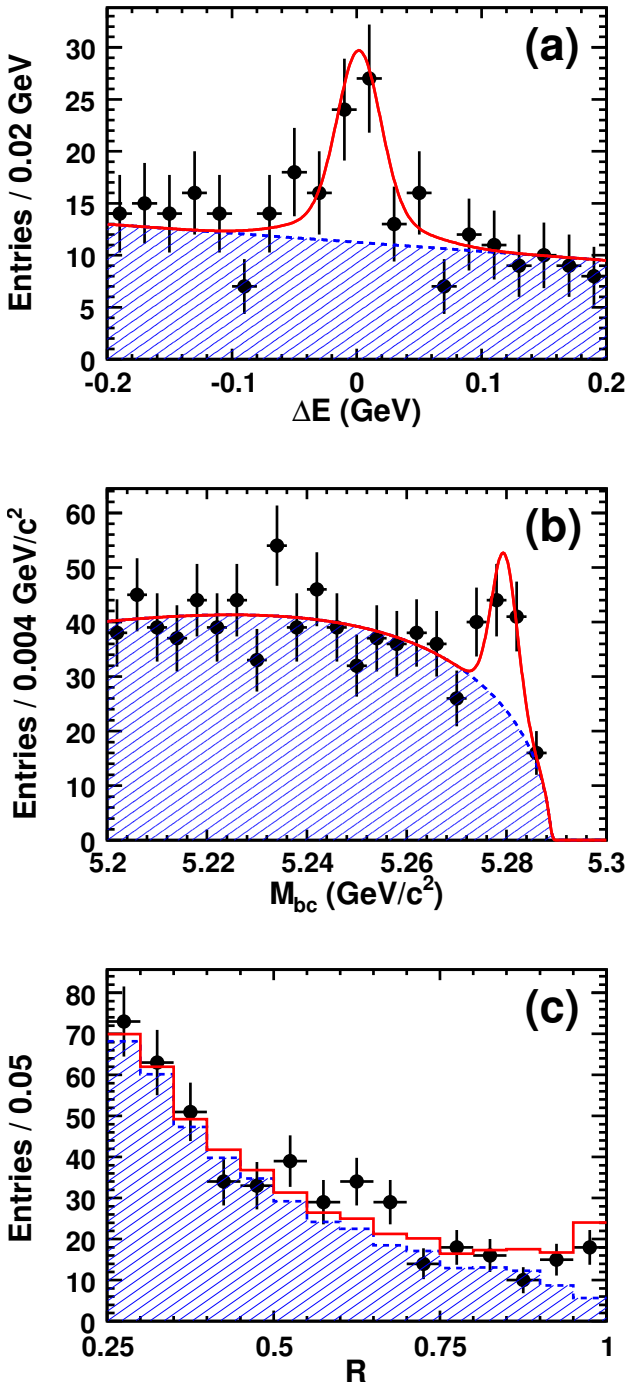

Figure 5.19: (a) ΔE, (b) $M_{\rm bc}$ and (c) $\mathcal{R}$ projections for $B^0 \to K^0_S K^0_S$ candidate events. (a) is enhanced by $\mathcal{R} > 0.6$ and $5.27 < \mathrm{GeV}/c^2$, (b) with $\mathcal{R} > 0.6$ and $|\Delta E| < 0.1$ GeV, and (c) in the signal region. The solid curves show the fit projections and the hatched areas show the background component. The points with error bars are the data.

Table 5.5: The obtained parameters in the $B^0 \to K^0_S K^0_S$ signal extraction fit.

	$N_{\rm tot}$	$N_{\rm sig}$	c (ΔE slope)	α (ARGUS parameter)
SVD1	1307 ± 36	13.0 ± 5.4	-0.78 ± 0.24	-25.4 ± 3.2
SVD2	4648 ± 69	45.9 ± 9.8	-0.77 ± 0.13	-18.8 ± 1.7

Branching Fraction Measurement of the $B \to K^0\overline{K^0}$ Decay

Since the statistics of the $B^0 \to K^0_S K^0_S$ decay is limited, the validity of event selection and the signal yield extraction is carefully checked by measuring the branching fraction of $B \to K^0\overline{K^0}$. Table 5.5.1 shows a summary of the obtained signal yields, $N_{\rm sig}$ and the reconstruction efficiencies, ϵ, estimated from $B^0 \to K^0_S K^0_S$ signal MC. The branching fraction of $B^0 \to K^0\overline{K^0}$ can be calculated using the weighted average [10],

$$\mathcal{B}(B^0 \to K^0\overline{K^0}) = \frac{2}{N(B\overline{B})} \sum_{i=\rm SVD1}^{\rm SVD2} \frac{N^i_{\rm sig}}{\epsilon_i(B^0 \to K^0_S K^0_S)}, \tag{5.24}$$

where $N(B\overline{B})$ is the number of $B\overline{B}$ events. The branching fraction of $B^0 \to K^0\overline{K^0}$ is obtained to be $(1.12 \pm 0.21) \times 10^{-6}$, which is consistent with previous measurements by both Belle [43] and BaBar [50].

Table 5.6: Signal yields ($N_{\rm sig}$) and reconstruction efficiencies (ϵ) for $B^0 \to K^0_S K^0_S$ in SVD1 and SVD2, respectively.

	Signal yields ($N_{\rm sig}$)	efficiency (ϵ) (%)
SVD1	13.0 ± 5.4	16.4
SVD2	45.9 ± 9.8	15.8

5.5.2 $B^0 \to K^0_S K^+ K^-$ Extraction

The procedure is nearly identical to that for $B^0 \to K^0_S K^0_S$. Because of the high statistics of the $B^0 \to K^0_S K^+ K^-$ decay channel, we can determine more parameters using data directly.

PDF Description

For the signal component, we use the ΔE and $M_{\rm bc}$ shapes defined in Eq. 5.20 and 5.21. The parameters, μ and $\sigma_{\rm main}$, of the ΔE PDF and σ of the $M_{\rm bc}$ PDF, are free in the fit. But

[10] $B^0 \to K^0\overline{K^0}$ includes only $B^0 \to K^0_S K^0_S$ and $B^0 \to K^0_L K^0_L$ assuming negligible CP-violation in K^0 system.

the ratio, $f_{\rm tail}$, and the width, $\sigma_{\rm tail}$, of the tail Gaussian in ΔE are fixed to the result of the fit to a $B^0 \to D[K^0_S\pi^-]\pi^+$ data control sample. The relative fraction of signal in each ℓ, which is the label for the interval of flavor quality r defined in § 5.4.2 and Table 5.2, is a free parameter in the fit.

For the continuum background component, the ΔE ($M_{\rm bc}$) shape is modeled with the function defined in Eq. 5.22 and 5.23 where the parameters, c and α, are free in the fit. The relative fraction of $q\overline{q}$ in each ℓ is a free parameter in the fit.

For the $B\overline{B}$ background component, the ΔE and $M_{\rm bc}$ PDFs are parameterized by two-dimensional binned histograms determined using generic B decay MC, excluding the B decays with $K^0_S K^+ K^-$ final states by MC-generated B decay channel information, as shown in Fig. 5.20. The relative fraction of $B\overline{B}$ in each ℓ is a fixed parameter in the fit.

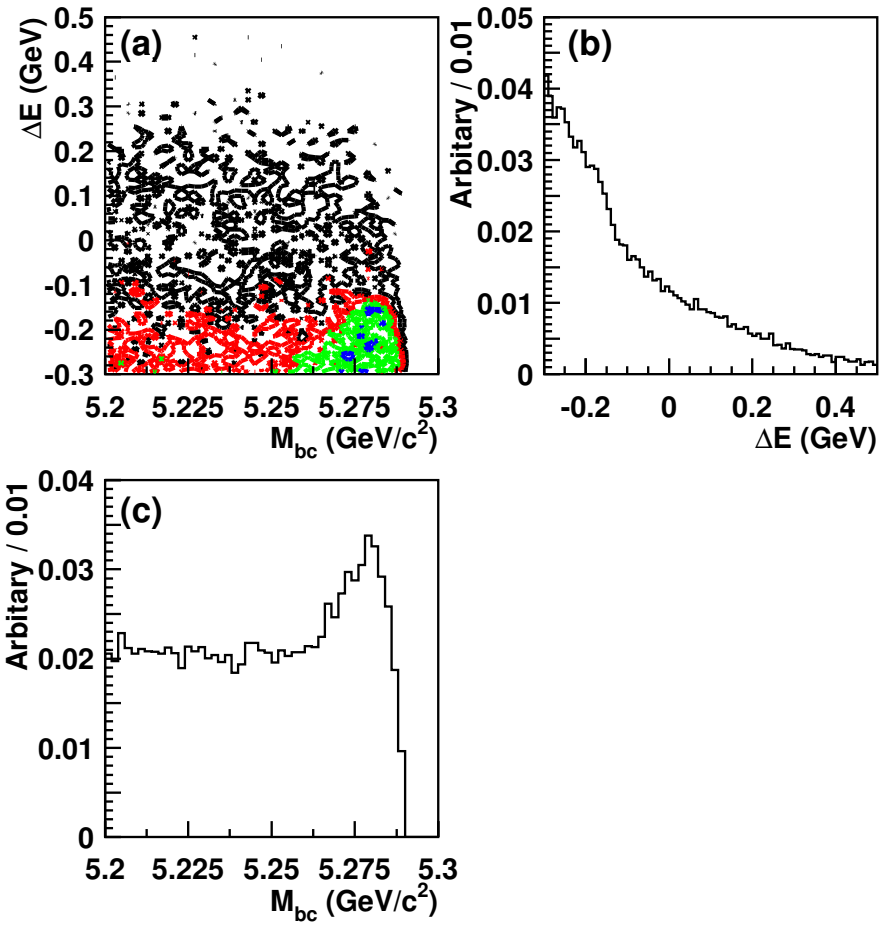

Figure 5.20: The $M_{\rm bc} - \Delta E$ two-dimensional binned histogram PDF $\mathcal{P}(\Delta E, M_{\rm bc})$ for $B\overline{B}$ background events.

Fitted Result

The three-dimensional ΔE-$M_{\rm bc}$-ℓ fit is performed to the 98982 candidates, combining SVD1 and SVD2. In the fit, the total signal, continuum and $B\overline{B}$ background yields are free parameters. The relative fraction for signal and $q\overline{q}$ in each ℓ is also free along with the parameters of the continuum ΔE-$M_{\rm bc}$ PDFs, c and α. The fit yields 1176 ± 51 signal events among 2333 $B^0 \to K^0_S K^+ K^-$ candidate events in the signal region, where the error is statistical only. The fitted results and the descriptions of the parameters are summarised in Table 5.7. The signal enhanced total projections of the ΔE, $M_{\rm bc}$ and ℓ distributions for the candidate events are shown in Fig. 5.21 and signal enhanced ΔE-$M_{\rm bc}$ projections in each ℓ are shown in Fig. 5.22 and 5.23. The average signal, $q\overline{q}$ and $B\overline{B}$ fractions in the signal ellipse are calculated to be $\sim$50 %, and $\sim$49 % and $\sim$1 %, respectively. Table 5.8 summarizes the signal, $q\overline{q}$ background and $B\overline{B}$ background yields and the purity in each ℓ in the signal region. The purity becomes better with larger ℓ because the b flavor of signal events can be determined with better quality than the continuum events, which are accidentally reconstructed.

Again, the event-by-event signal probability as a function of ΔE, $M_{\rm bc}$ and ℓ obtained with this fit are used to in the unbinned maximum likelihood fit in CP measurements described in § 6.2.

Table 5.7: The parameters determined in the $B^0 \to K^0_S K^+ K^-$ signal yield extraction fit where the errors are statistical only.

Parameter	Fitted result	Description
$N_{\rm sig}$	$1269.2^{+51.4}_{-50.7}$	The number of events
$N_{q\overline{q}}$	$92830.0^{+502.0}_{-508.7}$	for each component in the fitted region.
$N_{B\overline{B}}$	$4882.2^{+411.1}_{-400.9}$	
$\mu(\Delta E)$	0.00158 ± 0.00067	
$\sigma_{\rm main}(\Delta E)$	$0.01392^{+0.00072}_{-0.00070}$	
$f_{\rm tail}(\Delta E)$	0.22300 (fixed)	The parameters for the signal PDF $\mathcal{P}_{\rm sig}(\Delta E, M_{\rm bc})$.
$\sigma_{\rm tail}(\Delta E)$	0.041000 (fixed)	
$\mu(M_{\rm bc})$	5.2797 ± 0.0001	
$\sigma(M_{\rm bc})$	0.00258 ± 0.00009	
c	-0.726 ± 0.015	The parameters for the continuum PDF $\mathcal{P}_{q\overline{q}}(\Delta E, M_{\rm bc})$.
α	-22.85 ± 0.40	
$f^0_{\rm sig}$	0.229 ± 0.016	
$f^1_{\rm sig}$	0.162 ± 0.014	The relative fractions among ℓ
$f^2_{\rm sig}$	0.149 ± 0.013	of the signal component.
$f^3_{\rm sig}$	0.127 ± 0.012	$\sum_{\ell=0}^{6} f^\ell_{\rm sig} = 1$
$f^4_{\rm sig}$	0.102 ± 0.011	
$f^5_{\rm sig}$	$0.080^{+0.010}_{-0.009}$	
$f^0_{q\overline{q}}$	0.3157 ± 0.0016	
$f^1_{q\overline{q}}$	0.2228 ± 0.0014	The relative fractions among ℓ
$f^2_{q\overline{q}}$	0.1687 ± 0.0013	of the $q\overline{q}$ background component.
$f^3_{q\overline{q}}$	0.1047 ± 0.0010	$\sum_{\ell=0}^{6} f^\ell_{q\overline{q}} = 1$
$f^4_{q\overline{q}}$	0.1054 ± 0.0010	
$f^5_{q\overline{q}}$	0.0627 ± 0.0008	
$f^0_{B\overline{B}}$	0.2352 (fixed)	
$f^1_{B\overline{B}}$	0.2003 (fixed)	The relative fractions among ℓ
$f^2_{B\overline{B}}$	0.1926 (fixed)	of the $B\overline{B}$ background component.
$f^3_{B\overline{B}}$	0.1043 (fixed)	$\sum_{\ell=0}^{6} f^\ell_{B\overline{B}} = 1$
$f^4_{B\overline{B}}$	0.1025 (fixed)	
$f^5_{B\overline{B}}$	0.0702 (fixed)	

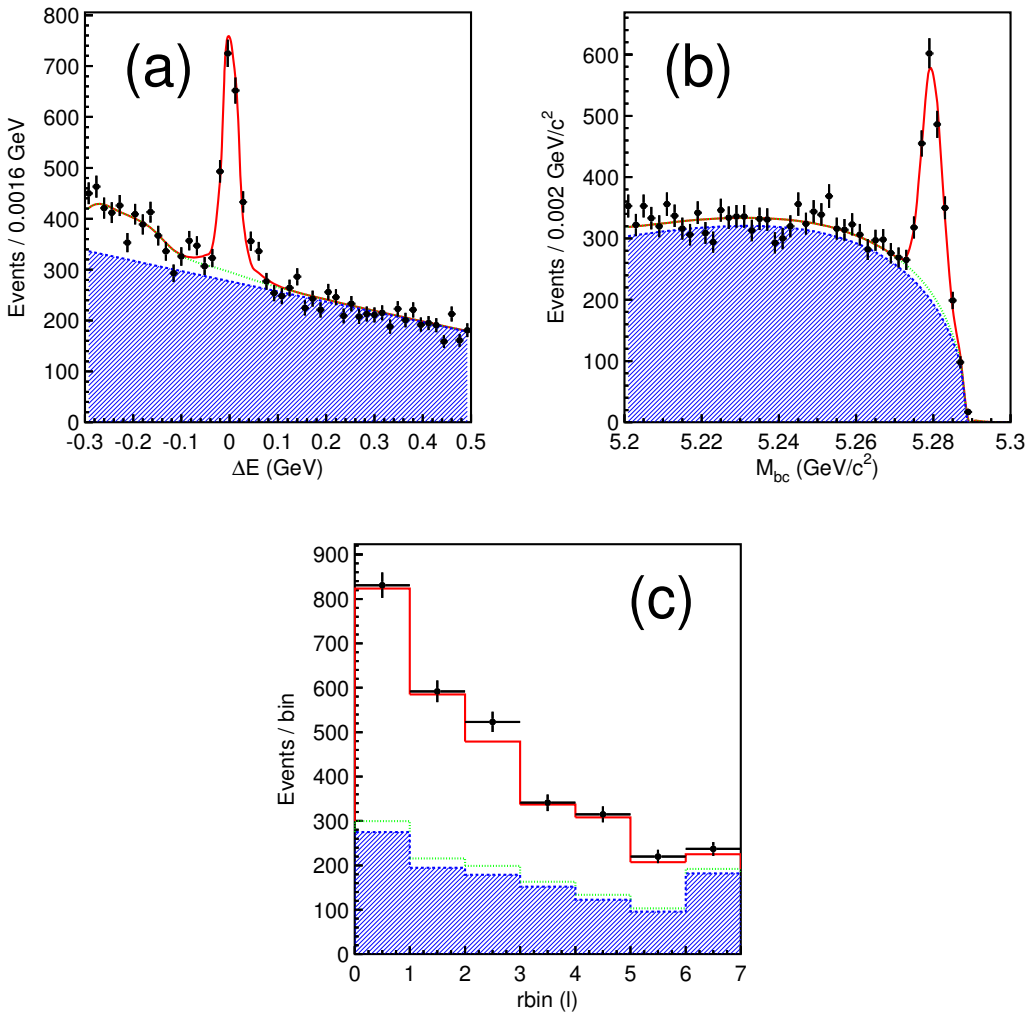

Figure 5.21: Signal enhanced total projections of (a) ΔE, (b) $M_{\rm bc}$ and (c) ℓ for the $B^0 \to K^0_S K^+ K^-$ candidate events. (a) is enhanced by 5.27 GeV/c^2 $< M_{\rm bc} <$ 5.30 GeV/c^2, (b) with $|\Delta E| < 0.05$ GeV, and (c) in the signal region. The solid curves show the fit projections, the hatched areas show the $q\overline{q}$ background component and the dotted curves show the total background contribution. The points with error bars are the data.

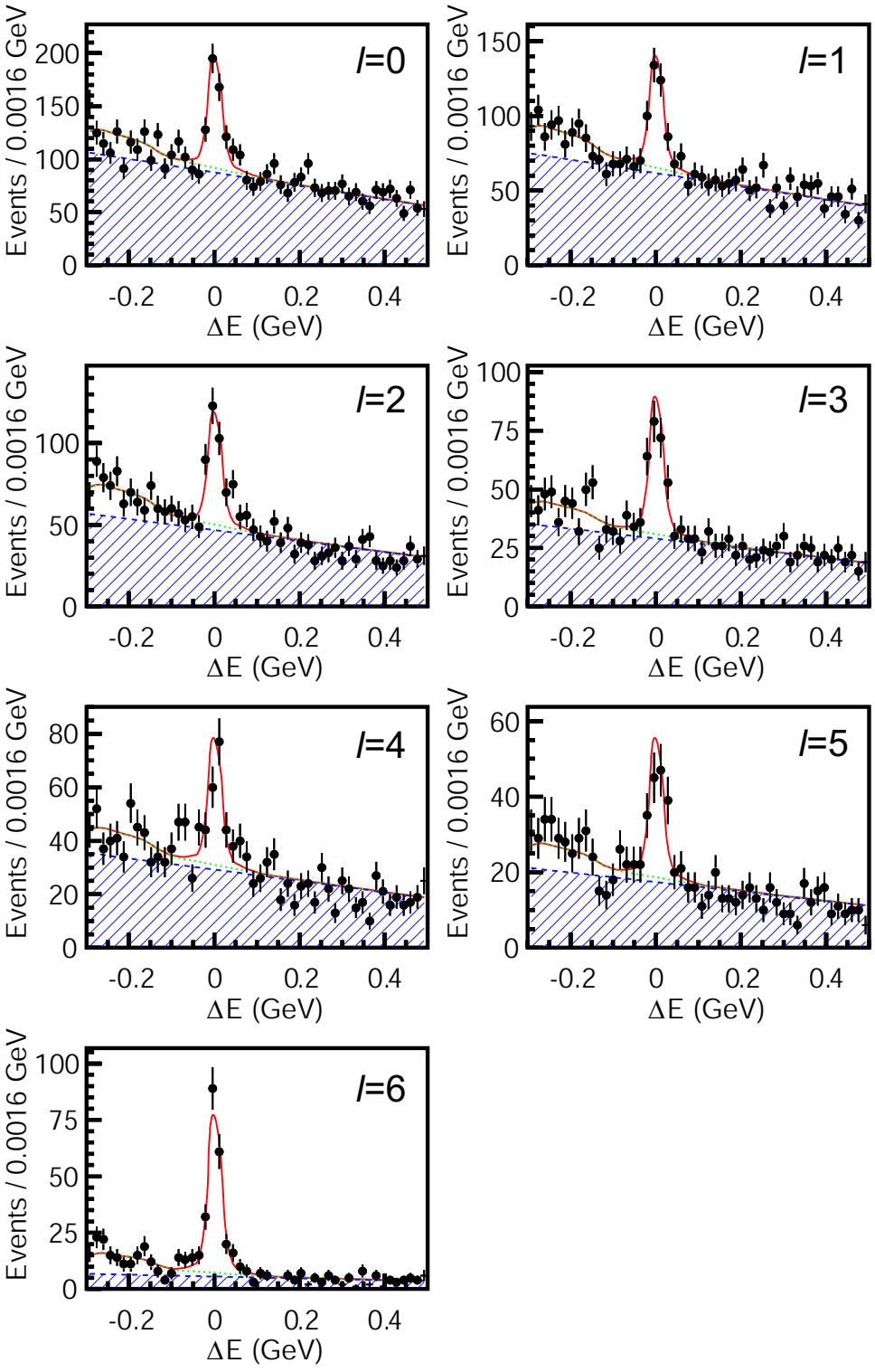

Figure 5.22: ΔE signal enhanced projection in each ℓ (from 0 to 6) for the $B^0 \to K^0_S K^+ K^-$ candidate events with 5.27 GeV/c^2 $< M_{\rm bc} <$ 5.30 GeV/c^2. The solid curves show the fit projections, the hatched areas show the $q\overline{q}$ background component and the dotted curves show the total background contribution. The points with error bars are the data.

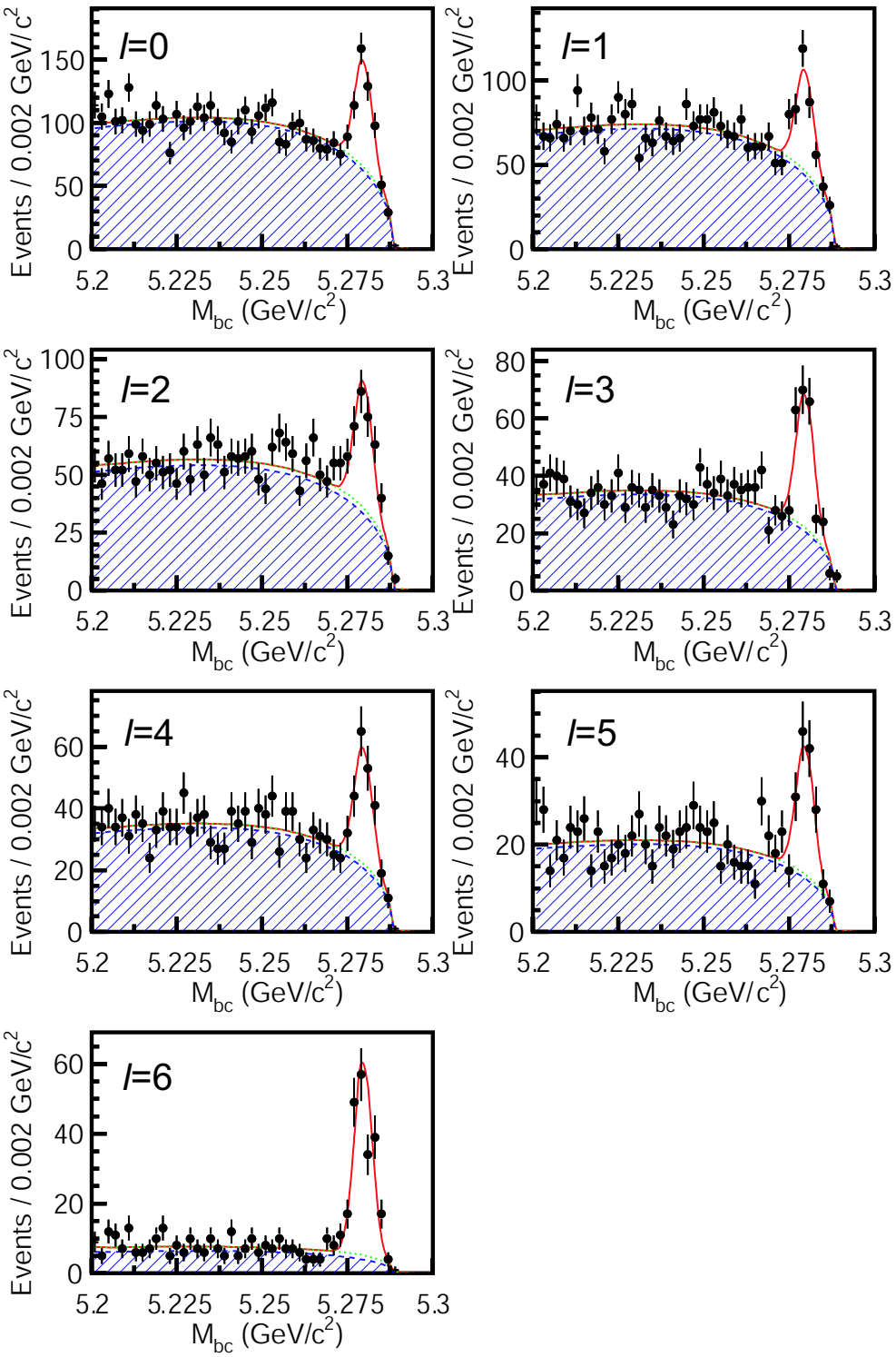

Figure 5.23: $M_{\rm bc}$ signal enhanced projection in each ℓ (from 0 to 6) for the $B^0 \to K^0_S K^+ K^-$ candidate events with $|\Delta E| < 0.05$ GeV. The solid curves show the fit projections, the hatched areas show the $q\overline{q}$ background component and the dotted curves show the total background contribution. The points with error bars are the data.

Table 5.8: Signal, $q\overline{q}$ and $B\overline{B}$ yields and the purity in each ℓ in the signal region.

ℓ	all	signal yield	$q\overline{q}$ yield	$B\overline{B}$ yield	purity
(a) 0	626	269.2	342.5	16.8	0.4283
(b) 1	447	190.5	241.6	14.3	0.4267
(c) 2	378	175.0	183.0	13.7	0.4708
(d) 3	267	149.0	113.6	7.4	0.5518
(e) 4	243	120.0	114.3	7.3	0.4972
(e) 5	164	93.6	68.1	5.0	0.5617
(f) 6	208	178.1	21.8	14.1	0.8325
sum	2332	1175.6	1084.7	71.3	0.5042

Chapter 6

Determination of CP Asymmetries

The time-dependent CP asymmetry parameters, $\mathcal{A}_{K^0_S K^0_S}$ and $\mathcal{S}_{K^0_S K^0_S}$, are determined using the unbinned maximum likelihood fit to the measured Δt and tagged b flavor for the selected $B^0 \to K^0_S K^0_S$ events in the signal region.

The time-dependent Dalitz plot analysis, described in § 4, is employed for the $B^0 \to K^0_S K^+ K^-$ decay. To treat the decay channels that have the same $B^0 \to K^0_S K^+ K^-$ final state including the interference between them, we simultaneously fit the Dalitz distribution, and Δt and the tagged b flavor distributions. We extract CP asymmetry parameters, $\mathcal{A}_{CP}$ and ϕ_1, as well as the relative decay amplitudes and phases.

After describing an event-by-event PDF to form the likelihood, the fitted results are shown. We estimate the systematic uncertainties of these measurements and perform various checks to validate the analysis procedures.

6.1 Determination of CP Asymmetries in the $B^0 \to K^0_S K^0_S$ Decay

6.1.1 Event-by-Event PDF for Time-Dependent CP Fit

For signal events, the Δt distribution of Eq. 2.47, modified to include the effects of incorrect flavor assignment described in § 5.4, is used. The distribution is convolved with the Δt detector resolution function, $R_{\rm sig}$ described in § 5.3.3 and is given by,

$$\mathcal{P}_{\rm sig}(\Delta t, \ell, q_{\rm tag}) = \frac{e^{-|\Delta t|/\tau_{B^0}}}{4\tau_{B^0}} \Big[(1 - q_{\rm tag}\Delta w_\ell) + \\ -q_{\rm tag} \cdot (1 - 2w_\ell)(\mathcal{A}_{K^0_S K^0_S} \cos\Delta m_d \Delta t + \mathcal{S}_{K^0_S K^0_S} \sin\Delta m_d \Delta t \Big] \otimes R_{\rm sig}, \tag{6.1}$$

where the symbol $\otimes$ indicates the convolution.

To determine the CP asymmetry parameters, $\mathcal{A}_{K^0_S K^0_S}$ and $\mathcal{S}_{K^0_S K^0_S}$ from the selected events, we include the contribution from the background component. The following likelihood value for each event, i, is calculated,

$$\begin{aligned}\mathcal{P}(\Delta t_i; \mathcal{S}_{K^0_S K^0_S}, \mathcal{A}_{K^0_S K^0_S}) = \\ (1-f_{\rm ol})\int_{-\infty}^{\infty} d\Delta t' \{ f_{K^0_S K^0_S}(\Delta E_i, M_{{\rm bc},i}, \mathcal{R}_i)\mathcal{P}_{\rm sig}(\Delta t', \ell_i, q_{{\rm tag},i}) R_{\rm sig}(\Delta t_i - \Delta t') \\ +[1-f_{K^0_S K^0_S}(\Delta E_i, M_{{\rm bc},i}, \mathcal{R}_i)]\mathcal{P}_{q\overline{q}}(\Delta t'; q_{\rm tag}, \mathcal{A}_{q\overline{q}}) R_{q\overline{q}}(\Delta t_i - \Delta t')\} \\ +f_{\rm ol}\mathcal{P}_{\rm ol}(\Delta t_i), \end{aligned} \tag{6.2}$$

where $\mathcal{P}_{\rm ol}(\Delta t)$ represents the outlier component described in § 5.3.3. The fraction, $f_{K^0_S K^0_S}$, is the event-by-event signal fraction as a function of ΔE, $M_{\rm bc}$ and $\mathcal{R}$, as determined by the signal extraction fit in § 5.5.1. The r dependence of $f_{K^0_S K^0_S}$ is also taken into account using signal MC (sideband events) for the signal (background) component, respectively.

For continuum background events, the Δt distribution, $P_{q\overline{q}}(\Delta t)$, is parameterized as the summation of a lifetime function with a lifetime of τ which represents the finite lifetime of the daughter D mesons produced in continuum, and a Dirac's δ function that represents the Δt distribution of short-lived particles,

$$P_{q\overline{q}}(\Delta t) = \left[(1-f^{trk}_{\delta})\frac{1}{2\tau}\exp\left(-\frac{|\Delta t - \mu|}{\tau}\right) + f^{trk}_{\delta}\delta^{\rm Dirac}(\Delta t - \mu)\right]. \tag{6.3}$$

In addition, $R_{q\overline{q}}(\Delta t)$ is introduced to describe the smearing effects as a sum of two Gaussians,

$$\begin{aligned} R_{q\overline{q}}(\Delta t) &= (1-f^{trk}_{\rm tail})G\left(\Delta t; 0, s^{trk}_{\rm main}\sqrt{\sigma^2_{\rm CP}+\sigma^2_{\rm tag}}\right) \\ &\quad + f^{trk}_{\rm tail}G\left(\Delta t; 0, s^{trk}_{\rm tail}\sqrt{\sigma^2_{\rm CP}+\sigma^2_{\rm tag}}\right), \end{aligned} \tag{6.4}$$

where $\sigma_{\rm CP}$ and $\sigma_{\rm tag}$ are the estimated position errors in the vertex reconstruction of the CP side and tag side, respectively. The superscript of "trk" denotes a category of the vertices: single or multi. We use trk = multi for events where vertices in both the CP and tag sides are reconstructed with multiple tracks, and trk = sgl for all other events.

Taking all the contributions above into account, the Δt PDF, $P_{q\overline{q}}(\Delta t)$, for the continuum background is parameterized as

$$\mathcal{P}_{q\overline{q}}(\Delta t'; q_{\rm tag}, \mathcal{A}_{q\overline{q}}) = P_{q\overline{q}}(\Delta t)\ P_{q\overline{q}}(q_{\rm tag}, \mathcal{A}_{q\overline{q}}), \tag{6.5}$$

$$P_{q\overline{q}}(q_{\rm tag}, \mathcal{A}_{q\overline{q}}) = \frac{1+q_{\rm tag}\mathcal{A}_{q\overline{q}}}{2}, \tag{6.6}$$

All the parameters in $P_{q\overline{q}}(\Delta t)$ and $R_{q\overline{q}}(\Delta t)$ are determined from sideband events as shown in Fig. 6.1 and as summarized in Table 6.1. The parameter $\mathcal{A}_{q\overline{q}}$ accounts for a possible flavor asymmetry in the continuum background, which might be originated from charge asymmetry

in PID in flavor tagging or from effect of weak interaction in $e^+e^- \to q\overline{q}$ and polar angle dependence of PID performance. In the nominal fit, we assume no flavor asymmetry in the continuum, however, the effect of a non-zero $\mathcal{A}_{q\overline{q}}$ value is accounted for in the systematic error study.

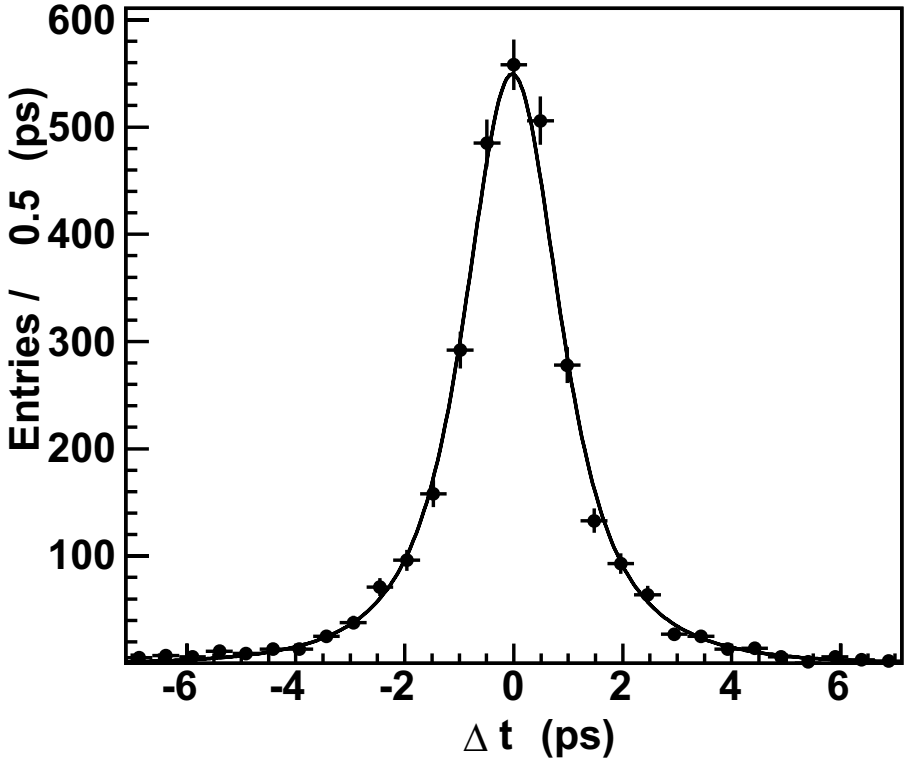

Figure 6.1: The Δt distribution and the fitted result for sideband events.

To improve the statistical sensitivity to $\mathcal{A}_{K^0_S K^0_S}$, we also use candidate events having no Δt information, where B vertices are not reconstructed because both K^0_S daughters decay outside the SVD. For these events, the PDF of Eq. 6.2 is integrated over Δt as follows,

$$\begin{aligned} \mathcal{P}(\mathcal{A}_{K^0_S K^0_S}) &= f_{K^0_S K^0_S}(\Delta E_i, M_{\mathrm{bc},i}, \mathcal{R}_i)\mathcal{P}_{\mathrm{sig}}(\ell_i, q_{\mathrm{tag},i}) \\ &+ [1 - f_{K^0_S K^0_S}(\Delta E_i, M_{\mathrm{bc},i}, \mathcal{R}_i)]\mathcal{P}_{q\overline{q}}(q_{\mathrm{tag}}, \mathcal{A}_{q\overline{q}}). \end{aligned} \tag{6.7}$$

The time-integrated signal PDF becomes

$$\mathcal{P}_{\mathrm{sig}}(\ell, q_{\mathrm{tag}}) = \frac{1}{2}[1 - q_{\mathrm{tag}}\Delta w_\ell + q_{\mathrm{tag}}(1 - 2w_\ell)(1 - 2\chi_d)\mathcal{A}_{K^0_S K^0_S}], \tag{6.8}$$

where $\chi_d = 0.186 \pm 0.004$ [35] is the time-integrated $B^0\overline{B^0}$ mixing probability defined as $\chi_d = x^2/[2(1+x^2)]$ where $x = \Delta m_d \tau_{B^0}$.
The time-integrated continuum PDF becomes 1/2 based on Eq. 6.6 with zero $\mathcal{A}_{K^0_S K^0_S}$.

Table 6.1: Parameters of the continuum background Δt PDF.

parameter	single	multi
f_δ	0.42±0.18	0.50±0.07
μ (ps)	0.042 ± 0.024	
τ (ps)	1.13 ± 0.11	
$s_{\rm main}$ (ps)	1.08 ± 0.15	1.076 ± 0.057
$s_{\rm tail}$ (ps)	12.3 ± 5.6	14.4 ± 2.5
$f_{\rm tail}$	0.42 ± 0.18	0.50 ± 0.07

6.1.2 Fitted Result

The CP violating parameters, $\mathcal{A}_{K^0_S K^0_S}$ and $\mathcal{S}_{K^0_S K^0_S}$, are determined by maximizing the likelihood function, $L = \prod P_i$, where the product is over all events. The fit to 476 $B^0 \to K^0_S K^0_S$ candidate events, in which 216 candidate events have no Δt information, yields

$$\mathcal{A}_{K^0_S K^0_S} = -0.38 \pm 0.38\ (\text{stat}) \pm 0.05\ (\text{syst}), \text{ and} \quad (6.9)$$

$$\mathcal{S}_{K^0_S K^0_S} = -0.38^{+0.69}_{-0.77}\ (\text{stat}) \pm 0.09\ (\text{syst}), \quad (6.10)$$

where the systematic errors are described below.

The Δt and $B^0\overline{B^0}$ raw asymmetry distributions are shown in Fig. 6.2. Raw asymmetry in each Δt interval is defined as $(N_+ - N_-)/(N_+ + N_-)$, where $N_{+(-)}$ is the number of candidate events with $q_{\rm tag} = +1(-1)$.

6.1.3 Systematic Uncertainty

The sources of systematic uncertainties and their contributions are summarized in Table 6.2 and we describe each source briefly in the following. The total systematic uncertainty is obtained by summing all these contributions in quadrature. The systematic error for $\mathcal{A}_{K^0_S K^0_S}$ is primarily due to the tag-side interference, while the systematic error for $\mathcal{S}_{K^0_S K^0_S}$ is primarily due to uncertainties in the descriptions of the Δt resolution function $R_{\rm sig}(\Delta t)$, the signal fraction $f_{K^0_S K^0_S}$ and the background Δt PDF.

The parameters included in the fit are varied by 1 σ (2 σ) from their central values if they are determined with data (MC). The fits are repeated and the difference from the nominal fitted result is quoted as a systematic error. The uncertainties originating from the Δt resolution function and vertex reconstruction are obtained from a 60 times larger statistics $B^0 \to J/\psi K^0_S$ control sample with vertices determined using only K^0_S. If the fit were performed to $B^0 \to K^0_S K^0_S$ data while varying the parameters of the Δt resolution function or vertex requirements, the fit differences could be overestimated as they contain the statistical fluctuation of a small data set.

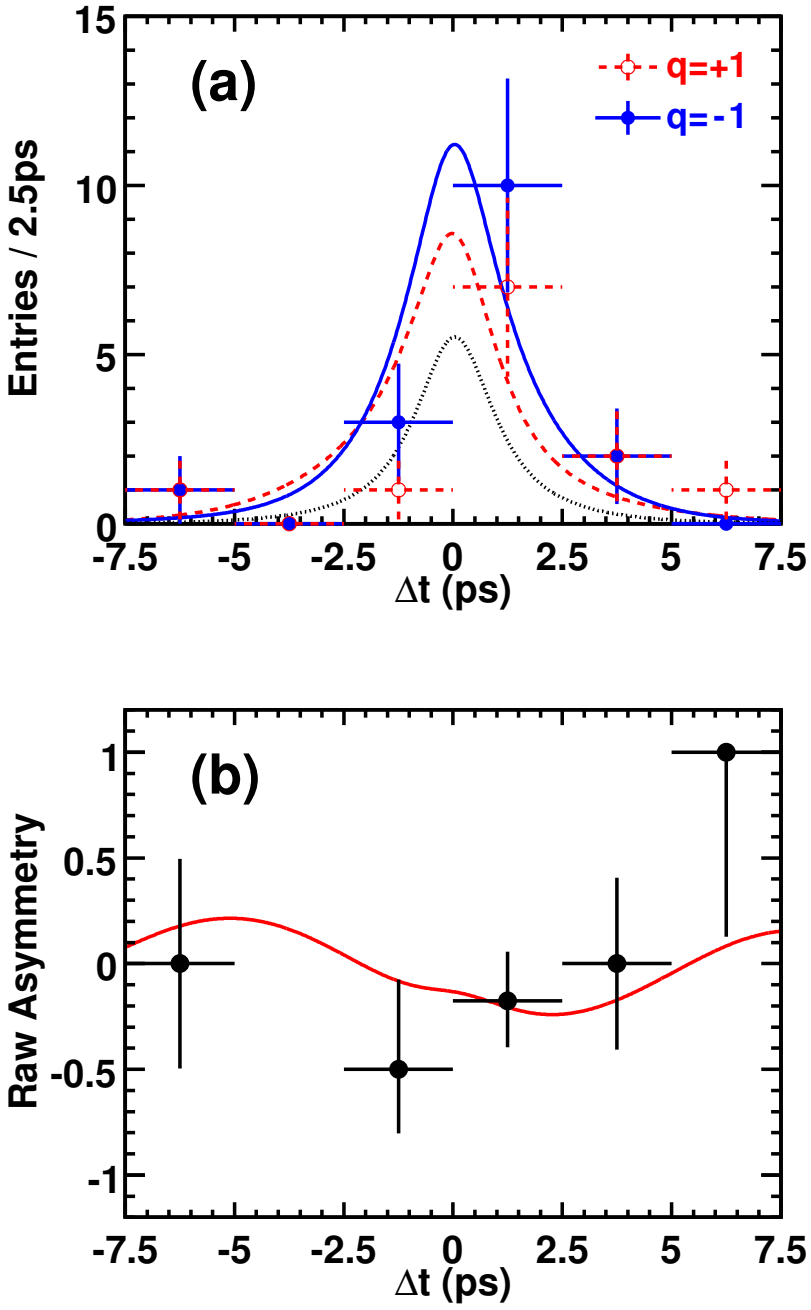

Figure 6.2: (a) Δt distribution and (b) raw asymmetry for the $B^0 \to K^0_S K^0_S$ candidate events in the signal region with good tags, $r > 0.5$, and $\mathcal{R} > 0.6$. Raw asymmetry in each Δt interval is defined as $(N_+ - N_-)/(N_+ + N_-)$, where $N_{+(-)}$ is the number of candidate events with $q_{\rm tag} = +1(-1)$. In (a), the solid and dashed curves show the fitted results with $q_{\rm tag} = \pm 1$, respectively. The dotted curve shows the background component. In (b), the solid curve shows the fit projection.

Table 6.2: Summary of the systematic uncertainties.

source	$\mathcal{A}_{K^0_S K^0_S}$	$\mathcal{S}_{K^0_S K^0_S}$
Wrong tag fraction	± 0.010	± 0.024
Physics parameters	± 0.007	± 0.014
Δt resolution function	± 0.003	± 0.056
Background Δt PDF	± 0.020	± 0.036
Signal fraction	± 0.027	± 0.043
Possible fit bias	± 0.007	± 0.017
Vertex reconstruction	± 0.020	± 0.009
Tag-side interference	± 0.034	± 0.004
total	± 0.054	± 0.086

Wrong Tag Fraction

Each wrong tag fraction, w_ℓ, and difference, Δw_ℓ, in Table 5.2 are varied sequentially by $\pm 1\sigma$ in the fit, and we add the CP-violating parameter deviations in quadrature.

Physics Parameters

The physics parameters, τ_{B^0} and Δm_d, are given as $(1.530 \pm 0.009) \times 10^{-12}$ s and $(0.507 \pm 0.005) \times 10^{12}$ $\hbar \mathrm{s}^{-1}$, respectively, according to the world average values given in PDG [35]. These are fixed in the nominal fit and varied by their respective errors to estimate systematic errors.

Δt Resolution Function

Each Δt resolution function (parameterization) parameter that is obtained by data (MC) is varied by ± 1 σ (± 2 σ) from the nominal value and the deviations of the fitted results are summed in quadrature.

Background Δt PDF

For the continuum Δt PDF, each parameter listed in Table 6.1 is varied by its error in Table 6.1 and the fit differences are summed in quadrature. The $q\overline{q}$ background PDF described in Eq. 6.6 assumes no flavor asymmetry with $\mathcal{A}_{q\overline{q}} = 0$. The asymmetry, $\mathcal{A}_{q\overline{q}}$, is varied by 0.035, which is obtained from a CP asymmetry fit to the sideband data. The fit difference is taken as a systematic error.

There is a possible contribution from $B\overline{B}$ background in the CP measurement. According

to a 40 times luminosity charmless and 3 times luminosity charmed $B\overline{B}$ MC sample, the expected number of $B\overline{B}$ background with (without) vertex information is estimated to be 0.3 ± 0.1 (0.3 ± 0.1) events. We include a new component in the Δt PDF, Eq. 6.2, for $B\overline{B}$ background using the same signal CP PDF. However, the CP asymmetries for the $B\overline{B}$ background component are varied from -1 to 1 and the differences taken as a systematic error.

Signal Fraction

The parameters defining the signal ΔE and $M_{\rm bc}$ shapes obtained in the signal extraction fit are varied by $\pm 1\sigma$. The number of events, N_i, in each bin of the $\mathcal{R}$ histograms, i, is varied by $\pm\sqrt{N_i}$ sequentially, and the CP asymmetry fit differences are taken as systematic uncertainties.

Possible Fit Bias

Two sources of bias are considered. The reconstruction bias is estimated using large statistics GEANT-based signal MC samples and the fit bias is estimated using a large number of pseudo-experiments. The details are described in § 6.1.4.

Vertex Reconstruction

Systematic errors due to vertex reconstruction are estimated by varying the selection criteria for the tracks and vertices.

- IP constraint
  In the B decay vertex reconstruction, the constraint of the transverse component of the IP is smeared by 21 μm to account for the finite flight length of the B meson in that direction. The systematic errors are estimated by varying the smearing effects by ± 10 μm and repeating the fit.

- Tag-side vertexing
  In the B decay vertex reconstruction on the tag side, the charged tracks with $dr <$ 0.05 cm and $\sigma_z < 0.05$ cm are selected. The systematic errors are estimated by varying these requirements by ± 0.01 cm and repeating the fit.

- Vertex reconstruction quality
  The B decay vertices reconstructed with good quality, $\xi < 250$, are used. The systematic errors are estimated by changing this ξ requirement by ± 50 and repeating the fit.

- $|\Delta t|$ requirement
  In the nominal fit, the events with $|\Delta t|$ shorter than 70 ps are selected. The associated systematic error is estimated by varying this Δt range by ± 30 ps and repeating the fit.

- Tracking error corrections
  The tracking errors depend on the transverse momentum of the track, which induces bias in the vertexing errors. To correct this bias, the tracking errors are scaled depending on the track parameters where these scaling factors are obtained by using cosmic ray data and MC. The systematic error is estimated by repeating the fit to the data sample without applying the scale factors.

- Bias in Δz measurement
  Small biases in the Δz measurement are observed in $e^+e^- \to \mu^+\mu^-$ samples. The systematic errors are estimated by applying correction functions designed to account for these observed biases and repeating the fit.

- SVD imperfect alignment
  Due to imperfect SVD alignment, a worse impact parameter resolution is observed in data when compared to MC. The systematic error due to this is determined using a MC sample that includes artificial misalignment effects so that it reproduces the worse impact parameter resolution of data.

Tag-Side Interference

As shown in Eq. 2.43, the effects of interference between CKM-favored and CKM-suppressed $B \to D$ transitions in the $f_{\rm tag}$ final states [49] are ignored in the nominal fit but are taken into account here. Pseudo-experiments are generated with and without tag-side interference and the difference is taken as a systematic error.

6.1.4 Validity Checks

Various checks are performed to validate each analysis procedure. The details are described as follows.

B^0 Lifetime Measurement in the $B^0 \to K^0_S K^0_S$ Decay

To check the validity of the Δt resolution function and an event-by-event signal fraction, the fit to extract the B^0 lifetime from the Δt distribution is performed using the same unbinned maximum likelihood fit integrated over flavor. The signal PDF simplifies to

$$\mathcal{P}(\Delta t) = \frac{1}{2\tau_{B^0}} \exp(-\frac{|\Delta t|}{\tau_{B^0}}). \tag{6.11}$$

The B^0 lifetime in $B^0 \to K^0_S K^0_S$ is measured to be $\tau_{B^0} = 1.58 \pm 0.44$ ps, which is consistent with the world average [35].

Linearity Check with Signal MC

To check $B^0 \to K^0_S K^0_S$ signal events for possible reconstruction bias, GEANT-based signal MC is generated with various mixing-induced CP asymmetry parameters, $\mathcal{S}_{K^0_S K^0_S}$, and the consistency between the generated CP asymmetry and the fitted one is tested. The statistics of each signal MC sample correspond to 200 times the data size. The results, shown in Fig. 6.3, indicates no evidence for the deviation from the expected $\mathcal{A}_{K^0_S K^0_S}$ and $\mathcal{S}_{K^0_S K^0_S}$.

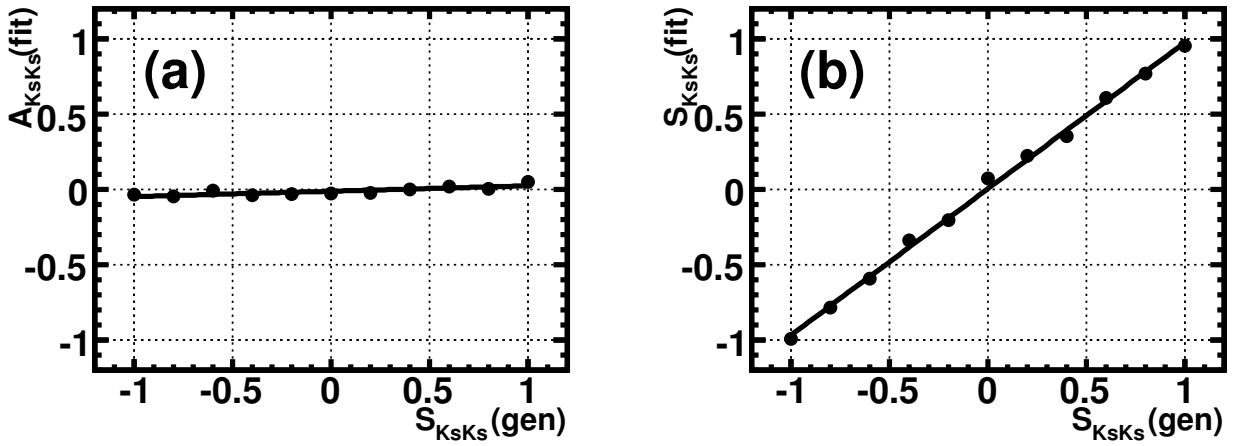

Figure 6.3: Linearity test using GEANT-based MC simulation for (a) $\mathcal{A}_{K^0_S K^0_S}$(fit) vs. $\mathcal{S}_{K^0_S K^0_S}$(gen) and (b) $\mathcal{S}_{K^0_S K^0_S}$(fit) vs. $\mathcal{S}_{K^0_S K^0_S}$(gen). The solid black lines show the fitted results.

Fit Bias Check with Pseudo-Experiments

The fit bias of the total PDF is checked by generating pseudo-experiments based on the total PDF. First, 1000 sets of pseudo-experiments containing the same number of events as data are generated without CP violation. Then, the CP measurement is repeated for each pseudo-experiment.

The mean of the residual distribution, defined as the difference between the fitted and generated CP parameter, is the fit bias. The region around the mean of the error distribution gives an expectation on the statistical error with the current sample size. Table 6.3 shows the expected error for each CP parameter. The expected statistical error from the pseudo-experiments and the statistical error in Eq. 6.10 with the data analysis agree well.

If the asymmetric errors are obtained correctly in the fit, the pull distributions, defined as the residual normalized by the fit error, should follow Gaussian distributions with a mean

of zero and a width of unity. Figure 6.4 shows the pull distributions of $\mathcal{A}_{K^0_S K^0_S}$ and $\mathcal{S}_{K^0_S K^0_S}$, respectively. The results of a fit to the pull distributions are given in Table 6.4, which demonstrates that the errors have been determined correctly.

Table 6.3: The estimated error for $\mathcal{A}_{K^0_S K^0_S}$ and $\mathcal{S}_{K^0_S K^0_S}$ from pseudo-experiments.

$\delta\mathcal{A}_{K^0_S K^0_S}$	$\delta\mathcal{S}_{K^0_S K^0_S}$
0.37±0.04	0.8±0.2

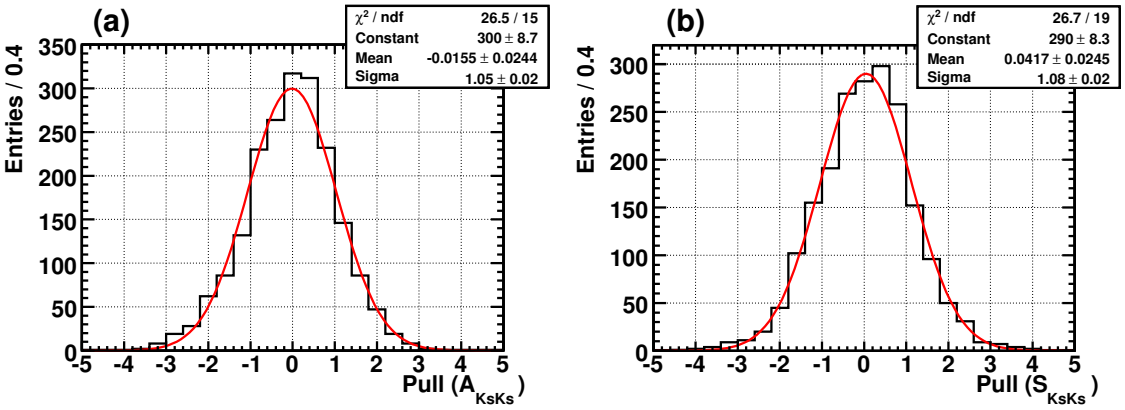

Figure 6.4: The pull distributions using pseudo-experiments for (a) $\mathcal{A}_{K^0_S K^0_S}$ and (b) $\mathcal{A}_{K^0_S K^0_S}$. The solid red lines show the fitted results onto the Gaussian distribution.

Table 6.4: The mean and width of the pull distributions for $\mathcal{A}_{K^0_S K^0_S}$ and $\mathcal{S}_{K^0_S K^0_S}$ from pseudo-experiments.

	$\mathcal{A}_{K^0_S K^0_S}$	$\mathcal{S}_{K^0_S K^0_S}$
μ	0.049±0.024	0.022±0.024
σ	1.07±0.02	1.04±0.02

CP Asymmetry Measurement in the non-CP-violating high statistics Control Sample Decay

To check the validity of the overall analysis procedure, the control sample decay is studied because it has higher statistics and no expected CP asymmetry. We extract 1993 ± 53 $B^+ \to K^0_S\pi^+$ events and only use the K^0_S to reconstruct the B^0 decay vertex. Applying the same fit procedure, the CP asymmetries are obtained to be $\mathcal{A}_{K^0_S\pi^+} = +0.014 \pm 0.063$ and $\mathcal{S}_{K^0_S\pi^+} = -0.13 \pm 0.13$, which is consistent with no CP asymmetry.

6.2 Determination of CP Asymmetries in the $B^0 \to K^0_S K^+ K^-$ Decay

In this section, we describe the PDFs and fitted results of the measurements of CP asymmetries in the $B^0 \to K^0_S K^+ K^-$ decay. We list the additional systematic uncertainties due to the Dalitz plot and provide validity tests.

6.2.1 Event-by-Event PDF for Time-Dependent Dalitz-Plot CP Fit

To determine the time-dependent Dalitz plot parameters, the event-by-event PDF is defined as follows,

$$\mathcal{P}(\vec{x}) = f_{\rm sig}\mathcal{P}_{\rm sig}(\vec{x}) + f_{q\overline{q}}\mathcal{P}_{q\overline{q}}(\vec{x}) + f_{B\overline{B}}\mathcal{P}_{B\overline{B}}(\vec{x}), \tag{6.12}$$

where $\mathcal{P}_{\rm sig}$, $\mathcal{P}_{q\overline{q}}$, and $\mathcal{P}_{B\overline{B}}$ are PDFs for signal, continuum background and $B\overline{B}$ background, respectively, and $f_{\rm sig}$, $f_{q\overline{q}}$ and $f_{B\overline{B}}$ are the corresponding fractions which satisfy the condition, $f_{\rm sig} + f_{q\overline{q}} + f_{B\overline{B}} = 1$. The vector, $\vec{x}$, represents a set of event-by-event variables, $\vec{x} = (m', \theta', \Delta t, q_{\rm tag}, \Delta E, M_{\rm bc}, \ell)$, where the indicator, ℓ, represents the region of the MC-determined flavor-tag dilution factor (r) as defined in Table 5.2. Events having large Δt are taken into account by including the outlier PDF, $f_{\rm ol}\mathcal{P}_{\rm ol}$.

The fraction of each signal and background component, f_m (m=sig, $q\overline{q}$, $B\overline{B}$) is calculated as follows,

$$f_m = \frac{N_m \cdot f^\ell_m \cdot \mathcal{P}_m(\Delta E, M_{\rm bc})}{N_{\rm sig} \cdot f^\ell_{\rm sig} \cdot \mathcal{P}_{\rm sig}(\Delta E, M_{\rm bc}) + N_{q\overline{q}} \cdot f^\ell_{q\overline{q}} \cdot \mathcal{P}_{q\overline{q}}(\Delta E, M_{\rm bc}) + N_{B\overline{B}} \cdot f^\ell_{B\overline{B}} \cdot \mathcal{P}_{B\overline{B}}(\Delta E, M_{\rm bc})}, \tag{6.13}$$

where $N_{\rm sig}$, $N_{q\overline{q}}$ and $N_{B\overline{B}}$ are the extracted yields of signal, continuum and $B\overline{B}$ background events, $f^\ell_{\rm sig}$, $f^\ell_{q\overline{q}}$ and $f^\ell_{B\overline{B}}$ are the relative fractions of the signal, $q\overline{q}$ and $B\overline{B}$ components in ℓ. Note that these yields, relative fractions and respective PDFs as a function of ΔE and $M_{\rm bc}$ are determined in the signal extraction fit in § 5.5.2 and the parameters that describe these are summarized in Table 5.7.

In this section, the time-dependent Dalitz PDF for each component is described.

Signal PDF

We treat all dominant decay channels that can decay to the $K^0_S K^+ K^-$ final state. Our signal model is composed of 7 amplitudes summarized in Table 4.1.

The PDF for the signal is parameterized by the product of event-by-event signal fraction $f_{\rm sig}$ and the shape $\mathcal{P}_{\rm sig}$ as

$$\begin{aligned}\mathcal{P}_{\rm sig}(\vec{x}) &= \mathcal{P}_{\rm sig}(m', \theta', \Delta t, q_{\rm tag}, \Delta E, M_{\rm bc}, \ell) \\ &= f_{\rm sig}(\Delta E, M_{\rm bc}, \ell) \cdot \mathcal{P}_{\rm sig}(m', \theta', \Delta t, \ell, q_{\rm tag}), \end{aligned} \tag{6.14}$$

where

$$\mathcal{P}_{\rm sig}(m', \theta', \Delta t, \ell, q_{\rm tag}) = \tag{6.15}$$

$$\begin{aligned}&\epsilon(m', \theta')|\det\, J|\frac{e^{-|\Delta t|/\tau_{B^0}}}{4\tau_{B^0}}\Big[(1 - q_{\rm tag}\Delta w_\ell)(|A|^2 + |\overline{A}|^2) \\ &-q_{\rm tag} \cdot (1 - 2w_\ell)(|A|^2 - |\overline{A}|^2)\cos\Delta m_d \Delta t \\ &+2q_{\rm tag} \cdot (1 - 2w_\ell){\rm Im}(\overline{A}A^*)\sin\Delta m_d \Delta t\Big] \otimes R_{\rm sig}, \end{aligned} \tag{6.16}$$

which accounts for CP dilution from the probability of incorrect flavor tagging, w_ℓ and the difference in w_ℓ between B^0 and $\overline{B^0}$, Δw_ℓ. This shape is convolved with the Δt resolution function $R_{\rm sig}$ [44], but detector resolution in the Dalitz plot is ignored because the decay width of the dominating resonances is large compared to the mass resolution [1]. The determinant of the Jacobian, $|\det\, J|$, is defined in Eq. 4.25, which originates from the Dalitz parameter transformation to the square Dalitz parameters, m' and θ'.

We consider the relative variations of the signal detection efficiency across the Dalitz plane $\epsilon(m', \theta')$ due to detector acceptance. We parametrize this variation from MC and is defined from generated information as follows,

$$\epsilon(m', \theta') \sim \epsilon(m'_{\rm true}, \theta'_{\rm true}) \equiv \frac{H(m'^{\rm rec}_{\rm true}, \theta'^{\rm rec}_{\rm true})}{H(m'^{\rm gen}_{\rm true}, \theta'^{\rm gen}_{\rm true})}. \tag{6.17}$$

We divide the Dalitz plane into 100×100 bins as shown in Fig. 6.5. Since the efficiency variations are determined from signal MC, the effect of efficiency corrections to account for the differences between data and MC due to the requirements on the K^0_S and kaon ID and tracking uncertainties across the Dalitz plane will be included in systematic errors.

We normalize the signal PDF by factorizing into a product of that over Δt and that over Dalitz plane (m' and θ'). For the normalization over Δt convolved with $R_{\rm sig}$, the analytical calculation package was developed for CP analyses at Belle and we employ it. For the normalization over m' and θ', we should calculate it numerically from 0 to 1 over m' and θ' with binning fine enough to represent the resonance ϕ. Since we choose the binning of 2000 in each m' and θ', and the average number of the iterations in our fit until converged is 2000, we had to calculate $\mathcal{O}(10^{10})$ times to obtain only the normalizations for one fit.

[1] The resonance that should be treated most carefully is ϕ, which has the narrow decay width of 4.26 MeV, but the detector resolution is smaller enough ($\sim$1 MeV from the study of $\tau^- \to \phi K^- \nu_\tau$ at Belle [52].) In addition, the binning of the continuum background PDF is set to be comparable to the ϕ mass resolution as will be described later. Thus, we can ignore the effect of the detector resolution both for the signal PDF and the background PDF.

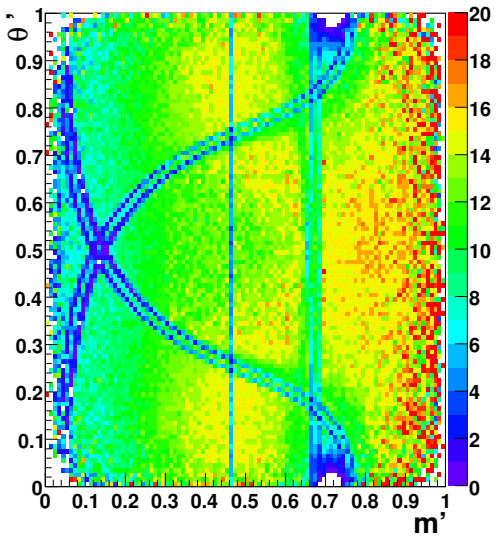

Figure 6.5: Efficiency variations, $\epsilon(m', \theta')$, across the Dalitz plane. The unit of the efficiency is %. Note that the low efficiency regions passing through the square Dalitz plot are due to charmed vetoes from Table 5.1, and the low efficiency areas around the edges correspond to the kinematic regions where one of the three kaons has low momentum.

Instead, we have developed the analytical calculation method of the normalization for Dalitz analyses in the case that the Dalitz-dependent amplitude, $F_i(s_+, s_-)$, for each resonance does not include free parameters in the fit. Once we calculate the variables related to the normalizations of $F_i(s_+, s_-)$ for the seven resonance and their interferences numerically at the beginning of the fit, we have only to combine these variables linearly with the coefficients related to the free parameters once every iteration. Therefore, we could reduce the calculation times by $\sim 1/1000$ and manage this analysis with the finite CPU power.

Continuum Background PDF

The PDF for the continuum background is

$$\mathcal{P}_{q\bar{q}}(\vec{x}) = \mathcal{P}_{q\bar{q}}(m', \theta', \Delta t, q_{\rm tag}, \Delta E, M_{\rm bc}, \ell) \quad (6.18)$$

$$= f_{q\bar{q}}(\Delta E, M_{\rm bc}, \ell) \cdot H_{q\bar{q}}(m', \theta') \cdot \left[\frac{1 + q_{\rm tag}\mathcal{A}_{q\bar{q}}(\theta')}{2}\right] \cdot P_{q\bar{q}}(\Delta t), \quad (6.19)$$

where $f_{q\bar{q}}$, $H_{q\bar{q}}$, $A_{q\bar{q}}$ and $P_{q\bar{q}}$ are the event fraction in ℓ obtained in the signal yield extraction, the Dalitz plot PDF, the Dalitz plot dependent flavor-asymmetry and the Δt PDF, respectively.

The continuum background Δt PDF, $P_{q\bar{q}}(\Delta t)$, is parameterized in Eq. 6.6. where the parameters are fixed from a fit to the Δt sideband defined in § 5.1.4. The fitted result is shown

Table 6.5: Parameters of the continuum background Δt PDF.

parameter	single	multi
f_δ	0.396027 ± 0.034	0.579 ± 0.030
μ (ps)	-0.0136 ± 0.0042	
τ (ps)	0.772 ± 0.033	
$s_{\rm main}$ (ps)	1.075 ± 0.020	1.165 ± 0.015
$s_{\rm tail}$ (ps)	7.16 ± 0.79	3.03 ± 0.14
$f_{\rm tail}$	0.0607 ± 0.0074	0.099 ± 0.011

in Fig. 6.6 and the obtained parameter values are summarized in Table 6.5.

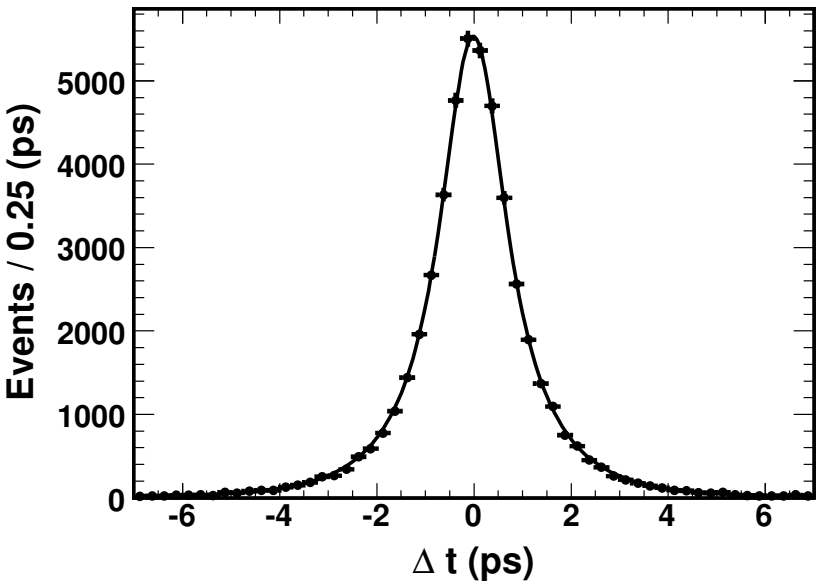

Figure 6.6: The Δt distribution and fitted results for sideband events.

The Dalitz plot PDF for continuum background is a two-dimensional binned histogram PDF shown in Fig. 6.7 with fine binning for the high m' region, where ϕK^0_S is populated. To determine the PDF, we use events in the tight Dalitz sideband defined in § 5.1.4 around the signal ellipse with a more relaxed requirement, $|\cos\theta_{\rm thrust}| < 0.92$, to increase statistics. We use 25623 events in total. By using continuum MC, we confirm that there is no systematic effects [2] coming from the difference in the amount of phase space between the signal ellipse and the tight sideband region.

There is a flavor asymmetry in the θ' direction due to the jet-like topology of continuum

[2]The mean and width of the ϕ mass are not shifted and there are no correlations between the Dalitz parameters and the kinematic variables, $M_{\rm bc}$, ΔE and $\cos\theta_{\rm thrust}$.

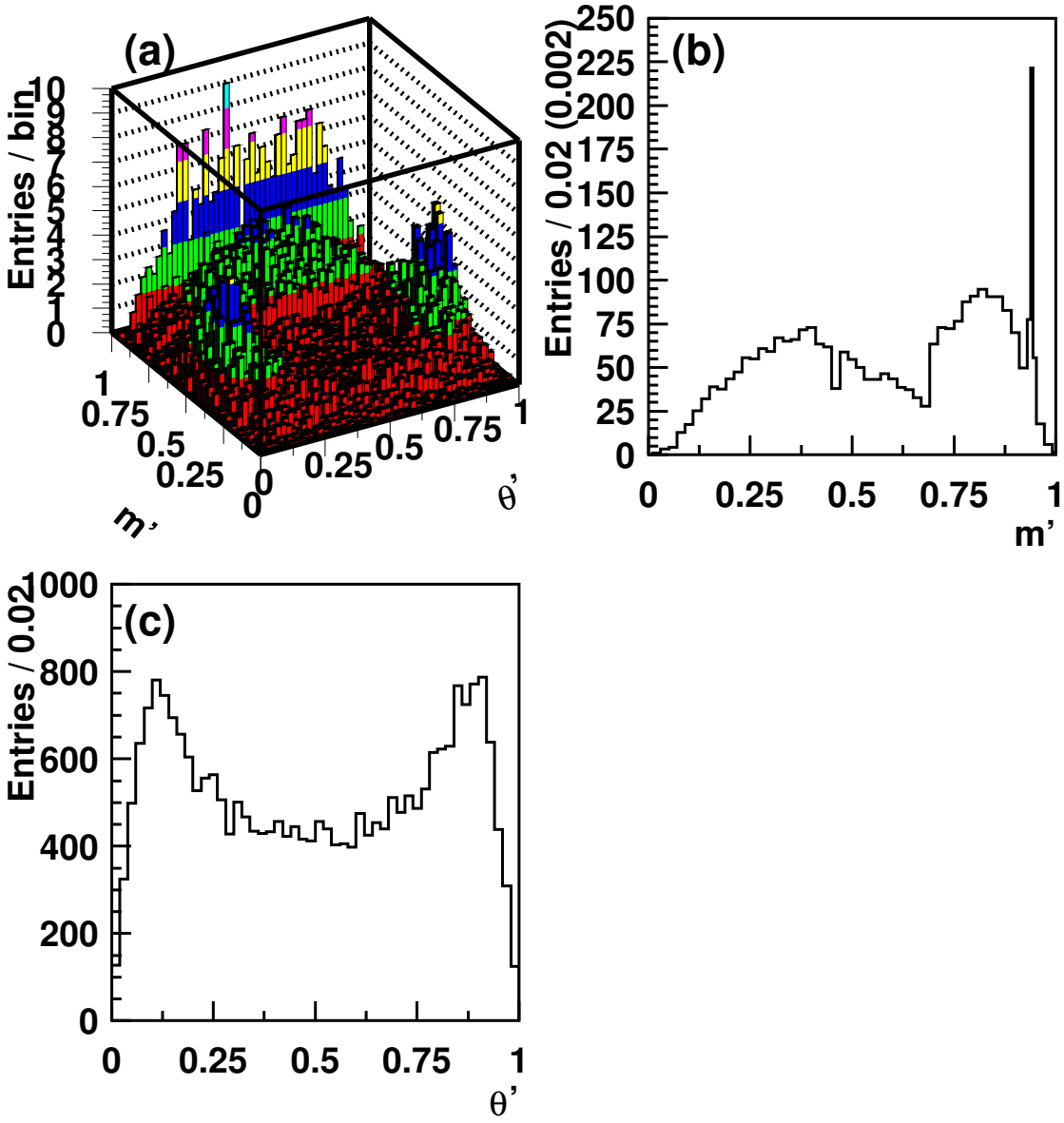

Figure 6.7: Two-dimensional binned histogram of the Dalitz PDF, $H_{q\overline{q}}(m', \theta')$ (a) and its projections onto the m' (b) and θ' (c) directions for $q\overline{q}$ background.

because a high momentum K^+ (K^-) on the CP side is accompanied with a high momentum K^- (K^+) on the tag side. Significant flavor asymmetry is found only in the high ℓ regions (ℓ=5, 6) as shown in Fig. 6.8, because those regions tend to have charged kaons in the tag side. The inclusion of the following term takes this effect into account,

$$\frac{1 + q_{\rm tag} A_{q\overline{q}}(\theta')}{2}, \tag{6.20}$$

where the asymmetry $A_{q\overline{q}}(\theta')$ in sideband is modelled with the first order polynomial function having the ℓ-dependent slope (c_ℓ) written as $A_{q\overline{q}}(\theta') = c_\ell(\theta' - 0.5)$. Since we find no correlation between θ' and $M_{\rm bc}$, we enlarge the lower limit of the sideband region in this fit from 5.24 GeV/c^2 to 5.2 GeV/c^2 in $M_{\rm bc}$ in order to increase statistics. A fit to the raw asymmetry distribution in the sideband gives the parameters, $c_5 = 0.459 \pm 0.051$ and $c_6 = 0.650 \pm 0.082$.

$B\overline{B}$ Background PDF

The treatment in the PDF for each $B\overline{B}$ background is different for $B^0\overline{B^0}$ modes and B^+B^- modes. We estimate the relative fraction of B^+B^- or $B^0\overline{B^0}$ to be $f_{B^0\overline{B^0}} = 0.52 \pm 0.067$, where $f_{B^+B^-} + f_{B^0\overline{B^0}} = 1$ using GEANT-based MC of generic B decays.

Using high statistics MC, we find no CP-violating asymmetry in the background coming from charmless and charmed B decays.

The PDF for the $B\overline{B}$ background PDF is

$$\begin{aligned} \mathcal{P}_{B\overline{B}}(\vec{x}) &= \mathcal{P}_{B\overline{B}}(m', \theta', \Delta t, (q_{\rm tag},)\Delta E, M_{\rm bc}, \ell) & (6.21) \\ &= f_{B\overline{B}}(\Delta E, M_{\rm bc}, \ell) \cdot \mathcal{P}_{B\overline{B}}(m', \theta', \Delta t, (\ell, q_{\rm tag})), & (6.22) \end{aligned}$$

where $f_{B\overline{B}}$ and $\mathcal{P}_{B\overline{B}}$ are the event fraction in ℓ obtained in the signal yield extraction, and the time-dependent Dalitz plot PDF, respectively.

The Δt PDF for $B^0\overline{B^0}$ (B^+B^-) modes is described by a mixing (lifetime) PDF. Instead of the nominal B^0 and B^+ lifetimes from PDG, we introduce the effective lifetimes to include the dilution in the following case. For example, if K^+ from the $B^0 \to K^0_S K^+ K^-$ candidate, K^- from the tag side B decay and IP constraint are used to reconstruct the $B^0 \to K^0_S K^+ K^-$ candidate decay vertex, the B decay vertex position could be reconstructed between those of the original $B^0 \to K^0_S K^+ K^-$ candidate and the original tag side B decay. Since similar situations could occur both in the reconstruction of the B vertices in the CP and tag sides, the measured lifetimes of these events could become shorter than those when the respective charged tracks are used to reconstruct the corresponding B decay vertices. We obtain the effective lifetime from a fit to high statistics $B\overline{B}$ MC in the region of -0.1 GeV $< \Delta E <$ 0.1 GeV and 5.24 GeV/c^2 $< M_{\rm bc} <$ 5.30 GeV/c^2. The fitted results are found to be 0.96 ± 0.04 ps and 0.99 ± 0.04 ps for $B^0\overline{B^0}$ and B^+B^- modes, respectively, and are shown in Fig. 6.9. We use the obtained effective lifetime in the Δt PDF for $B^0\overline{B^0}$ and B^+B^- modes, respectively.

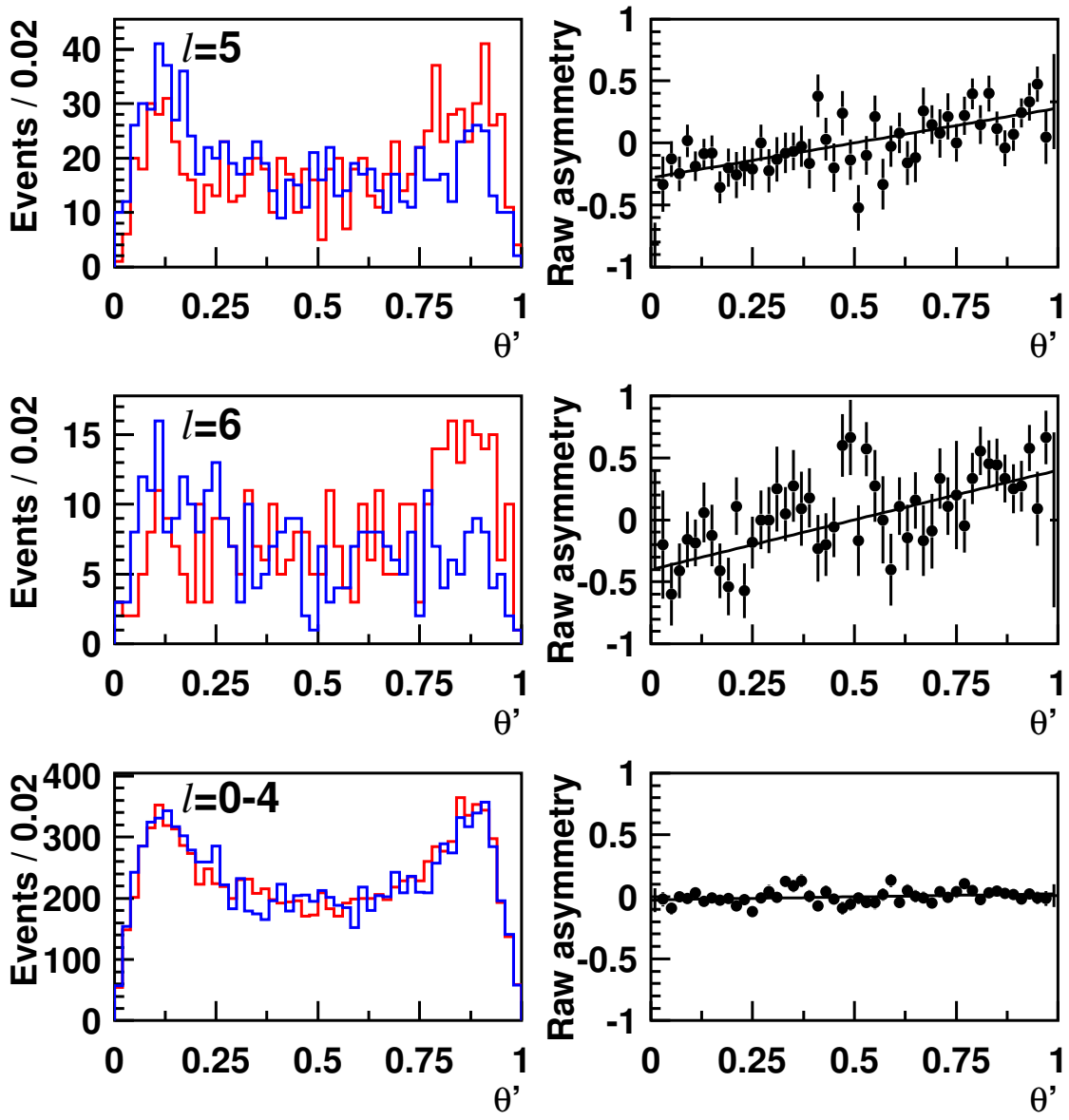

Figure 6.8: The plots on the left side show the θ' distributions with $q_{\rm tag} = +1$ (red) and $q_{\rm tag} = -1$ (blue) while those on the right show the raw asymmetries of the data sample in the sideband region as a function of θ'. In the high ℓ regions (ℓ=5, 6), the significant flavor-asymmetries are seen because those regions tend to have charged kaons in the tag side.

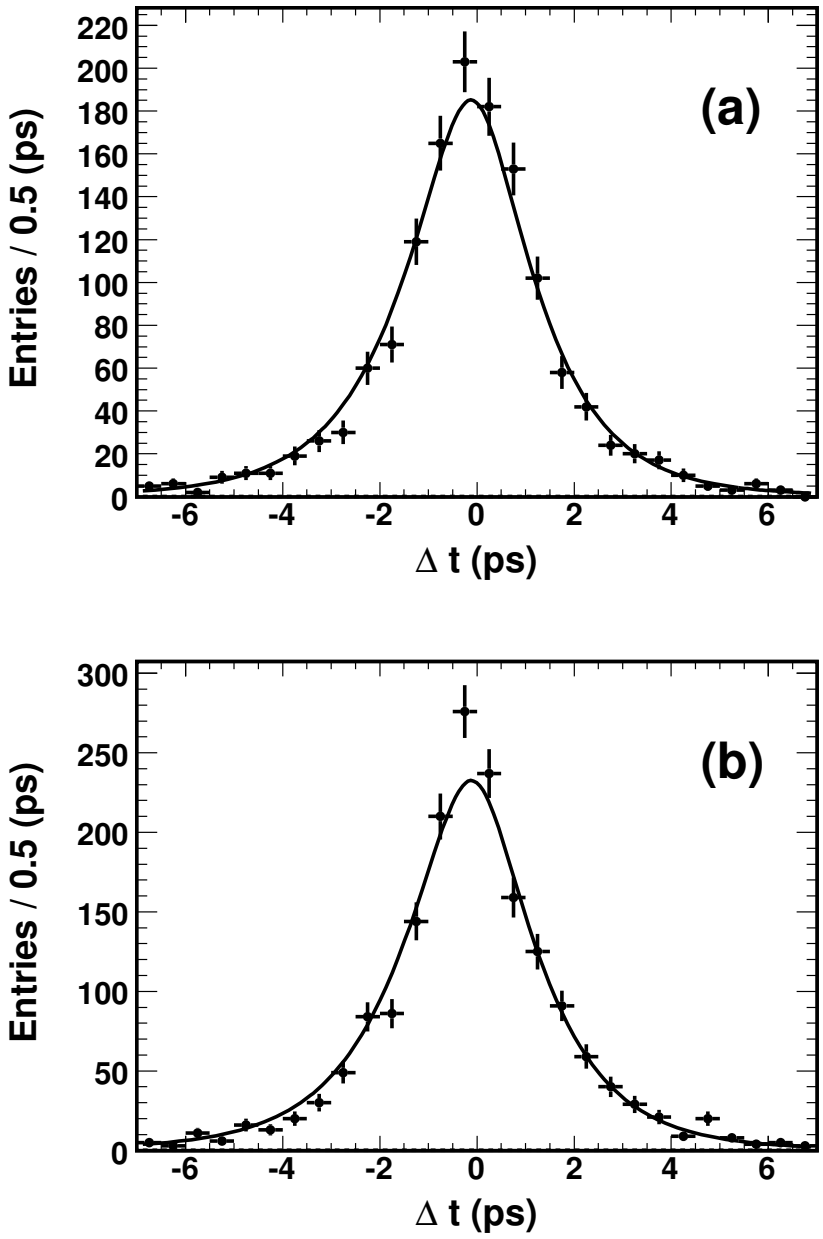

Figure 6.9: The Δt distributions and the fitted results for $B\overline{B}$ background MC for (a) $B^0\overline{B^0}$ and (b) B^+B^- modes.

The Dalitz plot PDFs are two-dimensional binned histogram PDFs obtained from high statistics MC as shown in Fig. 6.10.

Then, the PDF for the B^+B^- background is normalized over flavor,

$$\mathcal{P}_{B^+B^-}(m',\theta',\Delta t) = \frac{H_{B^+B^-}(m',\theta')\cdot P_{B^+B^-}(\Delta t)\otimes R_{B^+B^-}}{2}, \tag{6.23}$$

where $H_{B^+B^-}(m',\theta')$, $P_{B^+B^-}(\Delta t)$ and $R_{B^+B^-}$ are the Dalitz plot PDF, the Δt PDF and the resolution function in Δt for B^+B^- events, respectively.

Since $B^0\overline{B^0}$ events mix, a time-dependent CP PDF is used to model Δt and $q_{\rm tag}$,

$$P_{B^0\overline{B^0}}(\Delta t,\ell,q_{\rm tag}) \equiv \frac{e^{-|\Delta t|/\tau_{B^0}}}{4\tau_{B^0}}\left[1-q_{\rm tag}\Delta w_\ell+q_{\rm tag}(1-2w_\ell)\left(\mathcal{A}_{B^0\overline{B^0}}\cos\Delta m_d\Delta t+\mathcal{S}_{B^0\overline{B^0}}\sin\Delta m_d\Delta t\right)\right], \tag{6.24}$$

with $\mathcal{A}_{B^0\overline{B^0}}=\mathcal{S}_{B^0\overline{B^0}}=0$, as no CP asymmetry is expected from $B^0\overline{B^0}$ MC.

The PDF for the $B^0\overline{B^0}$ background becomes,

$$\mathcal{P}_{B^0\overline{B^0}}(m',\theta',\Delta t,\ell,q_{\rm tag}) = H_{B^0\overline{B^0}}(m',\theta')\cdot P_{B^0\overline{B^0}}(\Delta t,\ell,q_{\rm tag})\otimes R_{\rm sig}. \tag{6.25}$$

Outlier PDF

The PDF for the outlier is

$$\mathcal{P}_{\rm ol}(\vec{x}) = \mathcal{P}_{\rm ol}(m',\theta',\Delta t) = \frac{H_{\rm ol}(m',\theta')\cdot P_{\rm ol}(\Delta t)}{2}, \tag{6.26}$$

where $P_{\rm ol}(\Delta t)$ is Δt PDF provided in § 6.1, and $H_{\rm ol}(m',\theta')$ is the Dalitz plot PDF. Since the outlier is introduced to describe the Δt component that is categorized by neither signal nor background, the Dalitz plot PDF for the outlier can be described as $H_{\rm ol}=\int\mathcal{P}(\vec{x})d\Delta t$. Instead, we make two-dimensional binned histogram PDF of the Dalitz plot of data itself to be computationally practical.

Full Time-Dependent Dalitz plot PDF

The full time-dependent Dalitz Plot PDF is given by

$$\begin{aligned}
&\mathcal{P}(m',\theta',\Delta t,q_{\rm tag};\Delta E,M_{\rm bc},\ell) = \\
&(1-f_{\rm ol})\Big\{ f_{\rm sig}(\Delta E,M_{\rm bc},\ell)\mathcal{P}_{\rm sig}(m',\theta',\Delta t,\ell,q_{\rm tag}) + \\
&\qquad f_{q\overline{q}}(\Delta E,M_{\rm bc},\ell)\mathcal{P}_{q\overline{q}}(m',\theta',\Delta t,\ell,q_{\rm tag}) + \\
&\qquad f_{B\overline{B}}(\Delta E,M_{\rm bc},\ell)[f_{B^+B^-}\mathcal{P}_{B^+B^-}(m',\theta',\Delta t)+f_{B^0\overline{B^0}}\mathcal{P}_{B^0\overline{B^0}}(m',\theta',\Delta t,\ell,q_{\rm tag})]\Big\} \\
&+f_{\rm ol}\mathcal{P}_{\rm ol}(m',\theta',\Delta t),
\end{aligned} \tag{6.27}$$

where $f_{\rm ol}$ is the outlier fraction provided in § 6.1.

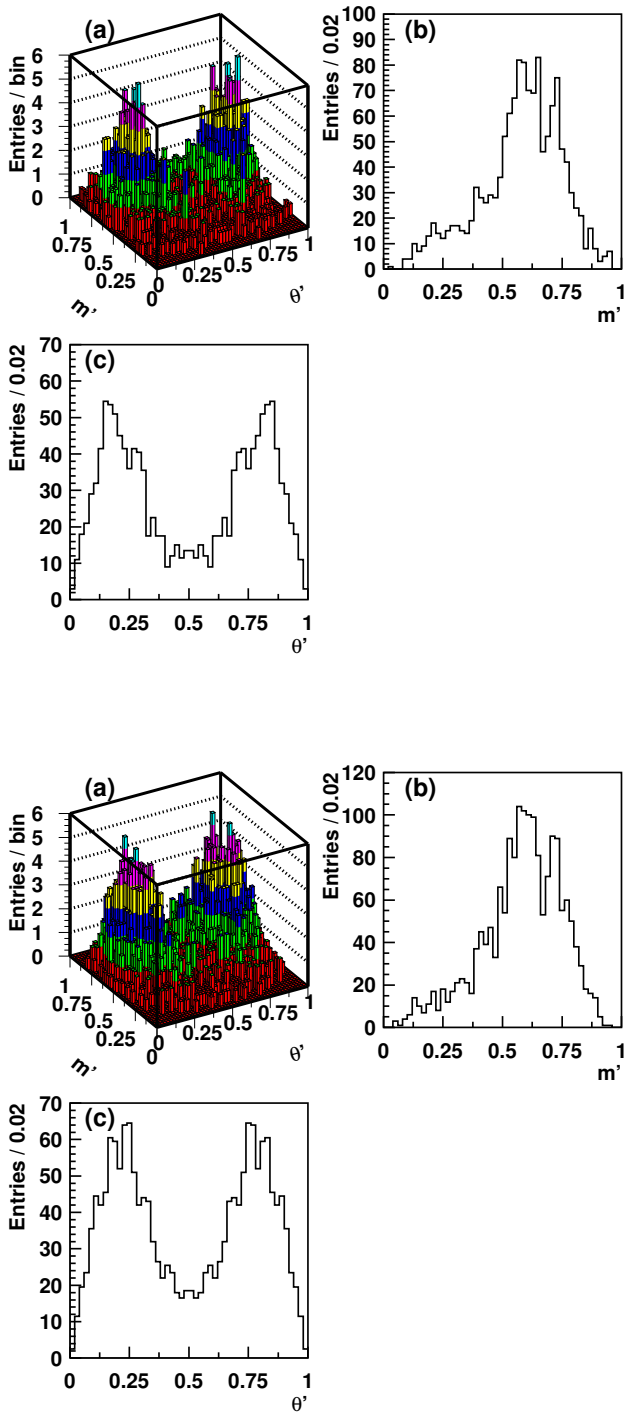

Figure 6.10: Top three figures are two-dimensional binned histogram of $H_{B\overline{B}}(m', \theta')$ (a) and its projections onto the m' (b) and θ' (c) directions for $B^0\overline{B^0}$ background. Bottom three figures are the ones corresponding to B^+B^- background.

6.2.2 Fitted Result

We perform an unbinned maximum likelihood fit by minimizing a likelihood function,

$$-2\log\mathcal{L} = -2\log\left(\prod_i \mathcal{P}_i\right) = -2\sum_i \log\left(\mathcal{P}_i\right), \tag{6.28}$$

where $\mathcal{P}$ is given in Eq. 6.12.

We have 4 free parameters per resonance as in Eq. 4.18. Since only the relative amplitudes and phases between the decay channels are needed to describe a Dalitz model, we fix $a_{(K^+K^-)_{\rm NR}} = 60$, $b_{(K^+K^-)_{\rm NR}} = 0$ in the fit. In addition, we combine the CP-asymmetry parameters, c_i and d_i, for f_X and the non-resonant components in the fit. Although this combined component is almost equal to the non-resonance, we call this component as "others" throughout this thesis. The CP-asymmetry parameters, $c_{\chi_{c0}}$ and $d_{\chi_{c0}}$, are fixed to the world average $b \to c\bar{c}s$ values of 21.5° and 0, respectively, from [20] throughout this analysis. We also fix the non-resonant shape, $\alpha = 0.14 \pm 0.02$ [53]. We determine 18 parameters of the Dalitz plot and CP asymmetries using the likelihood function in Eq. 6.28 with all the other parameters fixed in the fit.

There are large overlapping regions in the Dalitz plot between the broad s-waves, f_0 and the non-resonant component and similarly, $f_{\rm X}$ and the non-resonant component. Consequently, the fitted results suffer from multiple solutions that correspond to ambiguities in their interference terms. Therefore, we must identify the multiple solutions and determine the most likely minima among each solution. However, in Dalitz analyses with several fitted parameters, the selected minimum generally depends on the input parameters because a low statistics data sample is dominated by the statistical fluctuations. To overcome this difficulty, we repeat a large number of fits, $\mathcal{O}(1000)$, with random input parameters to find all the possible multiple solutions and local minima. Consequently, selecting a local minimum as the minimum of a solution is unlikely. This method is the most rigorous way to find the absolute minimum for each solution, otherwise, selecting a local minimum as the minimum of a solution is possible.

We found several minima with similar $-2\log\mathcal{L}$. Among these, we find 4 preferable solutions within 3 σ of the best minimum with the consistent CP parameters but significantly different amplitudes of $f_0K^0_S$ and $f_XK^0_S$. The fitted results are summarized in Table 6.6. Solution 1 has the best $-2\log\mathcal{L}$ among these four solutions. The interpretation on the four multiple solutions will be discussed in § 7.1.2.

To assess how well the fit to the Dalitz plot represents data, the square Dalitz fitted results for the 4 solutions are shown in Fig. 6.11, respectively. The mass projections onto (a) $M(K^0_SK^+)$, (b) $M(K^0_SK^-)$ and (c) $M(K^+K^-)$ distributions for the $B^0 \to K^0_SK^+K^-$ candidate events in the signal region are shown in Fig. 6.12.

By substituting the fitted results in Table 6.6 for Eq. 4.19 and 4.20, we measure the time-dependent CP parameters of the $B^0 \to f_0K^0_S$, $B^0 \to \phi K^0_S$ decays and the other component

of the B^0 decays with $K^0_S K^+ K^-$ final state,

$$\begin{aligned}
\text{Solution1}: \mathcal{A}_{CP}(f_0 K^0_S) &= -0.32^{+0.27}_{-0.29} \pm 0.10 \pm 0.09, \\
\phi_1(f_0 K^0_S) &= (30.5^{+8.6}_{-8.3} \pm 2.9 \pm 2.5)^\circ, \qquad (6.29) \\
\mathcal{A}_{CP}(\phi K^0_S) &= +0.04 \pm 0.20 \pm 0.10 \pm 0.02, \\
\phi_1(\phi K^0_S) &= (32.0^{+8.8}_{-8.3} \pm 1.8 \pm 0.8)^\circ, \qquad (6.30) \\
\mathcal{A}_{CP}(\text{others}) &= -0.14 \pm 0.11 \pm 0.08 \pm 0.03, \\
\phi_1(\text{others}) &= (24.4^{+6.2}_{-5.8} \pm 1.8 \pm 2.8)^\circ, \qquad (6.31)
\end{aligned}$$

$$\begin{aligned}
\text{Solution2}: \mathcal{A}_{CP}(f_0 K^0_S) &= -0.21^{+0.14}_{-0.15} \pm 0.08 \pm 0.08, \\
\phi_1(f_0 K^0_S) &= (26.9^{+6.6}_{-6.3} \pm 1.9 \pm 2.3)^\circ, \qquad (6.32) \\
\mathcal{A}_{CP}(\phi K^0_S) &= +0.10 \pm 0.18 \pm 0.10 \pm 0.03, \\
\phi_1(\phi K^0_S) &= (26.8^{+8.8}_{-8.4} \pm 2.5 \pm 1.2)^\circ, \qquad (6.33) \\
\mathcal{A}_{CP}(\text{others}) &= -0.03 \pm 0.14 \pm 0.07 \pm 0.03, \\
\phi_1(\text{others}) &= (29.5^{+6.5}_{-6.2} \pm 1.9 \pm 2.4)^\circ, \qquad (6.34)
\end{aligned}$$

$$\begin{aligned}
\text{Solution3}: \mathcal{A}_{CP}(f_0 K^0_S) &= -0.02 \pm 0.21 \pm 0.08 \pm 0.10, \\
\phi_1(f_0 K^0_S) &= (25.9^{+7.0}_{-6.6} \pm 2.1 \pm 1.1)^\circ, \qquad (6.35) \\
\mathcal{A}_{CP}(\phi K^0_S) &= -0.03 \pm 0.20 \pm 0.11 \pm 0.01, \\
\phi_1(\phi K^0_S) &= (27.5^{+8.4}_{-7.9} \pm 2.2 \pm 1.4)^\circ, \qquad (6.36) \\
\mathcal{A}_{CP}(\text{others}) &= -0.04 \pm 0.09 \pm 0.08 \pm 0.01, \\
\phi_1(\text{others}) &= (25.3^{+5.7}_{-5.2} \pm 1.9 \pm 2.0)^\circ, \qquad (6.37)
\end{aligned}$$

$$\begin{aligned}
\text{Solution4}: \mathcal{A}_{CP}(f_0 K^0_S) &= -0.20^{+0.12}_{-0.13} \pm 0.07 \pm 0.08, \\
\phi_1(f_0 K^0_S) &= (28.9^{+5.9}_{-5.6} \pm 1.9 \pm 2.8)^\circ, \qquad (6.38) \\
\mathcal{A}_{CP}(\phi K^0_S) &= +0.19 \pm 0.18 \pm 0.10 \pm 0.03, \\
\phi_1(\phi K^0_S) &= (26.8^{+8.2}_{-7.9} \pm 2.4 \pm 1.5)^\circ, \qquad (6.39) \\
\mathcal{A}_{CP}(\text{others}) &= +0.06 \pm 0.10 \pm 0.07 \pm 0.01, \\
\phi_1(\text{others}) &= (27.7^{+6.2}_{-5.7} \pm 1.7 \pm 2.0)^\circ, \qquad (6.40)
\end{aligned}$$

where the first error is statistical, the second is systematic and the third is the Dalitz plot model uncertainty. The Δt and raw asymmetry fit projections for the $B^0 \to K^0_S K^+ K^-$ candidates in the ϕK^0_S region, $|M_{K^+K^-} - M_\phi| < 0.01\text{GeV}/c^2$ in Solution 1 is shown in Fig. 6.13. The statistical correlation matrices between the CP parameters (ϕ_1 and $\mathcal{A}_{CP}$) are listed in Table 6.7, 6.8, 6.9, and 6.10. The full correlation matrices are are given in Tables D.1- D.4.

Table 6.6: Time-dependent Dalitz plot fitted results showing the four solutions within 3 σ.

Parameter	Solution 1	Solution 2	Solution 3	Solution 4
-2log $\mathcal{L}$	10202.001	10202.674	10206.036	10206.613
Dalitz Amplitude				
$a_{f_0K_S^0}$	$28.659\ ^{+2.294}_{-2.424}$	$56.496\ ^{+3.728}_{-3.232}$	$30.738\ ^{+2.600}_{-2.708}$	$61.606\ ^{+4.547}_{-3.912}$
$a_{\phi K_S^0}$	$0.501\ ^{+0.048}_{-0.041}$	$0.646\ ^{+0.080}_{-0.064}$	$0.505\ ^{+0.047}_{-0.040}$	$0.665\ ^{+0.082}_{-0.066}$
$a_{f_X K_S^0}$	$4.920\ ^{+0.612}_{-0.592}$	$6.502\ ^{+0.940}_{-0.891}$	$14.200\ ^{+1.189}_{-0.969}$	$22.126\ ^{+2.437}_{-1.916}$
$a_{\chi_{c0}K_S^0}$	$1.946\ ^{+0.255}_{-0.228}$	$2.504\ ^{+0.379}_{-0.321}$	$1.957\ ^{+0.249}_{-0.224}$	$2.591\ ^{+0.397}_{-0.333}$
$a_{(K_S^0K^+)_{\rm NR}K^-}$	$3.683\ ^{+3.732}_{-3.661}$	$9.916\ ^{+4.624}_{-4.631}$	$5.054\ ^{+3.661}_{-3.684}$	$11.023\ ^{+4.827}_{-4.871}$
$a_{(K_S^0K^-)_{\rm NR}K^+}$	$24.164\ ^{+2.825}_{-2.793}$	$30.749\ ^{+4.076}_{-3.751}$	$24.363\ ^{+2.824}_{-2.809}$	$30.395\ ^{+4.068}_{-3.848}$
$a_{K_S^0(K^+K^-)_{\rm NR}}$	60.0(fixed)	60.0(fixed)	60.0(fixed)	60.0(fixed)
Dalitz Phase (deg.)				
$b_{f_0K_S^0}$	$-11.935\ ^{+6.657}_{-8.429}$	$79.919\ ^{+7.042}_{-5.906}$	$6.683\ ^{+6.096}_{-7.701}$	$98.773\ ^{+6.845}_{-5.638}$
$b_{\phi K_S^0}$	$-33.477\ ^{+13.822}_{-14.130}$	$106.145\ ^{+15.579}_{-15.301}$	$-6.708\ ^{+13.661}_{-13.930}$	$129.207\ ^{+15.435}_{-15.030}$
$b_{f_X K_S^0}$	$-31.750\ ^{+8.134}_{-8.640}$	$-97.086\ ^{+11.862}_{-12.823}$	$85.712\ ^{+6.220}_{-6.011}$	$22.962\ ^{+4.714}_{-4.385}$
$b_{\chi_{c0}K_S^0}$	$-28.050\ ^{+21.495}_{-25.709}$	$-47.208\ ^{+20.674}_{-24.257}$	$-41.448\ ^{+21.479}_{-24.977}$	$-54.857\ ^{+20.714}_{-24.065}$
$b_{(K_S^0K^+)_{\rm NR}K^-}$	$117.215\ ^{+44.760}_{-44.760}$	$85.472\ ^{+22.742}_{-26.109}$	$89.738\ ^{+35.477}_{-50.312}$	$90.862\ ^{+21.688}_{-24.111}$
$b_{(K_S^0K^-)_{\rm NR}K^+}$	$-119.259\ ^{+10.527}_{-9.867}$	$-137.126\ ^{+10.252}_{-9.424}$	$-135.701\ ^{+10.177}_{-9.584}$	$-145.516\ ^{+11.386}_{-10.115}$
$b_{K_S^0(K^+K^-)_{\rm NR}}$	0.0(fixed)	0.0(fixed)	0.0(fixed)	0.0(fixed)
Amplitude difference between B^0 and $\overline{B^0}$				
$c_{f_0K_S^0}$	$0.163\ ^{+0.155}_{-0.143}$	$0.105\ ^{+0.076}_{-0.073}$	$0.008\ ^{+0.105}_{-0.105}$	$0.099\ ^{+0.065}_{-0.062}$
$c_{\phi K_S^0}$	$-0.019\ ^{+0.100}_{-0.100}$	$-0.052\ ^{+0.092}_{-0.092}$	$0.014\ ^{+0.101}_{-0.099}$	$-0.094\ ^{+0.092}_{-0.094}$
$c_{\rm others}$	$0.072\ ^{+0.058}_{-0.057}$	$0.015\ ^{+0.071}_{-0.072}$	$0.020\ ^{+0.044}_{-0.044}$	$-0.029\ ^{+0.051}_{-0.052}$
CP-violating Phase ϕ_1 (deg.)				
$d_{f_0K_S^0}$	$30.467^{+8.569}_{-8.265}$	$26.879\ ^{+6.647}_{-6.348}$	$25.942\ ^{+6.986}_{-6.607}$	$28.909\ ^{+5.890}_{-5.618}$
$d_{\phi K_S^0}$	$31.970^{+8.848}_{-8.322}$	$26.751\ ^{+8.810}_{-8.391}$	$27.497\ ^{+8.447}_{-7.895}$	$26.782\ ^{+8.186}_{-7.891}$
$d_{\rm others}$	$24.446^{+6.176}_{-5.849}$	$29.508\ ^{+6.475}_{-6.166}$	$25.327\ ^{+5.664}_{-5.245}$	$27.713\ ^{+6.209}_{-5.677}$

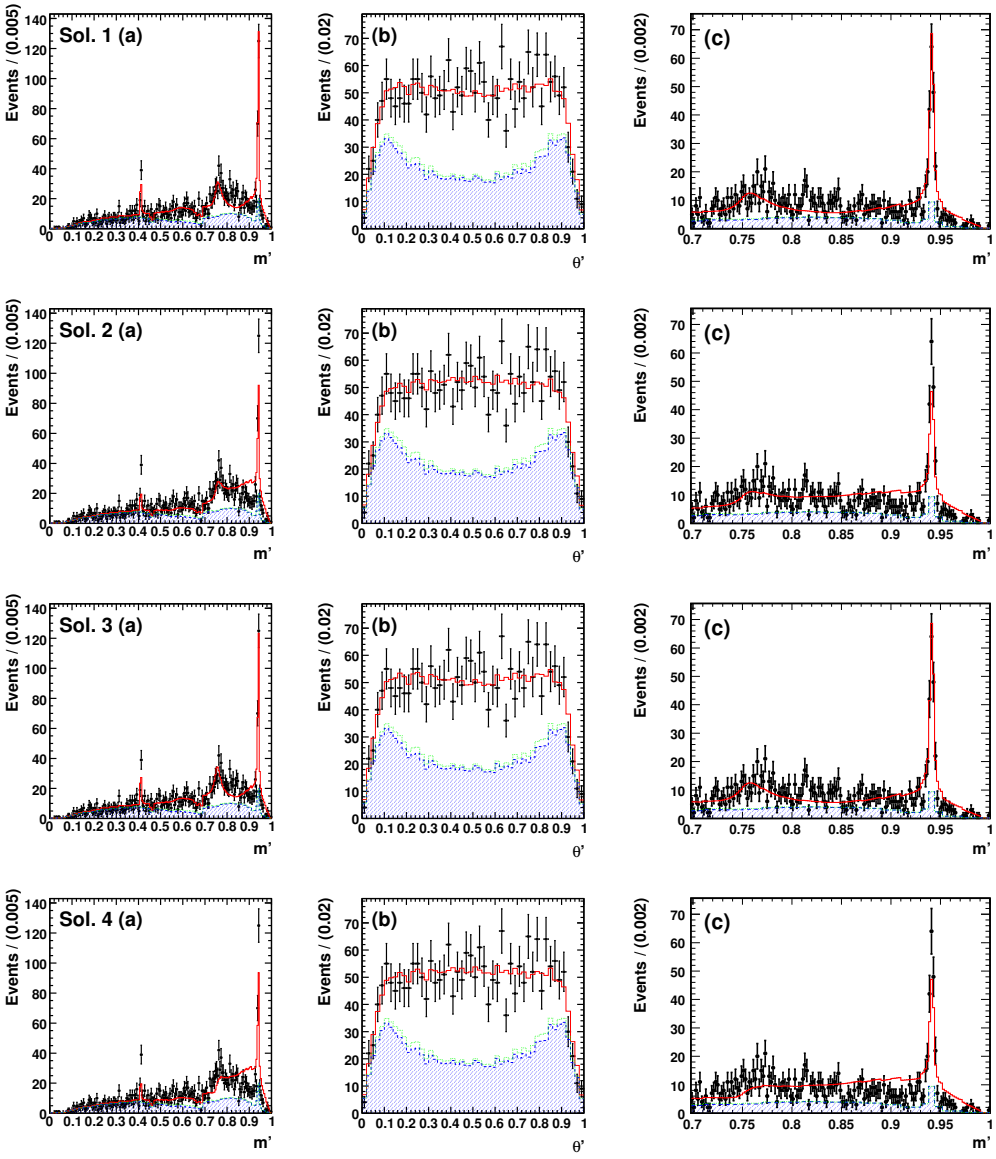

Figure 6.11: The projections of the Dalitz distributions onto (a) m' and (b) θ' directions for the $B^0 \to K^0_S K^+ K^-$ candidate events in the signal region. In (c), the high m' region ($m' > 0.7$) in 0.002 bins is shown. Each line from the top to the bottom corresponds to each solution. In (a-c), the solid curves show the fit projections for each solution while the hatched areas and the dashed curves show the $q\overline{q}$ and total background components, respectively. The points with error bars are the data.

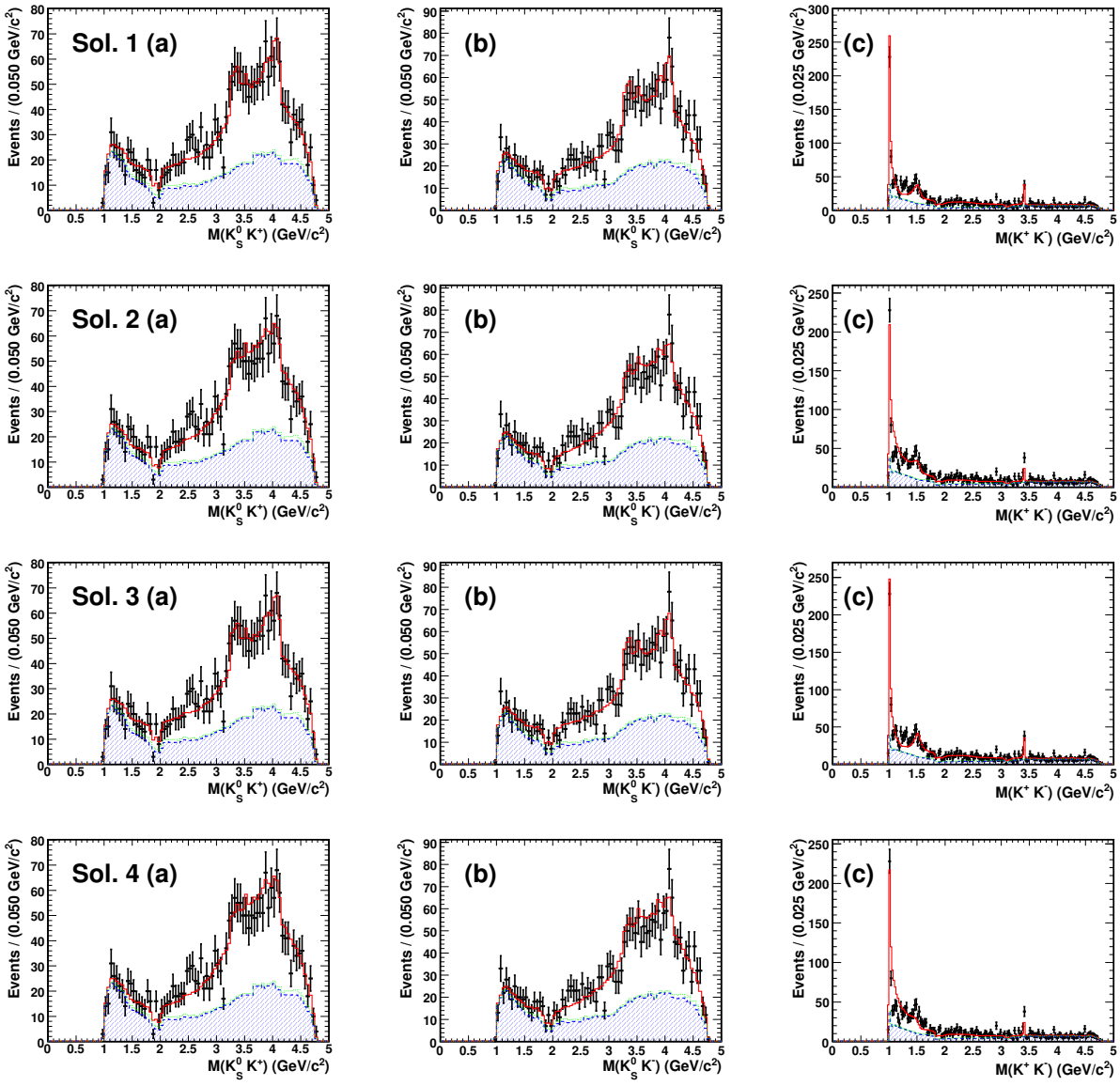

Figure 6.12: The mass projections onto (a) $M(K^0_S K^+)$, (b) $M(K^0_S K^-)$ and (c) $M(K^+K^-)$ distributions for the $B^0 \to K^0_S K^+ K^-$ candidate events in the signal region. Each line from the top to the bottom correspond to each solution. In (a-c), the solid curves show the fit projections for each solution while the hatched areas and the dashed curves show the $q\overline{q}$ and total background components, respectively. The points with error bars are the data.

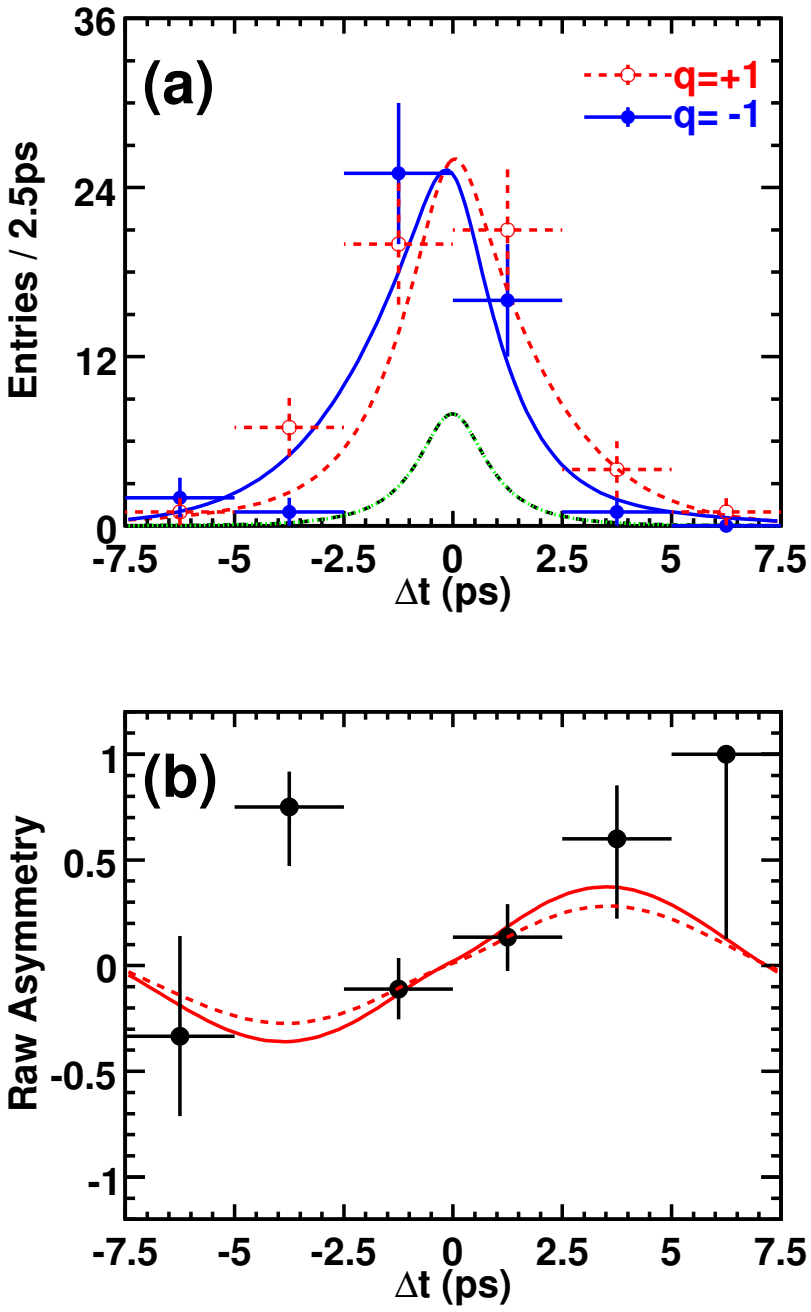

Figure 6.13: (a) Δt distribution and (b) raw asymmetry for the $B^0 \to K^0_S K^+ K^-$ candidates in the ϕK^0_S region, $|M_{K^+K^-} - M_\phi| < 0.01\text{GeV}/c^2$, with good tags, $r > 0.5$ using Solution 1. In (a), the solid and dashed curves show the fitted results with $q_{\rm tag} = \pm 1$, respectively. The dotted black (green) curve shows the background component with $q_{\rm tag} = +1$ (-1). In (b), the solid curve shows the fit projection and the dashed curve shows the Standard Model expectation from CP asymmetry measurement in the $b \to c\bar{c}s$ decays.

Table 6.7: Correlation matrix for CP parameters found in Solution 1.

	1	2	3	4	5	6
1 ϕ_1 $(f_0K^0_S)$	1.00	0.58	0.61	0.14	0.03	0.46
2 ϕ_1 (ϕK^0_S)		1.00	0.35	0.46	-0.08	0.37
3 ϕ_1 (others)			1.00	-0.37	0.09	-0.12
4 $\mathcal{A}_{CP}$ $(f_0K^0_S)$				1.00	-0.24	0.62
5 $\mathcal{A}_{CP}$ (ϕK^0_S)					1.00	-0.15
6 $\mathcal{A}_{CP}$ (others)						1.00

Table 6.8: Correlation matrix for CP parameters found in Solution 2.

	1	2	3	4	5	6
1 ϕ_1 $(f_0K^0_S)$	1.00	0.69	0.63	-0.002	-0.12	-0.48
2 ϕ_1 (ϕK^0_S)		1.00	0.32	-0.07	-0.01	-0.39
3 ϕ_1 (others)			1.00	0.44	-0.04	0.10
4 $\mathcal{A}_{CP}$ $(f_0K^0_S)$				1.00	-0.16	0.37
5 $\mathcal{A}_{CP}$ (ϕK^0_S)					1.00	0.08
6 $\mathcal{A}_{CP}$ (others)						1.00

Table 6.9: Correlation matrix for CP parameters found in Solution 3.

	1	2	3	4	5	6
1 ϕ_1 $(f_0K^0_S)$	1.00	0.64	0.64	0.21	0.05	0.15
2 ϕ_1 (ϕK^0_S)		1.00	0.44	0.44	-0.02	0.09
3 ϕ_1 (others)			1.00	-0.17	0.01	-0.05
4 $\mathcal{A}_{CP}$ $(f_0K^0_S)$				1.00	-0.18	0.31
5 $\mathcal{A}_{CP}$ (ϕK^0_S)					1.00	-0.07
6 $\mathcal{A}_{CP}$ (others)						1.00

Table 6.10: Correlation matrix for CP parameters found in Solution 4.

	1	2	3	4	5	6
1 ϕ_1 $(f_0K^0_S)$	1.00	0.61	0.78	0.04	-0.09	-0.22
2 ϕ_1 (ϕK^0_S)		1.00	0.36	-0.10	0.02	-0.18
3 ϕ_1 (others)			1.00	0.26	0.02	0.02
4 $\mathcal{A}_{CP}$ $(f_0K^0_S)$				1.00	-0.16	0.34
5 $\mathcal{A}_{CP}$ (ϕK^0_S)					1.00	0.01
6 $\mathcal{A}_{CP}$ (others)						1.00

6.2.3 Systematic Uncertainty

Table 6.11, 6.12, 6.13, and 6.14 summarize the systematic uncertainties for the four solutions. We also estimate the uncertainty in the description of the signal Dalitz model in Table 4.1, which is the largest contribution in the systematic uncertainties. The total systematic errors are obtained from the quadratic sum of all the systematic uncertainties. The systematic error for $\mathcal{A}_{CP}$ is primarily due to uncertainties in the B decay vertex reconstructions and the tag-side interference, while the systematic error for ϕ_1 is due to uncertainties in B decay vertex reconstructions, possible fit bias, background PDF, Δt resolution function, and the parameters used in the signal Dalitz model.

The sources of systematic uncertainties accounted for in $B^0 \to K^0_S K^0_S$ are also applied here, so only the items additionally included in the time-dependent Dalitz analysis are described in the following section.

Vertex Reconstruction

The procedures used to estimate the $B^0 \to K^0_S K^0_S$ systematic uncertainties for vertex reconstruction are applied but using the $B^0 \to K^0_S K^+ K^-$ data sample. The control sample, $B^0 \to J/\psi K^0_S$, is used to estimate the Δz bias and SVD mis-alignment. The systematic error for ϕ_1 is obtained by converting $\delta\mathcal{S}_{CP}$ to $\delta\phi_1$ using $\delta\phi_1 = \frac{1}{2}\arcsin(\delta\mathcal{S}_{CP})$.

Background PDF

The uncertainties from background Dalitz PDF and Δt PDF are considered. The contribution originating mainly from the statistical fluctuations of the sideband and MC samples is large because the Dalitz PDFs for continuum and $B\overline{B}$ background are modeled as binned histograms.

For the $q\overline{q}$ Dalitz PDF, 100 sets of pseudo-experiments are generated by statistically fluctuating sideband data to create Dalitz PDFs for continuum. The fit to data with these PDFs are repeated, one by one. These fitted results are compared with the nominal result to create a distribution of fitted residuals. This distribution is fitted with a Gaussian and the width is assigned as a systematic error.

For the $B\overline{B}$ background Dalitz PDF, the same procedure is repeated using $B\overline{B}$ MC to generate pseudo-experiments. The effect of the choice of binning, $N_{\rm bin}$, is also accounted for by changing from $N_{\rm bin} = 50$ to $N_{\rm bin} = 25$ or $N_{\rm bin} = 100$ and repeating the fit.

For the $q\overline{q}$ and $B\overline{B}$ Δt PDFs, the same procedure as that in $B^0 \to K^0_S K^0_S$ is used.

Mis-reconstructed Events

The effect of mis-reconstruction can be significant in the low momentum kaon regions as described in § 5.2. This effect is accounted for by comparing the fitted results of signal MC samples with and without mis-reconstructed events.

Efficiency

The nominal efficiency variations across the Dalitz plane is obtained using a large sample of signal MC from $B^0 \to K^0_S K^+ K^-$ phase-space three-body decays. Systematic errors in the Dalitz plot efficiency histogram arise from MC statistics and the possible differences between data and MC.

To estimate the former, the same procedure used to estimate the systematic uncertainties from the background Dalitz PDFs using histograms are applied here using signal MC.

The efficiency histogram may be systematically distorted by differences between data and MC in the K^0_S, kaon ID and tracking requirements. These differences depend on the momentum and the polar angle of the tracks. Dalitz-dependent correction factors for K^0_S, kaon ID and tracking selection are introduced into the efficiency histogram. The fit with these efficiency histograms are repeated and the resulting deviations are assigned as systematic errors.

Signal Model

Systematic errors due to the fixed masses and widths of the resonance form factors in the signal model, are varied by their errors. The systematic uncertainty due to Blatt-Weisskopf Barrier Factors is determined by taking the difference in the fitted results with and without these factors.

Dalitz Model

We estimate the uncertainty in the description of the signal Dalitz model in Table 4.1. The shape of the non-resonance component is empirically chosen, so different parameterizations are possible. This includes modeling the non-resonant part with the tail of a Breit-Wigner, $R_{NR}(s;\alpha) = i\alpha/(s+i\alpha)$ and a power law whose exponent is a fitted parameter, $R_{NR}(s;\alpha) = s^{-\alpha}$. A possible variation in the model of the f_0 Flatté function, is also considered using a different parametrization given in Ref. [54]. We also include the possible resonance, $f_2(1270)$, in the signal model and the fit is repeated.

The effect of the choice of binning, $N_{\rm bin}$, in calculating the normalization of signal Dalitz PDF both in the m' and θ' directions is accounted for by changing from $N_{\rm bin} = 2000$ to $N_{\rm bin} = 1500$ and $N_{\rm bin} = 2500$ and repeating the fit.

Table 6.11: Summary of systematic uncertainties for Solution 1.

	$f_0K^0_S$	ϕK^0_S	others	$f_0K^0_S$	ϕK^0_S	others
Category	$\delta\phi_1$			$\delta\mathcal{A}_{CP}$		
0. Vertex Reconstruction	1.09	1.04	1.20	0.044	0.079	0.023
1. Wrong tag fraction	0.17	0.19	0.16	0.004	0.006	0.002
2. Δt resolution function	0.69	0.64	0.53	0.016	0.011	0.009
3. Possible fit bias	2.22	0.92	0.42	0.066	0.008	0.026
4. Physics parameters	0.06	0.06	0.07	0.002	0.001	0.001
5. Background PDF	0.94	0.83	0.83	0.037	0.012	0.016
6. Signal fraction	0.25	0.47	0.28	0.013	0.006	0.004
7. Mis-reconstruction	0.09	0.01	0.04	0.000	0.000	0.001
8. Efficiency	0.16	0.17	0.11	0.011	0.004	0.005
9. Signal model	1.04	0.39	0.76	0.025	0.005	0.005
10. Tag-side interference	0.03	0.03	0.03	0.043	0.054	0.066
Total w/o Dalitz model	2.94	1.82	1.81	0.103	0.098	0.077
11. Dalitz model	2.48	0.83	2.84	0.094	0.017	0.026

Table 6.12: Summary of systematic uncertainties for Solution 2.

	$f_0K^0_S$	ϕK^0_S	others	$f_0K^0_S$	ϕK^0_S	others
Category	$\delta\phi_1$			$\delta\mathcal{A}_{CP}$		
0. Vertex reconstruction	1.46	1.79	0.82	0.034	0.079	0.027
1. Wrong tag fraction	0.19	0.19	0.21	0.004	0.005	0.003
2. Δt resolution function	0.41	0.38	0.55	0.013	0.009	0.012
3. Possible fit bias	0.83	0.80	1.34	0.016	0.010	0.019
4. Physics parameters	0.07	0.10	0.04	0.001	0.001	0.002
5. Background PDF	0.66	0.91	0.71	0.017	0.011	0.020
6. Signal fraction	0.25	0.31	0.24	0.006	0.008	0.006
7. Mis-reconstruction	0.09	0.01	0.04	0.000	0.000	0.001
8. Efficiency	0.16	0.17	0.11	0.011	0.003	0.003
9. Signal model	0.45	1.17	0.43	0.014	0.011	0.021
10. Tag-side interference	0.03	0.03	0.03	0.059	0.064	0.060
Total w/o Dalitz model	1.94	2.52	1.89	0.076	0.104	0.074
11. Dalitz model	2.32	1.19	2.40	0.080	0.026	0.032

Table 6.13: Summary of systematic uncertainties for Solution 3.

	$f_0K^0_S$	ϕK^0_S	others	$f_0K^0_S$	ϕK^0_S	others
Category	$\delta\phi_1$			$\delta\mathcal{A}_{CP}$		
0. Vertex reconstruction	1.20	0.85	1.29	0.032	0.084	0.022
1. Wrong tag fraction	0.21	0.23	0.17	0.005	0.005	0.003
2. Δt resolution function	0.73	0.68	0.53	0.017	0.010	0.009
3. Possible fit bias	1.32	1.65	0.96	0.014	0.007	0.016
4. Physics parameters	0.02	0.03	0.05	0.002	0.002	0.001
5. Background PDF	0.56	0.59	0.62	0.021	0.011	0.010
6. Signal fraction	0.23	0.48	0.26	0.009	0.006	0.004
7. Mis-reconstruction	0.09	0.01	0.04	0.000	0.000	0.001
8. Efficiency	0.16	0.16	0.11	0.011	0.003	0.003
9. Signal model	0.55	0.59	0.55	0.024	0.016	0.010
10. Tag-side interference	0.03	0.03	0.06	0.066	0.064	0.068
Total w/o Dalitz model	2.10	2.20	1.91	0.083	0.108	0.075
Dalitz model	1.09	1.39	1.96	0.102	0.009	0.013

Table 6.14: Summary of systematic uncertainties for Solution 4.

	$f_0K^0_S$	ϕK^0_S	others	$f_0K^0_S$	ϕK^0_S	others
Category	$\delta\phi_1$			$\delta\mathcal{A}_{CP}$		
0. Vertex reconstruction	1.40	2.07	1.19	0.033	0.073	0.023
1. Wrong tag fraction	0.17	0.17	0.21	0.004	0.005	0.003
2. Δt resolution function	0.45	0.34	0.63	0.011	0.009	0.009
3. Possible fit bias	0.78	0.54	0.57	0.024	0.006	0.021
4. Physics parameters	0.03	0.09	0.02	0.002	0.001	0.001
5. Background PDF	0.62	0.87	0.65	0.012	0.011	0.014
6. Signal fraction	0.28	0.27	0.26	0.005	0.006	0.005
7. Mis-reconstruction	0.09	0.01	0.04	0.000	0.000	0.001
8. Efficiency	0.16	0.15	0.12	0.011	0.003	0.003
9. Signal model	0.54	0.44	0.43	0.017	0.012	0.009
10. Tag-side interference	0.06	0.06	0.06	0.055	0.063	0.064
Total w/o Dalitz model	1.90	2.41	1.69	0.074	0.099	0.073
Dalitz model	2.79	1.48	2.04	0.081	0.027	0.011

6.2.4 Validity Checks

Various checks are performed to verify this analysis procedure and result in the same way as $B^0 \to K^0_S K^0_S$.

Measurement of the B^0 Lifetime in the $B^0 \to K^0_S K^+ K^-$ Decay

To check the validity of the Δt resolution function and signal fraction, we measure the B^0 lifetime in the $B^0 \to K^0_S K^+ K^-$ decay by the fit of the Δt distribution as the B^0 lifetime PDF in Eq. 6.11. The fitted result, shown in Fig. 6.14, gives a B^0 lifetime of 1.504 ± 0.060 ps, which is consistent with the world average [35].

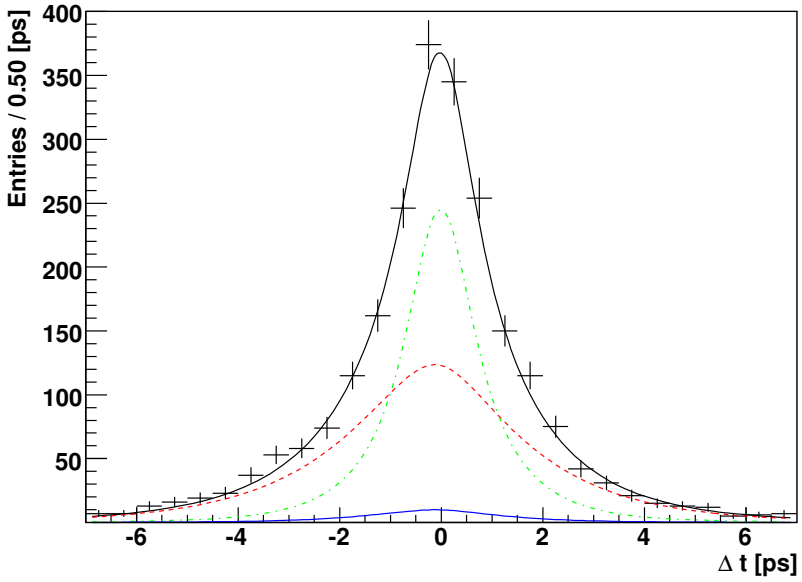

Figure 6.14: Δt distribution with the fitted result by the B^0 lifetime PDF. The solid black curve shows the fitted result and the red, green and blue curves show the signal, $q\overline{q}$ background and $B\overline{B}$ background components, respectively. The points with error bars are the data.

Linearity Check with Signal MC

To check for reconstruction bias in Δt, flavor tagging, wrong tag fraction and Dalitz variables, a large number of signal GEANT-based MC samples are generated using different ϕ_1 values as input. The size of each signal MC sample corresponds to 100 times the data size. The consistency between the input values and the fitted CP parameters are compared with a

linear fit as shown in Fig. 6.15. The total reconstructed bias is estimated using the deviation of the gradient from unity which shows no evidence for reconstruction bias.

Fit Bias Check with Pseudo-Experiments

The fit bias of the total PDF is checked by generating pseudo-experiments based on the total PDF using the same method described in § 6.1.4. The statistical errors obtained in the nominal fit are consistent with the error expected from pseudo-experiments, summarized in Table 6.15. The pull distribution results, given in Figure 6.16 and Table 6.16, shows no significant fit bias and thus we conclude that the asymmetric errors have been estimated properly. The small fit bias estimated in this pseudo-experiments study is included in the systematic uncertainty.

Table 6.15: The estimated errors for $\mathcal{A}_{CP}$ and ϕ_1 using Toy MC.

	ϕK^0_S	$f_0 K^0_S$	others
$\delta\mathcal{A}_{CP}$	0.19±0.02	0.40±0.09	0.11±0.01
$\delta\phi_1$ (deg)	8.6±1.2	11.6±2.1	6.7±0.8

Table 6.16: The mean and width of the pull distributions for $\mathcal{A}_{CP}$ and ϕ_1 from Toy MC.

$\mathcal{A}_{CP}$	ϕK^0_S	$f_0 K^0_S$	others
μ	-0.031±0.033	-0.065±0.031	-0.053±0.034
σ	0.96±0.03	0.90±0.03	0.97±0.03
ϕ_1	ϕK^0_S	$f_0 K^0_S$	others
μ	-0.042±0.035	-0.023±0.032	0.10±0.04
σ	1.02±0.03	0.92±0.03	1.03±0.03

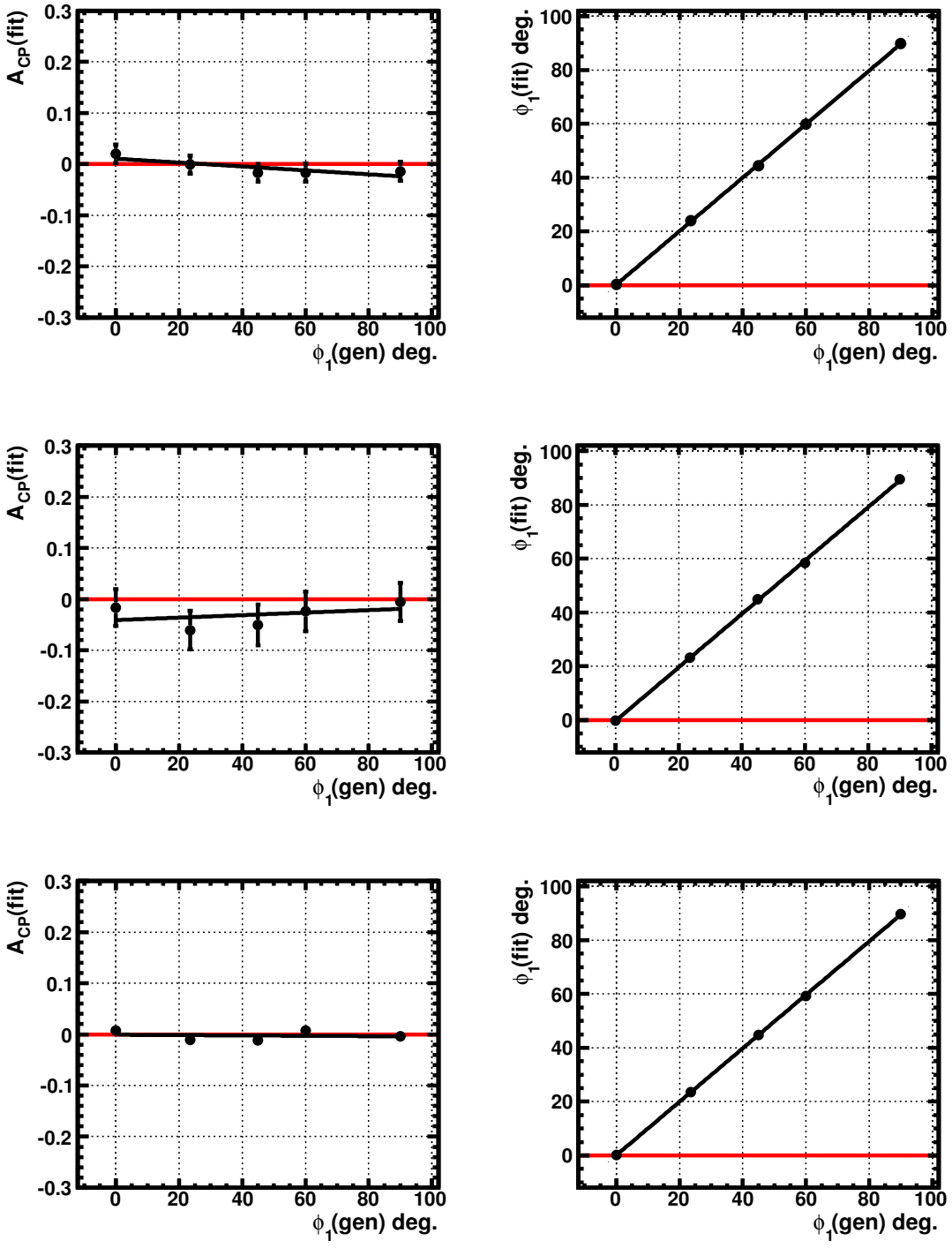

Figure 6.15: Linearity test using GEANT-based signal MC. The top, middle and bottom rows show the linearity test for ϕK^0_S, $f_0 K^0_S$ and the others, respectively. The left (right) column shows the linearity test for $\mathcal{A}_{CP}$ (ϕ_1).

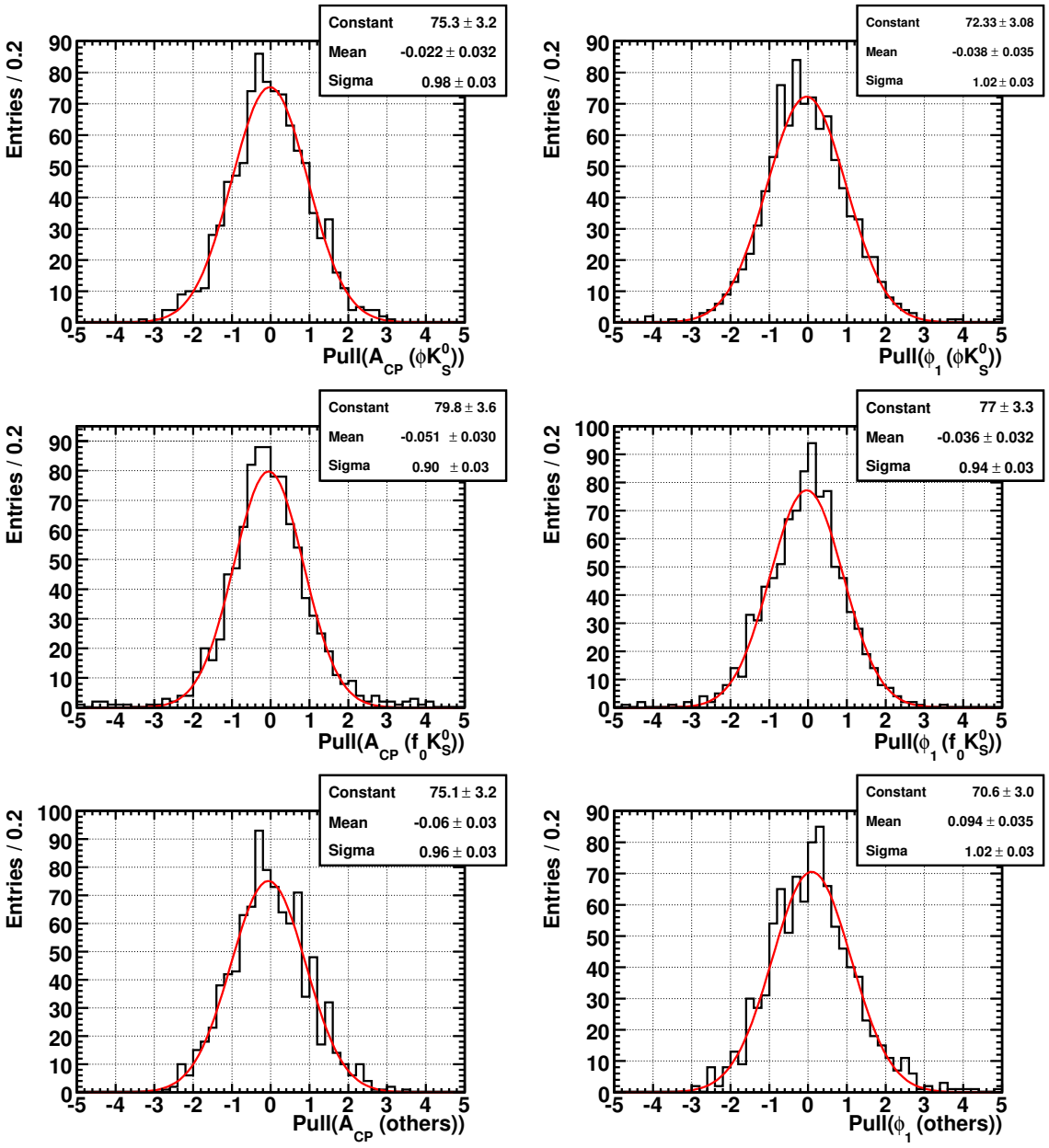

Figure 6.16: The top, middle and bottom rows show the pull distributions from Toy MC for ϕK^0_S, $f_0 K^0_S$ and the others, respectively. The left (right) column shows the fit bias test for $\mathcal{A}_{CP}$ (ϕ_1). The solid red lines show the fitted results onto the Gaussian distribution.

Chapter 7

Discussion

In this chapter, after interpreting the results of the CP asymmetry measurements in the $B^0 \to K^0_S K^0_S$ decay (Eq. 6.10) and the $B^0 \to K^0_S K^+ K^-$ decay (Table 6.6), we compare our results with various theoretical predictions within the Standard Model, thereby searching for possible new weak phases in these decays. We also demonstrate possible constraints to new weak phases using the results.

We discuss the differences in the fitted results between the time-dependent Dalitz plot CP analysis introduced in this thesis, and the quasi-two-body analysis done in the previous measurements, using both the data and the pseudo-experiments generated based on the fitted results of data. We also mention the results from the other B factory experiment.

7.1 Interpretation of the Fitted Results

7.1.1 Significance of CP Violation in the $B^0 \to K^0_S K^0_S$ Decay

The likelihood scans as a function of $\mathcal{A}_{K^0_S K^0_S}$ and $\mathcal{S}_{K^0_S K^0_S}$ are shown in Fig 7.1. These scans are produced by fixing one parameter and performing the fit to determine the remaining free parameter. These plots show that the minimum is stable. The contour plot of $\mathcal{A}_{K^0_S K^0_S}$ and $\mathcal{S}_{K^0_S K^0_S}$ is also shown in Fig 7.2. No significant CP asymmetry is found in the $B^0 \to K^0_S K^0_S$ decay as the deviation from zero is $\sim 1\sigma$.

7.1.2 Multiple Solutions of Time-Dependent Dalitz Plot Analysis in the $B^0 \to K^0_S K^+ K^-$ Decay

As shown in Table 6.6 and described in § 6.2.2, we have found four solutions in the fitted result. The multiple solutions in the Dalitz plot are caused by a large overlap between

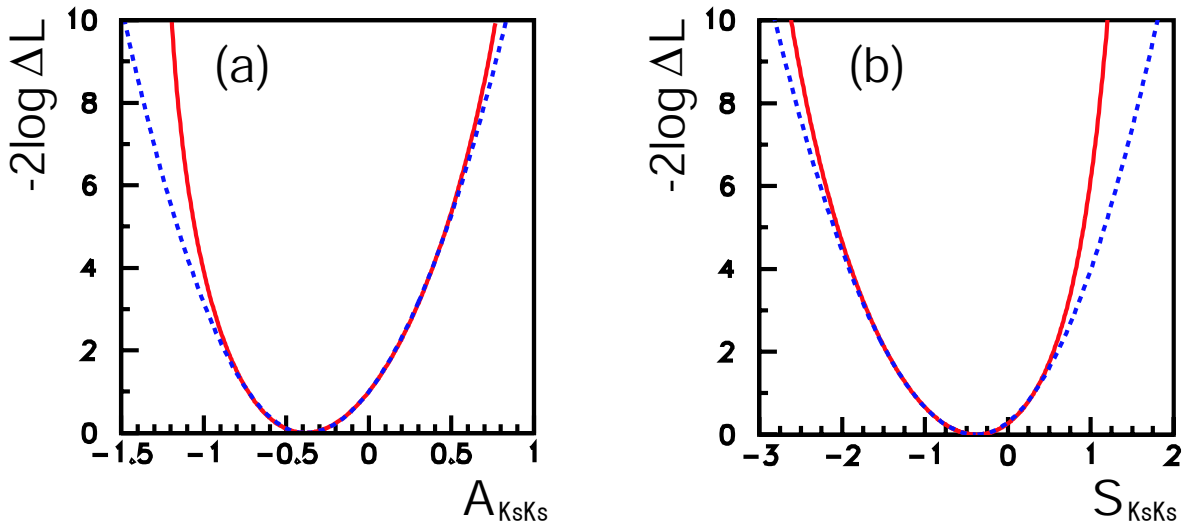

Figure 7.1: Likelihood scans as a function of (a) $\mathcal{A}_{K^0_S K^0_S}$ and (b) $\mathcal{S}_{K^0_S K^0_S}$, with (blue dashed line) and without (red solid line) the systematic uncertainties.

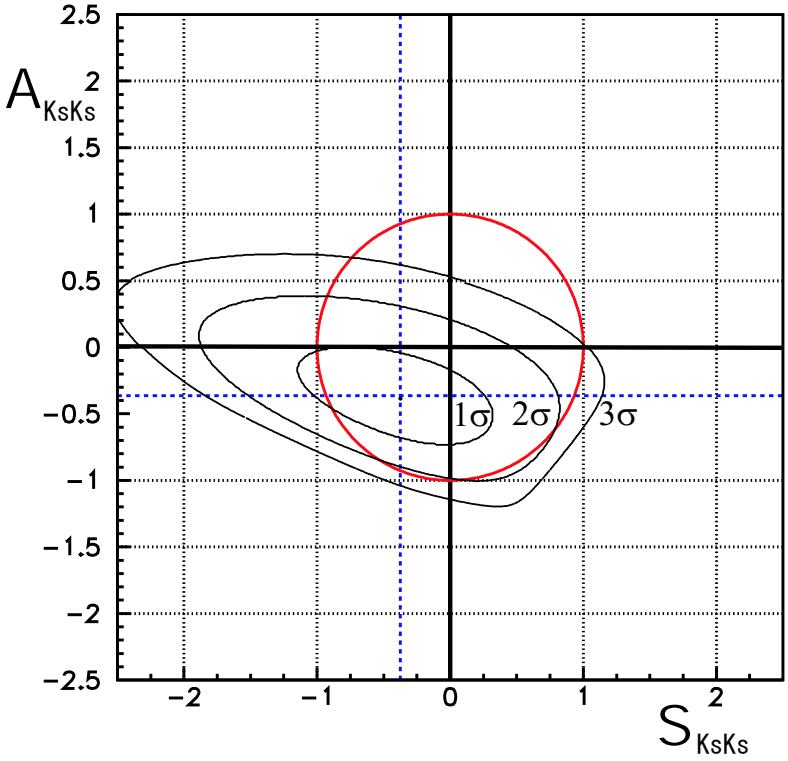

Figure 7.2: The contour plot for $\mathcal{A}_{K^0_S K^0_S}$ vs. $\mathcal{S}_{K^0_S K^0_S}$. The fitted values are represented by the black dot on the blue dotted lines and the physical boundary by the red circle.

s-waves. As a result there is an ambiguity in their relative interference terms.

In the Dalitz plot analysis, the interfering effects can be seen in the relative fractions of resonance (i) defined as

$$f_i = \frac{(|a_i|^2 + |\overline{a}_i|^2) \int F_i(s_+, s_-) F_i^*(s_+, s_-) ds_+ ds_-}{\int |A|^2 + |\overline{A}|^2 ds_+ ds_-}, \tag{7.1}$$

where the total fraction, which is defined as the sum of the relative fractions over all decay channels in the Dalitz plot, may not be 100% due to interference [1]. By substituting the fitted results of all solutions in Table 6.6 for Eq 7.1, we obtain the relative fractions of the decay channels included in the $B^0 \to K^0_S K^+ K^-$ signal model as summarized in Table 7.1. Note that only the relative fractions of $f_0 K^0_S$, $f_{\rm X} K^0_S$ and the $K^0_S(K^+K^-)_{\rm NR}$ are significantly different among the four solutions.

Table 7.1: Summary of relative fractions of the decay channels in the $B^0 \to K^0_S K^+ K^-$ signal model where only the statistical errors are given.

Decay channel	Solution 1 Fraction (%)	Solution 2 Fraction (%)	Solution 3 Fraction (%)	Solution 4 Fraction (%)
$f_0 K^0_S$	27.4 ± 8.7	63.7 ± 9.8	30.3 ± 9.5	71.6 ± 11.5
ϕK^0_S	14.2 ± 6.7	14.4 ± 8.4	14.2 ± 6.4	14.4 ± 8.5
$f_{\rm X} K^0_S$	5.0 ± 5.5	5.2 ± 6.4	41.1 ± 9.6	57.2 ± 15.1
$\chi_{\rm c0} K^0_S$	3.8 ± 4.8	3.8 ± 5.4	3.8 ± 4.7	3.8 ± 5.5
$(K^0_S K^+)_{\rm NR} K^-$	0.6 ± 14.0	2.2 ± 13.5	0.9 ± 13.6	2.4 ± 13.8
$(K^0_S K^-)_{\rm NR} K^+$	21.7 ± 10.8	20.5 ± 11.7	21.6 ± 10.7	19.1 ± 11.5
$K^0_S(K^+K^-)_{\rm NR}$	131.8 ± 11.5	79.1 ± 8.9	128.5 ± 11.3	74.9 ± 8.7
Total	204.3 ± 22.0	189.0 ± 23.6	240.3 ± 23.4	243.3 ± 28.0

In the Dalitz plot of the B^0 decays with $K^0_S K^+ K^-$ final state, there are two specific regions where two s-waves overlap, one around $m' \sim 0.9$ and the other around $m' \sim 0.8$ in the highlighted region in Fig. 4.3. As one can see in Fig. 4.2, they correspond to the regions where are,

between f_0 and the non-resonant component, and

between $f_{\rm X}$ and the non-resonant component, respectively.

We can see these interfering effects from the relative fractions of the decay channels through the s-wave resonances (f_0 and $f_{\rm X}$), $K^0_S(K^+K^-)_{\rm NR}$ and the total fractions for all solutions listed in Table 7.1.

We find that

[1] In the Dalitz plot analysis, the relative fraction, f_i, is often used to represent the fraction of each resonance (i) contribution in the total amplitude.

Solution 1 has a low $f_0 K^0_S$ and a low $f_{\rm X} K^0_S$ fraction,

Solution 2 has a high $f_0 K^0_S$ and low $f_{\rm X} K^0_S$ fraction,

Solution 3 has a low $f_0 K^0_S$ and a high $f_{\rm X} K^0_S$ fraction, and

Solution 4 has a high $f_0 K^0_S$ and high $f_{\rm X} K^0_S$ fraction.

By comparing the likelihood values on Table 6.6, the likelihood for Solution 1 is the best among the four solutions, although the differences are not significant with the current data sample. Therefore, these four solutions are treated as the results of this analysis.

Likelihood Scans for Each Multiple Solution Using Data

We estimate the significance of the nominal fitted result for $\phi_1^{\rm eff}$ compared to the mirror solution (the trigonometric reflection where $\phi_1^{\rm eff} \to \pi/2 - \phi_1^{\rm eff}$), $\pi/2 - \phi_1^{\rm eff}$. Many fits are repeated with varying the fixed $\phi_1^{\rm eff}$ value to determine the other 17 parameters. The change in the likelihood as a function of $\phi_1^{\rm eff}$ for each solution is shown in Fig 7.3. The true minima around the real solutions are seen. Local minima around the mirror solution for $\phi_1^{\rm eff}$ can be found at the hollows around ~ 80 deg. for Solution 1 and 3 in Fig 7.3 (b), however, they are excluded in the four solutions by greater than 3σ.

Likelihood Differences among Multiple Solutions Using Pseudo-Experiments

We generate 1000 toy MC samples with the same statistics as that of the data and with the fitted values of Solution 1, and repeat the fit to the samples to see the distributions of the likelihood values around the four solutions. Figure 7.4 shows the distributions of the difference in $-2\log\mathcal{L}$ between Solution 1 and the other solutions. The mean and the width of the distributions in each solution are summarized in Table 7.2. The likelihood differences in all solutions are not significant, thus we cannot rule out any of them with the current statistics.

The same procedure is repeated using high statistics pseudo-experiments, which corresponds to 10 times and 50 times the current statistics. Figure 7.5 shows these distributions of the difference in $-2\log\mathcal{L}$ between Solution 1 and the other solutions. Since these distributions do not overlap with Solution 1, these solutions may be distinguished by likelihood as the statistics increases in a future high luminosity B physics experiment. Note that according to the toy MC study with 50 times the current statistics, we can select Solution 1 and rule out the other solutions with the significance of $\sim 10\sigma$.

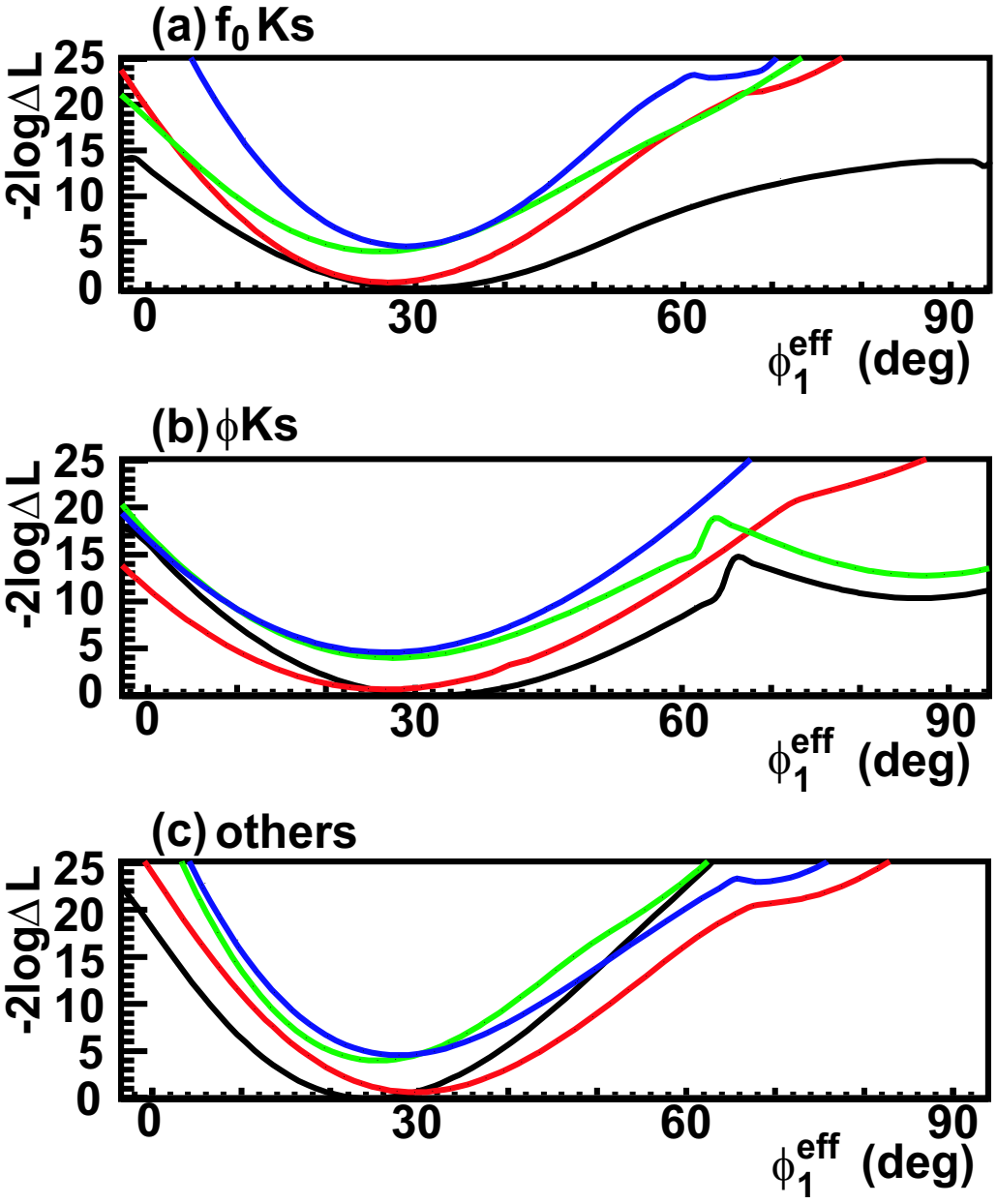

Figure 7.3: Likelihood scan as a function of $\phi_1^{\rm eff}$ for $f_0 K_S^0$ (top), ϕK_S^0 (middle) and the others (bottom) for Solution 1 (black), 2 (red), 3 (green) and 4 (blue).

Table 7.2: The mean and the width of the $-2\log\mathcal{L}$ differences in Fig 7.4.

$-2\Delta\log\mathcal{L}$	mean	width
$-2(\log\mathcal{L}_{\rm Sol.2} - \log\mathcal{L}_{\rm Sol.1})$	4.5 ± 0.4	5.2 ± 0.3
$-2(\log\mathcal{L}_{\rm Sol.3} - \log\mathcal{L}_{\rm Sol.1})$	3.9 ± 0.3	4.4 ± 0.3
$-2(\log\mathcal{L}_{\rm Sol.4} - \log\mathcal{L}_{\rm Sol.1})$	10.2 ± 0.6	7.0 ± 0.5

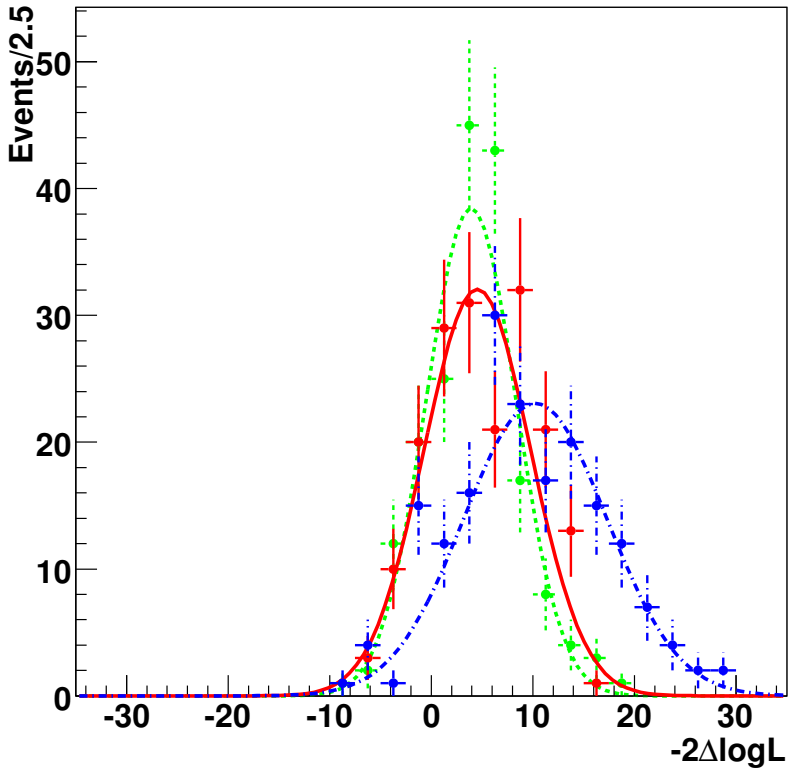

Figure 7.4: Difference in -2log$\mathcal{L}$ between Solution 1 and Solution 2 (red), Solution 3 (green) and Solution 4 (blue). The curves show the fits onto the Gaussian distribution.

Selection of the Most Preferable Solution Using External Information

In order to distinguish these solutions with the current statistics, we use the external information from $B^0 \to K^0_S\pi^+\pi^-$ and the property that f_0 decays to either $\pi^+\pi^-$ or K^+K^-.

We calculate the branching fraction, $\mathcal{B}(B^0 \to K^0_S f_0[\pi^+\pi^-])$, based on the branching fraction of $B^0 \to K^0_S\pi^+\pi^-$ and the relative fraction of $f_0K^0_S$ in the $B^0 \to K^0_S\pi^+\pi^-$ decay. Similarly, we can calculate the branching fraction, $\mathcal{B}(B^0 \to K^0_S f_0[K^+K^-])$ from Table 7.1. The fraction,

$$f_{f_0\to\pi^+\pi^-} = \frac{\mathcal{B}(f_0 \to \pi^+\pi^-)}{\mathcal{B}(f_0 \to \pi^+\pi^-) + \mathcal{B}(f_0 \to K^+K^-)}, \tag{7.2}$$

is calculated to be 0.64 ± 0.08 for Solution 1 and 0.38 ± 0.06 for Solution 2. The $f_{f_0\to\pi^+\pi^-}$ is also determined by the BES Collaboration, which uses the same parametrisation for the f_0, to be 0.75 ± 0.12 [39]. Therefore, the solutions with a low $f_0K^0_S$ fraction (Solution 1 and 3) are preferred.

It is likely that the $f_{\rm X}$ described in this analysis and the $B^0 \to K^0_S\pi^+\pi^-$ analysis, is the

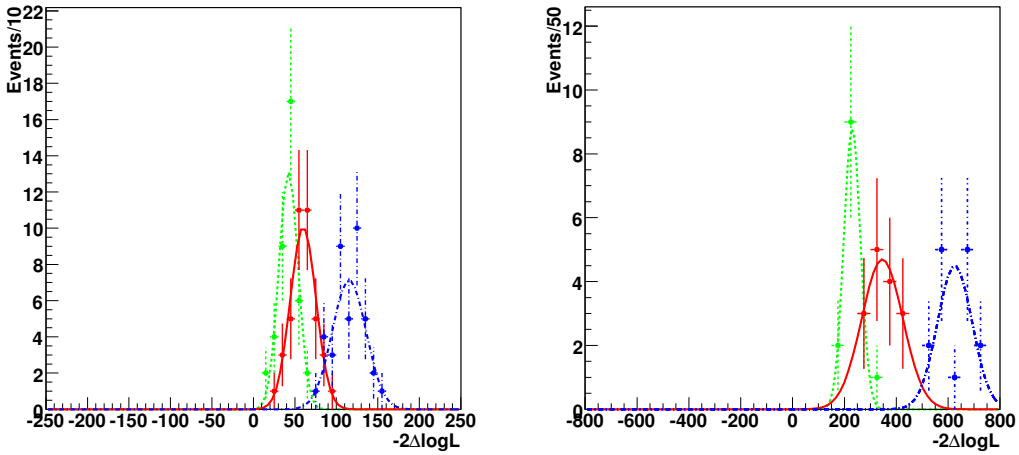

Figure 7.5: Difference in $-2\log\mathcal{L}$ using toy MC with 10 times (left) and 50 times (right) the current data set between Solution 1 and Solution 2 (red), Solution 3 (green) and Solution 4 (blue).

same state, $f_0(1500)$. If this is the case, the ratio,

$$\frac{\mathcal{B}(f_0(1500)\to\pi^+\pi^-)}{\mathcal{B}(f_0(1500)\to K^+K^-)}, \tag{7.3}$$

is calculated to be 3.6 ± 2.6 for Solution 1 and 24.5 ± 1.0 for Solution 3. As the world average of this ratio is 4.1 ± 2.5 [35], the solutions with a low $f_X K^0_S$ fraction (Solution 1 and 2) are preferred.

Altogether, we conclude Solution 1 is preferred from external measurements.

7.1.3 Significance of CP Violation in the $B^0\to K^0_S K^+K^-$ Decay

For Solution 1, we perform the likelihood scans that include the systematic uncertainties and the model uncertainties by convolving the likelihood with a Gaussian with the width equal to the quadratic sum of the systematic and model uncertainties. The results for $\phi_1^{\rm eff}$ are shown in Fig 7.6. We estimate the significance for the mixing-induced CP violation as the value, $\sqrt{-2\Delta\log\mathcal{L}}$ at $\phi_1^{\rm eff}=0$ (deg.) in Fig. 7.6, using the Bayesian approach (Appendix E). For the $B^0\to\phi K^0_S$ decay, we find that the CP-conserving case of $\phi_1^{\rm eff}=0$ is excluded and the existence of the mixing-induced CP violation is determined at a significance of 3.9 σ.

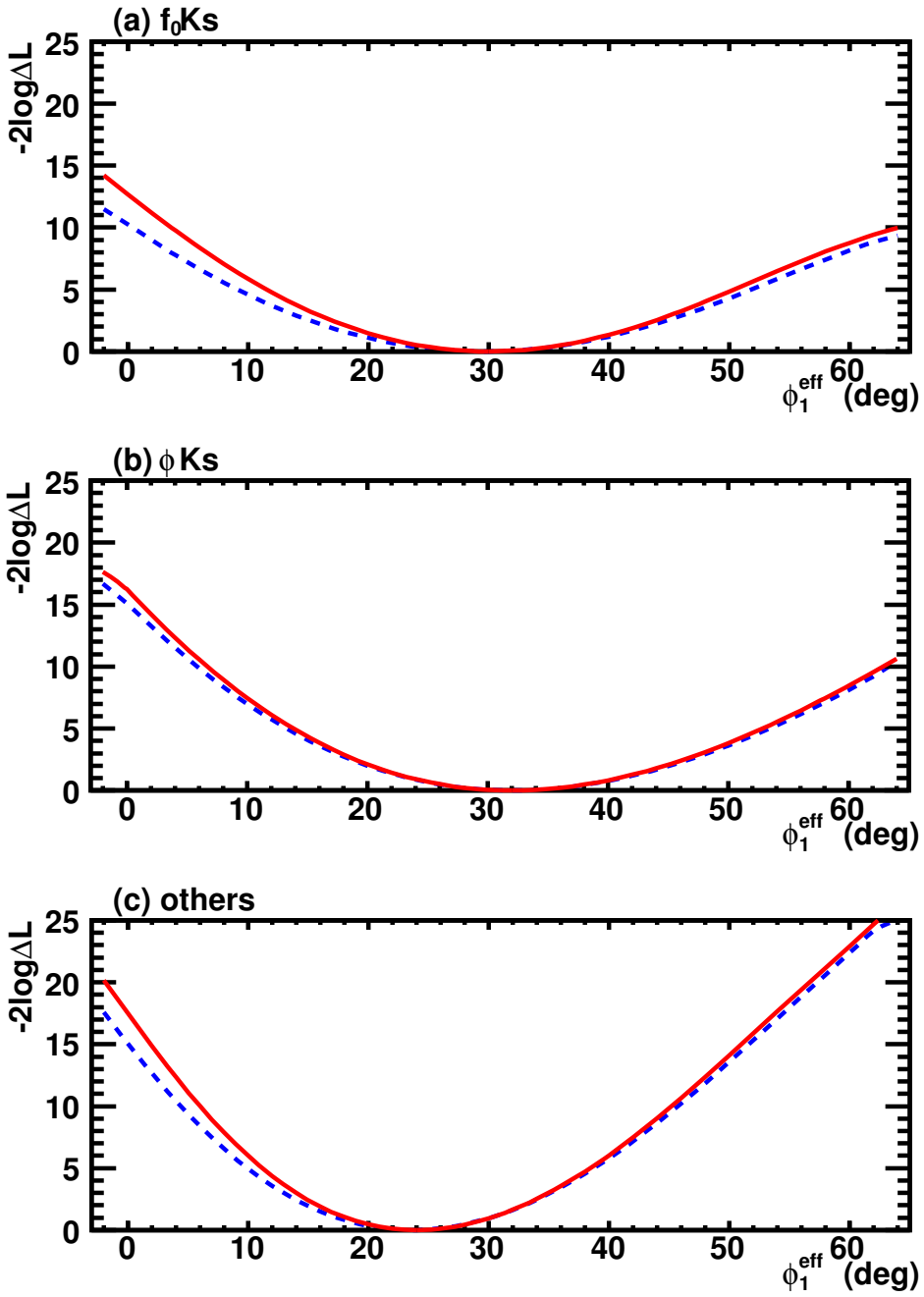

Figure 7.6: Likelihood scans for Solution 1 as a function of $\phi_1^{\rm eff}$ for $f_0K^0_S$ (top), ϕK^0_S (middle) and the others (bottom), with (blue dashed line) and without (red solid line) the systematic and Dalitz model uncertainties.

7.1.4 $\mathcal{S}_{CP}^{\rm eff}$ Measurements in the $B^0 \to K_S^0 K^+ K^-$ Decay Using Time-Dependent Dalitz Plot CP Fit

By converting $\phi_1^{\rm eff}$ to $\mathcal{S}_{CP}^{\rm eff}$ using Eq. 4.21 with the assumption of no correlations between $\phi_1^{\rm eff}$ and $\mathcal{A}_{CP}$, we obtain the quasi-two-body parameters, $-\eta_{CP}\mathcal{S}_{CP}^{\rm eff}$, for Solution 1 as follows,

$$-\eta_{CP}\mathcal{S}_{CP}^{\rm eff}(f_0 K_S^0) = +0.83^{+0.10}_{-0.18}, \quad (7.4)$$

$$-\eta_{CP}\mathcal{S}_{CP}^{\rm eff}(\phi K_S^0) = +0.89^{+0.10}_{-0.16}, \text{ and} \quad (7.5)$$

$$-\eta_{CP}\mathcal{S}_{CP}^{\rm eff}(\text{others}) = +0.75^{+0.12}_{-0.17}, \quad (7.6)$$

where the errors include the statistical, systematic and model uncertainties. The error is determined from a likelihood scan of $\mathcal{S}_{CP}^{\rm eff}$ with the $\mathcal{A}_{CP}$ parameter being fixed. The values of $\mathcal{S}_{CP}^{\rm eff}$ where $-2\log\mathcal{L}$ changes by unity, give estimates of the error, as shown by the green lines in Fig. 7.7.

7.2 Comparison between Quasi-Two-Body CP Fitted Result and Time-Dependent Dalitz Plot CP Fitted Result

We check the consistency in the fitted result between a quasi-two-body analysis and a time-dependent Dalitz plot analysis using both data sample and pseudo-experiments considering interferences. We use the subsample selected as $B^0 \to \phi K_S^0$ decays because this decay is experimentally clean and CP asymmetry measurement in it is our main physics motivation. We also estimate the validity of the quasi-two-body analysis using pseudo-experiments considering interferences.

Quasi-Two-Body Analysis to Data Sample

The $B^0 \to \phi K_S^0$ subsample of $B^0 \to K_S^0 K^+ K^-$ candidates is selected by additionally applying the requirement on the K^+K^- invariant mass to be consistent with the K^+K^- invariant mass, $|M_{K^+K^-} - M_\phi| < 0.01$ GeV/c^2. We find 226 $B \to \phi K_S^0$ candidate events in the signal region. The signal yield is obtained to be 181 ± 15 events and the result will be used to obtain an event-by-event signal fraction for the quasi-two-body analysis.

To determine the reference value that we compare with the fitted result to the $B^0 \to \phi K_S^0$ subsample using quasi-two-body analysis, we perform a time-dependent Dalitz plot fit to the $B^0 \to \phi K_S^0$ subsample where the signal parameters are fixed from the time-dependent Dalitz plot fit except for the two CP parameters of ϕK_S^0, c and d. We also check the statistical fluctuation in selecting the $B^0 \to \phi K_S^0$ sub sample among total events with $B^0 \to K_S^0 K^+ K^-$

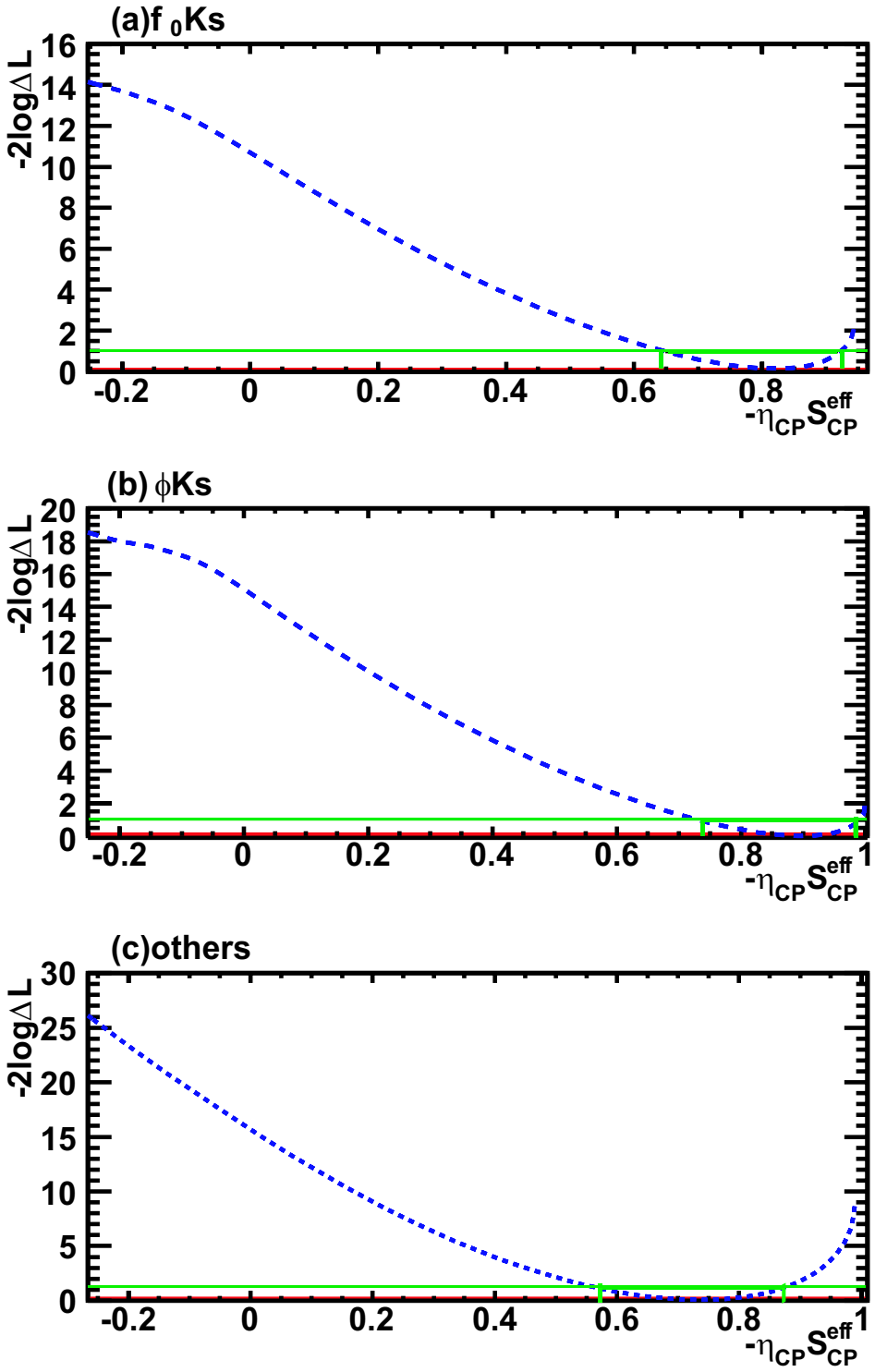

Figure 7.7: Likelihood scans for Solution 1 as a function of $-\eta_{CP}\mathcal{S}_{CP}^{\rm eff}$ for $f_0K_S^0$ (top), ϕK_S^0 (middle) and the others (bottom), including the systematic and Dalitz model uncertainties. The green lines indicate the $-\eta_{CP}\mathcal{S}_{CP}$ regions within the estimated errors.

final state. The fit yields

$$c(\phi K^0_S) = +0.07 \pm 0.10 \text{ (stat)} \quad \text{and} \quad d(\phi K^0_S) = (+26.9 \pm 8.6)^\circ \text{ (stat)}, \tag{7.7}$$

thus,

$$\mathcal{A}_{CP}(\phi K^0_S) \sim -0.14, \quad \text{and} \quad \mathcal{S}_{CP}(\phi K^0_S) \sim +0.80, \tag{7.8}$$

which is a deviation in ϕ_1 by 4° from the time-dependent Dalitz fitted result in Table 6.6. The statistical fluctuation of the $B^0 \to \phi K^0_S$ subsample is not so large comparing to the statistical error.

The CP asymmetry measurement is performed using the unbinned maximum likelihood fit as a function of Δt and $q_{\rm tag}$ without the event-by-event Dalitz dependence. This procedure becomes completely same as the quasi-two-body analysis used in the previous measurement by Belle [9]. The total PDF is written in Eq. 6.2 where the signal PDF is given by

$$\mathcal{P}_{\rm sig}(\Delta t, \ell, q_{\rm tag}) = \frac{e^{-|\Delta t|/\tau_{B^0}}}{4\tau_{B^0}} \Big[(1 - q_{\rm tag}\Delta w_\ell) + \\ -q_{\rm tag} \cdot (1 - 2w_\ell)(\mathcal{A}_{CP} \cos \Delta m_d \Delta t + \mathcal{S}_{CP} \sin \Delta m_d \Delta t \Big] \otimes R_{\rm sig}. \tag{7.9}$$

The fit yields

$$\mathcal{A}_{CP}(\phi K^0_S) = +0.14 \pm 0.19 \text{ (stat)} \quad \text{and} \quad \mathcal{S}_{CP}(\phi K^0_S) = +0.04 \pm 0.32 \text{ (stat)}, \tag{7.10}$$

thus,

$$c(\phi K^0_S) \sim -0.07 \quad \text{and} \quad d(\phi K^0_S) \sim 1.2^\circ \text{ or } 88.8^\circ, \tag{7.11}$$

which does not agree well with the time-dependent Dalitz plot fitted results given in Eq. 7.8 and Eq. 7.7.

Quasi-Two-Body Analysis to the Pseudo-Experiments Considering Interferences

We check the origin of this discrepancy in the fitted results to data by the two methods using the pseudo-experiments considering interferences. We consider two possibilities: the difference in the methods or the statistical uncertainty.

The difference in the signal PDF between the quasi-two-body analysis and the time-dependent Dalitz plot analysis is that the former ignores the Dalitz dependence, which is equal to the interferences, and the latter does not. We estimate the systematic contribution from the interferences between the $K^0_S K^+ K^-$ final state to the quasi-two-body fitted results in $B^0 \to \phi K^0_S$.

In this research, we apply the time-dependent Dalitz plot analysis to data sample of $B^0 \to K^0_S K^+ K^-$ system because there are large overlap regions among the wide non-resonance and the resonances in Dalitz plane (Fig. 4.3) and could potentially interfere with each other. In

the obtained fitted results to data, we actually see the sizable interference terms of the Dalitz relative phases as in Table 6.6. We generate 1000 signal pseudo-experiments with the same size of the signal yield using all the parameters of Solution 1. We select the $B^0 \to \phi K^0_S$ sub sample by the same requirement to $M_{K^+K^-}$ invariant mass as in the previous section and repeat the quasi-two-body fit to each sample.

Figure 7.8 shows the residual distribution for $\mathcal{A}_{CP}$ and $-\eta_{CP}\mathcal{S}_{CP}$, respectively. We can consider the mean values of the fit by the single Gaussian to the residual distributions as the systematic contributions. The measured $\mathcal{A}_{CP}$ has a small deviation from the generated $\mathcal{A}_{CP}$ by -0.04, while the measured $-\eta_{CP}\mathcal{S}_{CP}$ has a sizable systematic shift by -0.19 with the input value of 0.89. Since the deviation of the $-\eta_{CP}\mathcal{S}_{CP}(\phi K^0_S)$ is considered to originate from the contribution of $f_0 K^0_S$ with the opposite CP eigenvalue, we could define the dilution factor, $f_{\rm dilution}$, as,

$$\mathcal{S}_{CP}(\text{corrected}) = f_{\rm dilution} \times \mathcal{S}_{CP}(\text{measured}), \tag{7.12}$$

and therefore

$$f_{\rm dilution} = \frac{0.89}{0.89 - 0.19} \sim 1.27 \pm 0.02. \tag{7.13}$$

Since the dilution factor $f_{\rm dilution}$ significantly deviates from unity, we find that the fitted results using quasi-two-body analysis are inconsistent with the generated $\mathcal{S}_{CP}$ values. The pull distributions in Fig. 7.9 also support these tendencies. Note that we have already confirmed that the fitted results in the time-dependent Dalitz plot fit can reproduce the generated $\mathcal{A}_{CP}$ and ϕ_1 values using both the same toy MC samples, as described in § 6.2.4.

Therefore, we conclude the sizable interferences in the $B^0 \to K^0_S K^+ K^-$ system also influence the $B^0 \to \phi K^0_S$ region. To obtain the correct measurement values of CP asymmetries in $B^0 \to \phi K^0_S$, we should apply the time-dependent Dalitz analysis to $B^0 \to K^0_S K^+ K^-$ system, or apply the quasi-two-body analysis and assign the interference dilution factor, which is obtained using the time-dependent Dalitz analysis.

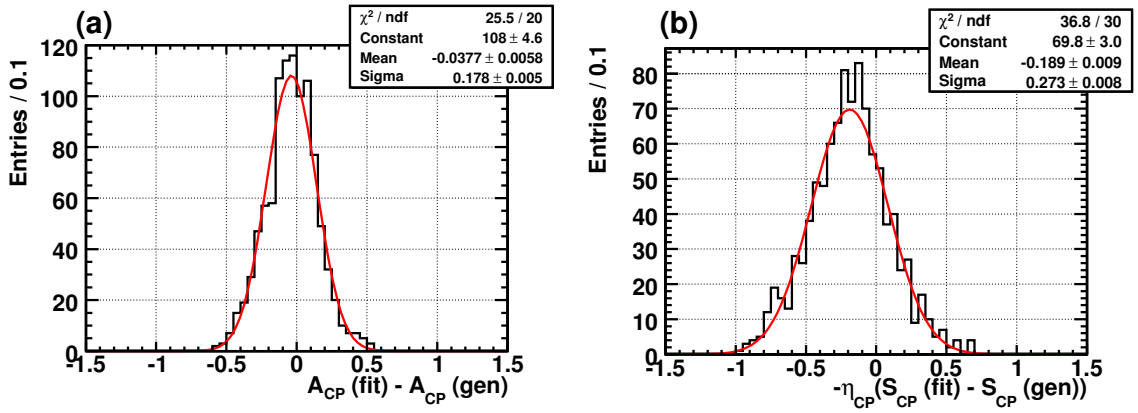

Figure 7.8: The residual distributions from the quasi-two-body fitted results using the pseudo-experiments considering interferences (a) $\mathcal{A}^{\rm fit}_{CP}$ - $\mathcal{A}^{\rm gen}_{CP}$ and (b) $-\eta_{CP}(\mathcal{S}^{\rm fit}_{CP}$ - $\mathcal{S}^{\rm gen}_{CP})$. The solid red curves show the fits onto the Gaussian distribution.

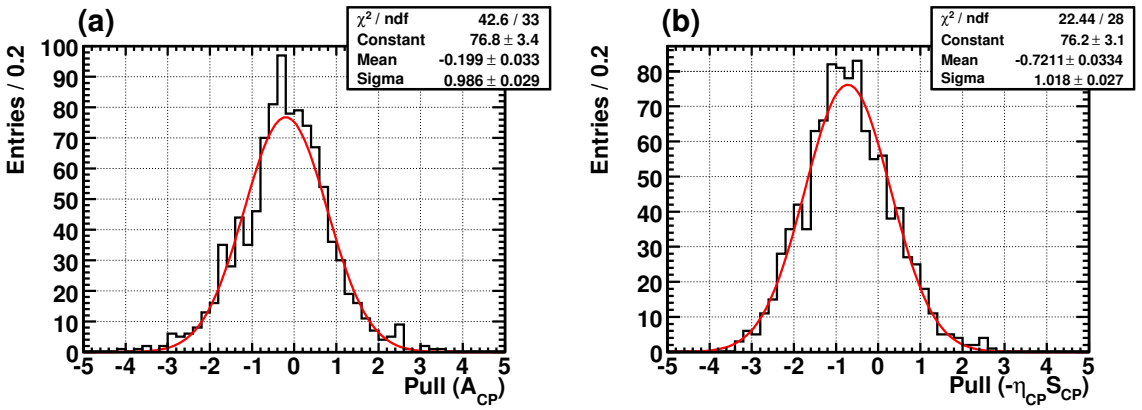

Figure 7.9: The pull distributions from the quasi-two-body fitted results using the pseudo-experiments considering interferences for (a) $\mathcal{A}_{CP}$ and (b) $-\eta_{CP}\mathcal{S}_{CP}$. The solid red curves show the fits onto the Gaussian distribution.

7.3 Comparison with Other Experiments

CP Asymmetry Measurements in the $B^0 \to K^0_S K^0_S$ Decay

Among $b \to d\overline{q}q$ transitions, $B^0 \to K^0_S K^0_S$ is the only decay channel whose CP asymmetry has been measured due to extremely small branching fractions of $b \to d$ transitions in the Standard Model. The BaBar experiment, which is the B factory experiment at SLAC, also made a measurement using $(347.5\pm3.8)\times10^6$ $B\overline{B}$ pair. Their results [50] are

$$\mathcal{A}_{K^0_S K^0_S} = +0.40 \pm 0.41 \text{ (stat)} \pm 0.06 \text{ (syst) and} \quad (7.14)$$

$$\mathcal{S}_{K^0_S K^0_S} = -1.28^{+0.80}_{-0.73} \text{ (stat)}^{+0.11}_{-0.16} \text{ (syst)}, \quad (7.15)$$

which are outside the physical region. Of their signal yield of 32 ± 8 events, 75 % (§ 5.3.1) can be used for the time-dependent CP measurement. This fraction is higher than that for Belle (56 %). It is because BaBar has a larger vertex detector, has a larger acceptance for K^0_S decays, and thus decay vertices of high momentum K^0_S particles and B decay vertices utilizing them can be efficiently reconstructed by their larger vertex detector. Due to the efficient B decay vertex reconstruction using K^0_S decay vertices, BaBar obtains the result with comparable errors although they use half as much as our statistics.

By combining the results in Eq. 7.14 and 7.15 from BaBar and in Eq. 6.9 and 6.10 [51] from Belle using the χ^2 fit that takes into account statistical and systematic errors, the averaged CP asymmetry in the $B^0 \to K^0_S K^0_S$ decay by the HFAG group [20] is shown in Figure 7.10 and obtained as,

$$\mathcal{A}_{K^0_S K^0_S} = +0.06 \pm 0.26 \text{ (total) and } \mathcal{S}_{K^0_S K^0_S} = -1.08 \pm 0.49 \text{ (total)}, \quad (7.16)$$

with the χ^2/degree of freedom of 2.5/2 at the confidence interval of 71%. Although both statistical errors are quite large, the results from BaBar and Belle are consistent within the

errors. In addition, our result shown in this thesis is the world's most precise measurement of CP asymmetry in the $B^0 \to K^0_S K^0_S$ decay.

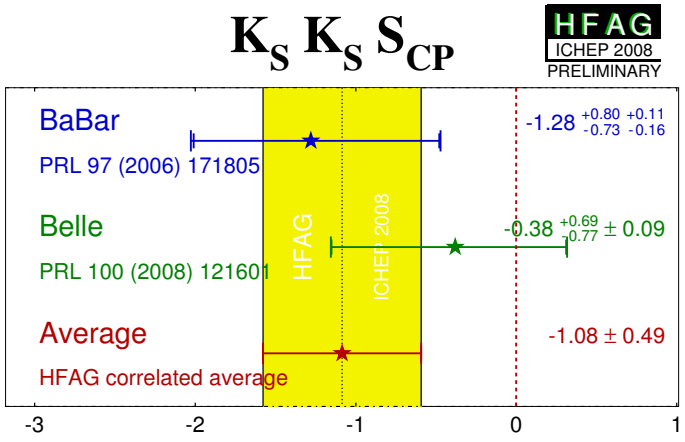

Figure 7.10: Complication of the results for the measured $\mathcal{S}_{K^0_S K^0_S}$ in BaBar, Belle and the averaged $\mathcal{S}_{K^0_S K^0_S}$ from the HFAG group.

CP Asymmetry Measurements in the $B^0 \to K^0_S K^+ K^-$ Decay

BaBar also measures CP-violation parameters in the $B^0 \to K^0_S K^+ K^-$ decay using the time-dependent Dalitz plot analysis with approximately 465×10^6 $B\overline{B}$ pairs [38]. BaBar's method involves fitting the Dalitz plot in which all components share the same CP parameters. They fix the Dalitz plot amplitudes and phases and perform a fit in the low mass region, $M(K^+K^-) < 1.1$ GeV/c^2, releasing the ϕK^0_S and $f_0 K^0_S$ CP parameters. After that, they perform a similar fit in the high mass region, $M(K^+K^-) > 1.1$ GeV/c^2 to obtain the CP parameters of the non-resonant component. They obtain,

$$\phi_1(\phi K^0_S) = (7.7 \pm 7.7 \pm 0.9)^\circ, \quad (7.17)$$
$$\mathcal{A}_{CP}(\phi K^0_S) = 0.14 \pm 0.19 \pm 0.02, \quad (7.18)$$
$$\phi_1(f_0 K^0_S) = (8.5 \pm 7.5 \pm 1.8)^\circ, \quad (7.19)$$
$$\mathcal{A}_{CP}(f_0 K^0_S) = 0.01 \pm 0.26 \pm 0.07, \quad (7.20)$$
$$\phi_1(\text{others}) = (29.5 \pm 4.5 \pm 1.5)^\circ, \text{ and} \quad (7.21)$$
$$\mathcal{A}_{CP}(\text{others}) = 0.05 \pm 0.09 \pm 0.04, \quad (7.22)$$

where the first errors are statistical and the second are systematic. The measured ϕ_1^{eff} in the $B^0 \to \phi K^0_S$ and $B^0 \to f_0 K^0_S$ decays from BaBar shown in Eq. 7.17 and Eq. 7.19 do not agree with those from Belle shown in Eq. 6.30 and Eq. 6.29. Those from BaBar are consistent with no CP-violation and are smaller than those from Belle although both have large statistical

errors of ~ 8 deg. On the other hand, the measured $\phi_1^{\rm eff}$ in the $B^0 \to K^0_S K^+ K^-$ decay in high mass region from BaBar shown in Eq. 7.21 is consistent with the measured ϕ_1 in the non-resonant $B^0 \to K^0_S K^+ K^-$ decay (called others) shown in Eq. 6.31, although both still have statistical errors of ~ 5 deg. to some extent. To validate these inconsistencies in the $B^0 \to \phi K^0_S$ and $B^0 \to f_0 K^0_S$ decays and consistency in the non-resonant $B^0 \to K^0_S K^+ K^-$ decay between Belle and BaBar, we should wait for more statistics from both experiments.

7.4 Search for New Weak Phases in Flavor-Changing Neutral Current Decays

7.4.1 Theoretical Expectation on CP Asymmetries within the Standard Model

In order to search for new weak phases in $b \to s$ and $b \to d$ transitions, we compare the measurements of mixing-induced CP asymmetry, $\mathcal{S}_{CP}$, in the $B^0 \to \phi K^0_S$, $B^0 \to K^0_S K^+ K^-$ and $B^0 \to K^0_S K^0_S$ decays with the Standard Model expectation. Even in the Standard Model, the expectation on $\mathcal{S}_{CP}$ in $b \to s$ transitions is not exactly equal to $\sin 2\phi_1$, while the expectation on $\mathcal{S}_{CP}$ in $b \to d$ transitions is not exactly equal to zero.

In this section, we describe the Standard Model uncertainties in $\mathcal{S}_{CP}$ originating from the higher order effects than that in the quark mixing with top quark dominance in the loop diagram.

To consider these effects, we employ the following approaches: SU(3) relations [55], QCD factorizations (QCDF) [56], charming penguin [57] and final state interactions (FSI) [58]. SU(3) relations give constraints to $\delta\mathcal{S}_{CP}$ bound by using the SU(3) relations to estimate the amplitudes of $V^*_{ub}V_{us}$, while QCD factorization approaches provide constraints on $\delta\mathcal{S}_{CP}$ in a model-dependent way. FSI includes the contributions from the intermediate states to the final state. On the other hand, for the non-resonant $B^0 \to K^0_S K^+ K^-$ decay, sizable dilution due to the color-allowed $b \to u$ tree transitions is expected in the high $M(K^+K^-)$ region [59]. The penguin dominance of this decay is estimated using the isospin relation in three kaon system [60]. For the $B^0 \to K^0_S K^0_S$ decay, we consider the Standard Model expectations including higher order effects from light quarks [61] as well as QCD factorizations [62]. The details of these models are given in the corresponding references. Table 7.3 summarizes the measurements and the theoretical expectations.

From Table 7.3, it is interesting to note that $\mathcal{S}_{CP}$ in the $B^0 \to \phi K^0_S$ decay has extremely small theoretical uncertainties ($\mathcal{O}(0.01)$) in every model above and the expectations are slightly above $\sin 2\phi_1$. For the non-resonant $B^0 \to K^0_S K^+ K^-$ decay, the theoretically uncertainties are larger ($\mathcal{O}(0.1)$) due to the color-allowed $b \to u$ transitions. In addition, there can be unknown wide resonances with s-wave, dilutions of which by the interferences are difficult to estimate. For the $B^0 \to K^0_S K^0_S$ decay, although the uncertainties are of order of $\mathcal{O}(0.1)$ [2], a large CP violation could indicate a new physics effect [10].

We compare the current experimental results with the expectations. For the $B^0 \to \phi K^0_S$ decay, the experimental uncertainty of ± 0.16 is much larger than the theoretical uncertainty of $\mathcal{O}(0.01)$. For the $B^0 \to K^0_S K^+ K^-$ decay, the experimental uncertainty of ± 0.17 is comparable to the theoretical uncertainty. For the $B^0 \to K^0_S K^0_S$ decay, the expected $\mathcal{A}_{K^0_S K^0_S}$ and $\mathcal{S}_{K^0_S K^0_S}$ values deviate from zero by $\sim +0.1$. Although this deviation is small comparing to

[2] This uncertainty comes from the measurements of the branching fractions in the other $b \to d$ decays, which will be improved as the statistics increases.

the current experimental central values, the direction of it is the opposite from the deviation of the current experimental central values from zero, which enlarge the significance of the difference between the experimental and the expected values.

We conclude that our results are consistent with the Standard Model expectation in both $B^0 \to \phi K^0_S$ and $B^0 \to K^0_S K^+ K^-$ decays in $b \to s$ transitions as well as the $B^0 \to K^0_S K^0_S$ decay in $b \to d$ transitions with in the current experimental uncertainties.

Table 7.3: Measurements and theoretical predictions of $\delta\mathcal{S}_{CP}$, in the $B^0 \to \phi K^0_S$ and $B^0 \to K^0_S K^+ K^-$ decays, $\mathcal{A}_{CP}$ and $\mathcal{S}_{CP}$ in the $B^0 \to K^0_S K^0_S$ decay from the various models within the Standard Model. The symbol, $\delta\mathcal{S}_{CP}$, corresponds $-\eta_{CP}\mathcal{S}_{CP} - \sin 2\phi_1$. The column, Quark Mixing, represents the first-order approximation assuming only top quark is mediated in the loop diagrams. For the $\sin 2\phi_1$ value, we employ the world average measurement in the $B^0 \to J/\psi K_0$ decay [20].

	Measured value	Quark mixing			
$\delta\mathcal{S}_{CP}(\phi K^0_S)$	$+0.22 \pm 0.16$	0			
$\delta\mathcal{S}_{CP}(K^0_S K^+ K^-)$	$+0.08 \pm 0.17$	0			
$\mathcal{S}_{CP}(K^0_S K^0_S)$	-0.38 ± 0.77	0			
$\mathcal{A}_{CP}(K^0_S K^0_S)$	-0.38 ± 0.38	0			
	SU(3) Relations	QCDF	Charming Penguins	FSI	U-spin
$\delta\mathcal{S}_{CP}(\phi K^0_S)$	$\lvert\delta\mathcal{S}_{CP}\rvert < 0.25$	[0.01∼0.05]	$+0.03 \pm 0.05$	$+0.029 \pm 0.037$	–
$\delta\mathcal{S}_{CP}(K^0_S K^+ K^-)$	$\lvert\delta\mathcal{S}_{CP}\rvert < 0.22$	–	–	–	+0.13
$\mathcal{S}_{CP}(K^0_S K^0_S)$	–	[0.15∼0.17]	$0.02 \leq \mathcal{A}^2_{CP}$	–	–
$\mathcal{A}_{CP}(K^0_S K^0_S)$	–	[0.02∼0.13]	$+\mathcal{S}^2_{CP} \leq 0.125$	–	–

7.4.2 Demonstration of Constraints to Weak Phases of New Physics using Measurements of CP asymmetries

Although the measured CP asymmetries in both $B^0 \to \phi K^0_S$ and $B^0 \to K^0_S K^0_S$ are found to be consistent to the Standard Model prediction, one can make some constraints on New Physics. In this section, we demonstrate how the measured CP asymmetries in the $B^0 \to \phi K^0_S$ and $B^0 \to K^0_S K^0_S$ decays can make constraints on new weak phase of New Physics.

First, we show the model-independent example in the $B^0 \to \phi K^0_S$ decay. Figure 7.11 shows the expectations of the $\mathcal{S}_{CP}$ in the $B^0 \to \phi K^0_S$ decay as a function of the weak phase of New Physics assuming some ratio of the amplitudes from New Physics and the Standard Model [63]. The orange region is preferable by the measurement corresponding to the region within 1 σ. The gray region is excluded by the measurement over 5 σ. Constraint on the new weak phase is possible if New Physics is found directly by the LHC.

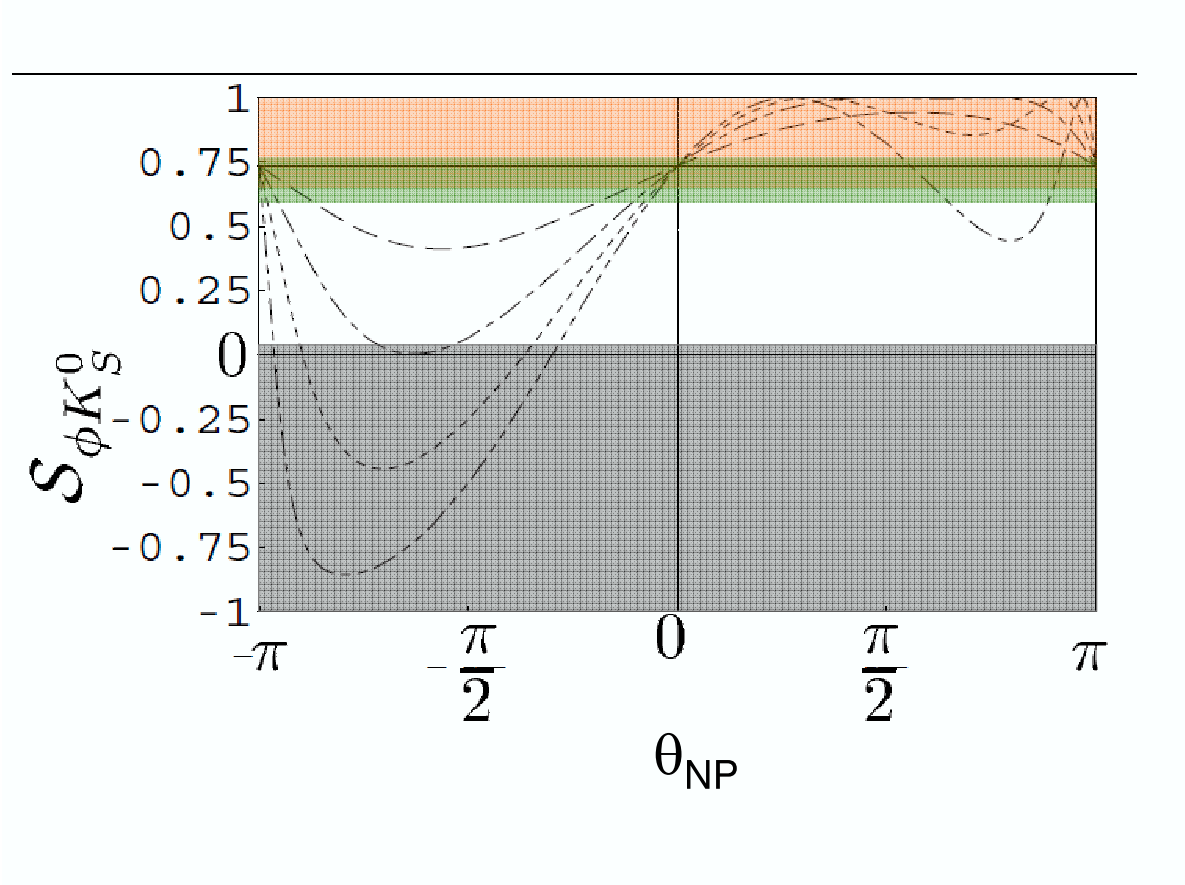

Figure 7.11: $\mathcal{S}_{CP}$ in the $B^0 \to \phi K^0_S$ decay including the New Physics contributions as a function of θ_{NP} for different values of $|A^{NP}/A_{\text{StandardModel}}|$: 0.2 (dashed), 0.4 (dashed-dotted), 0.6 (dotted), 0.8 (dashed-double-dotted). The green region represents the expectation from the measurement of $\mathcal{S}_{CP}$ in the $c\bar{c}s$ decays. The orange (gray) region is preferable (excluded) constraint from the measurement of $\mathcal{S}_{CP}$ in the $B^0 \to \phi K^0_S$ decay, respectively. Here, we assume that the strong phase difference between NP and the Standard Model is negligible.

Figure 7.12 shows the expectations of the $\mathcal{A}_{CP}$ versus $\mathcal{S}_{CP}$ in the $B^0 \to K^0_S K^0_S$ decay in the models of MSSM with LR mass insertion and MSSM with R-parity R mass violation [10]. The preferable constraint from the measurement of $\mathcal{A}_{CP}$ and $\mathcal{S}_{CP}$ in the $B^0 \to K^0_S K^0_S$ within 1 σ is very wide due to large statistical error of ~ 0.4 and ~ 0.7, respectively. We need more statistics to give concrete constraints on New Physics.

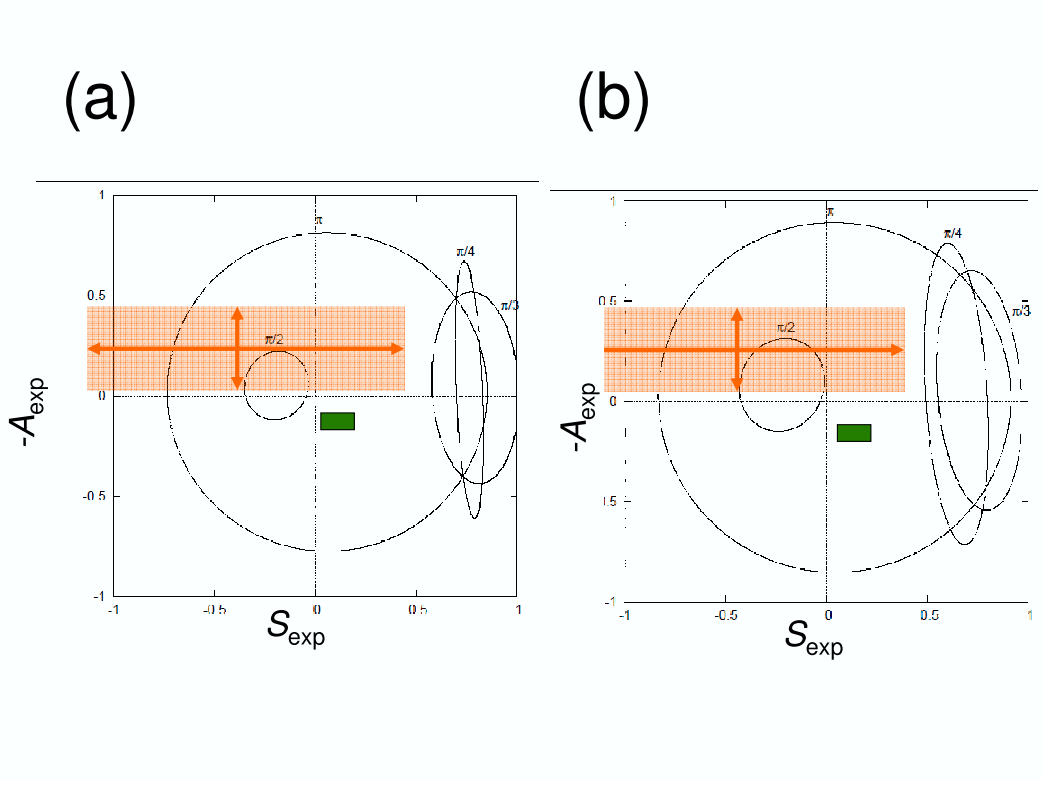

Figure 7.12: The correlations of $\mathcal{A}_{CP}$ and $\mathcal{S}_{CP}$ in the $B^0 \to K^0_S K^0_S$ decay including the New Physics contributions expected from (a) MSSM with LR insertion and (b) MSSM with R-parity R mass violation, respectively. The green region represents the expectation from the Standard Model. The orange region shows preferable constraint from the measurement of $\mathcal{A}_{CP}$ and $\mathcal{S}_{CP}$ in the $B^0 \to K^0_S K^0_S$ decay, respectively.

7.4.3 Future Prospects

The discussions in the previous sections are limited by the statistical uncertainties of the measurements except for that in the non-resonant $B^0 \to K^0_S K^+ K^-$ decay. In other words, the uncertainty improves if the statistics increases. One of the goals of this study is to establish the analysis methods and is to make reliable prospects of $B^0 \to \phi K^0_S$ and $B^0 \to K^0_S K^0_S$ results for future upgrade projects such as Super-KEKB [63].

The analysis methods of this thesis take into account all the uncertainties that were ignored

due to smaller statistics so far, such as the dilution from the interference effect among $B^0 \to K^0_S K^+ K^-$ final state to the CP asymmetry measurement in the $B^0 \to \phi K^0_S$ decay. These methods can be employed in the same way even when the statistics increase. Therefore, the decrease of the experimental uncertainties with larger statistics can be expected utilizing the current statistical and systematic errors with a relatively good precision. In this section, we give the expected experimental uncertainties with higher statistics and evaluate the feasibility of this search taking into account the luminosity designed in the Super-KEKB [63].

The main contributions of the systematic uncertainties are originating from the background, the vertex reconstruction and the wrong tag fraction as well as Dalitz model, as shown in Table 6.2, 6.11. With a larger integrated luminosity, some of the systematic uncertainties can be reduced. We estimate the uncertainties and treat the reducible and irreducible systematic sources, separately. The vertex reconstruction, Δt resolution function parameterization and tag-side interference are included in the former, while the remaining are in the latter.

We calculate the experimental uncertainties as a function of integrated luminosity as shown in Fig. 7.13. Until an integrated luminosity is lower than 5 ab^{-1}, the experimental uncertainties are dominant in all the decays expect for $B^0 \to K^0_S K^+ K^-$. We do not have to consider the theoretical uncertainties seriously.

At an integrated luminosity of 5 ab^{-1}, the errors of ϕ_1 in the $B^0 \to \phi K^0_S$ and $B^0 \to K^0_S K^+ K^-$ decays, and $\mathcal{S}_{CP}$ in the $B^0 \to K^0_S K^0_S$ decay become 3.3 deg., 2.5 deg. and 0.3, respectively. By converting $\delta\phi_1$ to $\delta\mathcal{S}_{CP}$, the experimental uncertainties for $\mathcal{S}_{CP}$ in $B^0 \to \phi K^0_S$ and $B^0 \to K^0_S K^+ K^-$ are ~ 0.12 and ~ 0.09, respectively. Note that this accuracy is sufficient only when the deviations are large enough ($\mathcal{O}(0.3)$).

At an integrated luminosity of 50 ab^{-1}, we could measure ϕ_1 in the $B^0 \to \phi K^0_S$ and $B^0 \to K^0_S K^+ K^-$ decays, and $\mathcal{S}_{CP}$ in the $B^0 \to K^0_S K^0_S$ decay with an accuracy of 1.5 deg., 1.6 deg. and 0.1, respectively, which could be comparable with the theoretical uncertainties. Some of the theoretical uncertainties are limited by the experimental results in rare B decays and furthermore only experimental upper bounds are available for many of these decays. For example, the prediction of CP asymmetry in $B^0 \to \phi K^0_S$ by SU(3) relation in Ref. [55] is limited by the unmeasured branching fraction of $B^0 \to \phi\pi^0$ and $B^0 \to \bar{K}^{*0} K^0$ via $b \to d$ transitions. As these bounds could become significantly stronger with larger statistics, the theoretical precision will also be improved. Therefore, this method will be powerful when such a high statistics becomes available.

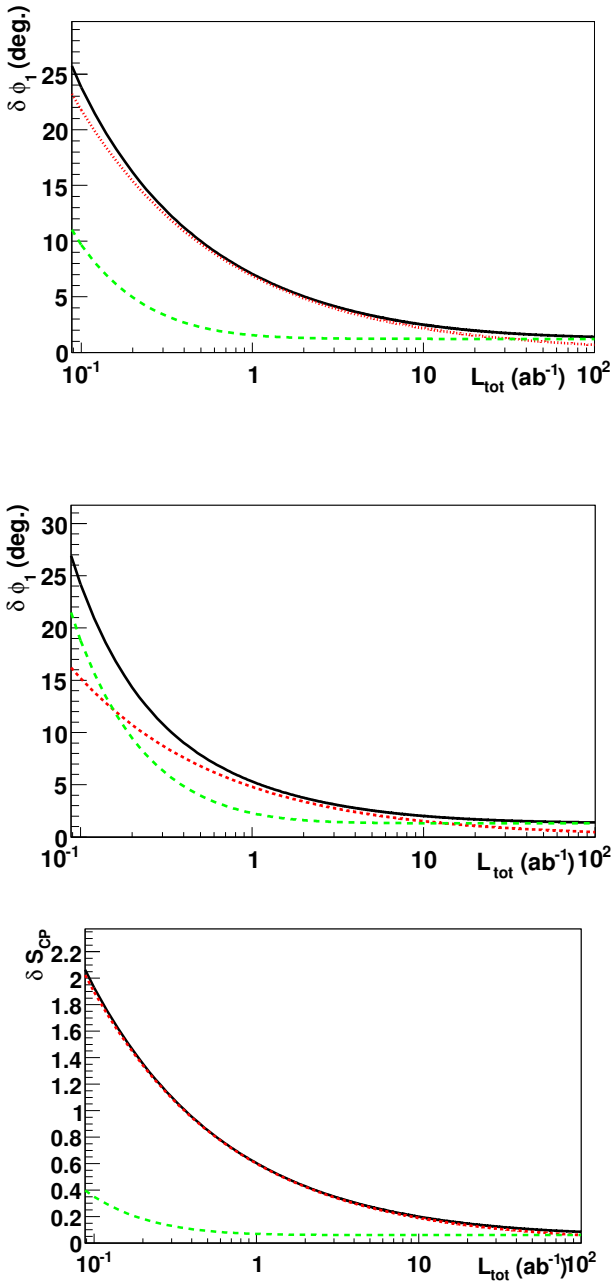

Figure 7.13: Estimated uncertainties as a function of the integrated luminosity in (top) $B^0 \to \phi K^0_S$, (middle) $B^0 \to K^0_S K^+ K^-$, and (bottom) $B^0 \to K^0_S K^0_S$ decays. The red dotted, and green dashed curves show the statistical and systematic errors, respectively. The solid black lines show the total error obtained by the quadratic sum of statistical and systematic errors.

Chapter 8

Conclusion

We measure time-dependent CP-violating asymmetry in the $B^0 \to K^0_S K^0_S$ decay, which is dominated by flavor-changing $b \to d\overline{s}s$ loop transitions, based on a data sample of 657×10^6 $B\overline{B}$ pairs recorded with the Belle detector. We obtain

$$\mathcal{A}_{K^0_S K^0_S} = -0.38 \pm 0.38\ (\text{stat}) \pm 0.05\ (\text{syst}) \text{ and} \tag{8.1}$$

$$\mathcal{S}_{K^0_S K^0_S} = -0.38\ ^{+0.69}_{-0.77}\ (\text{stat}) \pm 0.09\ (\text{syst}), \tag{8.2}$$

which is one of the most precise measurements of CP asymmetry in the $B^0 \to K^0_S K^0_S$ decay. $B^0 \to K^0_S K^0_S$ is a unique mode with pure $b \to d\overline{q}q$ transition and without any $b \to s$ background, and is the only decay mode whose CP asymmetry has been measured among $b \to d\overline{q}q$ transitions.

No significant CP asymmetry is found for the decay and this result is consistent with the Standard Model expectation with the current statistics.

In the B^0 decays with the $K^0_S K^+ K^-$ final state, the dominant decay channels, $B^0 \to \phi K^0_S$, non-resonant $B^0 \to K^0_S K^+ K^-$ and $B^0 \to f_0 K^0_S$, are dominated by $b \to s\overline{q}q$ loop transitions. We consider the interferences between the decay channels with the same final state by simultaneously fit to the Dalitz distribution in addition to Δt and the tagged b flavor distributions. We extract $\mathcal{A}_{CP}$ and CP-violating phases as well as the relative magnitudes and phases for each decay channel. The most preferable solution is as follows,

$$\mathcal{A}_{CP}(\phi K^0_S) = +0.04 \pm 0.20\ (\text{stat}) \pm 0.10\ (\text{syst}) \pm 0.02\ (\text{Dalitz model}), \tag{8.3}$$

$$\phi_1(\phi K^0_S) = (32.0^{+8.8}_{-8.3}\ (\text{stat}) \pm 1.8(\text{syst}) \pm 0.8(\text{Dalitz model}))^\circ \text{ and} \tag{8.4}$$

$$\mathcal{S}^{\text{eff}}_{CP}(\phi K^0_S) = +0.89^{+0.10}_{-0.16}\ (\text{total}). \tag{8.5}$$

We obtain evidence for CP violation in the $B^0 \to \phi K^0_S$ decay at a significance of 3.9 σ. We compare the results with the CP asymmetry measurements in $b \to c\overline{c}s$ transitions as well as the theoretical prediction from the various models within the Standard Model. Our measurement is consistent with Standard Model expectation.

Appendix A

Maximum Likelihood Method

A maximum likelihood method has been frequently employed in this analysis and is the preferred method for data samples with low statistics. This is because the usual χ^2 technique assumes a Gaussian distribution of errors in each bin instead of a Poisson distribution. This can lead to a bias in the estimation of parameters and their uncertainties.

Consider a set of N independently measured quantities, x_i, which follows a PDF, $P(x;\alpha_\mu)$, where α_μ is a set of μ unknown parameters. The maximum likelihood method is designed to determine the most probable set of α_μ, $\alpha_\mu^{\rm fit}$, for which the PDF product over all data points, $\mathcal{L}(\alpha_\mu)$, is maximised,

$$\mathcal{L}(\alpha_\mu) = \prod_i^N P(x_i;\alpha_\mu). \tag{A.1}$$

However, since $\mathcal{L}(\alpha_\mu)$ is small, it is computationally easier to work with $\log\mathcal{L}(\alpha_\mu)$, which is also maximised for the same set of $\alpha_\mu^{\rm fit}$. The set of α_μ which maximises $\mathcal{L}(\alpha_\mu)$ satisfies

$$\frac{\partial\mathcal{L}(\alpha_\mu)}{\partial\alpha_\mu} = 0. \tag{A.2}$$

We construct the quantity, $-2\log\mathcal{L}(\alpha_\mu)$, which behaves like a χ^2 distribution. Therefore, the set of α_μ for which the difference between $-2\log\mathcal{L}(\alpha_\mu)$ and $-2\log\mathcal{L}(\alpha_\mu^{\rm fit})$ is unity, corresponds to one standard deviation from $\alpha_\mu^{\rm fit}$ and thus provides the basic error estimate of $\alpha_\mu^{\rm fit}$.

The most probable set of parameters, $\alpha_\mu^{\rm fit}$, is determined numerically with the fitting package, MINUIT [64]. Another set of errors can be calculated taking into account non-linearities and correlations between parameters. These errors are typically asymmetric and are known as the MINOS errors.

Appendix B

Particle Identification

B.1 $K^{\pm}/\pi^{\pm}$ Identification

Charged kaon identification is crucial for selecting $K^{\pm}$ to form $B \to K^0_S K^+ K^-$ decays. To discriminate between kaons and pions over a wide momentum range, the following three variables are used,

dE/dx measurement in the CDC,

time-of-flight measurement in the TOF and

number of photoelectrons measured in the ACC.

The momentum coverage by each detector is shown in Fig. B.1. Using the product of the particle identification (PID) modeling PDFs of each sub-detector, the PID likelihood ratio, $\mathcal{R}_{i/j}$ for a hypothesized signal particle species, i, against the background particle species, j is given as follows,

$$\mathcal{R}_{i/j} = \frac{P_i}{P_i + P_j} \text{ where } P_i \equiv P_i^{dE/dx} \times P_i^{\rm TOF} \times P_i^{\rm ACC} \ (i = e, \mu, \pi, K \text{ and } p). \tag{B.1}$$

The typical requirement for high purity kaons against pions is $R_{K/\pi} > 0.6$. The difference between MC and data in the likelihood, $\mathcal{R}_{K/\pi}$, in terms of track momentum and the polar angle is calibrated using inclusive $D^{*+} \to D^0[K^-\pi^+]\pi^+$ tagged control sample data. Figure B.2 (a) shows a scatter plot of the likelihood ratio, $\mathcal{R}_{K/\pi}$, as a function of the track momentum. With the requirement, $\mathcal{R}_{K/\pi} > 0.6$, kaons are clearly separated against pions up to $\sim 4\,\mathrm{GeV}/c$. Kaon efficiency and pion fake rate are also estimated using the same inclusive D^{*+} tagged sample as shown in Fig. B.2 (b). Kaon ID efficiency is estimated to be $\sim$80% and the pion fake rate is estmiated to be $\sim$10% with a track momemtum between 1 GeV/c and 3 GeV/c.

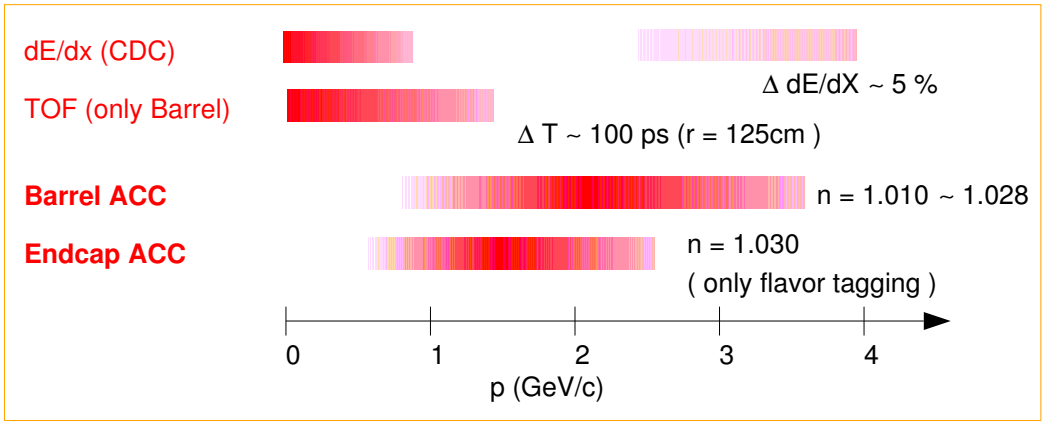

Figure B.1: Kaon ID coverage.

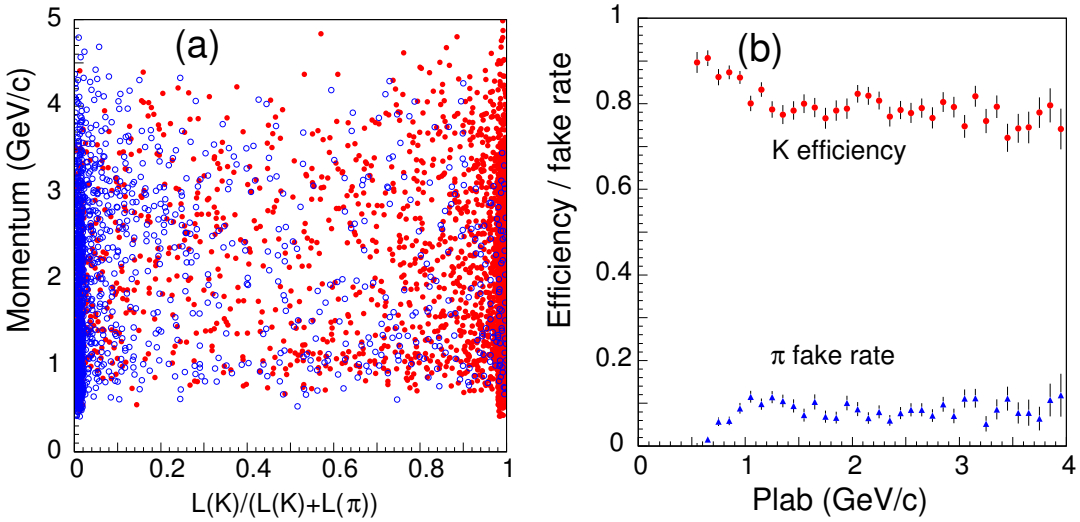

Figure B.2: (a) shows the total likelihood ratio, $\mathcal{R}_{K/\pi}$, as a function of the track momentum using an inclusive D^{*+} tagged control sample. (b) shows the kaon ID efficiency and pion fake rate as a function of track momentum for $\mathcal{R}_{K/\pi} > 0.6$.

B.2 Electron Identification

Electron identification is crucial for flavor-tagging and the reconstruction of control sample modes such as $B \to D(^*)e\nu$. To distinguish electrons from hadrons, two differences in their properties are used.

(1) The difference in the electronic magnetic shower caused by electrons and the hadronic shower (mainly pions) caused by hadrons.

(2) The difference in the velocity of electrons and hadrons with the same momentum.

The following five variables are used to form the electron ID likelihood. The former three make use of property (1) and the latter two make use of property (2), which is similar to the way kaon identification is performed.

The position of the charged track extrapolated to the ECL and the energy cluster position measured by ECL are compared. Electrons fully lose their energy in the ECL by electronic magnetic interaction and make a single shower, while hadrons partly lose their energy by hadronic interactions such as $\pi^- p \to \pi^0 n$, where $\pi^0 \to \gamma\gamma$, and make multiple showers. The electron's cluster position matches with the extrapolated track position better than that of the pion's, as shown in Fig. B.3a.

The ratio of the cluster energy measured by the ECL and the charged track momentum measured by the CDC, E/p, is measured. For electrons, $E/p \sim 1$ within measurement uncertainties in the interesting momentum range, $p > 1$ GeV/c. For hadrons, E/p is smaller because hadrons have smaller energy loss in the ECL as can be seen in Fig. B.3b.

The ratio of energy in the ECL summed in 3×3 crystals to that in 5×5 crystals in the transverse plane, E9/E25, is also measured. Electronic magnetic showers grow in the transverse direction by an order of the radiation length, $X_0 = 1.85$ cm, while hadronic showers grow wider due to multiple showers while hadrons are passing through the ECL. Electrons peak at E9/E25 ~ 0.95 with a small tail in the lower region, while pions have more events in the lower region and peak at E9/E25 ~ 1. Figure B.3c shows the E9/E25 distribution for electrons and pions with momentum between 0.5 GeV/c and 3.0 GeV/c.

The dE/dx measurement in the CDC and the number of photoelectrons measured in the ACC can also discriminate between electrons and pions.

By calculating the electron likelihood, $\mathcal{L}_e$, and non-electron likelihood, $\mathcal{L}_{non-e}$, the total electron likelihood ratio, $\mathcal{R}_{e/\mathrm{non}-e}$, is given as,

$$\mathcal{R}_{e/\mathrm{non}-e} = \frac{\mathcal{L}_e}{\mathcal{L}_e + \mathcal{L}_{\mathrm{non}-e}}. \tag{B.2}$$

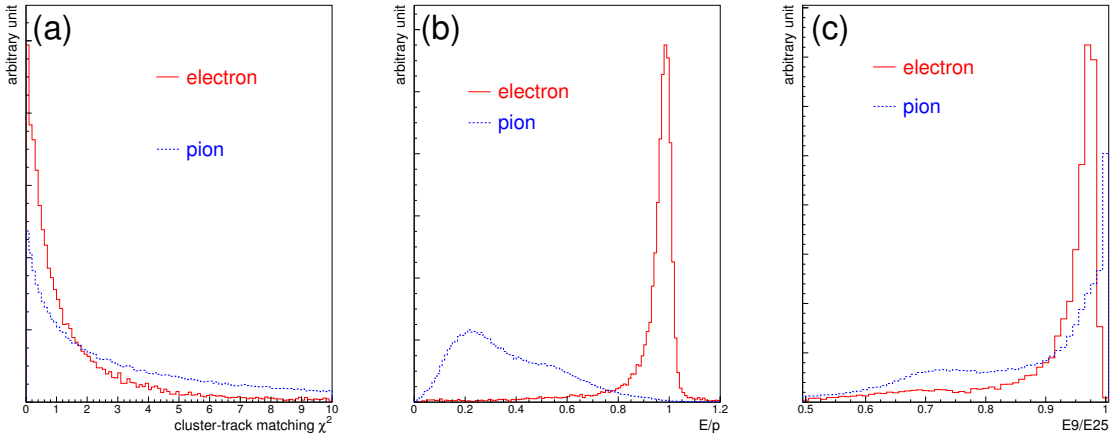

Figure B.3: (a) shows the cluster-track matching χ^2 distributions, (b) shows the E/p distributions and (c) shows the E9/E25 distributions for electrons and pions.

Figure B.4 shows the distribution of $\mathcal{R}_{e/\mathrm{non}-e}$ for electrons and charged pions using all the discriminants. A significant *epi* separation is achieved by $\mathcal{R}_{e/\mathrm{non}-e}$.

To calculate the non-electron PDFs, dedicated hadronic MC sample consisting of $B\overline{B}$ and $q\overline{q}$ events with the same ratio as data are used, which includes all decay channels without electrons. Since each variables depends on the momentum and polar angle of the charged track, each PDF is calculated in several bins of momentum and polar angle.

The typical electron ID requirement is $\mathcal{R}_{e/\mathrm{non}-e} > 0.5$. The efficiency in radiative Bhabha $e^+e^- \rightarrow e^+e^-\gamma$ events is measured and compared with MC expectations. As shown in Fig. B.5a, the measured efficiency in data agrees with the MC expectation in the momentum range between 1 GeV/c and 3 GeV/c, which covers almost the whole range used in flavor tagging. Fig.B.5b shows the polar angle dependence of the efficiency. In the barrel region, $35^\circ < \theta < 125^\circ$, there is good agreement between data and MC. However, in the end-cap region, the agreement is degraded since more material exists in the end-cap region.

Using the dedicated hadronic MC sample, the electron ID efficiency is estimated to be ∼92%. From an inclusive $K^0_S \rightarrow \pi^+\pi^-$ sample, the fake rate is estimated to be ∼0.5% for momemta between 1 GeV/c and 3 GeV/c.

B.3 Muon Identification

The muon identification algorithm is based on the following property: muons pass through the KLM with small deflections through multiple scattering, while hadrons, mainly pions, are scattered heavily by the material through strong interactions. The reconstructed charged track is extrapolated from the CDC into the KLM. By using the associated KLM hits with the

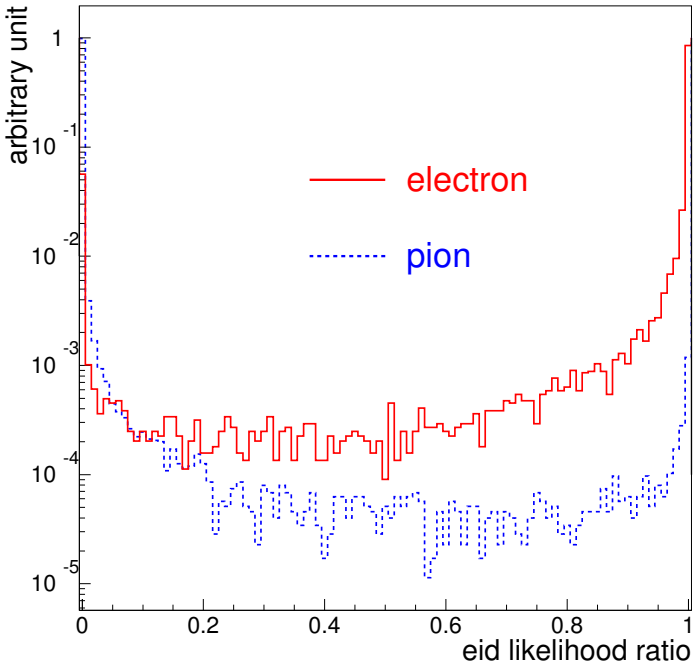

Figure B.4: The distribution of the electron ID likelihood ratio $\mathcal{R}_{e/\mathrm{non}-e}$ for electrons and charged pions.

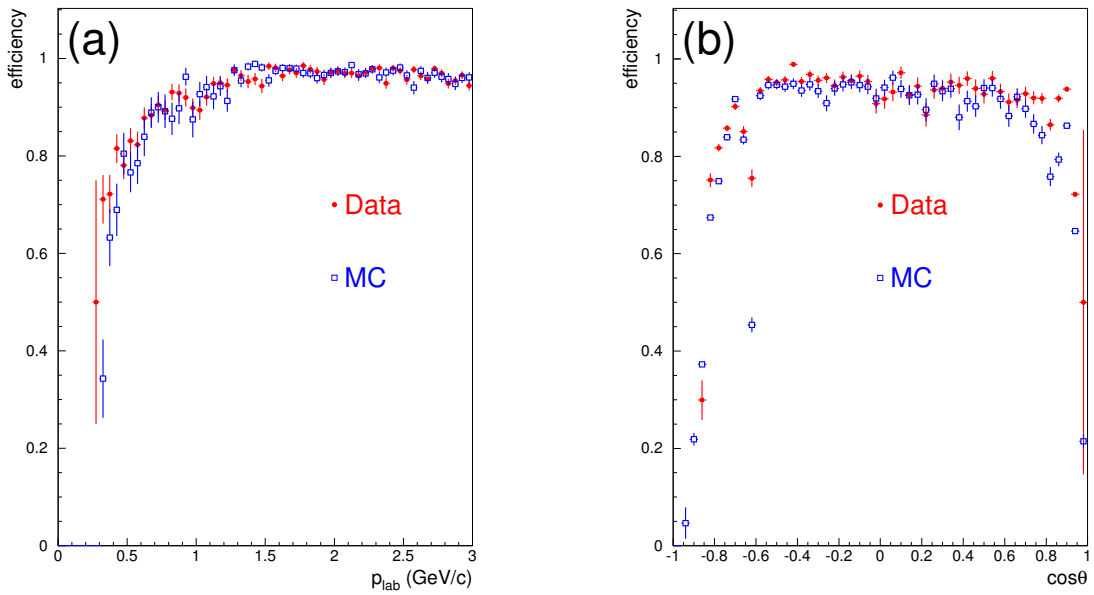

Figure B.5: The efficiency in radiative Bhabha events for data and for MC. (a) shows the efficiency as a function of momentum in the laboratory frame and (b) shows the efficiency as a function of cosθ.

extrapolated track, the charged track is refitted minimizing the χ^2, defined as the deviation of the associated KLM hits from the extrapolated KLM crossing points in the transverse direction. Two variables, ΔR and reduced χ^2, are used to form the muon likelihood. The variable, ΔR, is the difference between the measured hit from the associated KLM hits, and the expected hit extrapolated from the CDC in the outermost KLM layer with associated hits. By calculating the muon likelihood for μ, π and K using MC, the total muon likelihood ratio, R_μ, is given as follows,

$$R_\mu = \frac{\mathcal{L}_\mu}{\mathcal{L}_\mu + \mathcal{L}_\pi + \mathcal{L}_K}, \text{ where } \mathcal{L}_i = \mathcal{L}_i^{\Delta R} \times \mathcal{L}_i^{\chi^2} \ (i = \mu,\ \pi,\ K \text{ hypotheses}). \tag{B.3}$$

The muon ID efficiency and pion fake rate are estimated using the two-photon control sample, $e^+e^- \to e^+e^-\mu^+\mu^-$, and the inclusive $K^0_S \to \pi^+\pi^-$ sample, respectively, as shown in Fig. B.6. For charged tracks with momentum between 1.0 GeV/c and 3.0 GeV/c, the muon ID efficiency is measured to be ∼90% and the pion fake rate is measured to be below 2%.

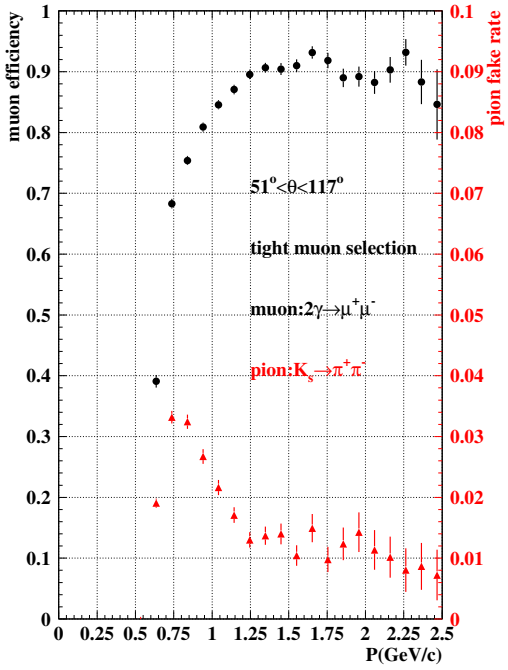

Figure B.6: Muon ID efficiency and fake rate as a function of momentum with the typical requirement for μ with high purity, $R_\mu > 0.9$.

Appendix C

Lineshapes of Resonances

C.1 Relativistic Breit-Wigner

Most resonances are described with the Relativistic Breit-Wigner (RBW) function [35] given by

$$\mathrm{RBW}_J(s) = \frac{1}{m_0^2 - s - im_0\Gamma_J(s)}, \tag{C.1}$$

where

$$\Gamma_J(s) = \Gamma\left(\frac{q(s)}{q_0}\right)^{2J+1}\left(\frac{m_0}{\sqrt{s}}\right)\frac{X_J^2(q(s))}{X_J^2(q_0)}. \tag{C.2}$$

The variable, s, is the Dalitz variable, J, is the relative orbital angular momentum between the resonance and the remaining particle, $m_0(\Gamma_0)$ is the mass (width) of the resonance, $q(s)(q_0)$, is the momentum of the resonance daughter in the $\sqrt{s}(m_0)$ frame, and $X_J(q)$ are the Blatt-Weisskopf barrier factors [34].

C.2 Flatté

The Flatté function [36] is a coupled-channel RBW that includes different contributions from π and K given by

$$\text{Flatté}(s) = \frac{1}{m_0^2 - s - i\Gamma(s)}, \tag{C.3}$$

where

$$\Gamma(s) = \Gamma_\pi(s) + \Gamma_K(s) \tag{C.4}$$

and

$$\Gamma_\pi(s) = 2g_\pi \frac{q(s)}{\sqrt{s}}, \tag{C.5}$$

$$\Gamma_K(s) = 2g_K \frac{q(s)}{\sqrt{s}}. \tag{C.6}$$

Below the $K-K$ threshold, $2ig_K q(s)/\sqrt{s}$ continues analytically to $-g_K\sqrt{(4m_K^2/s)-1}$.

We also try another description of the Flatté function [54] that was used in previous Dalitz analyses at Belle. $\Gamma(s)$ is replaced as follows,

$$\Gamma(s) = \Gamma_\pi(s) + \Gamma_K(s) \tag{C.7}$$

and

$$\Gamma_\pi(s) = g_\pi\sqrt{q(s)}, \tag{C.8}$$

$$\Gamma_K(s) = g_K\sqrt{q(s)}. \tag{C.9}$$

Appendix D

Full Correlation Matrices of the Four Solutions

Full correlation matrices of the four solutions are given in Table D.1, D.2, D.3 and D.4.

Table D.1: Correlation between each fit parameter for Solution 1.

	1	2	3	4	5	6	7	8	9	10	11	12	13	14	15	16	17	18
1 $a_{f_0 K_S^0}$	1.00	-0.22	-0.26	-0.09	-0.02	-0.19	0.33	0.30	-0.11	0.12	-0.10	0.19	0.04	-0.02	0.09	-0.20	0.06	-0.02
2 $a_{\phi K_S^0}$		1.00	-0.19	0.56	0.15	0.32	-0.75	-0.34	-0.32	0.19	-0.13	0.44	0.10	0.03	-0.05	0.12	-0.03	0.11
3 $a_{f_X K_S^0}$			1.00	-0.15	-0.06	0.01	-0.06	-0.01	-0.06	-0.11	0.13	-0.25	-0.02	-0.05	0.04	-0.08	0.01	-0.07
4 $a_{\chi_{c0} K_S^0}$				1.00	0.11	0.17	-0.56	-0.24	-0.24	0.41	-0.01	0.37	0.09	0.03	-0.01	0.07	-0.03	0.07
5 $a_{(K_S^0 K^+)_{\rm NR} K^-}$					1.00	-0.27	-0.20	-0.14	-0.11	-0.13	-0.06	-0.39	-0.05	-0.04	-0.24	0.15	-0.02	0.09
6 $a_{(K_S^0 K^-)_{\rm NR} K^+}$						1.00	-0.38	-0.03	-0.20	-0.08	-0.55	-0.03	0.10	0.03	0.15	-0.07	0.02	-0.08
7 $b_{f_0 K_S^0}$							1.00	0.38	0.36	-0.10	0.05	-0.35	-0.22	-0.09	0.09	-0.22	0.05	-0.23
8 $b_{\phi K_S^0}$								1.00	0.14	-0.02	-0.13	-0.15	0.05	-0.09	0.14	-0.22	0.03	-0.10
9 $b_{f_X K_S^0}$									1.00	-0.02	0.00	-0.17	-0.06	-0.03	0.01	-0.03	0.01	-0.03
10 $b_{\chi_{c0} K_S^0}$										1.00	-0.01	0.32	0.10	0.05	0.14	-0.05	0.00	0.02
11 $b_{(K_S^0 K^+)_{\rm NR} K^-}$											1.00	0.37	-0.05	-0.02	-0.06	0.03	-0.02	0.04
12 $b_{(K_S^0 K^-)_{\rm NR} K^+}$												1.00	0.05	0.01	0.04	-0.00	-0.03	0.05
13 $d_{f_0 K_S^0}$													1.00	0.58	0.61	0.14	0.03	0.46
14 $d_{\phi K_S^0}$														1.00	0.35	0.46	-0.08	0.37
15 $d_{\rm others}$															1.00	-0.37	0.09	-0.12
16 $c_{f_0 K_S^0}$																1.00	-0.24	0.62
17 $c_{\phi K_S^0}$																	1.00	-0.15
18 $c_{\rm others}$																		1.00

Table D.2: Correlation between each fit parameter for Solution 2.

	1	2	3	4	5	6	7	8	9	10	11	12	13	14	15	16	17	18
1 $a_{f_0 K_S^0}$	1.00	0.52	0.31	0.48	-0.01	0.26	0.03	0.01	-0.56	0.15	-0.28	0.29	-0.10	-0.05	-0.08	-0.20	0.09	0.05
2 $a_{\phi K_S^0}$		1.00	0.23	0.68	0.07	0.52	0.64	0.34	-0.35	0.15	-0.17	0.39	-0.08	-0.08	-0.02	0.00	0.09	0.01
3 $a_{fX K_S^0}$			1.00	0.20	-0.06	0.05	-0.21	-0.10	-0.04	0.14	-0.18	0.28	-0.05	-0.02	-0.02	0.03	-0.01	0.06
4 $a_{\chi_{c0} K_S^0}$				1.00	0.02	0.36	0.49	0.27	-0.31	0.34	-0.08	0.32	-0.05	-0.06	-0.00	0.00	0.04	0.01
5 $a_{(K_S^0 K^+)_{\rm NR} K^-}$					1.00	0.29	0.20	0.14	0.05	0.14	0.17	0.49	0.13	0.08	0.08	-0.05	0.01	-0.05
6 $a_{(K_S^0 K^-)_{\rm NR} K^+}$						1.00	0.48	0.18	-0.27	-0.08	-0.51	-0.06	-0.00	-0.02	0.05	-0.01	0.07	0.02
7 $b_{f_0 K_S^0}$							1.00	0.52	0.11	0.06	0.02	0.17	-0.07	-0.10	0.02	0.07	0.05	0.03
8 $b_{\phi K_S^0}$								1.00	0.08	0.05	0.14	0.19	0.07	-0.07	0.03	-0.09	0.01	-0.04
9 $b_{fX K_S^0}$									1.00	-0.00	0.17	-0.09	0.07	0.04	0.00	0.06	-0.05	-0.05
10 $b_{\chi_{c0} K_S^0}$										1.00	-0.02	0.28	0.04	0.01	0.09	0.05	-0.00	0.06
11 $b_{(K_S^0 K^+)_{\rm NR} K^-}$											1.00	0.47	0.07	0.03	-0.01	0.01	-0.05	-0.12
12 $b_{(K_S^0 K^-)_{\rm NR} K^+}$												1.00	0.02	-0.00	0.01	0.02	-0.02	-0.04
13 $d_{f_0 K_S^0}$													1.00	0.69	0.63	-0.00	-0.12	-0.48
14 $d_{\phi K_S^0}$														1.00	0.32	-0.07	-0.01	-0.39
15 $d_{\rm others}$															1.00	0.44	-0.04	0.10
16 $c_{f_0 K_S^0}$																1.00	-0.16	0.37
17 $c_{\phi K_S^0}$																	1.00	0.08
18 $c_{\rm others}$																		1.00

Table D.3: Correlation between each fit parameter for Solution 3.

	1	2	3	4	5	6	7	8	9	10	11	12	13	14	15	16	17	18
1 $a_{f_0 K_S^0}$	1.00	-0.21	-0.31	-0.08	0.07	-0.23	0.45	0.34	-0.04	0.08	-0.06	0.13	0.03	0.02	0.02	-0.01	0.05	0.05
2 $a_{\phi K_S^0}$		1.00	0.79	0.54	-0.07	0.33	-0.69	-0.24	0.51	0.17	-0.24	0.37	-0.05	-0.03	0.00	-0.02	-0.08	-0.00
3 $a_{f_X K_S^0}$			1.00	0.57	-0.08	0.33	-0.76	-0.26	0.55	0.17	-0.24	0.37	-0.06	-0.04	-0.00	-0.03	-0.06	-0.02
4 $a_{\chi_{c0} K_S^0}$				1.00	-0.07	0.16	-0.50	-0.16	0.39	0.39	-0.09	0.32	-0.03	-0.02	0.03	-0.03	-0.04	0.00
5 $a_{(K_S^0 K^+)_{\rm NR} K^-}$					1.00	0.33	0.15	0.21	0.05	0.16	0.22	0.40	0.10	0.03	0.19	-0.11	0.02	0.00
6 $a_{(K_S^0 K^-)_{\rm NR} K^+}$						1.00	-0.40	-0.06	0.35	-0.11	-0.49	-0.10	0.04	0.02	0.13	-0.07	-0.02	-0.11
7 $b_{f_0 K_S^0}$							1.00	0.34	-0.71	-0.09	0.16	-0.29	0.05	0.04	0.00	0.03	0.06	0.03
8 $b_{\phi K_S^0}$								1.00	-0.13	0.01	0.05	0.02	0.06	-0.09	0.05	-0.11	0.01	0.00
9 $b_{f_X K_S^0}$									1.00	0.11	-0.14	0.19	-0.04	-0.02	0.05	-0.07	-0.04	-0.06
10 $b_{\chi_{c0} K_S^0}$										1.00	0.04	0.30	0.05	0.02	0.12	-0.06	-0.00	0.03
11 $b_{(K_S^0 K^+)_{\rm NR} K^-}$											1.00	0.48	0.03	-0.00	0.00	-0.01	0.01	0.12
12 $b_{(K_S^0 K^-)_{\rm NR} K^+}$												1.00	0.02	-0.02	0.05	-0.06	-0.02	0.11
13 $d_{f_0 K_S^0}$													1.00	0.64	0.64	0.21	0.05	0.15
14 $d_{\phi K_S^0}$														1.00	0.44	0.44	-0.02	0.09
15 $d_{\rm others}$															1.00	-0.17	0.01	-0.05
16 $c_{f_0 K_S^0}$																1.00	-0.18	0.31
17 $c_{\phi K_S^0}$																	1.00	-0.07
18 $c_{\rm others}$																		1.00

Table D.4: Correlation between each fit parameter for Solution 4.

	1	2	3	4	5	6	7	8	9	10	11	12	13	14	15	16	17	18
1 $a_{f_0 K_S^0}$	1.00	0.52	0.63	0.48	-0.04	0.21	0.09	0.02	-0.34	0.15	-0.25	0.29	-0.08	-0.01	-0.07	-0.15	0.06	0.01
2 $a_{\phi K_S^0}$		1.00	0.87	0.69	0.01	0.45	0.72	0.36	0.33	0.17	-0.15	0.42	-0.07	-0.07	-0.05	0.09	0.07	0.01
3 $a_{fX K_S^0}$			1.00	0.72	0.00	0.44	0.73	0.36	0.31	0.18	-0.16	0.43	-0.09	-0.07	-0.07	0.06	0.02	0.06
4 $a_{\chi_{c0} K_S^0}$				1.00	-0.03	0.31	0.56	0.29	0.22	0.35	-0.07	0.34	-0.05	-0.05	-0.04	0.07	0.00	0.01
5 $a_{(K_S^0 K^+)_{\rm NR} K^-}$					1.00	0.21	0.14	0.03	0.21	0.15	0.16	0.49	0.13	0.08	0.10	0.04	-0.01	0.02
6 $a_{(K_S^0 K^-)_{\rm NR} K^+}$						1.00	0.49	0.16	0.27	-0.09	-0.57	-0.12	0.06	0.02	0.08	0.06	0.02	-0.00
7 $b_{f_0 K_S^0}$							1.00	0.50	0.76	0.10	-0.01	0.24	-0.05	-0.08	-0.03	0.11	0.01	0.01
8 $b_{\phi K_S^0}$								1.00	0.38	0.06	0.08	0.15	0.10	0.02	0.02	-0.04	-0.03	-0.02
9 $b_{fX K_S^0}$									1.00	0.06	0.07	0.03	0.05	-0.02	0.03	0.16	-0.03	-0.07
10 $b_{\chi_{c0} K_S^0}$										1.00	-0.00	0.28	0.06	0.03	0.06	0.04	-0.01	0.03
11 $b_{(K_S^0 K^+)_{\rm NR} K^-}$											1.00	0.47	-0.05	-0.04	-0.06	0.05	-0.03	0.03
12 $b_{(K_S^0 K^-)_{\rm NR} K^+}$												1.00	-0.03	-0.03	-0.05	0.11	-0.03	0.07
13 $d_{f_0 K_S^0}$													1.00	0.61	0.77	0.04	-0.09	-0.22
14 $d_{\phi K_S^0}$														1.00	0.36	-0.10	0.02	-0.18
15 $d_{\rm others}$															1.00	0.26	0.02	0.02
16 $c_{f_0 K_S^0 K_S^0}$																1.00	-0.16	0.34
17 $c_{\phi K_S^0}$																	1.00	0.01
18 $c_{\rm others}$																		1.00

Appendix E

Estimation of The Confidence Level Using Bayesian Method

After a brief introduction of Bayes' theorem, we describe how to calculate a confidence level in the Bayesian method, which is employed to determine the confidence level in the CP asymmetry in $B^0 \to \phi K^0_S$ decays.

The marginal probability density function (PDF) as a function of x, which is the distribution in terms of x with an unobserved y, is

$$P_1(x) = \int_{-\infty}^{\infty} f(x,y)dy, \tag{E.1}$$

and the marginal PDF in terms of y, $P_2(y)$, is also defined in the similar way. The conditional PDF as a function of x at a given fixed y is defined as follows,

$$f_1(y|x)P_1(x) = f(x,y), \tag{E.2}$$

and the conditional PDF as a function of y at a given fixed x is also defined in a similar way as follows,

$$f_2(x|y)P_2(y) = f(x,y). \tag{E.3}$$

From these definitions, Bayes' theorem [65] is deduced as follows,

$$f_2(x|y) = \frac{f_1(y|x)P_1(x)}{P_2(y)} = \frac{f_1(y|x)P_1(x)}{\int f_1(y|x)P_1(x)dx}. \tag{E.4}$$

Suppose that we want to make an interval about a parameter, α, whose true value is fixed but unknown. Here we assume that we measure an observable x once and the PDF to obtain x depends on the unknown parameter, α, in a known PDF, $f(x|\alpha)$. Although one measurement provides $f(x|\alpha)$, what we really want to know is $g(\alpha|x)$; if we measure x, the true α lies between α and $\alpha + d\alpha$ with a probability of $g(\alpha|x)d\alpha$. By using Eq. E.4, this

condition is expressed as follows,

$$g(\alpha|x) = \frac{f(x|\alpha)P(\alpha)}{\int f(x|\alpha)P(\alpha)d\alpha}, \tag{E.5}$$

where $P(\alpha)$ is a prior PDF. A Bayesian interval, $[\alpha_1, \alpha_2]$, that corresponds to a confidence level, ϵ, has the relation,

$$\int_{\alpha_1}^{\alpha_2} g(\alpha_t|x)d\alpha_t = \epsilon. \tag{E.6}$$

The Bayesian concept on probability is not based on a limited frequency but more general, which includes degrees of belief. This is often employed for experiments that cannot be repeated, where a frequency definition on probability would be difficult to parameterize, and thus is well adapted to decision-making situations. In addition, Bayesian methods allow us to add more information such as physical boundaries and subjective information; they require a prior distribution for an estimated parameter as an input.

Bibliography

[1] K. Abe *et al.* [Belle Collaboration], "Observation of Large CP Violation in the Neutral B Meson System," Phys. Rev. Lett, **87**, 091801 (2001)

[2] B. Aubert *et al.* [BaBar Collaboration], "Observation of CP Violation in the B^0 Meson System," Phys. Rev. Lett, **87**, 091801 (2001)

[3] Belle Collaboration, http://belle.kek.jp/.

[4] BaBar Collaboration, http://www.slac.stanford.edu/BFROOT/.

[5] M. Kobayashi and T. Maskawa, "CP violation in the renormalizable theory of weak interaction," Prog. Theor. Phys., **49**, 652-657 (1973)

[6] A. B. Carter and A. I. Sanda, "CP Violation in Cascade Decays of B Mesons," Phys. Rev. Lett. **45**, 952 (1980); A. B. Carter and A. I. Sanda, "'CP Violation in B Decays," Phys. Rev. D **23**, 1567 (1981); I. I. Bigi and A. I. Sanda, "Notes on the Observability of CP Violation in B Decays," Nucl. Phys. **193**, 85 (1981).

[7] http://lhc.web.cern.ch/lhc

[8] Y. Grossman and M. P. Worah, Phys. Lett. B **395**, 241 (1997); D. London and A. Soni, Phys. Lett. B **407**, 61 (1997); T. Moroi, Phys. Lett. B **493**, 366 (2000); D. Chang, A. Masiero and H. Murayama, Phys. Rev. D **67**, 075013 (2003); S. Baek, T. Goto, Y. Okada and K. Okumura, Phys. Rev. D **64**, 095001 (2001).

[9] K.-F. Chen *et al.* (Belle Collaboration), "Observation of time-dependent CP violation in $B^0 \to \eta\prime\, K^0$ decays and improved measurements of CP asymmetries in $B^0 \to \phi\, K^0$, $B^0 \to K^0_S K^0_S K^0_S$ and $B^0 \to J/\psi\, K^0$ decays", Phys. Rev. Lett **98**, 031802 (2007).

[10] R. Fleischer, Phys. Lett. B **341**, 205 (1994). A. K. Giri and R. Mohanta, J. High Energy Phys. **11**, 084 (2004).

[11] Events are generated with the Evtgen generator, D. J. Lange, Nucl. Instrum. Methods Phys. Res., Sect. A **462**, 152 (2001); the detector response is simulated with GEANT, R. Brun *et al.*, GEANT 3.21, CERN Report No. DD/EE/84-1, 1984.

[12] L. Wolfenstein, "Parametrization of the Kobayashi-Maskawa Matrix", Phys. Rev. Lett. **51**, 1945 (1983).

[13] N. Cabibbo, "Unitary Symmetry and Leptonic Decays," Phys. Rev. Lett. **10**, 531-532 (1963).

[14] T. Inami and C.S. Lim, Prog. Theor. Phys. **65**, 297 (1981)

[15] F. Gilman and M. Wise, Phys. Rev. D **27**, 1128 (1983).

[16] A.J. Buras, M. Jamin and P.H. Weisz, Nucl. Phys. B **347**, 491 (1990).

[17] J.S. Hagelin, Nucl. Phys. B **193**, 123 (1981).

[18] I. I. Bigi and A. I. Sanda, "CP Violation. No. 9 in Cambridge monographs on particle physics, nuclear physics, and cosmology," Cambridge University Press (2000).

[19] H. n. Li and S. Mishima, "Penguin pollution in the $B^0 \to J/\psi K^0_S$ decay," JHEP **0703**, 009 (2007).

[20] Heavy Flavor Averaging Group (HFAG), "Results on Time-Dependent CP Violation, and Measurements Related to the Angles of the Unitarity Triangle (Summer2008)", http://www.slac.stanford.edu/xorg/hfag/triangle/index.html.

[21] CKMfitter Group, "Results as of summer 2007", http://www.slac.stanford.edu/xorg/ckmfitter/ckm_results_beauty2007.html.

[22] S. Kurokawa and E. Kikutani, *Nucl. Instrum. Meth.*A **499**, 1 (2003), and other papers included in this volume.

[23] A. Abashian *et al.* [Belle Collaboration], "The Belle Detector," *Nucl. Instrum. Meth.*A **479**, 117 (2002).

[24] Y. Ushiroda, "Belle silicon vertex detectors," *Nucl. Instrum. Meth.*A **511**, 6 (2003).

[25] H. Hirano *et al.*, "A high resolution cylindrical drift chamber for the KEK B-factory," *Nucl. Instrum. Meth.*A **455**, 294 (2000).

[26] T. Iijima *et al.*, "Aerogel Cherenkov counter for the BELLE detector," *Nucl. Instrum. Meth.*A **453**, 321 (2000).

[27] H. Kichimi *et al.*, "The BELLE TOF system," *Nucl. Instrum. Meth.*A **453**, 315 (2000).

[28] H. Ikeda *et al.*, "A detailed test of the CsI(Tl) calorimeter for BELLE with photon beams of energy between 20 MeV and 5.4 GeV," *Nucl. Instrum. Meth.*A **441**, 401 (2000).

[29] Belle Collaboration, A. Abashian *et al.*, "The K^0_L/μ detector subsystem for the BELLE experiment at the KEK B-factory," *Nucl. Instrum. Meth.*A **449**, 112 (2000).

[30] A. Garmash *et al.* [Belle Collaboration], Phys. Rev. D **69**, 012001 (2004).

[31] Y. Chao *et al.* (Belle Collaboration), "Measurements of time-dependent CP violation in $B^0 \to \omega K^0_S, f_0(980)K^0_S, K^0_S\pi^0$ and $K^+K^-K^0_S$ decays," Phys. Rev. D **76**, 091103 (2007).

[32] B. Aubert *et al.* [BaBar Collaboration], Phys. Rev. D **71**, 032005 (2005). B. Aubert *et al.* [BaBar Collaboration], Phys. Rev. D **74**, 091101 (2006). B. Aubert *et al.* [BaBar Collaboration], Phys. Rev. Lett. **99**, 231802 (2007). R. Itoh *et al.* [Belle Collaboration], Phys. Rev. Lett. **95**, 091601 (2005). P. Krokovny *et al.* [Belle Collaboration], Phys. Rev. Lett. **97**, 081801 (2006). J. Dalseno *et al.* [Belle Collaboration], Phys. Rev. D **76**, 072004 (2007).

[33] Wayne J. Holman, "Modified Isobar Approximation for $\pi - \rho$ Scattering," Phys. Rev. **138**, 5B, 1286-1303 (1965).

[34] J. Blatt and V. E. Weisskopf, *Theoretical Nuclear Physics*, J. Wiley & Sons, New York (1952).

[35] W.-M. Yao *et al.*, J. Phys. **G** 33, 1 (2006).

[36] S. M. Flatté, Phys. Lett. B **63**, 224 (1976).

[37] A. Garmash *et al.* (Belle Collaboration), "Dalitz analysis of the three-body charmless decays $B^+ \to K^+\pi^+\pi^-$ and $B^+ \to K^+K^+K^-$", Phys. Rev. D **71**, 092003 (2005).

[38] B. Aubert *et al.* [BaBar Collaboration], "Measurement of CP-Violating Asymmetries in the $B^0 \to K^+K^-K^0_S$ Dalitz Plot," arXiv:0808.0700 [hep-ex].

[39] M. Ablikim *et al.* [BES Collaboration], "Resonances in $J/\psi \to \phi\pi^+\pi^-$ and ϕK^+K^-," Phys. Lett. B **607**, 243 (2005).

[40] B. Aubert *et al.* [BaBar Collaboration], "An amplitude analysis of the decay $B^\pm \to \pi^\pm\pi^\pm\pi^\pm$ decays," Phys. Rev. D **72**, 052002 (2005).

[41] B. Casey, "Hadron$B$," Belle Note #390 (Private Internal Note).

[42] G. C. Fox and S. Wolffram, Phys. Rev. Lett. **41**, 1581 (1978), K. Abe *et al.* [Belle Collaboration], Phys. Rev. Lett. **87**, 101801 (2001) and S. H. Lee *et al.* [Belle Collaboration], Phys. Rev. Lett. **91**, 261801 (2003).

[43] S.-W. Lin *et al.* [Belle Collaboration], Phys. Rev. Lett. **98**, 181804 (2007).

[44] H. Tajima *et al.*, *Nucl. Instrum. Meth.*A **533**, 370 (2004).

[45] B. Aubert *et al.* [BaBar Collaboration], "Measurements of CP violating asymmetries in $B^0 \to K^0_S\pi^0$ decays," Phys. Rev. Lett. **93**, 131805 (2004).

[46] K. Sumisawa *et al.* [Belle Collaboration], "Measurement of time-dependent CP-violating asymmetries in $B^0 \to K^0_S K^0_S K^0_S$ decay," Phys. Rev. Lett. **95**, 061801 (2005).

[47] H. Kakuno *et al.*, "Neutral B flavor tagging for the measurement of mixing-induced CP violation at Belle," *Nucl. Instrum. Meth.*A **533**, 516 (2004).

[48] H. Albrecht *et al.* [ARGUS Collaboration], Phys. Lett. B **241**, 278 (1990).

[49] O. Long *et al.*, Phys. Rev. D **68**, 034010 (2003).

[50] B. Aubert *et al.* [BaBar Collaboration], "Observation of $B^+ \to \overline{K^0}K^+$ and $B^0 \to K^0\overline{K^0}$," Phys. Rev. Lett. **97**, 171805 (2006).

[51] Y. Nakahama *et al.* [Belle Collaboration], Phys. Rev. Lett. **100**, 121601 (2008).

[52] K. Inami *et al.* [Belle Collaboration], "First observation of the Decay $\tau^- \to \phi K^- \nu_\tau$," Phys. Lett. B **643**, 5 (2006).

[53] B. Aubert *et al.* [BaBar Collaboration], "Dalitz analysis of the three-body charmless decays $B^+ \to K^+\pi^+\pi^-$ and $B^+ \to K^+K^+K^-$", Phys. Rev. D **71**, 092003 (2005).

[54] E. M. Aitala *et al.* [Fermilab E791 Collaboration], "Study of the $D_S \to \pi^-\pi^+\pi+$ Decay and Measurement of f_0 Masses and Width" Phys. Rev. Lett. **86**, 765 (2001).

[55] Y. Grossman, Z. Ligeti, Y. Nir, and H. Quinn, "SU(3) Relations and the CP Asymmetries in B decays to $\eta' K^0_S$, ϕK^0_S and $K^+K^-K^0_S$," Phys. Rev. **D68**(2003) 015004, hep-ph/0303171.

[56] M. Beneke, "Corrections to $\sin(2\beta)$ from CP Asymmetries in $B^0 \to (\pi^0, \eta^0, \eta, \eta', \omega, \phi)K^0_S$ Decays, "hep-ph/0505075."

[57] M. Ciuchini *et al.* "Two-body nonleptonic B decays in the Standard Model and beyond," hep-ph/0407073

[58] H.-Y. Cheng, C.-K. Chua, and A. Soni, "Effects of Final-state Interactions on Mixing-induced CP Violation in Penguin-dominated B Decays" Phys. Rev. **D72** 014006 (2005).

[59] H.-Y. Cheng, C.-K. Chua, and A. Soni, "Charmless Three-body Decays of B Mesons," Phys. Rev. **D76** 094006 (2007).

[60] M. Gronau and J. L. Rosner, "I-spin, U-spin, and penguin dominance in $B \to KK\overline{K}$," Phys. Lett. B **341**, 90 (2003).

[61] R. Fleischer, Phys. Lett. B **341**, 205 (1994).

[62] A. K. Giri and R. Mohanta, J. High Energy Phys. **11**, 084 (2004).

[63] K. Abe *et al.*, "Letter Of Intent for KEK Super B Factory," hep-ex/0406071.

[64] http://seal.web.cern.ch/seal/MathLibs/Minuit/html/index.html.

[65] A. Stuart and A. K. Ord, Kendall's Advanced Theory of Statistics, Vol. 1 Distribution Theory 5th Ed., Oxford Univ. Press, (1987).

Index of Symbols

ΔE : Difference between the reconstructed B energy and the beam energy in CMS **Page 67, Eq. 5.1**

$M_{\rm bc}$: Beam-energy constrained mass of B **Page 67, Eq. 5.2**

$\mathcal{R}$: Likelihood ratio based on the event shape of $B\overline{B}$ pairs against $q\overline{q}$ background **Page 73, Eq. 5.10**

Δt : Proper time difference **Page 78, Eq. 5.11**

$R_{\rm sig}(\Delta t)$: Δt resolution function for $B^0\overline{B^0}$ decays **Page 80**

$R_{B^+B^-}(\Delta t)$: Δt resolution function for B^+B^- decays **Page 81**

$q_{\rm tag}$: Flavor of $f_{\rm tag}$ **Page 84**

r : MC-determined dilution factor from 0 to 1 in flavor tagging **Page 84, Eq. 5.12**

ℓ : r-interval region from 0 to 6 **Page 88, Table 5.2**

w_ℓ : Wrong tag fraction in ℓ **Page 88, Table 5.2**

Δw_ℓ : Wrong tag fraction difference between B^0 and $\overline{B^0}$ in ℓ **Page 88, Table 5.2**

P : Factorized PDF **Page 90, Eq. 5.19**

χ_d : Time-integrated $B^0\overline{B^0}$ mixing probability **Page 104, Eq. 6.8**